

# First Realization of a Multi-Turn Energy-Recovery Mode at the S-DALINAC

**Erste Realisierung eines Energierückgewinnungsmodus mit mehreren  
Rezirkulationssollbahnen am S-DALINAC**

Zur Erlangung des akademischen Grades Doctor rerum naturalium (Dr. rer. nat.)  
genehmigte Dissertation von Felix Schließmann

Datum der Einreichung: 14. Mai 2024

Datum der Prüfung: 26. Juni 2024

Jahr der Publikation: 2024


1. Gutachten: Prof. Dr. rer. nat. Dr. h.c. mult. Norbert Pietralla
2. Gutachten: Prof. Dr. rer. nat. Joachim Enders

Fachbereich Physik, Technische Universität Darmstadt, Darmstadt



TECHNISCHE  
UNIVERSITÄT  
DARMSTADT

Fachbereich Physik  
Institut für Kernphysik  
AG Pietralla

Accepted dissertation by Felix Schließmann (ORCID  0000-0002-4900-7508)  
for the academic degree of Doctor rerum naturalium (Dr. rer. nat.)

Original title:

First Realization of a Multi-Turn Energy-Recovery Mode at the S-DALINAC

German title:

Erste Realisierung eines Energierückgewinnungsmodus mit mehreren  
Rezirkulationsollbahnen am S-DALINAC

1. Review: Prof. Dr. rer. nat. Dr. h.c. mult. Norbert Pietralla

2. Review: Prof. Dr. rer. nat. Joachim Enders

Date of submission: May 14, 2024

Date of thesis defense: June 26, 2024

Year of publication in TUprints: 2024

Darmstadt, Technische Universität Darmstadt

Identifier:

DOI: 10.26083/tuprints-00027811

URN: urn:nbn:de:tuda-tuprints-278116

URL: <https://tuprints.ulb.tu-darmstadt.de/27811>

Original citation:

F. Schließmann, “First Realization of a Multi-Turn Energy-Recovery Mode at the S-DALINAC”,  
Dissertation, TU Darmstadt (2024). <https://doi.org/10.26083/tuprints-00027811>

Transliterated citation:

F. Schliessmann, “First Realization of a Multi-Turn Energy-Recovery Mode at the S-DALINAC”,  
Dissertation, TU Darmstadt (2024). <https://doi.org/10.26083/tuprints-00027811>



Figures 4.3, 4.4 and 4.8 are copyrighted under exclusive license to Springer Nature Limited. Any other content from this work may be used under the terms of the Creative Commons Attribution 4.0 International (CC BY 4.0) license. Details on the license are provided at <https://creativecommons.org/licenses/by/4.0/>.

---

## Erklärung zur Dissertation

Ich versichere hiermit: Die vorliegende Arbeit wurde, abgesehen von den in ihr ausdrücklich genannten Hilfen und Quellen, selbstständig verfasst. Die „Grundsätze zur Sicherung guter wissenschaftlicher Praxis an der Technischen Universität Darmstadt“ und die „Leitlinien zum Umgang mit digitalen Forschungsdaten an der TU Darmstadt“ wurden in den jeweils aktuellen Versionen bei der Verfassung der Dissertation beachtet. Zu einem vorherigen Zeitpunkt wurde noch keine Promotion versucht. Diese Arbeit hat bisher noch nicht zu Prüfungszwecken gedient.

Darmstadt, 14.05.2024

Felix Schließmann



---

# Abstract

The main topic of this work is the first realization of a multi-turn energy-recovery mode at the superconducting Darmstadt electron linear accelerator (S-DALINAC). In such an operation mode, electrons first pass the main linear accelerator (LINAC) multiple times to accumulate the energy gain per pass, which – for a given main-LINAC capability per pass – enables higher electron energies compared to a one-pass operation. During this acceleration, energy is withdrawn from the alternating electric fields located inside the cavities of the main LINAC and supplied to the electrons. After this multiple acceleration, the electrons pass the main LINAC for a multiple deceleration, while the number of passes for the acceleration and the number of passes for the deceleration are equal. Deceleration is possible by passing the alternating electric fields with a corresponding phase offset. During the deceleration, the process is reversed, that is, energy is withdrawn from the electrons and restored to the alternating electric fields and thus recovered in the main LINAC. Due to the use of superconducting cavities, the recovered energy is temporarily stored almost losslessly and can thus be almost completely recycled during the acceleration of subsequent electrons. Compared to the corresponding conventional operation, operating the main LINAC as an energy-recovery LINAC (ERL) therefore requires less externally provided radio-frequency power to accelerate a given number of electrons per time, that is, a given beam current. Consequently, operating the main LINAC as an ERL enables the acceleration of higher beam currents for a given externally provided radio-frequency power compared to the corresponding conventional operation. In summary, a multiple acceleration with an ERL enables both high electron energies and high beam currents, and thus high beam powers.

Multiple passing of the main LINAC is possible since its exit is connected to its entrance via recirculation beamlines. In a multi-turn energy-recovery mode at the S-DALINAC, beams are superimposed in at least one recirculation beamline. Such a common recirculation transport provides less degrees of freedom compared to a separate recirculation transport; however, the former transport scheme is more cost-efficient. Furthermore, a high machine efficiency can be achieved if the electron energy when leaving the injector LINAC (injector energy) is as low as possible since energy delivered to the electrons in upstream located sections cannot be recovered at the S-DALINAC and therefore cannot be recycled. However, a low injector energy results in an electron speed that differs significantly from speed of light, which leads to significant phase slippage during a main-LINAC pass, which in turn affects the acceleration and the deceleration, respectively. The occurring phase slippage in combination with the common recirculation transport makes beam-dynamics simulations necessary to determine a suitable working point.

---

This work covers the necessary preparations to realize a two-turn energy-recovery mode at the S-DALINAC, in particular beam-dynamics simulations and beamline modifications, as well as the successful realization of the operation mode itself. Within the scope of this work, wire scanners were constructed, installed and utilized for quasi–non-destructive beam-diagnostics while operating in the two-turn energy-recovery mode. Furthermore, beam-dynamics simulations have been conducted to study a potential three-turn energy-recovery mode at the S-DALINAC.

---

# Zusammenfassung

Hauptgegenstand der vorliegenden Arbeit ist die erste Realisierung eines Energierückgewinnungsmodus mit mehreren Rezirkulationssollbahnen am supraleitenden Darmstädter Elektronenlinearbeschleuniger (deutsch für superconducting Darmstadt electron linear accelerator, S-DALINAC). In einem solchen Betriebsmodus passieren Elektronen den Hauptlinearbeschleuniger zunächst mehrmals für eine Akkumulation des pro Durchgang erzielten Energiegewinns, was – bei gegebenem Hauptlinearbeschleunigerleistungsvermögen pro Durchgang – im Vergleich zu einem Betrieb mit einem einzigen Durchgang höhere Elektronenenergien ermöglicht. Während dieser Beschleunigung wird den elektrischen Wechselfeldern, die sich in den Kavitäten des Hauptlinearbeschleunigers befinden, Energie entzogen und den Elektronen zugeführt. Nach dieser mehrfachen Beschleunigung passieren die Elektronen den Hauptlinearbeschleuniger für eine mehrfache Abbremsung, wobei die Anzahl der Durchgänge für die Beschleunigung und die Anzahl der Durchgänge für die Abbremsung gleich sind. Abbremsung ist durch das Passieren der elektrischen Wechselfelder mit einem entsprechenden Phasenversatz möglich. Während der Abbremsung ist der Vorgang umgekehrt, das heißt, Energie wird den Elektronen entzogen und an die elektrischen Wechselfelder zurückgegeben und somit im Hauptlinearbeschleuniger zurückgewonnen. Durch die Verwendung von supraleitenden Kavitäten wird die zurückgewonnene Energie nahezu verlustfrei zwischengespeichert und kann daher bei der Beschleunigung nachfolgender Elektronen fast vollständig wiederverwendet werden. Somit benötigt der Betrieb des Hauptlinearbeschleunigers als Energierückgewinnungslinearbeschleuniger (deutsch für energy-recovery linear accelerator, ERL) im Vergleich zum entsprechenden konventionellen Betrieb weniger extern bereitgestellte Hochfrequenzleistung, um eine bestimmte Anzahl an Elektronen pro Zeit, das heißt einen bestimmten Strahlstrom, zu beschleunigen. Infolgedessen ermöglicht der Betrieb des Hauptlinearbeschleunigers als ERL bei gegebener extern bereitgestellter Hochfrequenzleistung im Vergleich zum entsprechenden konventionellen Betrieb die Beschleunigung höherer Strahlströme. Zusammenfassend ermöglicht eine mehrfache Beschleunigung mit einem ERL sowohl hohe Elektronenenergien als auch hohe Strahlströme und somit hohe Strahlleistungen.

Mehrfaches Passieren des Hauptlinearbeschleunigers ist möglich, da sein Ausgang über Rezirkulationsstrahlführungen mit seinem Eingang verbunden ist. In einem Energierückgewinnungsmodus mit mehreren Rezirkulationssollbahnen am S-DALINAC überlagern sich Strahlen in mindestens einer Rezirkulationsstrahlführung. Solch ein gemeinsamer Rezirkulationstransport bietet weniger Freiheitsgrade als ein getrennter Rezirkulationstransport; allerdings ist das erstgenannte Transportschema kosteneffizienter. Darüber hinaus kann

---

eine hohe Maschineneffizienz erreicht werden, wenn die Elektronenenergie beim Verlassen des Injektorlinearbeschleunigers (Injektorenergie) möglichst gering ist, da die den Elektronen in flussaufwärts gelegenen Sektionen zugeführte Energie am S-DALINAC nicht zurückgewonnen und folglich nicht wiederverwendet werden kann. Eine geringe Injektorenergie bringt jedoch eine sich deutlich von der Lichtgeschwindigkeit unterscheidende Elektronengeschwindigkeit mit sich, was zu signifikantem Phasenschlupf während eines Hauptlinearbeschleunigerdurchgangs führt, was sich wiederum auf die Beschleunigung beziehungsweise die Abbremsung auswirkt. Der auftretende Phasenschlupf in Kombination mit dem gemeinsamen Rezirkulationstransport macht Strahldynamiksimulationen notwendig, um einen geeigneten Arbeitspunkt ermitteln zu können.

Diese Arbeit umfasst die notwendigen Vorbereitungen zur Realisierung eines Energierückgewinnungsmodus mit zwei Rezirkulationssollbahnen am S-DALINAC, insbesondere Strahldynamiksimulationen und Strahlführungsmodifikationen, sowie die erfolgreiche Realisierung des Betriebsmodus selbst. Im Rahmen dieser Arbeit wurden Drahtscanner konstruiert, installiert und zur quasizerstörungsfreien Strahldiagnose während des Betriebs im Energierückgewinnungsmodus mit zwei Rezirkulationssollbahnen genutzt. Darüber hinaus wurden Strahldynamiksimulationen durchgeführt, um einen möglichen Energierückgewinnungsmodus mit drei Rezirkulationssollbahnen am S-DALINAC zu untersuchen.



---

# Contents

<b>1</b>	<b>Introduction</b>	<b>1</b>
1.1	Terminology . . . . .	2
1.2	Operating Principle and Characteristics of ERLs . . . . .	3
1.3	History and Future of ERLs . . . . .	10
1.4	Potential for Energy Saving and Sustainability Using ERLs . . . . .	11
1.5	Motivation for This Work . . . . .	12
<b>2</b>	<b>S-DALINAC</b>	<b>15</b>
2.1	Layout and Operation Modes . . . . .	15
2.2	Beam Diagnostics . . . . .	22
<b>3</b>	<b>Fundamentals on Beam Dynamics</b>	<b>23</b>
3.1	Coordinate System in Motion . . . . .	23
3.2	Equation of Motion and Lorentz Force . . . . .	24
3.3	Energy Gain and Reduction in Alternating Electric Fields . . . . .	24
3.4	Deflection in Static Magnetic Fields . . . . .	33
3.5	Transverse and Longitudinal Dispersion . . . . .	39
3.6	Phase Space and Trace Space . . . . .	44
3.7	Influencing the Longitudinal Phase Space . . . . .	47
3.8	Instability Effects . . . . .	47
3.8.1	Beam Breakup Due to Wakefields and Higher-Order Modes . . . . .	49
3.8.2	Space-Charge Effects . . . . .	51
3.8.3	Synchrotron Radiation . . . . .	52
<b>4</b>	<b>Multi-Turn Energy-Recovery Modes at the S-DALINAC</b>	<b>57</b>
4.1	Details on the Operating Principle . . . . .	57
4.2	Two-Turn Energy-Recovery Mode . . . . .	61
4.2.1	Objectives and Degrees of Freedom . . . . .	61
4.2.2	Beam-Dynamics Simulations . . . . .	63
4.2.3	Necessary Upgrades of the S-DALINAC . . . . .	70
4.2.4	Setting up the S-DALINAC . . . . .	71
4.2.5	Verification of the Realized 2-ER Mode and Measurement Results . . . . .	76
4.2.6	Energy Saving Aspects . . . . .	82
4.3	Three-Turn Energy-Recovery Mode . . . . .	83
4.3.1	Objectives and Degrees of Freedom . . . . .	84

---

4.3.2	Beam-Dynamics Simulations . . . . .	85
4.3.3	Conclusion . . . . .	88
<b>5</b>	<b>Measurement of Beam Quantities in Energy-Recovery Modes</b>	<b>91</b>
5.1	Choice of the Diagnostic Device . . . . .	91
5.2	Locations of the Wire Scanners . . . . .	93
5.3	Design and Construction of the Measurement Systems . . . . .	95
5.4	Measurement Results . . . . .	98
5.4.1	Commissioning Measurements . . . . .	98
5.4.2	Comparison of Operating Voltages of the Linear Actuator . . . . .	99
5.4.3	Comparison of Beam Properties in the 2-CA and the 2-ER Mode . . .	100
5.5	Conclusion . . . . .	103
<b>6</b>	<b>Conclusion and Outlook</b>	<b>105</b>
<b>A</b>	<b>Details on the Beam-Dynamics Simulations</b>	<b>109</b>
<b>B</b>	<b>Parameters of the Simulations</b>	<b>113</b>
<b>C</b>	<b>Relations Between Matrix Elements</b>	<b>115</b>
C.1	Causing and Influencing Dispersion . . . . .	115
C.2	Matrix Component Relating to the Relative Distance Traveled . . . . .	116
C.3	Properties of an Achromat . . . . .	116
<b>D</b>	<b>Impacts Due to Space-Charge Effects and Synchrotron Radiation</b>	<b>121</b>
<b>E</b>	<b>Determination of the Longitudinal Dispersion</b>	<b>127</b>
	<b>Bibliography</b>	<b>135</b>

---

# 1 Introduction

Electron linear accelerators (LINACs) are essential devices for a variety of applications utilized in fundamental research [1], industry [2] and medicine [3]. While conventional LINAC facilities (see section 1.1 for its definition) have the potential to provide beams of high quality [4], they have the drawback of high energy requirements to provide beams of high current [5]. Depending on the experiment, a high beam current and a high electron energy can be required for an intended interaction, while only a small amount of the beam's kinetic energy may be transferred during that interaction. If this is the case for an experiment conducted at a conventional LINAC facility, the beam is dumped after the intended interaction with its remaining large amount of energy. Thus, the vast majority of the electrons' kinetic energy supplied during acceleration is almost completely converted into heat load at the beam dump. If the corresponding thermal energy is not exploited, nearly the entire amount of energy supplied to the electrons during acceleration is wasted.

However, if the electron beam is of sufficient quality after the intended interaction in order to be guided to a location of appropriate deceleration, the technology of energy recovery can be used to recycle a substantial part of the kinetic energy of the electrons: if deceleration takes place in electric fields and the electron's energy lost during deceleration is restored in the electric fields, the restored energy can afterward be reused to accelerate subsequent electrons. Using such an energy-recovery LINAC (ERL) has the potential to reduce the need of externally provided power significantly (see section 1.4). Furthermore – due to the deceleration as part of the energy-recovery process – an electron to be dumped is of lower energy compared to the case of corresponding conventional dumping at maximum energy, and thus energy-recovery operation enables reduction of induced radioactivity at the beam dump [6].

A sufficient beam quality for further beam transport can be ensured if the overall electron beam is only slightly affected during the intended interaction. This is the case if either (i) all electrons interact but are only slightly affected or (ii) only a small fraction of the electrons interacts at all such that the vast majority of the electrons remain undisturbed. As a consequence of such an interaction, the energy spread and/or normalized transverse emittance of the electron beam may increase; however, because not the beam itself<sup>1</sup> is recycled but only its energy (see section 1.2 for details), such an impairment of the beam

---

<sup>1</sup>In this work, the focus is on machine designs in which particles pass through a system only once. However, there is a proposal in which particles themselves are recycled as well [7], and thus pass through the system several times; in this proposal, the particles are not dumped after energy recovery but damped in rings to cool them to low emittances prior to reuse.

---

quality is irrelevant as long as a loss-free beam transport to the intended beam dump with an upstream energy withdrawal for energy recovery can be ensured.

Therefore, ERLs are suitable for (i) beam–beam collision experiments [8], (ii) beam–target collision experiments if the density of the target is small such as at a windowless gas jet target [9], (iii) coolers [10], or (iv) light sources in the form of a free-electron laser (FEL) [11] or based on laser Compton backscattering (LCB) [12].

In particle accelerators, energy recovery is possible in static [13] and dynamic [14] electric fields. In this work, only the latter is addressed. More precisely, the focus is on energy recovery in a LINAC in which the radio frequency (RF) fields form a standing wave. Acceleration and deceleration can take place at the same location [15] or spatially separated [16]. In the latter case, the energy recovered during deceleration is transferred via bridge couplers so that it can be recycled during acceleration [17]. The subject of this work is on acceleration and deceleration at the same location. Utilizing alternating electric fields enables energy recovery at the same location, where beams to be decelerated travel either in the same [18] or opposite [4] direction as beams to be accelerated. In this work, the focus is on the former case.

The mentioned concretizations arise from the fact that – within the scope of this work – energy recovery had to be realized in an *enhanced* operation mode at an *existing accelerator that may be capable of this*, which is the superconducting Darmstadt electron linear accelerator (S-DALINAC) [19, 20] at Technische Universität Darmstadt: This machine has the potential to be operated in various energy-recovery modes, where energy may be recovered in standing-wave RF fields, while the location of acceleration and deceleration, as well as the direction of travel of accelerated and decelerated electrons through the LINAC that is suitable for energy recovery, is identical. Further details on the S-DALINAC are provided in chapter 2.

This enhanced operation mode is a *multi-turn* energy-recovery mode in which a LINAC is first passed several times for acceleration and subsequently passed equally often for deceleration. Further details on this operation mode are provided in sections 1.2 and 4.1. While a one-turn energy-recovery operation (see section 1.2 for the definition) already can outperform conventional operation by providing higher beam currents, multi-turn energy-recovery operation has the potential to further increase the machine efficiency by providing higher electron energies for a given LINAC, which thus justifies a study on this enhanced operation mode. A detailed motivation for this work is given in section 1.5.

## 1.1 Terminology

The term “LINAC” is used in a variety of ways: Sometimes, an entire accelerator facility is called “LINAC” if the substantial change in kinetic energy is along a straight line. In this work, such a facility will be referred to as “LINAC facility”. Sometimes, the term “LINAC” is being used more strictly and it describes a device in which both of the following conditions are met: (i) an intended change in kinetic energy is caused by RF fields and (ii) a particle’s

---

design trajectory is necessarily a straight line. That definition of “LINAC” is used in this work, which allows distinguishing between (i) a device used for an exclusive one-way change in kinetic energy (acceleration, as defined below) and (ii) a device used for a two-way change in kinetic energy (acceleration followed by deceleration, as defined below, for energy recovery). Using this definition is appropriate since the S-DALINAC is built in this way: the machine consists of two LINACs of which one is capable for energy recovery (see chapter 2 for details). Consequently, in this work, the term “ERL” refers exclusively to a LINAC as defined above with the potential for energy recovery – and not to an entire facility.

Although the term “acceleration” usually describes any change of the velocity<sup>2</sup> with respect to time, a strict distinction is made in this work: Relating to particles or beams, the term “acceleration” is always to be understood as the net supply of kinetic energy, while the term “deceleration” is always to be understood as the net withdrawal of kinetic energy (and similar for the corresponding adjectives, adverbs and verbs). However, this does not apply to the term “accelerator”, which is why a LINAC (linear accelerator) can – depending on the design – be used for both acceleration and deceleration (and therefore especially for energy recovery).

## 1.2 Operating Principle and Characteristics of ERLs

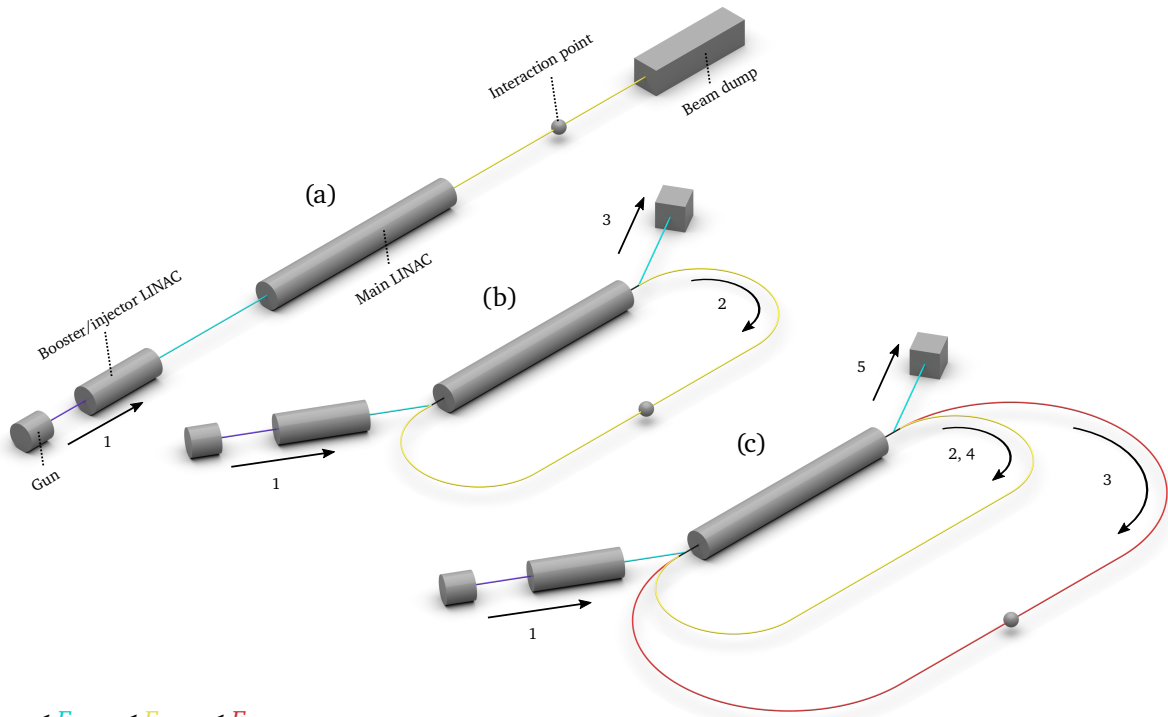
In this section, ERL concepts are briefly explained. More detailed explanations with focus on the S-DALINAC are provided in section 4.1.

To approach the multi-turn energy-recovery concept, a LINAC facility is iteratively re-designed in the following. Using the above given definitions, a common LINAC facility consists of a gun to generate a beam of low-energy particles, one or more LINAC sections, an interaction region for the accelerated particle beam, and a beam dump to stop the particle beam at high energy, see Fig. 1.1(a). Here, the LINAC sections are divided into a booster-LINAC section and a main-LINAC section, where – not in the LINAC facility but in the following redesign – only the latter is intended for energy recovery.

In order to transform a LINAC facility iteratively to a multi-turn energy-recovery accelerator, first the machine’s layout downstream of the main LINAC is rearranged so that the beam is guided back to the main LINAC after the maximum acceleration and the intended interaction as shown in Fig. 1.1(b). If the LINAC consists of appropriate alternating electric fields, a deceleration of the recirculated beam is possible if the particles to be decelerated arrive at the fields with a certain phase offset relative to the accelerating phase (the necessary phase offset depends on the shape of the alternating electric fields and the particle properties); this can be ensured by a certain path length of the recirculation beamline connecting the exit and the entrance of the main LINAC section: if the path length – and therefore the time

---

<sup>2</sup>A strict distinction is made between velocity (the vector) and speed (the vector’s magnitude).



$$E_{\text{kin},0} < E_{\text{kin},0} < E_{\text{kin},0} < E_{\text{kin},0}$$

**Figure 1.1: Transformation from a LINAC facility to a multi-turn energy-recovery accelerator.** The numbers indicate the order of the section passes. The color of a beamline indicates the value of  $E_{\text{kin},0}$ , which is the kinetic energy of the design particle when passing the corresponding beamline; black colored beamlines are passed by design particles of different kinetic energies. (a) A common LINAC facility. The particle beam is initially generated in a gun, is accelerated in LINACs, intentionally interacts in an experiment and is finally dumped with high energy. For the following, it is useful to distinguish between the individual LINACs: there is a booster/injector LINAC and a main LINAC. In a common LINAC facility, both LINACs are dedicated for acceleration only. (b) A one-turn energy-recovery concept. The exit and the entrance of the main LINAC section are connected via a recirculation beamline. After the intended interaction, a particle is decelerated in the main LINAC and finally dumped with an energy that is equal to the one it had after leaving the booster/injector LINAC. Thus, the beam-dump design may be simpler (depending on the deposited beam power), here indicated by a smaller beam dump. (c) A two-turn energy-recovery concept. After the first main-LINAC pass, a particle is guided through the main LINAC for a second acceleration to reach a higher energy. After the intended interaction, the particle is decelerated in the main LINAC to an energy that is equal to the one it had after the first main-LINAC pass. Further downstream, the particle is again guided into the first recirculation beamline due to its rigidity. Here, the once decelerated particle beam is superimposed with a fresh particle beam that was recently accelerated in the main LINAC for the first time. After a second deceleration in the main LINAC, the particle is dumped with an energy that is equal to the one it had after leaving the booster/injector LINAC. (b)–(c) As a result of the deceleration in the main LINAC, energy is recovered in the main LINAC, which makes the main LINAC an ERL. The recovered energy is then almost completely recycled during the acceleration of subsequent particles.

---

of flight – is chosen appropriately, the particles arrive at the main LINAC when the RF field leads to a deceleration.

While the particles are accelerated when they pass the main LINAC for the first time and thereby withdraw energy from the electric fields inside the main LINAC, they are decelerated during the second main-LINAC pass and return energy to the electric field, which makes the main LINAC an ERL. Apart from minor energy losses (due to the finiteness of the quality factors of the cavities), the recovered energy is then almost completely recycled during the acceleration of subsequent particles. In the same way, the recovered energy consumed by these subsequent particles is later on again recovered during the deceleration of these subsequent particles. Hence, apart from small losses, the energy is continuously recycled. As a result, less externally provided RF power is required in this energy-recovery mode compared to the corresponding conventional acceleration mode if an equal number of particles per time (that is, an equal beam current) is accelerated in both operation modes. However, if the externally provided RF power during operation in the energy-recovery mode is equal to the one during operation in the corresponding conventional acceleration mode, recycling of the recovered energy in addition with utilizing of the externally provided RF power enables a higher number of particles to be supplied with the same energy per particle per time when operating in the energy-recovery mode; that is, for a given externally provided RF power, the maximum beam current available in an energy-recovery mode exceeds the one available in the corresponding conventional acceleration mode.

If static magnetic fields are used for beam deflection, particles of the same type but with different kinetic energy travel on different trajectories with different bending radii<sup>3</sup>. Therefore, the beam leaving the main LINAC after acceleration travels with high energy through the recirculation beamline, while the beam leaving the main LINAC after deceleration travels with low energy to the beam dump. Due to the presence of static magnetic fields, the trajectories from the booster LINAC to the main LINAC and from the main LINAC to the beam dump are affected, which has to be taken into account. The following applies if the design trajectory is only horizontally deflected with respect to a coordinate system at rest: On the one hand, if the gun, the booster LINAC and the beam dump would be placed so that they are enclosed by the main LINAC and the recirculation beamline, less dipole magnets would be necessary. On the other hand, placing the gun, the booster LINAC and the beam dump so that they are not enclosed by the main LINAC and the recirculation beamline supports – for a given main LINAC and recirculation beamline – (i) larger components of the gun, the booster LINAC and the beam dump, (ii) larger beamlines for beam manipulation and diagnostics, and (iii) more appropriate shielding of radiation produced at the beam dump.

Due to the deceleration in the main LINAC, the particles arrive at the beam dump with a centroid energy that is equal to the one they had after leaving the booster LINAC (booster

---

<sup>3</sup>If static magnetic fields are used, the absolute value of the bending radius for a given particle type is a function of the kinetic energy only and strictly monotonically increasing (see Eq. (3.27)). Here, the absolute value is addressed since the bending radius may be negative; the sign indicates the direction of deflection.

---

energy<sup>4</sup>) and is thus lower compared to the maximum particle energy after the acceleration in the main LINAC. As a result, the original beam dump used in the LINAC facility can be replaced by one sufficient for lower particle energies<sup>5</sup>.

In the presented energy-recovery concept, the particles pass through the system only once. Thus, only the particles' kinetic energy is recycled but not the particles themselves. Consequently, a decreasing beam quality after the intended interaction after the maximum acceleration is insignificant as long as the interacted beam can still be transported to the intended dump location as well as the kinetic energy can be recovered in the LINAC (which is located downstream of the interaction point and upstream of the intended dump location, respectively). That is, in the presented energy-recovery concept, energy of the particles that form a beam whose quality is reduced as a consequence of the intended interaction is withdrawn during deceleration and later on recycled during the acceleration of subsequent particles of a fresh beam of high quality.

In the presented design, a recirculation beamline is used to link acceleration and deceleration at the same location. Due to this circular structure, the booster LINAC is also referred to as injector LINAC<sup>6</sup>, and the design trajectory is also referred to as design orbit.

The concept shown in Fig. 1.1(b) corresponds to a one-turn energy-recovery operation. Here, the main LINAC was passed by a particle once for acceleration and once for deceleration. If otherwise the main LINAC is passed by a particle several times for acceleration before passed equally often for deceleration, it is referred to as multi-turn energy-recovery concept. As a consequence, the number of recirculations increases. Here, the main LINAC is passed  $J$  times, that is,  $J/2$  times for acceleration and  $J/2$  times for deceleration. Consequently, the beam is recirculated  $J - 1$  times ( $J/2$  accelerated beams and  $J/2 - 1$  decelerated beams are recirculated, while the last decelerated beam travels to the beam dump). If the main LINAC withdraws the same amount of kinetic energy from a particle per pass during deceleration in reverse order that it previously delivered to the very particle per pass during acceleration, and if there are no instability effects influencing the energy of the very particle, then there are  $J/2 - 1$  out of  $J/2$  accelerated beams downstream of the main LINAC (all accelerated beams except the last one) each of which has the same design energy as one of  $J/2 - 1$  out of  $J/2$  decelerated beams downstream of the main LINAC (all decelerated beams except the

---

<sup>4</sup>In the same way, the momentum present after leaving the booster LINAC is referred to as booster momentum.

<sup>5</sup>The particle energy is reduced at the beam dump while operating in an energy-recovery mode compared to operating in the corresponding conventional acceleration mode. However, for a given externally provided RF power, the beam current is higher while operating in an energy-recovery mode compared to operating in the corresponding conventional acceleration mode. Thus, the beam power (which is proportional to the beam current times the centroid particle energy present at the addressed location) deposited at the beam dump while operating in an energy-recovery mode can exceed the one deposited while operating in the corresponding conventional acceleration mode. Consequently, when designing a beam dump, the maximum particle energy during dumping *and* the maximum deposited beam power have to be taken into account.

<sup>6</sup>Thus, the booster energy is also referred to as injector energy, and the booster momentum is also referred to as injector momentum.



---

last one). If static magnetic fields are used, those beams share the same design orbit pairwise (one pair per design energy), which is called common recirculation transport [21]. In this concept, there are  $J/2$  design recirculation orbits ( $J/2-1$  design recirculation orbits with two superimposed beams (an accelerated one and a decelerated one) and one design recirculation orbit for the single beam after maximum acceleration). Following the convention given in Ref. [22], this energy-recovery concept using common recirculation transport is referred to in this work as  $J/2$ -turn energy-recovery mode, which allows highlighting the number of design recirculation orbits as well as the number of main-LINAC passes for deceleration and thus the number of energy-recovery processes<sup>7</sup>. Here, the smallest possible multi-turn energy-recovery configuration is a two-turn energy-recovery mode as shown in Fig. 1.1(c).

Consecutive accelerations or consecutive decelerations in a multi-turn concept, respectively, result if the times of flight through the corresponding recirculation beamlines – also provided by certain path lengths – lead to almost zero phase offset when arriving at the RF fields (here as well: the necessary phase offsets depend on the shape of the alternating electric fields and the particle properties). Similar to the one-turn concept, the first deceleration in a multi-turn concept results if the time of flight through the corresponding recirculation beamline – again provided by a certain path length – leads to an appropriate phase offset when arriving at the RF fields (again, the necessary phase offset depends on the shape of the alternating electric fields and the particle properties).

Multiple passing a main LINAC enables accumulation of the particles' energy gain per pass, which thus supports higher particle energies compared to only one-pass operation; comparing a multi-turn to a one-turn energy-recovery concept in which both provide the same total energy gain for a particle (that is, either (i) a main LINAC of the same size with a higher acceleration capability per distance or (ii) a longer main LINAC with the same acceleration capability per distance is required in the one-turn case compared to the multi-turn case), multi-turn concepts can in principle be realized at lower costs [23]. However, multiple passing a main LINAC increases the cumulative beam current in the main LINAC due to beam superpositions; here, limits of the main LINAC and the lattice design specify the maximum possible cumulative beam current and thus determine the maximum number of possible main-LINAC passes (see section 3.8.1 for details).

A multi-turn design entails a certain number of recirculations, which in turn entails a certain number of degrees of freedom to influence the particle beam; as a result, a more sophisticated manipulation of the longitudinal phase space can be achieved compared to a one-turn design (see sections 4.2.2 and 4.3.2). However, a multi-turn design (especially with common recirculation transport) is inherently more complex and entails more complex

---

<sup>7</sup>For conventional acceleration the following applies: The main LINAC is passed  $J$  times, that is,  $J$  times for acceleration and zero times for deceleration. The beam is recirculated  $J-1$  times (each time with another design energy), and thus the number of design recirculation orbits is  $J-1$ . Therefore, this is referred to as  $(J-1)$ -turn conventional acceleration operation. In the case of conventional acceleration, this convention also highlights the number of design recirculation orbits, and since there is no superposition in the recirculation beamlines, it additionally highlights the number of recirculations itself.

---

constraints compared to a one-turn design (see sections 4.2.2 and 4.3.2).

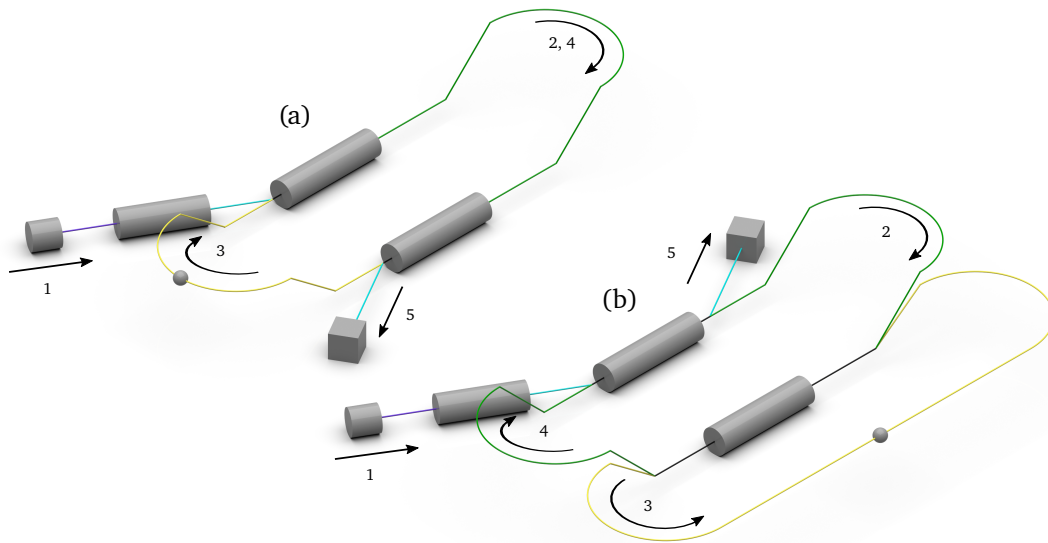
As an alternative to common recirculation transport, there is separate recirculation transport in which each beam has an individual design orbit apart from the superposition in the main-LINAC section [21]. However, separate recirculation transport requires a change of the presented design: either time-dependent magnetic fields have to be used, or if static magnetic fields are used, a particle must not leave the main LINAC after a deceleration with a kinetic energy value that was present when leaving the main LINAC after an acceleration. The latter can be realized by splitting the main LINAC into at least two spatially separated main LINACs, which provides the possibility to bypass one main LINAC in a definite situation [21]: the particles pass through both main LINACs alternately until maximum acceleration, then the LINAC utilized for the last acceleration is used for the first deceleration before both main LINACs are again passed alternately. Possible machine layouts with two spatially separated main LINACs and common or separate recirculation transport, respectively, based on static magnetic fields are shown in Fig. 1.2 to enable a direct comparison.

In the above presented concepts, only the main LINAC is capable of energy recovery but not the booster LINAC. Thus, after maximum deceleration in the main LINAC, the particle energy is equal to the booster energy. Consequently, higher machine efficiencies can be achieved if no booster LINAC is needed or if even the booster LINAC's delivered energy can be recovered and afterward recycled.

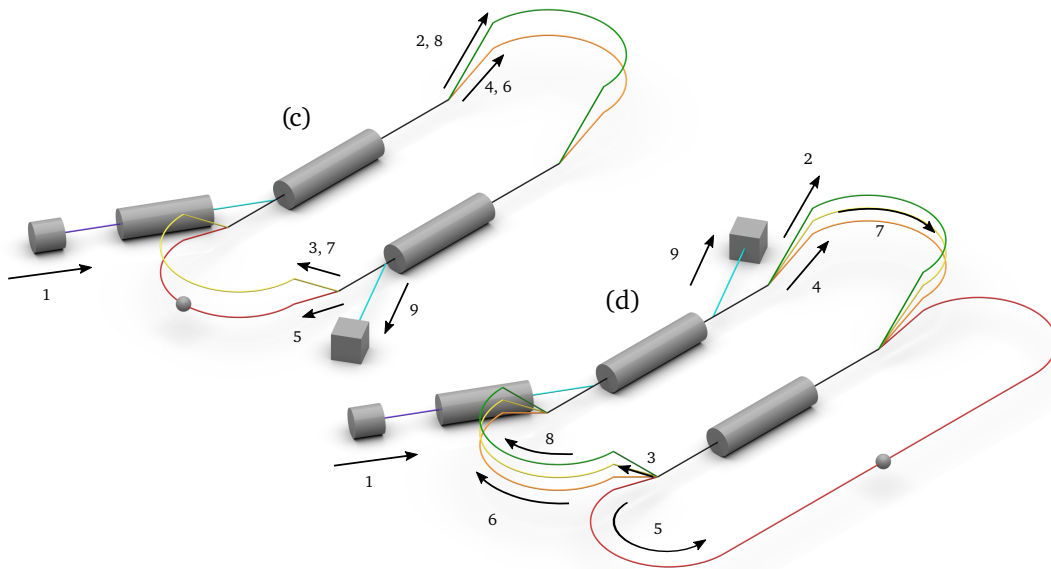
The booster LINAC serves a few purposes: (i) the ratios between the momenta and thus – in the case of static magnetic fields – the ratios between the deflection radii in splitter and merger sections located downstream are reduced, (ii) phase slippage in the main LINAC is reduced (see section 3.3), and (iii) the beam leaving the gun is accelerated without a long delay to keep space-charge effects at a minimum (see section 3.8.2). The latter requires a compact design, which makes it a challenge to realize an appropriate configuration that allows passing the booster LINAC again for energy recovery.

This challenge is more pronounced if particles for acceleration and deceleration shall travel in the same direction: The advantage of reducing deflection radii for merging at other locations in the machine would especially not apply for the two beams entering the booster LINAC and would thus be one of the major challenges under the condition of a compact design. Since the particles' speed is usually changing significantly in the booster LINAC, which is often taken into account by an adapted cavity design, this entails an additional challenge. Here, a possible solution could be particles for acceleration and deceleration traveling in opposite direction in the booster LINAC (independent of the situation in the main LINAC), where a particle to be accelerated and a particle to be decelerated have the same energy at a given longitudinal location (with respect to a Cartesian coordinate system at rest). To avoid collisions, a transverse offset could be realized by using correspondingly designed dual-axis cavities [24].

As already mentioned, acceleration and deceleration can take place spatially separated.



$$E_{\text{kin},0} < E_{\text{kin},0} < E_{\text{kin},0} < E_{\text{kin},0}$$



$$E_{\text{kin},0} < E_{\text{kin},0} < E_{\text{kin},0} < E_{\text{kin},0} < E_{\text{kin},0} < E_{\text{kin},0}$$

**Figure 1.2: Comparison of common and separate recirculation transport.** The number, element and color code is identical to the one of Fig. 1.1. A comparison of the transport schemes requires that the main LINAC is split into at least two spatially separated sections. The sum capability of two main LINACs shown in this figure is equal to the capability of one main LINAC shown in Fig. 1.1. (a)–(b) Single acceleration and deceleration per main LINAC. (c)–(d) Double acceleration and deceleration per main LINAC. (a)+(c) Common recirculation transport. (b)+(d) Separate recirculation transport. (a)–(d) In a common (separate) recirculation transport layout, increasing the number of acceleration and deceleration per main LINAC by one requires two (four) additional arcs – one (two) arc(s) for each side of the main LINACs. Figure created based on Ref. [21].

---

Thus, another possibility to recovery energy provided by the booster LINAC is the use of an additional LINAC that is located upstream of the beam dump and that is dedicated for deceleration and thus energy recovery only, while the recovered energy can be transferred from that additional LINAC to the booster LINAC via coupling waveguides [25].

However, these proposals make the machine design significantly more complex. If the booster LINAC's delivered energy cannot be recovered and if the goal is to increase the machine efficiency for a given maximum particle energy as well as to reduce induced radioactivity at the beam dump, it is desirable to operate with the lowest possible injector energy that enables appropriate beam transport [6]. Thus, a low injector energy is one of the specifications of this work in order to investigate the general feasibility; however, at the S-DALINAC, the injector momentum and the maximum particle momentum are in a fixed ratio (see Table 4.1), and thus the ratio of recoverable to non-recoverable particle energy is almost constant<sup>8</sup> at this machine.

### 1.3 History and Future of ERLs

The idea of energy recovery in an electron LINAC was proposed by M. Tigner in 1965 [4]. Published in 1975, acceleration and deceleration in the normal-conducting reflexotron at Chalk River Nuclear Laboratories was realized by passing it twice, while the decelerated beam traveled in the opposite direction to the accelerated one [15]. Deceleration in normal-conducting cavities can be useful since in this way a particle to be dumped has less energy leading to the associated benefits mentioned. However, high-efficient energy recycling requires almost lossless temporary energy storage in the RF fields inside the cavities. In order to minimize dissipation of the returned energy as heat due to induced currents within the cavity walls, superconducting cavities with a high quality factor are needed [5]. Energy recovery using superconducting cavities was first realized at the superconducting accelerator driven free electron laser (SCA/FEL) at Stanford University in 1986 [26]. Here, accelerated and decelerated beams passed the ERL in the same direction (as explained in section 1.2). Such a concept is used in many energy-recovery configurations [11, 26–30].

In the above mentioned realizations, the one-turn energy-recovery concept was applied. For a given LINAC, higher particle energies can be realized by passing it several times for acceleration. Followed by the same number of passes for deceleration to ensure maximum energy recovery leads to multi-turn energy-recovery operation. This kind of operation using normal-conducting cavities was first realized at the Novosibirsk FEL facility (NovoFEL) at Budker Institute of Nuclear Physics: reports on a two-turn [31] and a four-turn operation [32] have been given in 2008 and 2013, respectively. In 2020, the first multi-turn acceleration and deceleration using superconducting cavities at the Cornell-Brookhaven National Laboratory ERL Test Accelerator (CBETA) at Cornell University was reported [33], but substantial saving

---

<sup>8</sup>Due to the energy–momentum relation, the ratio of injector energy to maximum particle energy – and consequently the ratio of recoverable to non-recoverable particle energy – cannot be constant if the momentum ratio is constant.

---

of RF power requirements during multi-turn operation has not been demonstrated. Within the scope of this work, a quantitative demonstration of substantial energy recycling via beam-loading reduction during a multi-turn energy-recovery operation using superconducting cavities has been shown for the first time at the S-DALINAC in 2021 (details are provided in section 4.2.5).

Utilizing the energy-recovery technology can provide beams of high virtual<sup>9</sup> beam power. With to date realized accelerators supporting energy recovery, the following milestones have been achieved: At Thomas Jefferson National Accelerator Facility (JLab), (i) a beam of 9.1 mA average beam current and 160 MeV centroid particle energy (and thus approx. 1.5 MW virtual beam power) has been realized at the superconducting JLab high power ERL light source [11], and (ii) energy recovery has been demonstrated for an electron energy of approx. 1 GeV at the superconducting Continuous Electron Beam Accelerator Facility (CEBAF) [34]. An average beam current of 30 mA was realized during energy-recovery operation at the normal-conducting NovoFEL [32].

New ERL projects aim at demonstrating operation with a particle energy [35], beam current [36] or virtual beam power [37], respectively, that is an order of magnitude higher than realized to date by utilizing ERLs. This paves the way for future large-scale projects aiming at nuclear and particle physics research in which the energy-recovery technology shall be exploited [7, 8, 38–40]. As an example to be highlighted, the proposed Large Hadron–Electron Collider (LHeC) project aims at using a multi-turn energy-recovery configuration to provide an electron beam with a maximum electron energy of 50 GeV and a beam current of 20 mA, that is, a virtual beam power of 1 GW [8]. Such beam properties can only be reasonably realized if the beam itself or – as primarily intended in ERL concepts – its energy is recycled (see section 1.4).

## 1.4 Potential for Energy Saving and Sustainability Using ERLs

Climate change and energy crisis have increased the urgency for sustainability, in particular for large-scale accelerator complexes [41]. Here, the gigawatt power scale should be considered as an unsurpassable borderline since it is hardly compatible with reasonable impacts on society and governmental approvals [38]. Utilizing the energy-recovery technology has the potential for enormous energy savings when the power necessary for acceleration in conventional operation predominates the other power components necessary to operate the entire facility:

In both a LINAC facility or a conventional recirculation machine in which electrons pass through the system only once, providing an electron beam of 1 GW beam power would

---

<sup>9</sup>The ERL concept requires that the vast majority of the energy stored in the beam, which is in principle available at the interaction point, remains stored in the beam after the intended interaction. Thus, a certain large amount of energy can be considered as available per time as long as no substantial amount of energy is withdrawn from the beam and minor energy losses are compensated by external energy supply. Consequently, the stored energy available per time (that is, power) is only *virtually* available.

---

already require 1 GW of RF power for acceleration. Here, RF power needed but not transferred into kinetic energy of the electrons as well as any other power component necessary to operate the facility has not been taken into account. Consequently, the total power required in that case would exceed 1 GW. For comparison: the LHeC project aims at providing an electron beam of 1 GW virtual beam power by not exceeding 0.1 GW wall-plug power for the entire facility part dealing with the electron beam [8]. This demonstrates the potential for energy saving if the intended experiment supports utilizing the energy-recovery technology.

Additionally, energy requirements can be further decreased by using more energy-efficient technologies currently under research and development. Desired improvements are, for example, higher quality factors for superconducting cavities in order to reduce losses, and the possibility to operate at higher temperatures to reduce power needed for cooling [42,43]. Further energy savings are possible if no electrical power is needed for beam guiding elements during operation. Here, energy-recovery concepts with static magnetic fields as described in section 1.2 can benefit from permanent magnets. However, the materials involved in the production of the permanent magnets are crucial with focus on sustainability [41]. Furthermore, sustainability can be increased if the number of recirculation beamlines for a given number of recirculations in a multi-turn concept can be reduced so that beams of different design energies share the same recirculation beamline. Both a reduced number of recirculation beamlines and permanent magnets have already been implemented in a multi-turn energy-recovery machine design [33].

## 1.5 Motivation for This Work

As described above, ERLs are suitable for delivering high quality beams and have the potential for energy saving. Using the energy-recovery technology can enable higher beam currents compared to conventional acceleration in facilities where particles pass through the system only once, while a multiple acceleration enables higher particle energies. Since beam power is proportional to beam current times centroid particle energy, orders of magnitude higher virtual beam powers can be realized by combining energy recovery and multiple acceleration. Although both techniques are widely-used individually, the combination of both techniques is a challenge, especially if common recirculation transport is used.

At the beginning of this work, energy recovery in combination with multiple acceleration using superconducting cavities had not yet been demonstrated. Therefore, the question whether the combination of energy recovery and multiple acceleration leads to an increased machine efficiency was unanswered. An answer to this question is essential since it is related to the feasibility of those proposed high-power projects mentioned above that are based on multi-turn energy-recovery concepts. Hence, the main goal of this work was to realize a multi-turn energy-recovery mode at a suitable accelerator with superconducting cavities and to investigate its recovery efficiency.

Due to its superconducting cavities and multiple recirculation beamlines, a suitable accel-

---

erator meeting the requirements for this operation mode is the S-DALINAC. Here, a potential multi-turn energy-recovery operation would inevitably be realized with common recirculation transport. Thus, a potential realization could demonstrate whether this cost-efficient machine layout is suitable for multi-turn energy-recovery operation. The S-DALINAC is operated with a low injector energy; while this can be desirable in an ERL configuration because it can further increase the cost efficiency as mentioned, it entails phase slippage (see section 3.3) during main-LINAC passes, which is crucial in combination with common recirculation transport. Hence, a potential realization of a multi-turn energy-recovery operation at the very machine would also address the challenge of an adequate compensation of phase slippage in a common recirculation transport layout. For these reasons, the objective of this work was to realize a multi-turn energy-recovery operation *at the S-DALINAC*. Associated results are provided in chapter 4.

A related question is whether the beam quality is impaired due to an energy-recovery process. Answering this question requires a diagnostic possibility that allows comparing beam quantity values present during an energy-recovery operation with those present during operation in the corresponding conventional acceleration mode. For this reason, the implementation of a suitable diagnostic possibility was part of the above mentioned goal. Associated results are provided in chapter 5.





---

## 2 S-DALINAC

The particle accelerator at which a multi-turn energy-recovery mode was realized within the scope of this work is the superconducting Darmstadt electron linear accelerator (S-DALINAC) [19,20] at Technische Universität Darmstadt. The machine's name has a historical origin: the S-DALINAC is the superconducting successor of the normal-conducting Darmstadt electron linear accelerator (DALINAC) [44], which in turn consisted of a single LINAC. However, the S-DALINAC is not a LINAC facility but a recirculating machine that consists of two LINACs (with respect to the definition given in section 1.1).

The S-DALINAC is used for research in nuclear spectroscopy and accelerator science. In particular, its layout enables studies on energy-recovery modes. In the following, the machine is briefly described with focus on its layout present at the time of the realization of the multi-turn energy-recovery operation and the associated beam tuning described in this work, that is, from July to August 2021 (see Fig. 2.1). All figures in this work related to the layout include the upgrades mentioned in section 4.2.3 as well as the wire scanners that have been constructed and installed within the scope of this work (see chapter 5). Further information about the S-DALINAC, including its historical development, is provided in Ref. [45].

### 2.1 Layout and Operation Modes

At the S-DALINAC, an electron beam is generated by using one of two available electrostatic guns: (i) At the S-DALINAC polarized injector (SPIN) gun, a 3 GHz laser diode or a 75 MHz titanium:sapphire laser is utilized for photo emission, which can provide a bunched beam with a spin polarization of up to 86 %, a kinetic energy of 100 keV per electron and a current of up to 50  $\mu\text{A}$  [46,47]. (ii) A tungsten-filament-based thermionic gun can provide a continuous beam with a kinetic energy of 250 keV per electron [48] and a current of several hundred microamperes.

Downstream of both guns, a normal-conducting “chopper” cavity (I0NC01, see Fig. 2.2) [49,50] is located, which is utilized to trim the bunched beam of the SPIN gun or to generate a bunched beam from the continuous beam provided by the thermionic gun, respectively: At I0NC01, a modified first transverse magnetic dipole ( $\text{TM}_{110}$ ) mode of the RF field is utilized to deflect each electron of the beam in a specific direction, depending on its arrival time. Due to different deflection directions, only a fraction of the electrons of the beam passes an aperture located downstream while the vast majority of the beam is stopped at the corresponding aperture plate. This leads to a trimmed or bunched beam, respectively,

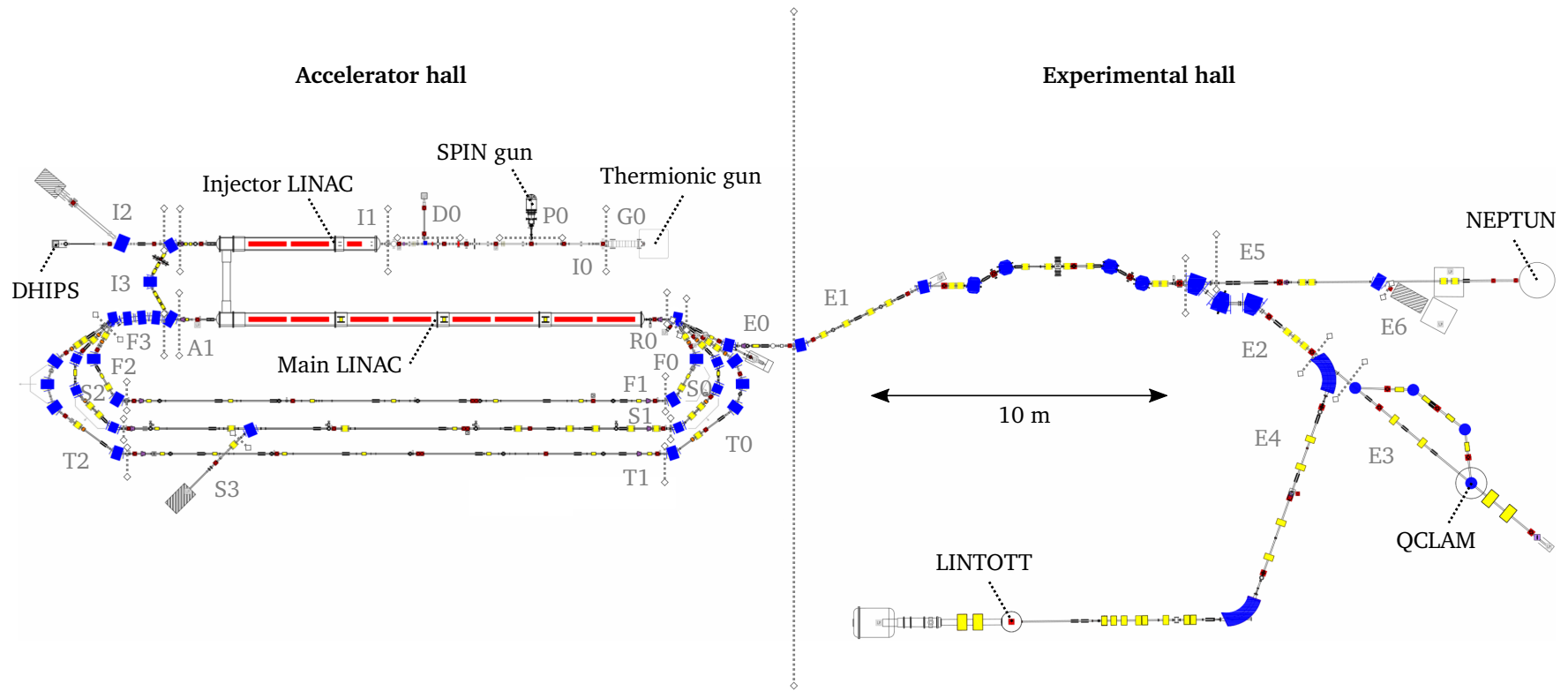


**Figure 2.1: Layout of the S-DALINAC.** Overview of the entire beamline of the machine. Individual sections and locations are highlighted: thermionic gun (G); photo gun (P); gun diagnostic section (D); injector section (I); main-LINAC section (A); first (F), second (S), and third (T) recirculation beamline; extraction beamline (E); and energy-recovery related destination (R). These sections are subdivided and the corresponding subdivisions are identified by a sequential number. Shown elements are: dipole magnets for design orbit bending (blue); correction dipole magnets (dark gray/black); quadrupole magnets (yellow); sextupole magnets (orange); cavities with an externally coupled field (red); cavity monitors (purple); Faraday cups and beam dumps (cup symbol on a light gray background); screens (black cross on a red background); wire scanners (fork symbol on a light gray background); and path length adjustment systems (dark gray arrow). The S-DALINAC extends over the accelerator hall and the experimental hall, while the focus of this work is on those parts of the machine that are located in the former. Figure adapted from Ref. [51].

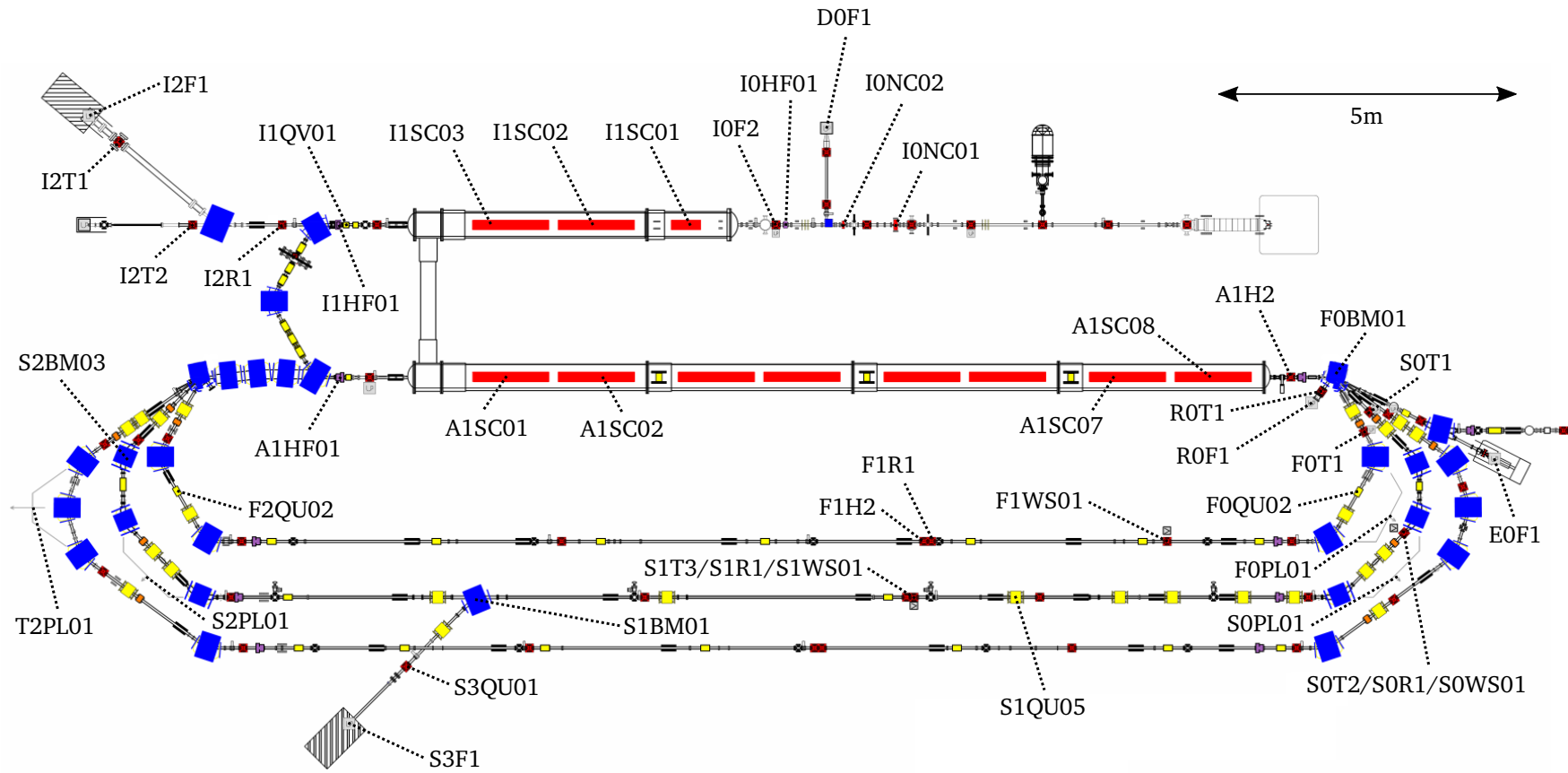


**Figure 2.2: Details on the part of the S-DALINAC located in the accelerator hall.** Detailed view on the sections relevant for a multi-turn energy-recovery mode. The color and symbol code is identical to the one of Fig. 2.1. Elements mentioned in this work are named here. Figure adapted from Ref. [51].

---

downstream of that very aperture. Depending on the requirements of the experiment, either a large aperture is installed to enable high beam currents after trimming or bunched beam generation, respectively (hereinafter abbreviated as chopping), or a small aperture is installed to provide a high beam quality after chopping. However, for radiation protection reasons, the maximum permitted beam current after chopping is 80  $\mu\text{A}$  (as explained below, there are more restrictive current limits – depending on the operation mode). For the realization of the multi-turn energy-recovery mode presented in this work, the thermionic gun together with IONC01 and the downstream following aperture was used to provide the bunched beam, while an appropriate aperture size was chosen to provide a high beam quality and a maximum beam current after chopping of 20  $\mu\text{A}$  (which was the maximum beam current permitted in an energy-recovery mode for radiation protection reasons as discussed below). IONC01 is operated at a frequency of approx. 3 GHz, which thus defines the bunch repetition rate<sup>1</sup>. All further cavities described below in this chapter are operated with the same frequency (referring to the corresponding mode of the RF field that is intentionally utilized).

Downstream of IONC01, a normal-conducting “buncher” cavity (IONC02) is located to initiate velocity bunching [49,50]: At IONC02, the fundamental transverse magnetic ( $\text{TM}_{010}$ ) mode of the RF field is utilized to decelerate electrons located in the bunch’s head (which arrive early at IONC02) and to accelerate electrons located in the bunch’s tail (which arrive late at IONC02). As a result, early-arriving electrons of a bunch have a lower speed compared to the late-arriving electrons of the same bunch, and thus the latter can catch up with the former after a certain drift distance. In this way, bunches are longitudinally compressed after a certain drift distance. For all further cavities described below in this chapter, the corresponding  $\text{TM}_{010}$  mode is utilized; here, if a cavity has more than one cell, the corresponding  $\text{TM}_{010}$  mode is the one for which the phase difference of the electromagnetic field in adjacent cells is  $180^\circ$  ( $\pi$ -mode).

Downstream of IONC02, the electrons can be guided into the gun diagnostic section or into the injector LINAC (see Fig. 2.3 for the possible operation modes). The injector LINAC consists of one 6-cell (I1SC01) and two 20-cell (I1SC02 and I1SC03) superconducting cavities made of niobium, which are operated at a temperature of approx. 2 K. Each cell of I1SC01 is designed for an electron speed equal to 86 % of speed of light<sup>2</sup> [52], and the entire cavity can provide an energy gain of up to 1.4 MeV [53]. This cell design takes into account that the speed of an electron changes significantly during a pass through the entire cavity and thus provides suitable acceleration: electrons enter I1SC01 with a kinetic energy of 100 keV or 250 keV, that is, at a speed of approx. 55 % or approx. 74 % of speed of light, respectively, while the kinetic energy can increase up to 1.65 MeV at the exit of I1SC01, that is, the speed can increase up to approx. 97 % of speed of light. All cavities located downstream of I1SC01 consist of cells designed for a particle speed equal to the

---

<sup>1</sup>There is at least one electron per RF cycle if the beam current after chopping is greater than or equal to 0.5 nA.

<sup>2</sup>In this work, speed of light always refers to the speed of light in vacuum.

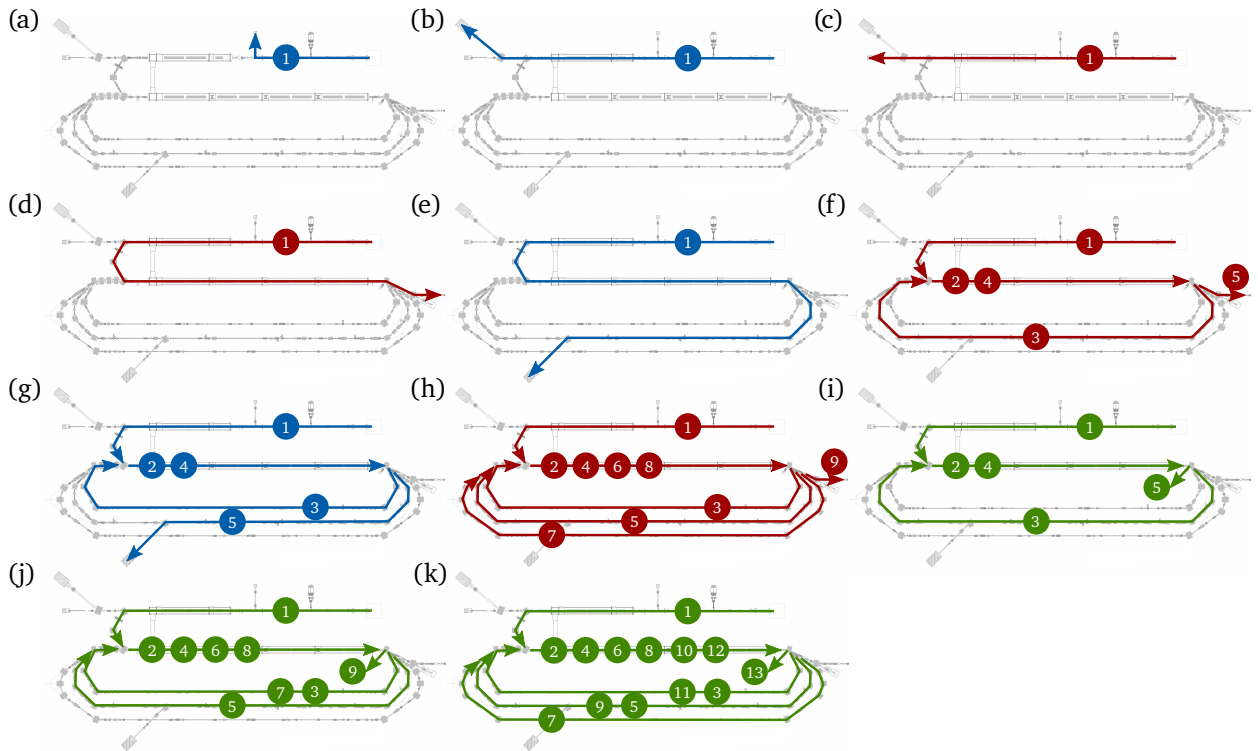


**Figure 2.3: Realized and potential operation modes of the S-DALINAC starting from the thermionic gun.** Diagnostic modes (blue), conventional acceleration modes to serve experiments (red) and energy-recovery modes (green). Numbers denote the chronological sequence of the corresponding section passes. (a) Gun-beam diagnostics, dumping at DOF1. (b) Injector-beam diagnostics, dumping at I2F1. (c) Injector acceleration for DHIPS. (d) Single main-LINAC pass conventional acceleration into the experimental hall. (e) One-turn conventional-acceleration diagnostics, dumping at S3F1. (f) One-turn conventional acceleration into the experimental hall. (g) Two-turn conventional-acceleration diagnostics, dumping at S3F1. (h) Three-turn conventional acceleration into the experimental hall. (i) One-turn energy recovery, dumping at ROF1. (j) Two-turn energy recovery, dumping at ROF1. First realized within the scope of this work. (k) Three-turn energy recovery, dumping at ROF1. Not yet realized, first studied within the scope of this work. (a)–(i) Realized prior to this work. (d)+(f)+(h) Diagnostics possible by dumping the beam at EOF1 instead of guiding it into the experimental hall. (a)–(k) Taking the preceding sentence into account, the shown operation modes are the only possible operation modes with the requirement to end in a stationary beam dump and if an excessively strong net off-crest acceleration and/or deceleration in the main LINAC is to be avoided. Figure created based on Ref. [45] using the S-DALINAC–adaptation based on Ref. [51].

speed of light. The injector LINAC can boost an electron’s energy up to approx. 10 MeV for a maximum beam current after chopping of 60  $\mu\text{A}$  [45, 53].

Downstream of the injector LINAC, the beam can be guided to the Darmstadt High-Intensity Photon Setup (DHIPS) to perform photon-scattering and photodissociation experiments [54], or through the injector arc (I3) to pass the main LINAC for further acceleration.

The main LINAC consists of eight 20-cell superconducting cavities (A1SC01 to A1SC08), which have the same properties as I1SC02 and I1SC03, respectively. The maximum energy gain per main-LINAC pass is 30 MeV for a maximum beam current after chopping that is dependent on the number of main-LINAC passes [45]: In a conventional acceleration

---

mode, the technical limit of the main LINAC is a cumulative beam current resulting from all superimposed beams of approx. 79  $\mu\text{A}$  [45] to provide the mentioned maximum energy gain per pass. This limit results from the limited maximum externally provided RF power that can be coupled into the main LINAC. However, there is still the limit of 60  $\mu\text{A}$  for a single beam passing through the main LINAC due to the technical limit of the injector LINAC that has to be passed by the beam. Furthermore, there is a limit of 20  $\mu\text{A}$  for a single beam in a recirculation beamline for radiation protection reasons.

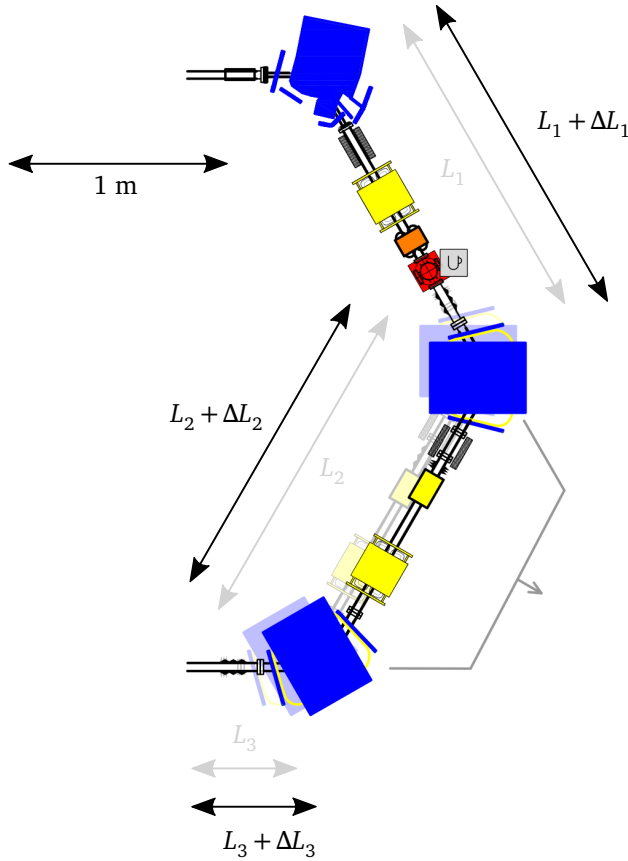
Downstream of the main LINAC, the beam can be guided either directly into the experimental hall to one of the experimental setups described below or through recirculation beamlines. By passing through up to three recirculation beamlines [45], the electron beam can pass the main LINAC several times: (i) After two or four conventional acceleration passes through the main LINAC, the beam can be guided into the experimental hall. Four passes are necessary to reach the maximum kinetic energy of approx. 130 MeV [45]. (ii) Alternatively, the main LINAC can be passed two, four or six times for energy-recovery operation as discussed below.

In the experimental hall, the beam can be used at one of three available experimental setups: A low-energy photon tagging spectrometer (NEPTUN) enables a precise energy determination of a bremsstrahlung photon by measuring the remaining energy of a scattered electron, and thus energy-dependent reaction cross-sections can be determined [55]. A large-aperture spectrometer (QCLAM) enables electron-scattering experiments and measurements at different angles, in particular at an angle of  $180^\circ$  [56]. An additional spectrometer (LINTOTT) supports high-resolution electron-scattering experiments [57].

Besides the conventional acceleration modes, the S-DALINAC can be or has the potential to be operated in one of several energy-recovery modes, respectively, as shown in Fig. 2.3. Here, electrons are first accelerated in the main LINAC and afterward decelerated at the very location. Deceleration instead of acceleration is possible because alternating electric fields are present in the main LINAC, and thus acceleration or deceleration takes place depending on the electrons' arrival time (see sections 3.3 and 4.1). The arrival time is influenced by changing the time of flight through a recirculation beamline, which in turn is realized by a change of the length of the orbit to be traveled: the path length of the design electron can be set by using path length adjustment systems [58], which are available in each recirculation beamline<sup>3</sup> (see Fig. 2.4). When operating in an energy-recovery mode, energy required for acceleration of electrons is provided due to the deceleration of other electrons rather than from externally provided RF power; hence, the above mentioned technical limit for the main LINAC's maximum cumulative beam current resulting from the limited maximum

---

<sup>3</sup>It has to be emphasized that the path length adjustment systems are also necessary for the conventional acceleration modes: Depending on the operation mode of the S-DALINAC, a certain operation-mode-dependent off-crest acceleration may be necessary, which is realized by controlling the arrival time of the electrons via the path length adjustment systems. Furthermore, since the operation modes of the S-DALINAC can be realized for a wide range of design energies, the arrival time is also dependent on the corresponding design energy of a section (that is, dependent on the corresponding design speed of a section), which additionally has to be taken into account when tuning the path length adjustment systems.



Selected relations:

- (i)  $\Delta L_2 = -\Delta L_1$
- (ii)  $\Delta L_3 = \Delta L_1$
- (iii)  $\Delta L_1 + \Delta L_2 + \Delta L_3 = \Delta L_1$

**Figure 2.4: Path length adjustment system.** The figure shows the path length adjustment system FOPL01, which is located in the first arc of the first recirculation beamline. The color and symbol code is identical to the one of Fig. 2.1. The given relations refer to the changes in the corresponding effective lengths,  $\Delta L$  (see section 3.4 for the definition of the effective length  $L$ ). By tuning the path length adjustment system, the net orbit length of the design particle changes by  $\Delta L_1 + \Delta L_2 + \Delta L_3$ . Figure adapted from Ref. [51].

externally provided RF power that can be coupled into the main LINAC does not apply when operating in an energy-recovery mode. However, the technical limit for the injector LINAC (a maximum beam current after chopping of  $60 \mu\text{A}$ ) remains unchanged because it is not part of the energy-recovery process. Furthermore, the limit due to radiation protection reasons (a maximum current of  $20 \mu\text{A}$  for a single beam in a recirculation beamline) applies when operating in an energy-recovery mode because a recirculation beamline is inevitably involved in such an operation mode. Consequently, the maximum possible beam current after chopping can not exceed  $20 \mu\text{A}$  for an energy-recovery mode at the S-DALINAC, while instability effects can further lower that limit (see section 3.8.1). Prior to this work, a one-turn energy-recovery mode has been realized at the S-DALINAC [14]. Within the scope of this work, a two-turn energy-recovery mode was realized at the very machine for the first time (see section 4.2) as well as a three-turn energy-recovery mode studied based on beam-dynamics simulations (see section 4.3).

---

## 2.2 Beam Diagnostics

Multiple beam diagnostic devices are installed at the S-DALINAC and several measurement techniques are used to determine properties of the electron beam:

Cavity monitors [59–61] can provide information on the relative time of flight as well as on the beam current. For the detection of the latter, Faraday cups [45] are used as well. Beam-loss monitors [62] are available to determine the location of beam loss in case it occurs as well as to indicate its intensity. Two types of destructive screens are installed at several locations enabling the measurement of the transverse beam profile: One screen type is made of coarse beryllium oxide (BeO) coated with gold (Au) suitable to investigate low-current beams, and one is made of plain Kapton coated with aluminum (Al) suitable to investigate high-current beams [63]. BeO is a scintillator [64] while Au dims the emitted light and conducts electric charge as well as heat. Al conducts electric charge as well as heat and emits optical transition radiation [65] in an appropriate geometry due to the smooth surface provided by the Kapton. The light emitted by a screen during electron bombardment is detected with a charge-coupled device (CCD) camera. At some locations, screens with a hole [14] are installed, which allow detecting beam properties in the case of beam superpositions: while the first beam(s) pass(es) the hole of the screen undisturbed, later arriving beam(s) can be observed on the outer region of the screen if the later arriving beam(s) is/are slightly deflected. Moreover, wire scanners [66, 67] are available, which can be used to determine the projection of the transverse beam profile. Further details on wire scanners are provided in chapter 5.

The transverse emittance can be determined via a quadrupole-magnet scan [63, 68] by measuring the transverse beam envelope as a function of the focus strength of a quadrupole magnet. From the (projected) transverse beam profile measured in a dispersive section, the momentum spread can be determined (see section 3.6). The superconducting cavities can be used to determine the bunch length via the RF zero-crossing method [53, 69]; here, a momentum spread depending on the bunch length is intentionally generated and afterward measured, from which the bunch length can be determined. The beam loading for the superconducting cavities can be determined with an RF power measurement system [70], which allows comparing power requirements for conventional acceleration with power requirements for energy-recovery operation. The centroid momentum can be determined by using the RF power measurement system as well as by imaging the transverse beam profile in a dispersive section.



---

## 3 Fundamentals on Beam Dynamics

In particle accelerators, the velocity of a charged particle is influenced by electromagnetic fields. In the case of the S-DALINAC, the charged particles are electrons whose main acceleration and deceleration for energy recovery takes place in standing-wave RF fields and main deflection takes place in static magnetic fields. The interaction between electrons and these fields is the basis for this work and is therefore described in detail in this chapter. Principles are discussed for charged particles in general or for electrons only if appropriate.

### 3.1 Coordinate System in Motion

For a more suitable description of particle dynamics, a coordinate system in motion is used (see Fig. 3.1). The location  $s$  on the design orbit is linked to the origin of the coordinate system at rest by the vector  $\vec{r}_0(s)$ , where  $s = 0$  is the start point of the design orbit. The position of an individual particle is described in the coordinate system at rest by the vector  $\vec{r}(s)$ , which in turn is a combination of the vector  $\vec{r}_0(s)$  and those vectors relative to the origin of the coordinate system in motion which represent the deviation from the design orbit:

$$\vec{r}(s) = \vec{r}_0(s) + x(s)\vec{u}_x(s) + y(s)\vec{u}_y(s) + z(s)\vec{u}_z(s) \quad (3.1)$$

with

$$\left| \vec{u}_x(s) \right| = \left| \vec{u}_y(s) \right| = \left| \vec{u}_z(s) \right| = 1 \quad \text{and} \quad \vec{u}_x(s) \times \vec{u}_y(s) = \vec{u}_z(s). \quad (3.2)$$

At the location  $s$ , the vectors  $\vec{u}_x(s)$  and  $\vec{u}_y(s)$  are perpendicularly oriented to the design orbit while the vector  $\vec{u}_z(s)$  is tangentially oriented to the design orbit. At the location  $s$ , the plane containing  $\vec{u}_x(s)$  and  $\vec{u}_z(s)$  is referred to as horizontal plane, and the plane containing  $\vec{u}_y(s)$  and  $\vec{u}_z(s)$  is referred to as vertical plane. Furthermore,  $x(s)$  is the horizontal position,  $y(s)$  is the vertical position and  $z(s)$  is the longitudinal position with respect to  $s$ .

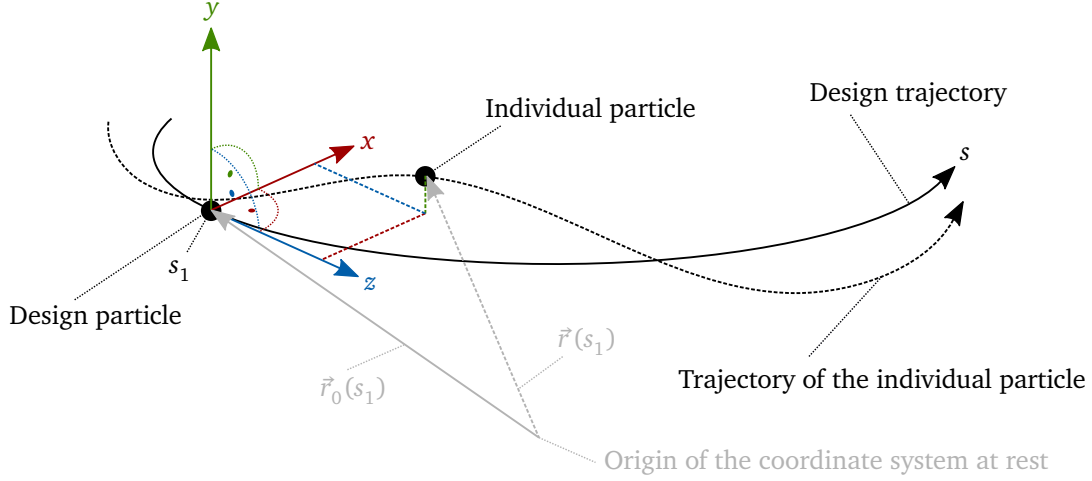


**Figure 3.1: Coordinate system in motion.** At a fixed point in time, the figure shows the coordinate system in motion with origin at location  $s_1$ . While the position of an individual particle can in principle be described by a coordinate system in motion with origin at any location  $s$ , the position of an individual particle is usually described using the coordinate system in motion whose origin is at the position of the design particle at the corresponding point in time.

## 3.2 Equation of Motion and Lorentz Force

The change of the momentum vector  $\vec{p}$  of a particle with charge  $q$  with respect to time  $t$  is equal to the Lorentz force  $\vec{F}_L$  [71]:

$$\frac{d\vec{p}}{dt} = \vec{F}_L = q \cdot (\vec{\mathcal{E}} + \vec{v} \times \vec{B}), \quad (3.3)$$

where  $\vec{\mathcal{E}}$  is the electric field,  $\vec{v}$  is the particle's velocity and  $\vec{B}$  is the magnetic field. The fields  $\vec{\mathcal{E}}$  and  $\vec{B}$  are collectively referred to as electromagnetic field. If the electromagnetic field oscillates at a certain high frequency, it is referred to as RF field. The Lorentz force is the basis for the beam-dynamics simulations conducted in this work. Depending on a particle's location, Eq. (3.3) is solved with different numerical methods. The most important methods used in this work are discussed below.

## 3.3 Energy Gain and Reduction in Alternating Electric Fields

In this section, the design trajectory is along a straight line. Thus, for a consistent description, it is sufficient to set  $s = 0$  and use  $z$  only to describe a longitudinal position.

At the S-DALINAC, the RF field inside a superconducting cavity  $j$  is a standing wave. In this section, the focus is on the  $TM_{010}$ - $\pi$ -mode of the alternating electric field; this mode is used for acceleration or deceleration, respectively, and the corresponding electric field  $\vec{\mathcal{E}}_j$  has an axial and a radial component while the corresponding magnetic field  $\vec{B}_j$  is azimuthally directed (see Figs. 3.2 and 3.3, simulated with CST Studio Suite [72] based on the cavity

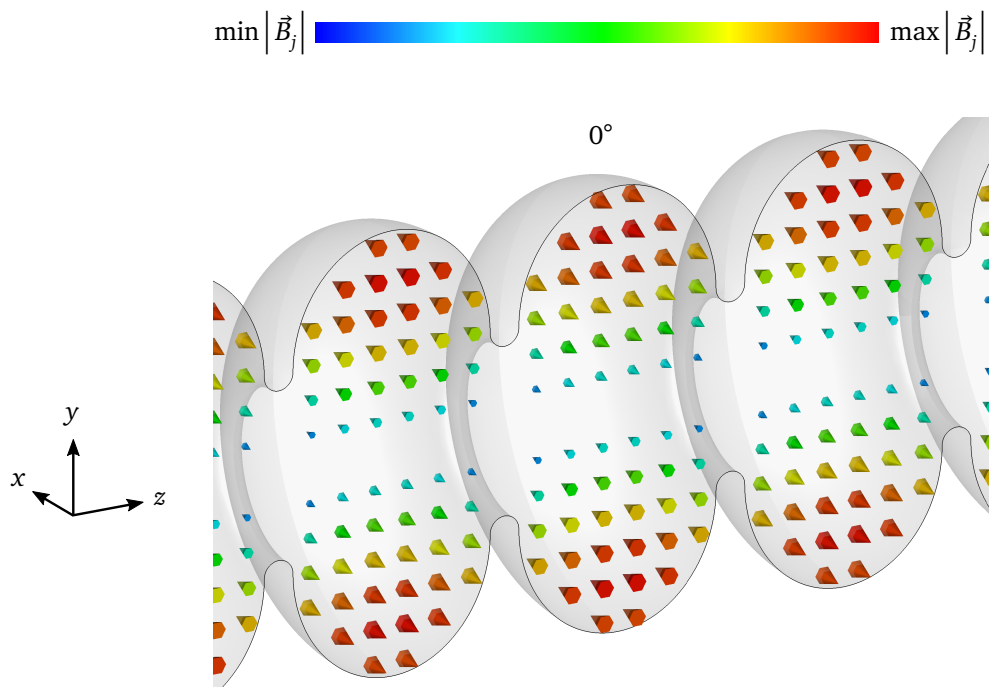
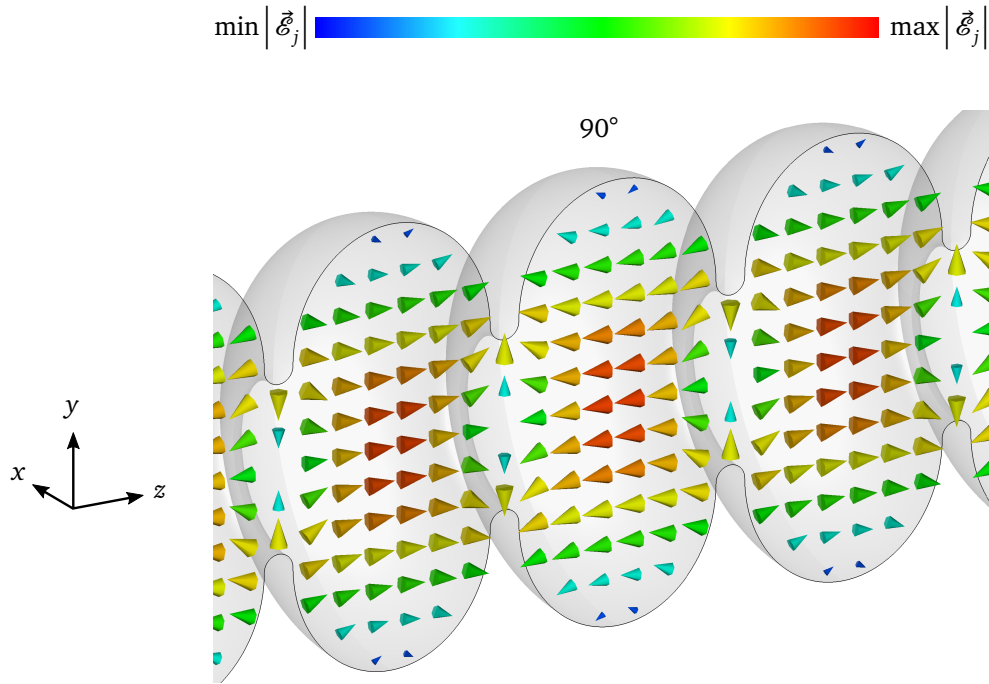


**Figure 3.2: Electric and magnetic field in cavity cells (1/2).** The figure shows the shape of the electric field  $\vec{\mathcal{E}}_j$  (top) and the magnetic field  $\vec{B}_j$  (bottom) of the  $\text{TM}_{010}$ - $\pi$ -mode for  $x = 0$  inside adjacent cells of the 20-cell cavity  $j$ . Field shapes are shown for different fixed points in time  $t$ ; mentioned phase values relate to  $(\omega t + \psi_j) \bmod 360^\circ$  with a constant  $\psi_j$ .

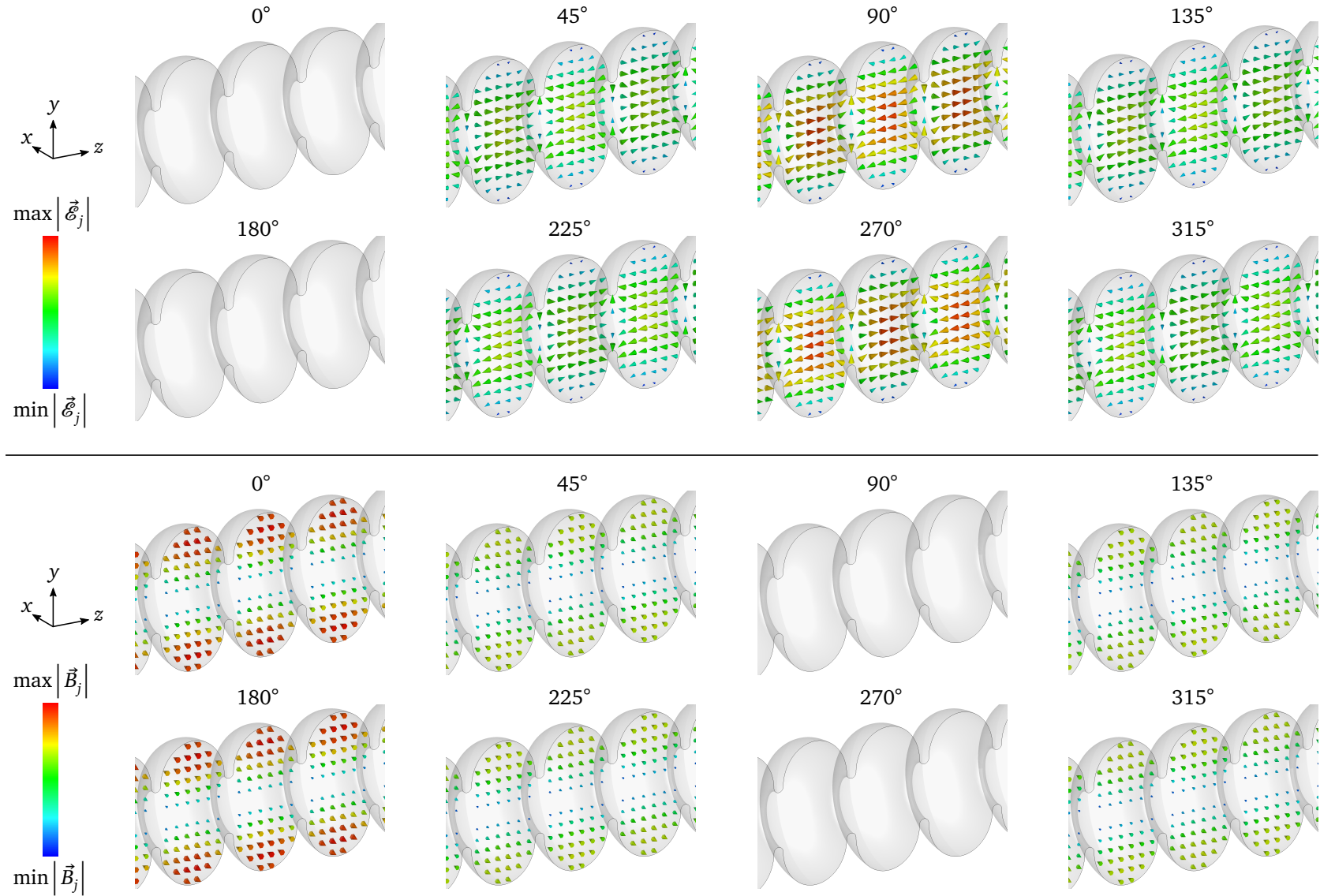
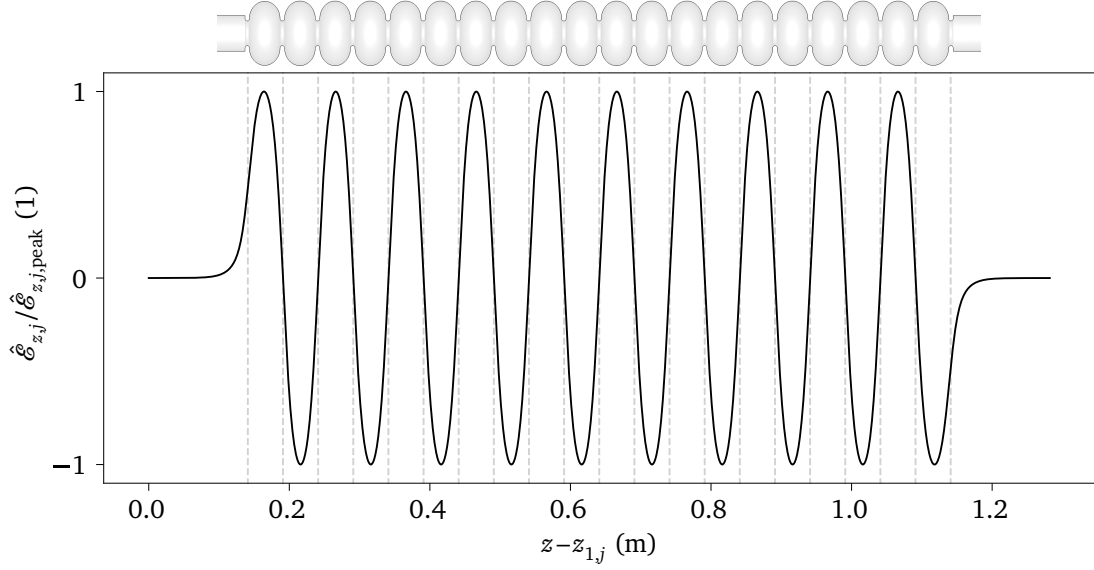


Figure 3.3: Electric and magnetic field in cavity cells (2/2). Similar to Fig. 3.2.



**Figure 3.4: Amplitude of the electric field.** The figure shows the time-independent amplitude of the on-axis  $z$ -component of the electric field,  $\hat{\mathcal{E}}_{z,j}$ , for the 20-cell cavity  $j$  relative to its maximum value  $\hat{\mathcal{E}}_{z,j,\text{peak}}$  and relative to the longitudinal location  $z_{1,j}$ . Dashed vertical lines indicate the entrances and the exits of the cavity cells, respectively. There is a non-zero field component beyond the end cells.

model used in Ref. [73]). In the following, the energy gain or reduction, respectively, of a particle passing the electric field inside a cavity will be discussed. To approach this, it is assumed until the end of this section that a particle travels along the central axis. Here, the radially directed electric field and the azimuthally directed magnetic field vanish. In that case, Eq. (3.3) simplifies to  $dp_z/dt = q\mathcal{E}_z$ .

For a given cavity  $j$ , the electric field  $\vec{\mathcal{E}}_j$  is limited in  $z$ -direction from  $z_{1,j}$  to  $z_{2,j}$ ; thus, the on-axis  $z$ -component of the electric field of that cavity,  $\mathcal{E}_{z,j}$ , can be described as [71]:

$$\mathcal{E}_{z,j}\left(z, \hat{\mathcal{E}}_{z,j}(z), t(z), \psi_j\right) = \begin{cases} \hat{\mathcal{E}}_{z,j}(z) \cos\left(\omega t(z) + \psi_j\right), & z \in [z_{1,j}, z_{2,j}] \\ 0, & z \notin [z_{1,j}, z_{2,j}] \end{cases}. \quad (3.4)$$

Here,  $\hat{\mathcal{E}}_{z,j}(z)$  is the time-independent amplitude of the on-axis  $z$ -component of the electric field (see Fig. 3.4),  $\omega$  is the angular frequency of the RF field with  $\omega/(2\pi) \approx 3$  GHz for the  $\text{TM}_{010}$ - $\pi$ -mode of each superconducting cavity at the S-DALINAC,  $\psi_j$  is an initial phase of the RF field and

$$t(z) = \int_0^z \frac{1}{v(z')} dz' \quad (3.5)$$

is the arrival time of the particle at location  $z$  depending on the particle's speed  $v > 0$ . For cavities  $j$  and  $k$ ,  $[z_{1,j}, z_{2,j}] \cap [z_{1,k}, z_{2,k}] = \emptyset$  applies in the case of  $j \neq k$ .

In this work, the shape of  $\hat{\mathcal{E}}_z(z)$  is equal for all cavities of the main LINAC while the magnitude of  $\hat{\mathcal{E}}_z(z)$  may differ per cavity, that is,  $\hat{\mathcal{E}}_{z,j}(z - z_{1,j})/\hat{\mathcal{E}}_{z,k}(z - z_{1,k})$  is constant for a non-zero divisor for given cavities  $j$  and  $k$ . Therefore, it is convenient to define the

peak of the time-independent amplitude of the on-axis  $z$ -component of the electric field,  $\hat{\mathcal{E}}_{z,j,\text{peak}} := \max_z |\hat{\mathcal{E}}_{z,j}(z)|$ , for comparison purposes.

While traveling through an electric field, a charged particle will be accelerated and/or decelerated, respectively, and thus the kinetic energy  $E_{\text{kin}}$  changes. The change in kinetic energy,  $\Delta E_{\text{kin},j}$ , while traveling on the axis of symmetry through cavity  $j$  with a field as described in Eq. (3.4) is given by [71]:

$$\Delta E_{\text{kin},j}(\hat{\mathcal{E}}_{z,j}(z), \psi_j) = q \int_{z_{1,j}}^{z_{2,j}} \mathcal{E}_{z,j} dz = q \int_{z_{1,j}}^{z_{2,j}} \hat{\mathcal{E}}_{z,j}(z) \cos(\omega t(z) + \psi_j) dz. \quad (3.6)$$

Equation (3.6) takes into account that the particle traveling through an electric field has a variable speed  $v$  due to the continuously changing kinetic energy. This equation is solved numerically by using a non-adaptive Runge-Kutta method in the field-map tracking (see appendix A). The relation between speed and kinetic energy is given by [71]:

$$v(z) = c \cdot \beta(z) = c \cdot \sqrt{1 - \frac{1}{\gamma^2(z)}} = c \cdot \sqrt{1 - \frac{1}{\left(1 + \frac{E_{\text{kin}}(z)}{E_{\text{rest}}}\right)^2}}, \quad (3.7)$$

where

$$\beta(z) := \frac{v(z)}{c} \quad (3.8)$$

is the relative speed,

$$\gamma(z) = \frac{1}{\sqrt{1 - \beta^2(z)}} = 1 + \frac{E_{\text{kin}}(z)}{E_{\text{rest}}} \quad (3.9)$$

is the Lorentz factor,  $c$  is the speed of light and  $E_{\text{rest}} \neq 0$  is the rest energy of the charged particle. Because the change in kinetic energy while traveling through an alternating electric field is dependent on the particle's travel speed, the dimensions of a cavity to form the RF field are designed depending on the speed of the particles in order to optimally exploit the RF field. However, in the case of a multi-turn energy-recovery concept, cavities are passed by the same particle several times, while that very particle's energy is different from pass to pass. Consequently, a particle has a different entry speed (and possibly a different arrival phase  $\omega t \bmod 360^\circ$ ) each time it arrives at a certain cavity, and therefore, the change in kinetic energy while passing a certain cavity usually is different from pass to pass.

The above mentioned time dependence can also be expressed by a given setup  $S_j$  upstream of  $z_{1,j}$  (that is, set time-depending elements such as cavities 1 to  $j - 1$  as well as given type of particle and initial kinetic energy and starting time of that particle). For a given setup  $S_j$  and a given time-independent amplitude of the on-axis  $z$ -component of the electric field,  $\hat{\mathcal{E}}_{z,j}(z)$ , there exists an initial phase  $\hat{\psi}_j(S_j, \hat{\mathcal{E}}_{z,j}(z)) \in [0^\circ, 360^\circ)$ , so that the change in kinetic

energy  $\Delta E_{\text{kin},j}(S_j, \hat{\mathcal{E}}_{z,j}(z), \psi_j)$  during the first<sup>1</sup> pass through cavity  $j$  is maximum:

$$\hat{\psi}_j(S_j, \hat{\mathcal{E}}_{z,j}(z)) := \min \left( \operatorname{argmax}_{\psi_j \in [0^\circ, 360^\circ)} \left( \Delta E_{\text{kin},j}(S_j, \hat{\mathcal{E}}_{z,j}(z), \psi_j) \right) \right). \quad (3.10)$$

It has to be emphasized that this phase is dependent on the speed of the particle and does not necessarily refer to a particle traveling with a speed that provides maximum possible energy gain while passing cavity  $j$ . Figure 3.5 (simulated using the tracking tool ASTRA [74]) illustrates that context: If the speed and thus the time of flight of a particle through a cavity cell is unmatched to the half oscillation period of the RF field inside the cavity cell, an arrival-time deviation with respect to a downstream located cavity cell will be the result. That arrival-time deviation can be expressed by a phase deviation and is referred to as phase slippage. The effect accumulates from cell to cell and thus from cavity to cavity, while it may be compensated between cavities by an appropriate phase tuning. The amount to be added to the accumulated phase deviation becomes smaller (larger) as the speed increases (decreases) as a result of acceleration (deceleration).

Similarly, for a given setup  $S_j$  and a given time-independent amplitude of the on-axis  $z$ -component of the electric field,  $\hat{\mathcal{E}}_{z,j}(z)$ , there exists an initial phase  $\check{\psi}_j(S_j, \hat{\mathcal{E}}_{z,j}(z)) \in [0^\circ, 360^\circ)$  so that the change in kinetic energy  $\Delta E_{\text{kin},j}(S_j, \hat{\mathcal{E}}_{z,j}(z), \psi_j)$  during the *first* pass through cavity  $j$  is minimum:

$$\check{\psi}_j(S_j, \hat{\mathcal{E}}_{z,j}(z)) := \min \left( \operatorname{argmin}_{\psi_j \in [0^\circ, 360^\circ)} \left( \Delta E_{\text{kin},j}(S_j, \hat{\mathcal{E}}_{z,j}(z), \psi_j) \right) \right). \quad (3.11)$$

It has to be emphasized that usually

$$\min_{\psi_j \in [0^\circ, 360^\circ)} \left( \Delta E_{\text{kin},j}(S_j, \hat{\mathcal{E}}_{z,j}(z), \psi_j) \right) \neq - \max_{\psi_j \in [0^\circ, 360^\circ)} \left( \Delta E_{\text{kin},j}(S_j, \hat{\mathcal{E}}_{z,j}(z), \psi_j) \right) \quad (3.12)$$

and

$$\left( \check{\psi}_j(S_j, \hat{\mathcal{E}}_{z,j}(z)) - \hat{\psi}_j(S_j, \hat{\mathcal{E}}_{z,j}(z)) \right) \bmod 360^\circ \neq 180^\circ \quad (3.13)$$

apply (see Fig. 3.6).

Using  $\hat{\psi}_j$  and  $\check{\psi}_j$ , the off-crest acceleration phase

$$\hat{\phi}_j(S_j, \hat{\mathcal{E}}_{z,j}(z)) := \left( \psi_j - \hat{\psi}_j(S_j, \hat{\mathcal{E}}_{z,j}(z)) + 180^\circ \right) \bmod 360^\circ - 180^\circ \quad (3.14)$$

and the off-crest deceleration phase

$$\check{\phi}_j(S_j, \hat{\mathcal{E}}_{z,j}(z)) := \left( \psi_j - \check{\psi}_j(S_j, \hat{\mathcal{E}}_{z,j}(z)) + 180^\circ \right) \bmod 360^\circ - 180^\circ \quad (3.15)$$

are defined. If  $\hat{\phi}_j = 0^\circ$  or  $\check{\phi}_j = 0^\circ$  applies, this is called on-crest acceleration or on-crest deceleration in cavity  $j$ , respectively.

---

<sup>1</sup>The definition of  $\hat{\psi}_j$  (as well as of  $\check{\psi}_j$ ,  $\hat{\phi}_j$  and  $\check{\phi}_j$ ) refers explicitly only to the *first* pass of cavity  $j$  because (i) the phases of the main LINAC are only set during the first main-LINAC pass (see section 4.2.4) and (ii) the acting phases of subsequent main-LINAC passes may differ from the ones of the first main-LINAC pass.

Figure	Curve	$p(z_{1j})$ (MeV/c)	$\psi_j$ (°)	$\hat{\phi}_j(p(z_{1j}))$ (°)
(a)+(c)	—	5.00	66.2	9.0
	- - -	7.34	66.2	5.0
	⋯	23.66	66.2	0.0
(b)+(d)	—	5.00	66.2–9.0	0.0
	- - -	7.34	66.2–5.0	0.0
	⋯	23.66	66.2–0.0	0.0

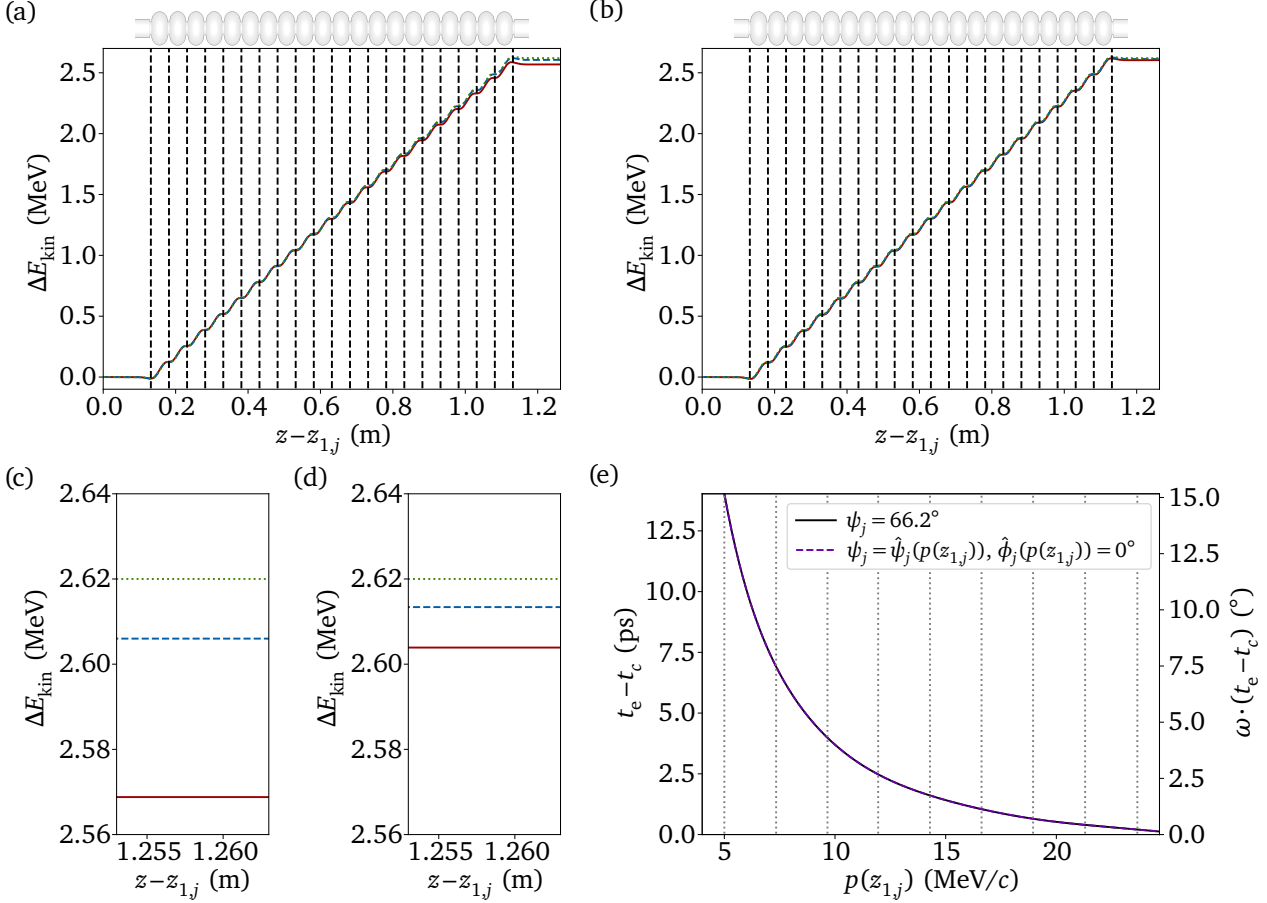


**Figure 3.5: Change in kinetic energy during a cavity pass (1/3).** An electron is entering the fringe-field region of cavity  $j$  at time  $t = 0$ . For the cavity's RF field,  $\hat{\mathcal{E}}_{z,j,\text{peak}} = 5$  MV/m applies. An electron's energy gain along the cavity and the time of flight through the cavity are dependent on the electron's entry momentum  $p(z_{1j})$  and the cavity's initial phase  $\psi_j$ . Highlighted momenta values occur as design value or centroid value, respectively, at certain locations in the two-turn energy-recovery mode (see Table B.1): after passing the injector LINAC (5.00 MeV/c), after passing the first cavity of the main LINAC (A1SC01) for the first time (7.34 MeV/c), and after the first entire main-LINAC pass (23.66 MeV/c). (a)–(d) Change in kinetic energy. (a)+(b) Dashed vertical lines indicate the entrances and the exits of the cavity cells, respectively. (a)+(c) Initial phase  $\psi_j$  identical for all electrons and thus only suitable for maximum possible energy gain if a particle travels at speed of light. (b)+(d) Initial phase  $\psi_j = \hat{\psi}_j(p(z_{1j}))$ , that is,  $\hat{\phi}_j(p(z_{1j})) = 0^\circ$ , and thus suitable for maximum possible energy gain of a particle entering the cavity with the speed  $v(p(z_{1j}))$ . (c) Zoom into end section of figure (a). (d) Zoom into end section of figure (b). (e) For a given  $p(z_{1j})$ , an electron needs the time  $t_e$  to pass a cavity including fringe-field regions, while the continuous change in speed due to the continuous change in kinetic energy while passing a cavity is taken into account. A particle traveling at speed of light – what the cavity is designed for – needs the time  $t_c$  to pass the same section. Thus, there is a time difference  $t_e - t_c$  that is dependent on  $p(z_{1j})$  and  $\psi_j$ . Due to the high frequency of the RF field, even a small time difference can lead to a significant phase offset  $\omega \cdot (t_e - t_c)$  at an immediately following cavity. This phase slippage will be correspondingly larger if a certain drift section between the cavities exists. Dotted vertical lines indicate centroid momenta present at a cavity entrance or exit during the first main-LINAC pass in the two-turn energy-recovery mode, respectively (see Table B.1).



Curve	$p(z_{1j})$ (MeV/c)	$\psi_j$ (°)	$\hat{\phi}_j(p(z_{1j}))$ (°)	$\check{\phi}_j(p(z_{1j}))$ (°)
—	7.34	66.2	5.0	-180+2.0+5.0
- - -	7.34	66.2-5.0	0.0	-180+2.0
⋯	7.34	66.2-5.0+180	180	2.0
- · -	7.34	66.2-5.0+180-2.0	180-2.0	0.0

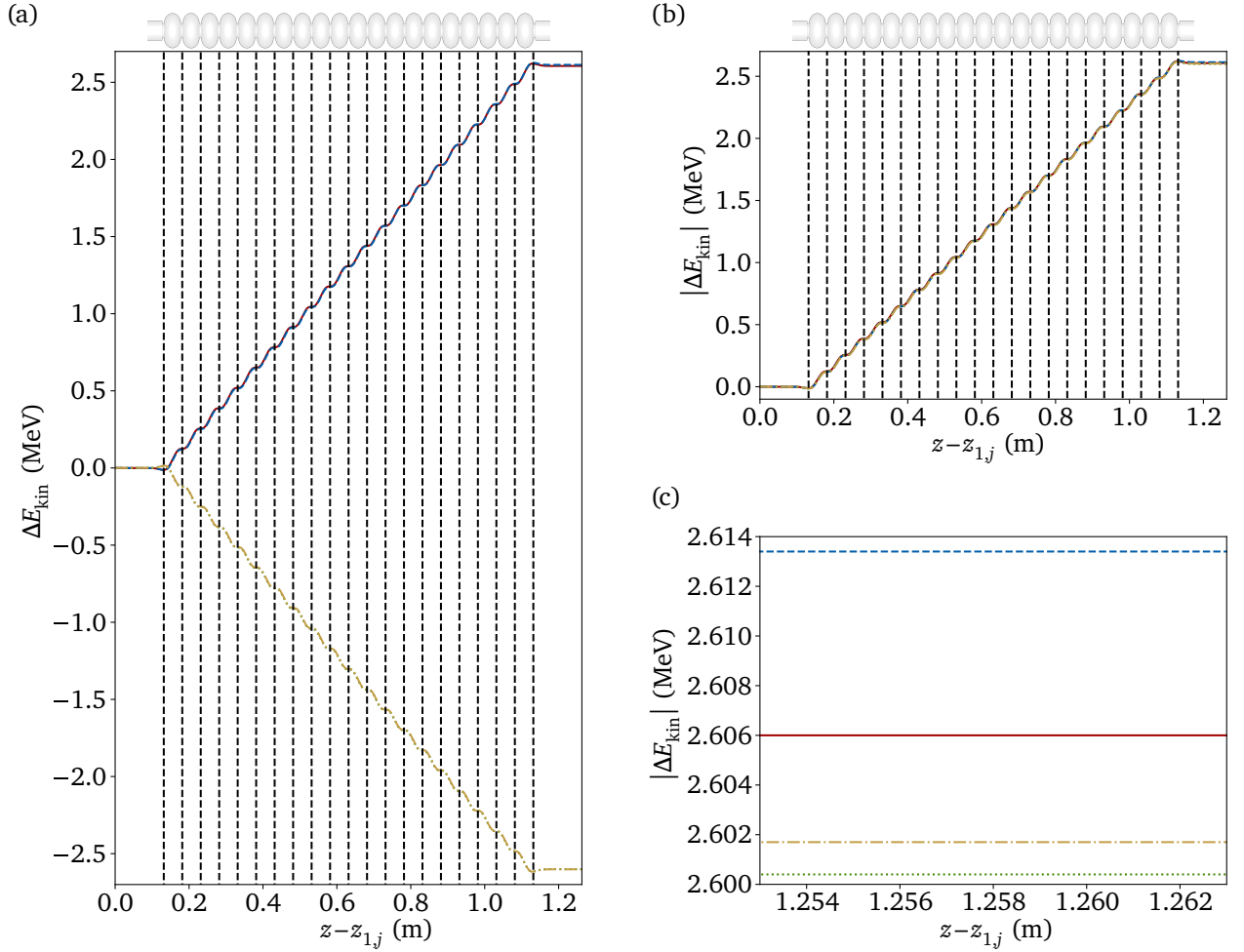


**Figure 3.6: Change in kinetic energy during a cavity pass (2/3).** An electron is entering the fringe-field region of cavity  $j$  at time  $t = 0$  with a momentum  $p(z_{1j}) = 7.34$  MeV/c. For the cavity's RF field,  $\hat{\mathcal{E}}_{z,j,\text{peak}} = 5$  MV/m applies. The change in kinetic energy of an electron is dependent on the cavity's initial phase  $\psi_j$ . (a) Change in kinetic energy along cavity  $j$ . (b) Absolute value of the change in kinetic energy along cavity  $j$ . (a)–(b) Dashed vertical lines indicate the entrances and the exits of the cavity cells, respectively. (c) Zoom into end section of figure (b). Here, it can be seen that the inequations (3.12) and (3.13) apply.

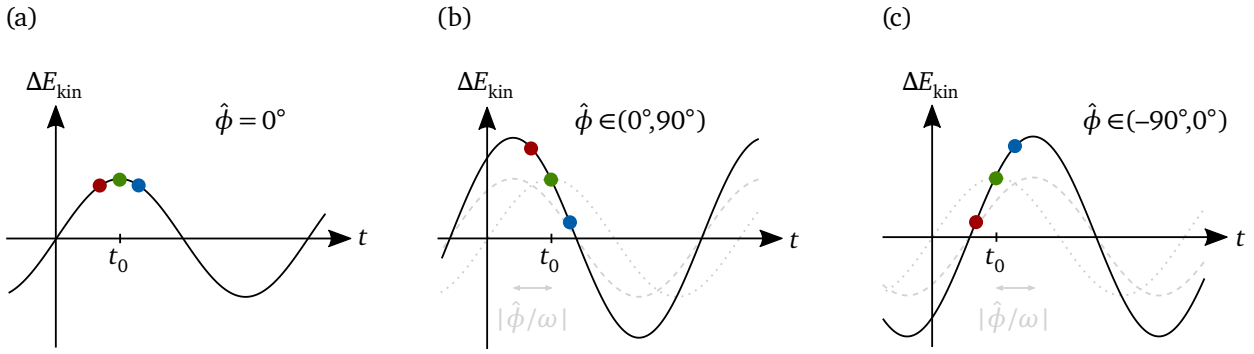


**Figure 3.7: Change in kinetic energy during a cavity pass (3/3).** For the cases investigated in this work, there is approximately a trigonometric dependence between change in kinetic energy as a result of a cavity pass,  $\Delta E_{\text{kin}}$ , and arrival time of a particle at the entrance of the corresponding cavity,  $t$  (black solid). The figure shows the behavior for three different particles in a bunch passing a cavity, where the central particle (green) is the design particle with arrival time at the entrance of a cavity,  $t_0$ . (a) In the case of an on-crest acceleration (that is,  $\hat{\phi} = 0^\circ$ ) the design particle experiences the maximum possible energy gain, while particles arriving earlier or later gain less energy than the design particle. (b)–(c) In the case of an off-crest acceleration (that is,  $\hat{\phi} \neq 0^\circ$ ), the design particle does not experience the maximum possible energy gain. Instead, particles arriving at the time  $t_0 - \hat{\phi}/\omega$  experience the maximum possible energy gain. Compared to the on-crest case (grey dotted), the curve has an absolute offset of  $|\hat{\phi}/\omega|$  (grey dashed). Compared to an on-crest acceleration, the amplitude of the electric field has to be increased by a factor of  $1/\cos(\hat{\phi})$  to provide equal change in kinetic energy for the design particle during an off-crest acceleration. (a)–(c) Depending on the value of  $\hat{\phi}$ , the correlation between  $E_{\text{kin}} - E_{\text{kin},0}$  and  $t - t_0$  is influenced, where  $E_{\text{kin},0}$  is the kinetic energy of the design particle.

The usage of alternating electric fields for acceleration or deceleration, respectively, requires the particles of the beam to be grouped in bunches. Here, all particles of a bunch can be described relative to a notional design particle inside that bunch. Properties of the design particle may differ from the ones of a calculated centroid particle, but the differences are usually small and therefore negligible. Values for  $\hat{\phi}$  or  $\check{\phi}$  mentioned in this chapter always refer to the design particle, while – due to the capabilities of the used simulation software – values mentioned in sections 4.2.2 and 4.3.2 refer to the centroid particle.

Due to the dependence of a particle's change in kinetic energy on the particle's speed and the particle's arrival time at the cavity, particles in a bunch may experience different changes in kinetic energy when passing the very cavity. If the speeds of the particles inside a bunch hardly differ from each other, and if the particles' times of flight through a cell of a cavity almost match the half oscillation period of the standing wave in that very cavity, then there is approximately a trigonometric dependence between the change in kinetic energy during a cavity pass and the arrival time at the very cavity (see Fig. 3.7). By choosing a suitable value for  $\hat{\phi}$  or  $\check{\phi}$ , respectively, a favorable correlation between the energy of a particle and the longitudinal position within the bunch can be created. More details on bunch structures and correlations within a bunch are discussed in sections 3.6 and 3.7.

In this section, a particle traveling on the center axis of a cavity was discussed in order to introduce phase slippage and off-crest acceleration. However, in the beam-dynamics

simulations, off-axis particles have to be taken into account as well. Here, the non-simplified Eq. (3.3) has to be solved (numerically) when the particle is traveling through an RF field.

### 3.4 Deflection in Static Magnetic Fields

In this section, the change of a particle's trajectory due to static magnetic fields is described. Thus, there is no time dependence in describing the trajectory of an individual particle.

The transverse slopes of  $x(s)$  and  $y(s)$  are defined as follows:

$$x'(s) := \left. \frac{dx(s')}{ds'} \right|_{s'=s} \quad \text{and} \quad y'(s) := \left. \frac{dy(s')}{ds'} \right|_{s'=s}. \quad (3.16)$$

The total distance traveled related to  $s$  is given by  $\hat{l}(s)$  for an individual particle and  $\hat{l}_0(s)$  for the design particle. Since  $\hat{l}_0(s) = s$ , the relative distance traveled,  $l$ , is defined as follows:

$$l(s) := \hat{l}(s) - \hat{l}_0(s) = \hat{l}(s) - s. \quad (3.17)$$

The relative momentum

$$\delta(s) := \frac{p(s) - p_0(s)}{p_0(s)} \quad (3.18)$$

results from the magnitude of the momentum vector<sup>2</sup> [71]

$$p(s) = \frac{1}{c} \cdot \sqrt{(E_{\text{kin}}(s) + E_{\text{rest}})^2 - E_{\text{rest}}^2} \quad (3.19)$$

and the momentum of the design particle,  $p_0(s)$ .

Using these definitions, an individual particle can be described by the coordinate vector

$$\vec{X}(s) = (X_1(s) \ \cdots \ X_6(s))^T = (x(s) \ x'(s) \ y(s) \ y'(s) \ l(s) \ \delta(s))^T. \quad (3.20)$$

Here, each coordinate  $X_i(s)$  of an individual particle's coordinate vector  $\vec{X}(s)$  can be calculated approximately by first-order terms  $R_{ij}$  and second-order terms  $T_{ijk}$  [75]:

$$X_i(s_2) = \sum_{j=1}^6 R_{ij,s_1 \rightarrow s_2} X_j(s_1) + \sum_{j=1}^6 \sum_{k=j}^6 T_{ijk,s_1 \rightarrow s_2} X_j(s_1) X_k(s_1). \quad (3.21)$$

For a first approach,  $T_{ijk}$  is zero until the end of this section. Non-zero values for  $T_{ijk}$  are discussed in section 3.5. If  $T_{ijk} = 0$  applies, the transformation from  $\vec{X}(s_1)$  to  $\vec{X}(s_2)$  can be calculated using the  $6 \times 6$ -dimensional transport matrix  $R(s_1 \rightarrow s_2)$ :

$$\vec{X}(s_2) = R(s_1 \rightarrow s_2) \cdot \vec{X}(s_1). \quad (3.22)$$

<sup>2</sup>In the following, the magnitude of the momentum vector is referred to as momentum; if the vector quantity is addressed, it is always referred to as momentum vector.

The transformation from  $\vec{X}(s_1)$  to  $\vec{X}(s_N)$  can be described by a single matrix  $R(s_1 \rightarrow s_N)$  that is the product of matrices, each representing an iterative transformation:

$$R(s_1 \rightarrow s_N) = R(s_{N-1} \rightarrow s_N) \cdot \dots \cdot R(s_2 \rightarrow s_3) \cdot R(s_1 \rightarrow s_2). \quad (3.23)$$

In the following, transport matrices for different magnet types are provided. The magnets are separated by drift sections. The transport of an individual particle through a drift section of effective length  $L = s_2 - s_1$  is described by the matrix [75]

$$R_D(s_1 \rightarrow s_2) = \begin{pmatrix} 1 & L & 0 & 0 & 0 & 0 \\ 0 & 1 & 0 & 0 & 0 & 0 \\ 0 & 0 & 1 & L & 0 & 0 \\ 0 & 0 & 0 & 1 & 0 & 0 \\ 0 & 0 & 0 & 0 & 1 & 0 \\ 0 & 0 & 0 & 0 & 0 & 1 \end{pmatrix}. \quad (3.24)$$

Here, the term “effective” appears for the following reason: The field-free drift section links two sections with non-zero fields. Starting from a drift section, an individual particle passes a field that changes from zero to a certain value and further downstream changes from a certain value to zero when arriving at the next drift section. In real magnets, the fields are continuous functions of the location. For beam-dynamics simulations, it is suitable to approximate these continuous functions by step functions. Figure 3.8 indicates how the effective length is determined. For a given beam guiding element with quantity  $\chi$  as specified below, its effective length is given by [76]

$$L = \frac{1}{\mathcal{P}(\chi)} \int_{-\infty}^{\infty} \chi(s) ds, \quad (3.25)$$

where

$$\mathcal{P}(\chi) = \begin{cases} \max(\chi), & \max(\chi) \geq -\min(\chi) \\ \min(\chi), & \max(\chi) < -\min(\chi) \end{cases} \quad (3.26)$$

is the plateau value of the quantity  $\chi$ . Superpositions of beam guiding elements are not taken into account; only the field generated by a single element is considered.

Besides slight vertical deflections in the gun and the chopper section, the design orbit of those sections of the S-DALINAC tuned within this work contains only deflections in the horizontal plane (with respect to a coordinate system at rest), for which dipole magnets are used (see Fig. 3.9). In an ideal horizontal deflecting dipole magnet, there is only the vertical magnetic component  $B_y$  (edge fields are discussed below), thus  $\chi = B_y$ . Here, the bending radius is given by [76]

$$\rho(s) = \frac{p(s)}{qB_y(s)} = \frac{\sqrt{(E_{\text{kin}}(s) + E_{\text{rest}})^2 - E_{\text{rest}}^2}}{cqB_y(s)} = \frac{\beta(s)\gamma(s)\tilde{m}_{\text{rest}}c}{qB_y(s)}, \quad (3.27)$$

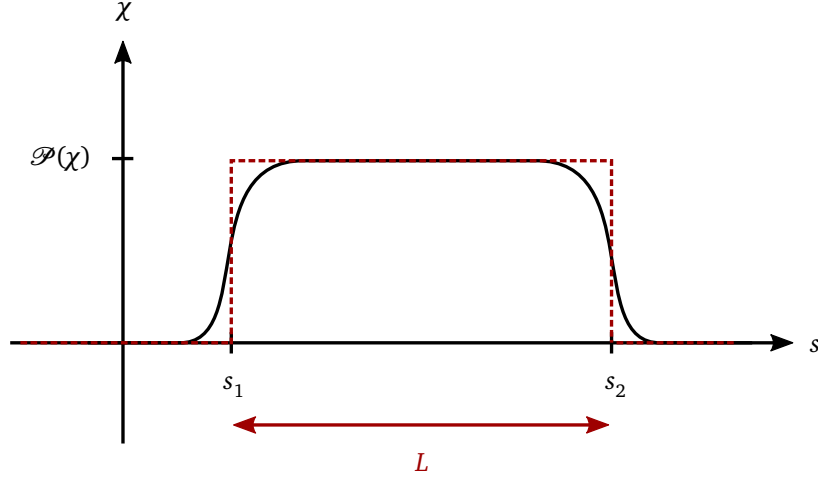


**Figure 3.8: Effective Length.** Example of a continuous function  $\chi$  (black) that is approximated by a step function (red dashed) to determine the effective length  $L$ .

where  $\tilde{m}_{\text{rest}}$  is the rest mass of the particle. A positive (negative)  $\rho$  leads to deflection to the right (left). A dipole magnet has a bending radius for the design particle,  $\rho_0(s) = p_0(s)/(q\mathcal{P}(B_y))$ , a bending angle for the design particle,  $\alpha_0 = L/\rho_0$ , as well as an entrance (exit) edge angle  $\Omega_{\text{in}}$  ( $\Omega_{\text{out}}$ ) describing the orientation of the  $x$ - $y$ -plane of the coordinate system in motion with origin at the entrance (exit) of the dipole magnet relative to the yoke's plane at the entrance (exit). Two special types of dipole magnets are (i) the sector dipole magnet, where  $\Omega_{\text{in}} = \Omega_{\text{out}} = 0^\circ$  applies, and (ii) the rectangular dipole magnet, where  $\Omega_{\text{in}} = \Omega_{\text{out}} = \alpha_0/2$  with the limit  $|\alpha_0| < 180^\circ$  applies (see Fig. 3.9).

The transport matrix for an ideal sector dipole (SD) magnet deflecting in the horizontal plane is given by [75]

$$R_{\text{SD}}(s_1 \rightarrow s_2) = \begin{pmatrix} \cos(\alpha_0) & \rho_0 \sin(\alpha_0) & 0 & 0 & 0 & \rho_0(1 - \cos(\alpha_0)) \\ -\frac{\sin(\alpha_0)}{\rho_0} & \cos(\alpha_0) & 0 & 0 & 0 & \sin(\alpha_0) \\ 0 & 0 & 1 & L & 0 & 0 \\ 0 & 0 & 0 & 1 & 0 & 0 \\ \sin(\alpha_0) & \rho_0(1 - \cos(\alpha_0)) & 0 & 0 & 1 & L - \rho_0 \sin(\alpha_0) \\ 0 & 0 & 0 & 0 & 0 & 1 \end{pmatrix}. \quad (3.28)$$

General shapes of dipole magnets are taken into account by the transport matrix for a magnet's edge [75]

$$R_{\text{edge}}(\Omega) = \begin{pmatrix} 1 & 0 & 0 & 0 & 0 & 0 \\ \frac{\tan(\Omega)}{\rho_0} & 1 & 0 & 0 & 0 & 0 \\ 0 & 0 & 1 & 0 & 0 & 0 \\ 0 & 0 & -\frac{\tan(\tilde{\Omega})}{\rho_0} & 1 & 0 & 0 \\ 0 & 0 & 0 & 0 & 1 & 0 \\ 0 & 0 & 0 & 0 & 0 & 1 \end{pmatrix}, \quad (3.29)$$

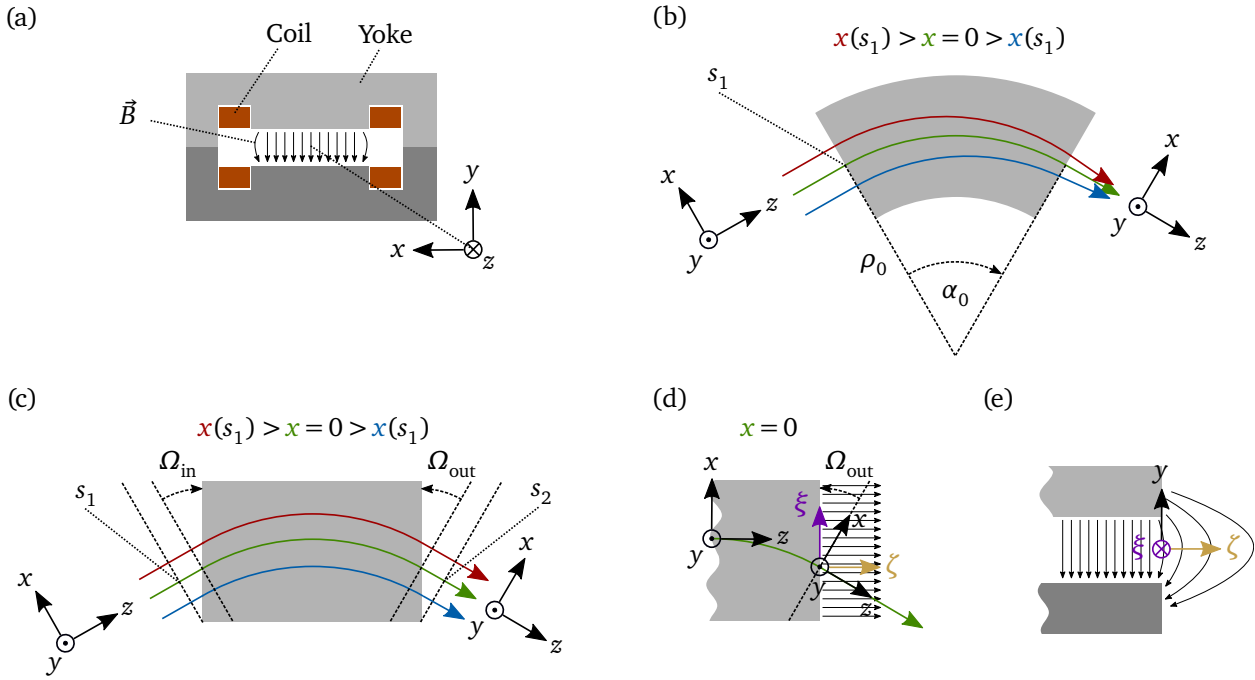


**Figure 3.9: Dipole magnet.** (a) Cut in the  $x$ - $y$ -plane of the center of a dipole magnet. The magnetic field oriented from the north (light gray) to the south (dark gray) pole is generated by coils and strengthened by the yoke. The latter shapes the field so that it is approximately homogeneous in the center region of the magnet. (b)–(c) Top view. Trajectories are shown for electrons with a vector  $\vec{X}(s_1) = (x \ 0 \ 0 \ 0 \ 0 \ 0)^T$ . (b) Sector dipole magnet. For different  $x$  values, the lengths of the electrons' paths through a non-zero magnetic field are different if  $|\alpha_0| \neq 180^\circ$ , leading to a weak (de)focusing in the horizontal plane if  $0^\circ < |\alpha_0| \leq 90^\circ$  or if  $180^\circ < |\alpha_0| \leq 270^\circ$  ( $90^\circ < |\alpha_0| < 180^\circ$  or if  $270^\circ < |\alpha_0| < 360^\circ$ ); if  $|\alpha_0| = 180^\circ$ , the lengths of the electrons' paths through a non-zero magnetic field are equal and there is no focusing or defocusing in the horizontal plane. (c) Rectangular dipole magnet. The lengths of the electrons' paths through a non-zero magnetic field is equal so that  $x(s_1) = x(s_2)$  applies per electron. (d)–(e) The magnetic-field lines at the exit edge are shown for a part of a rectangular dipole magnet. (d) Top view of a part of a rectangular dipole magnet. The trajectory is given for the design electron. The origin of the  $\zeta$ -axis is located where the design trajectory crosses the yoke's plane at the exit, and the  $\zeta$ -axis is oriented away from the magnet and perpendicularly to the yoke's plane at the exit. As long as  $y \neq 0$ , the magnetic-field lines at the exit edge are not perpendicular to the  $x$ -axis, that is, they have a non-zero  $x$ -component,  $B_x \neq 0$ . This causes vertical deflection, while the deflection direction is dependent on the sign of  $y$  and – in general – the value of the exit edge angle  $\Omega_{\text{out}}$  (which is given in the case of a rectangular dipole magnet); in the case of a rectangular dipole magnet, the deflection results in vertical focusing. (e) Cut in the  $y$ - $\zeta$ -plane of a part of a rectangular dipole magnet. Since the  $x$ -axis is in the  $\xi$ - $\zeta$ -plane, magnetic-field lines are perpendicular to the  $x$ -axis if they are perpendicular to both the  $\xi$ -axis and the  $\zeta$ -axis, which is only the case if  $y$  is zero. Consequently, if  $y = 0$  applies,  $B_x = 0$  applies and vertical deflection does not occur. (b)–(e) Coils are not shown.

leading to the transport matrix of a general dipole (GD) magnet with individual entrance and exit edge angles:

$$R_{\text{GD}}(s_1 \rightarrow s_2) = R_{\text{edge}}(\Omega_{\text{out}}) \cdot R_{\text{SD}}(s_1 \rightarrow s_2) \cdot R_{\text{edge}}(\Omega_{\text{in}}). \quad (3.30)$$

The quantity

$$\tilde{\Omega} = \Omega - \frac{1 + \sin^2(\Omega)}{\rho_0 \mathcal{P}^2(B_y) \cos(\Omega)} \int_{\zeta_1}^{\zeta_2} B_y(\zeta) \cdot (\mathcal{P}(B_y) - B_y(\zeta)) d\zeta \quad (3.31)$$

appearing in Eq. (3.29) is an adjusted edge angle in which the finiteness of the edge field is taken into account. Here,  $\zeta_1$  and  $\zeta_2$  are two locations on a path that is (i) orthogonal to the plane of the corresponding edge, (ii) crossing the design trajectory at the very edge, and (iii) oriented from the inside to the outside of the magnet where  $B_y(\zeta_1) = \mathcal{P}(B_y)$  and  $B_y(\zeta_2) = 0$  apply for  $\zeta_1 < \zeta_2$  (see Fig. 3.9(d)–(e)).

Transverse confinement is mainly realized by utilizing the focusing properties of quadrupole magnets (see Fig. 3.10). In an ideal quadrupole magnet, the magnetic field is proportional to the transverse deviation from the design orbit, which leads to a location-dependent gradient

$$\tilde{g}(s) := \frac{\partial B_y(s, x)}{\partial x} = \frac{\partial B_x(s, y)}{\partial y} \quad (3.32)$$

and thus  $\chi = \tilde{g}$ . A quadrupole magnet can focus in one plane only while at the same time it is defocusing in the plane perpendicular to the former. Therefore, net focusing in two planes that are perpendicular to each other requires several quadrupole magnets with well-chosen gradients installed in series. A special combination of quadrupole magnets is a quadrupole-magnet triplet, which can provide a point-to-point map (see Fig. 3.10). With the location-independent gradient  $g := \mathcal{P}(\tilde{g})$ , the focusing strength  $\kappa := gq/p_0$  and the compact notation parameter  $\Gamma := L\sqrt{\kappa}$  ( $\Gamma \in \mathbb{C}$ ), the transport matrix for an ideal quadrupole magnet is given by [75]

$$R_Q(s_1 \rightarrow s_2) = \begin{pmatrix} \cos(\Gamma) & \frac{\sin(\Gamma)}{\sqrt{\kappa}} & 0 & 0 & 0 & 0 \\ -\sqrt{\kappa} \sin(\Gamma) & \cos(\Gamma) & 0 & 0 & 0 & 0 \\ 0 & 0 & \cosh(\Gamma) & \frac{\sinh(\Gamma)}{\sqrt{\kappa}} & 0 & 0 \\ 0 & 0 & \sqrt{\kappa} \sinh(\Gamma) & \cosh(\Gamma) & 0 & 0 \\ 0 & 0 & 0 & 0 & 1 & 0 \\ 0 & 0 & 0 & 0 & 0 & 1 \end{pmatrix}. \quad (3.33)$$

There are transport elements that are the rotation of other transport elements. For example, a vertical deflecting dipole magnet is a horizontal deflecting dipole magnet rotated by  $90^\circ$  around the  $z$ -axis. If an element with transport matrix  $R$  is rotated by the transformation angle  $\Phi$  around the  $z$ -axis, its new transport matrix  $\hat{R}$  is given by [77]

$$\hat{R}(s_1 \rightarrow s_2, \Phi) = R_{\text{rot}}(-\Phi) \cdot R(s_1 \rightarrow s_2) \cdot R_{\text{rot}}(\Phi), \quad (3.34)$$

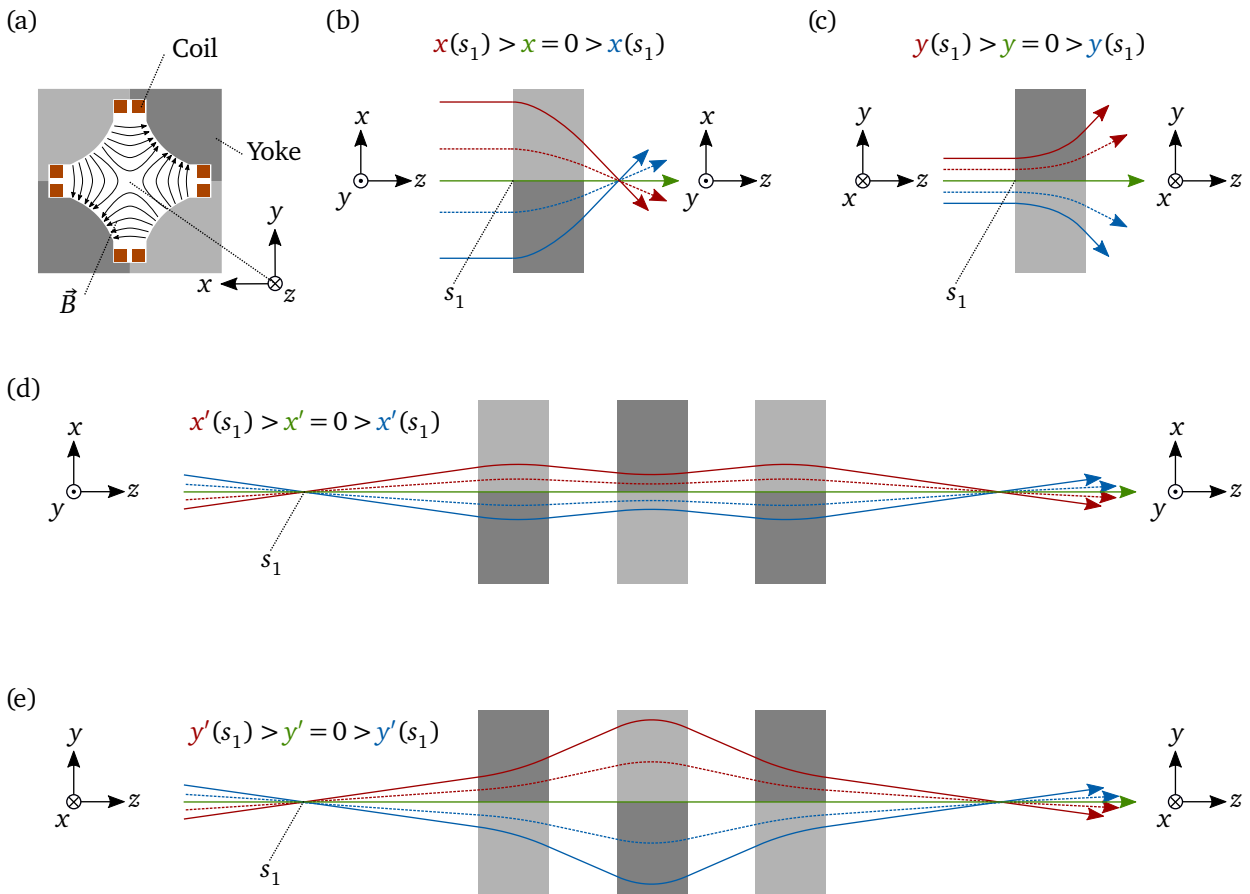


**Figure 3.10: Quadrupole magnet.** (a) Cut in the  $x$ - $y$ -plane of the center of a quadrupole magnet. The magnetic field oriented from the north (light gray) to the south (dark gray) pole is generated by coils and strengthened by the yoke. The latter shapes the field so that it is approximately proportional to the distance from the center of the magnet. (b) Top view. Trajectories are shown for electrons with a vector  $\vec{X}(s_1) = (x \ 0 \ 0 \ 0 \ 0)^T$ . Electrons traveling on the design trajectory are not influenced, electrons with non-zero  $x$  are bent toward the design trajectory. (c) Side view. Trajectories are shown for electrons with a vector  $\vec{X}(s_1) = (0 \ 0 \ y \ 0 \ 0)^T$ . Electrons traveling on the design trajectory are not influenced, electrons with non-zero  $y$  are bent away from the design trajectory. (b)–(c) By swapping the magnet’s polarity, the effects can be swapped. (d)–(e) Quadrupole-magnet triplet. Trajectories are shown for electrons with a vector  $\vec{X}(s_1) = (0 \ x' \ 0 \ y' \ 0)^T$  with  $x'(s_1) = y'(s_1)$ . A beam with a circular transverse profile in front of the quadrupole-magnet triplet will be a beam with a circular transverse profile behind the quadrupole-magnet triplet as well (point-to-point map). The gradients of the first and the third quadrupole magnets are equal, while the gradient of the second quadrupole magnet has an opposite sign and an larger absolute value compared to the gradient of the first and the third quadrupole magnet, respectively. (d) Top view. (e) Side view. (b)+(d)+(e) Per figure, the focus length is constant for all electrons with  $\delta = 0$ . (b)–(e) Coils are not shown.



where

$$R_{\text{rot}}(\Phi) = \begin{pmatrix} \cos(\Phi) & 0 & \sin(\Phi) & 0 & 0 & 0 \\ 0 & \cos(\Phi) & 0 & \sin(\Phi) & 0 & 0 \\ -\sin(\Phi) & 0 & \cos(\Phi) & 0 & 0 & 0 \\ 0 & -\sin(\Phi) & 0 & \cos(\Phi) & 0 & 0 \\ 0 & 0 & 0 & 0 & 1 & 0 \\ 0 & 0 & 0 & 0 & 0 & 1 \end{pmatrix} \quad (3.35)$$

is the rotation matrix.

By passing the above described beam guiding elements, the total distance traveled  $\hat{l}$  changes. The time of flight of a particle needed to pass a distance

$$\hat{l}(s_2) - \hat{l}(s_1) = (s_2 + l(s_2)) - (s_1 + l(s_1)) \quad (3.36)$$

is given by utilizing Eq. (3.5):

$$t(s_1 \rightarrow s_2) = \int_0^{\hat{l}(s_2)} \frac{1}{v(s)} ds - \int_0^{\hat{l}(s_1)} \frac{1}{v(s)} ds = \int_{\hat{l}(s_1)}^{\hat{l}(s_2)} \frac{1}{v(s)} ds = \int_{s_1+l(s_1)}^{s_2+l(s_2)} \frac{1}{v(s)} ds. \quad (3.37)$$

If the speed of an individual particle is constant from  $s_1$  to  $s_2$ ,

$$t(s_1 \rightarrow s_2) = \frac{(s_2 + l(s_2)) - (s_1 + l(s_1))}{v} = \frac{s_2 - s_1 + (l(s_2) - l(s_1))}{v} \quad (3.38)$$

applies. Within the scope of this work, suitable values for  $t(s_1 \rightarrow s_2)$  have to be provided, which in turn is realized by influencing  $l(s_2) - l(s_1)$ . The corresponding technique is described in section 3.5.

### 3.5 Transverse and Longitudinal Dispersion

As mentioned, the first-order transport of an individual particle through an entire section can be described by using Eq. (3.23). The matrix elements describing a dependence on the momentum are referred to as first-order dispersion, and are of high interest in this work.

The matrix element  $R_{16}$  is the first-order horizontal dispersion,  $R_{26}$  its derivative,  $R_{36}$  is the first-order vertical dispersion,  $R_{46}$  its derivative, and  $R_{56}$  is the first-order longitudinal dispersion. To realize a transport matrix from  $s_1$  to  $s_2$  with non-zero dispersion values as a combination of transport matrices given in section 3.4, at least one dipole magnet matrix is required (see appendix C.1). If there is no vertical deflection, the vertical dispersion remains zero, that is,  $R_{36,s_1 \rightarrow s_2} = R_{46,s_1 \rightarrow s_2} = 0$ . Due to deflection in the horizontal plane at the S-DALINAC, non-zero  $R_{16}$  and  $R_{26}$  result. Although it requires at least one dipole magnet to yield non-zero dispersion values, the (first-order) dispersion can be influenced by a quadrupole magnet if  $R_{16} \neq 0$  and/or  $R_{26} \neq 0$  applies at the entry of the very quadrupole magnet (see Figs. 3.11, 3.12 and 5.1 as well as appendix C.1). Since dipole magnets influence

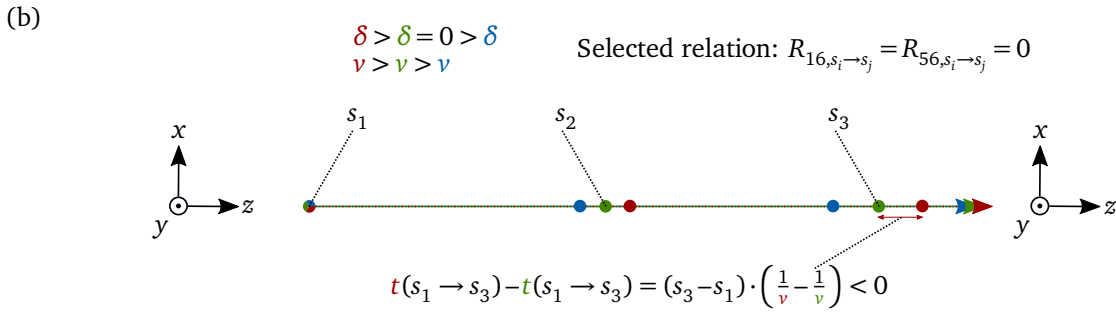
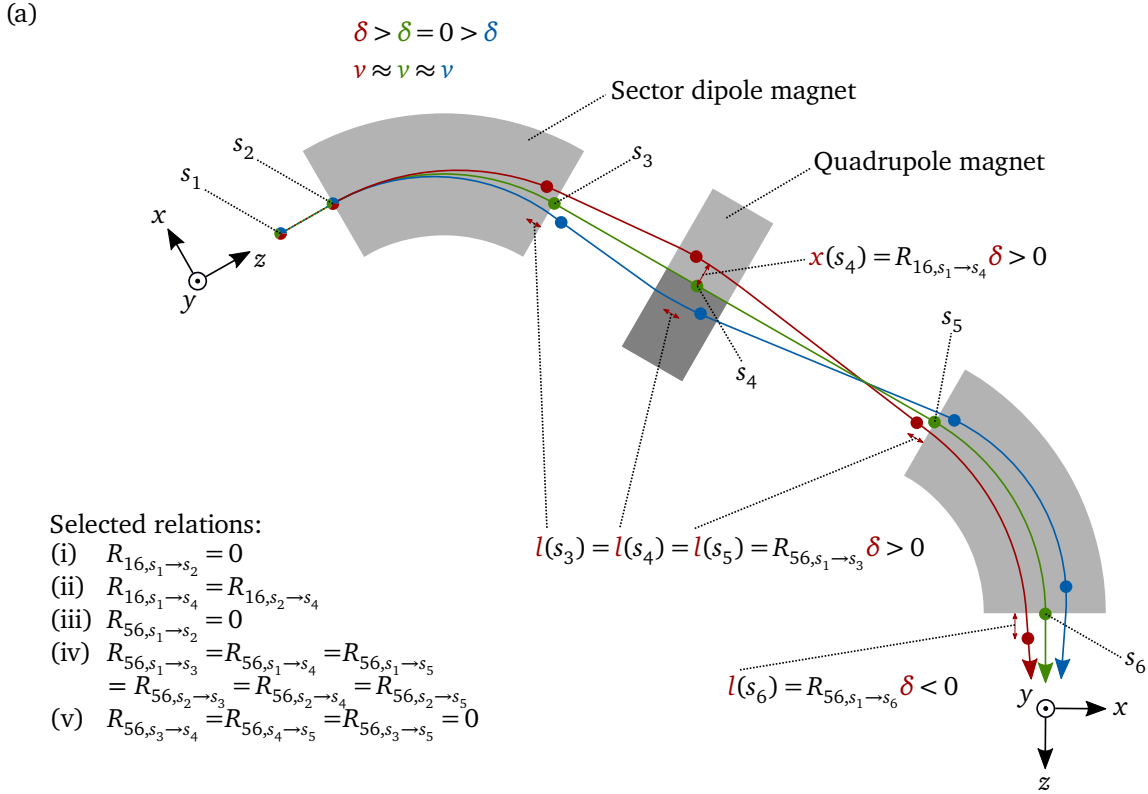


**Figure 3.11: Dispersion and time of flight.** (a)–(b) Trajectories are shown for electrons with a vector  $\vec{X}(s_1) = (0 \ 0 \ 0 \ 0 \ 0 \ \delta)^T$ . (a) Electrons with different relative momenta have different trajectories and may cover different total distances traveled to reach location  $s$ , depending on the dispersion. Here, differences in the speed of the electrons are insignificant. In linear approximation, the coordinates  $x$  and  $l$  can be expressed by  $R_{16}$  and  $R_{56}$ , respectively, if  $\delta$  is given. While  $R_{16,s_1 \rightarrow s}$  is continuously changing from  $s_2$  to  $s_6$ ,  $R_{56,s_1 \rightarrow s}$  can only change inside a dipole magnet (compare  $l$  at  $s_3$ ,  $s_4$  and  $s_5$ , see Eq. (3.39)). By a combination of dipole and quadrupole magnets, the first-order dispersion terms can be manipulated. Trajectories are not to scale; higher-order terms are not taken into account; higher-order longitudinal dispersion terms can change outside a dipole magnet as well (see Eq. (3.43)). (b) If differences in the speed of electrons with different relative momenta are significant, the times of flight through a section differ even if the total distances traveled are equal.

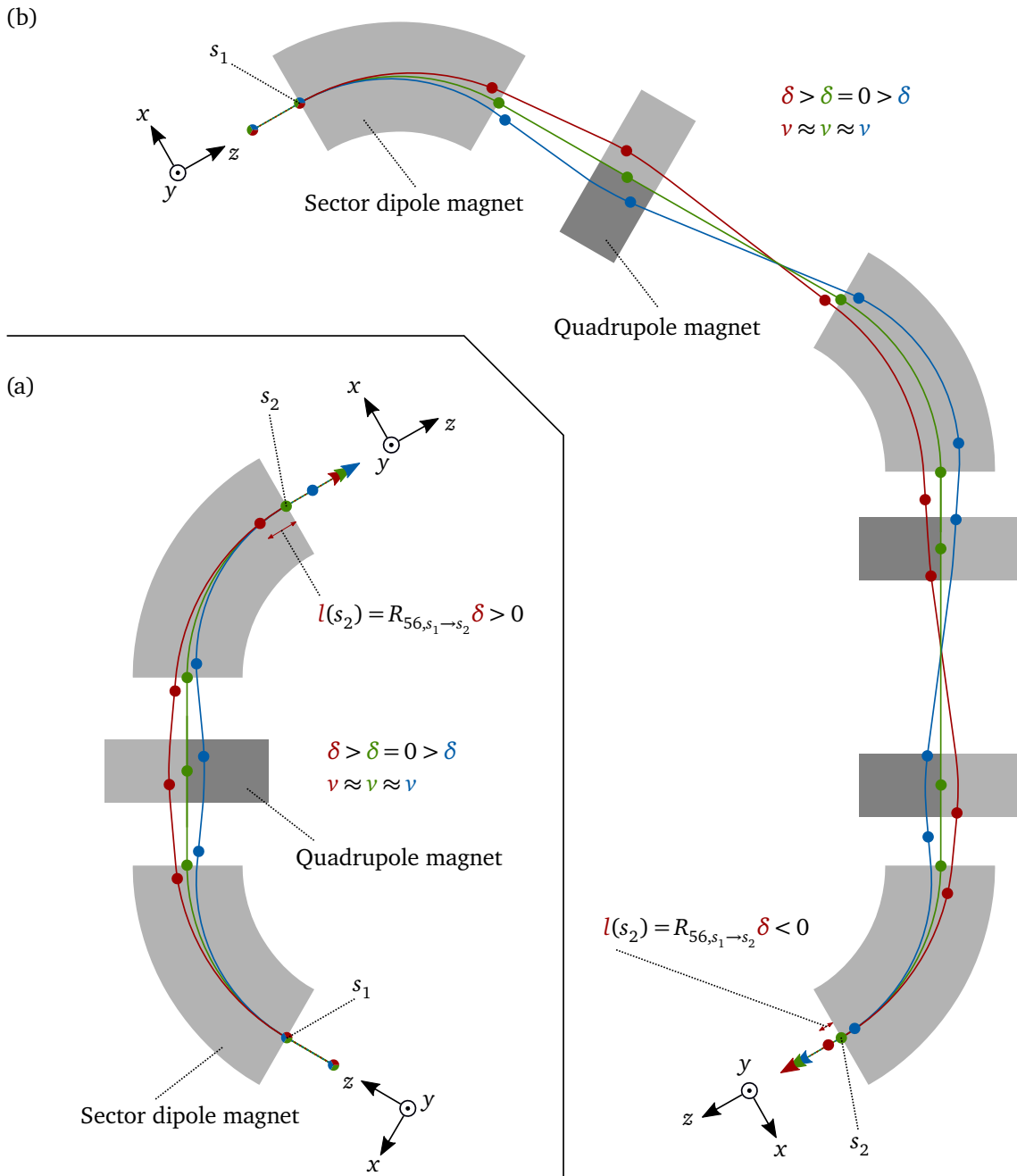


**Figure 3.12: Achromat condition and individual longitudinal dispersion.** (a)–(b) Trajectories are shown for electrons with a vector  $\vec{X}(s_1) = (0 \ 0 \ 0 \ 0 \ 0 \ \delta)^T$ . If all quadrupole magnets between the first and the last dipole magnet are suitable tuned, the first-order achromat condition  $R_{16, s_1 \rightarrow s_2} = R_{26, s_1 \rightarrow s_2} = 0$  is met. In this case, the section from the first to the last dipole magnet is called first-order achromat. However, if the transverse dispersion and its derivative is zero in front of the first dipole magnet, fulfillment of the achromat condition requires always that the last dipole magnet cancels out the transverse dispersion and its derivative, regardless of how many dipole or quadrupole magnets are located between the first and the last dipole magnet. (a) Since  $R_{56}$  can only change inside a dipole magnet and since the behavior in the first and the last dipole magnet is predetermined in order to meet the achromat condition, a certain constant  $R_{56, s_1 \rightarrow s_2} > 0$  results inevitably for a first-order achromat if there are only two dipole magnets. (b) If there are at least three dipole magnets and at least three quadrupole magnets available in a first-order achromat,  $R_{56, s_1 \rightarrow s_2}$  can be tuned to an individual value – especially to a non-positive value, as shown – while the first-order achromat condition is still met.

$R_{16}$  and  $R_{26}$  but provide no degrees of freedom for tuning,  $R_{16}$  and  $R_{26}$  have to be adjusted by quadrupole magnets. As discussed below, it is desirable to realize  $R_{16,s_1 \rightarrow s_2} = R_{26,s_1 \rightarrow s_2} = 0$  for a certain section from  $s_1$  to  $s_2$ .

If there is no coupling of the horizontal and the vertical phase space, and if there are only horizontal deflections, the first-order longitudinal dispersion  $R_{56}$  for a section from  $s_1$  to  $s_2$  can be expressed by [78]<sup>3</sup>

$$R_{56,s_1 \rightarrow s_2} = \int_{s_1}^{s_2} \frac{R_{16,s_1 \rightarrow s}}{\rho_0(s)} ds. \quad (3.39)$$

Here, it follows that  $R_{56}$  only changes in a dipole magnet: the design bending radius  $\rho_0$  is non-zero and finite only in a dipole magnet, while there is no design deflection anywhere else and thus  $\rho_0 = \infty$  applies outside of a dipole magnet so that the contribution to the integral in Eq. (3.39) is zero outside of a dipole magnet. In this work,  $R_{56}$  is used to influence the relative distance traveled (see below) and thus the longitudinal phase space as described in section 3.7. As mentioned, the dipole magnets define the design orbit and thus provide no degrees of freedom (that is,  $\rho_0$  is constant); for this reason, quadrupole magnets located upstream of a dipole magnet have to be used to vary  $R_{16}$  at the location of that very dipole magnet to influence  $R_{56}$  as follows from Eq. (3.39).

From Eqs. (3.20) and (3.21),

$$\begin{aligned} l(s_2) = & R_{51,s_1 \rightarrow s_2} x(s_1) + R_{52,s_1 \rightarrow s_2} x'(s_1) + R_{53,s_1 \rightarrow s_2} y(s_1) \\ & + R_{54,s_1 \rightarrow s_2} y'(s_1) + R_{55,s_1 \rightarrow s_2} l(s_1) + R_{56,s_1 \rightarrow s_2} \delta(s_1) \end{aligned} \quad (3.40)$$

follows for the relative distance traveled if  $T_{ijk}$  is zero. For any transport matrix resulting from an arbitrary combination of the transport matrices given in section 3.4,  $R_{55} = 1$  holds (see appendix C.2). For any transport matrix resulting from an arbitrary combination of the transport matrices given in section 3.4 excluding  $R_{\text{rot}}(\Phi)$ , (i)  $R_{53,s_1 \rightarrow s_2} = R_{54,s_1 \rightarrow s_2} = 0$  applies (see appendix C.3) and (ii) if additionally the condition  $R_{16,s_1 \rightarrow s_2} = R_{26,s_1 \rightarrow s_2} = 0$  is met (which is called first-order achromat condition and in this case the corresponding magnet system is called first-order achromat), then  $R_{51,s_1 \rightarrow s_2} = R_{52,s_1 \rightarrow s_2} = 0$  applies (see appendix C.3). If these conditions are met, Eq. (3.40) simplifies to

$$l(s_2) = l(s_1) + R_{56,s_1 \rightarrow s_2} \delta(s_1) \quad (3.41)$$

$$\Leftrightarrow l(s_2) - l(s_1) = R_{56,s_1 \rightarrow s_2} \delta(s_1), \quad (3.42)$$

so that  $R_{56}$  is the only first-order degree of freedom to influence the relative distance traveled of an individual particle with given  $\delta$ . At least three dipole magnets and three degrees of freedom (that is, three quadrupole magnets) per section  $s_1$  to  $s_2$  are necessary to force  $R_{16,s_1 \rightarrow s_2} = R_{26,s_1 \rightarrow s_2} = 0$  and to realize an individual value for  $R_{56}$ : One quadrupole magnet

---

<sup>3</sup>Equation (3.39) has the opposite sign compared to the equation given in Ref. [78] since a different definition of the longitudinal coordinate is used in this work.

located downstream of the first dipole magnet of the achromat can be used to change  $R_{16}$  inside further downstream located dipole magnets that are part of the achromat (apart from the last dipole magnet of the achromat) and thus can be used to change  $R_{56}$  (see Eq. (3.39)), while two quadrupole magnets located upstream of the last dipole magnet of the achromat have to ensure suitable values for  $R_{16}$  and  $R_{26}$  at the entrance of the last dipole magnet of the achromat so that these two quantities are zero when a particle leaves the last dipole magnet of the achromat (see Fig. 3.12). If Eq. (3.41) applies for a given particle type, the case  $R_{56,s_1 \rightarrow s_2} = 0$ , which describes equal first-order path lengths from  $s_1$  to  $s_2$  for all particles of the given type (including types of particles with non-zero rest mass) is unfortunately referred to in the literature as isochronicity; however, equal times of flight from  $s_1$  to  $s_2$  for all particles of the given type follow only in the case of the ultra-relativistic limit ( $v \rightarrow c$ ) if  $R_{56,s_1 \rightarrow s_2} = 0$  applies [75], while otherwise  $R_{56,s_1 \rightarrow s_2} \neq 0$  is necessary to reach (almost) equal times of flight from  $s_1$  to  $s_2$  for all particles of the given type if they have a non-zero rest mass (see Fig. 4.6).

Depending on the bunch dimensions, non-zero  $T_{ijk}$  have to be taken into account. Element dependent values  $T_{ijk,s_1 \rightarrow s_2}$  are provided in Ref. [75]. The resulting value of  $T_{ijk,s_1 \rightarrow s_N}$  acting from  $s_1$  to  $s_N$  can be obtained from the iterative transformations  $\vec{X}(s_1) \mapsto \vec{X}(s_2)$ ,  $\vec{X}(s_2) \mapsto \vec{X}(s_3)$ , ...,  $\vec{X}(s_{N-1}) \mapsto \vec{X}(s_N)$  utilizing Eq. (3.21).

The second-order dispersion terms with a quadratic dependence on the momentum,  $T_{i66}$ , are of particular interest. Similar to the first-order terms,  $T_{366} = T_{466} = 0$  applies if there is no vertical deflection along the design orbit. For a section from  $s_1$  to  $s_2$ ,  $T_{166,s_1 \rightarrow s_2} = T_{266,s_1 \rightarrow s_2} = 0$  is desirable as well as an individual value for  $T_{566,s_1 \rightarrow s_2}$ . However, an adequate setting of these values requires usually three sextupole magnets per section from  $s_1$  to  $s_2$ , which are not available at the S-DALINAC in the required quantity. Independent of this, for small bunch dimensions as present for low beam currents (see chapter 4) it is not required to consider the second-order longitudinal dispersion  $T_{566}$  as a degree of freedom in this work in order to find an optimum two dimensional (2D) working point for a multi-turn energy-recovery operation. However, its impact becomes noticeable during measurements of the longitudinal dispersion since here large deviations from the design momentum intentionally caused are present (see Fig. 4.6).

If there is no coupling of the horizontal and the vertical phase space, and if there are only horizontal deflections, the second-order longitudinal dispersion  $T_{566}$  for a section from  $s_1$  to  $s_2$  can be expressed by [78]<sup>4</sup>

$$T_{566,s_1 \rightarrow s_2} = \int_{s_1}^{s_2} \left( \frac{R_{26,s_1 \rightarrow s}^2}{2} + \frac{T_{166,s_1 \rightarrow s}}{\rho_0(s)} \right) ds. \quad (3.43)$$

Here, it follows that  $T_{566}$  also changes outside a dipole magnet if there is a non-zero  $R_{26}$ .

---

<sup>4</sup>Equation (3.43) has the opposite sign compared to the equation given in Ref. [78] since a different definition of the longitudinal coordinate is used in this work.

### 3.6 Phase Space and Trace Space

In the previous sections of this chapter, individual particles have been addressed. Each particle has its three location coordinates  $(x, y, z)$  and three momentum-vector coordinates  $(p_x, p_y, p_z)$ . In this section, the bunch structure as an ensemble will be discussed. This ensemble forms the six dimensional (6D)  $(x, p_x, y, p_y, z, p_z)$ -phase space. The 2D horizontal, the 2D vertical and the 2D longitudinal phase space result from the corresponding projections. Due to the used simulation software, it is advantageous to represent the longitudinal phase space in this work by  $(l, p - p_0)$ ,  $(t - t_0, E_{\text{kin}} - E_{\text{kin},0})$  and  $(t - t_0, p - p_0)$  rather than  $(z, p_z)$ . Furthermore, since  $p_x$  and  $p_y$  cannot be measured but  $x'$  and  $y'$  can be measured, the horizontal and the vertical trace space  $((x, x')$  and  $(y, y')$ ) are used in this work rather than  $(x, p_x)$  and  $(y, p_y)$ .

In the following, the horizontal trace space  $(x, x')$  at location  $s$  will be discussed as a representative. Here, the particles form a shape that can be surrounded by an ellipse containing the standard deviation of the quantities in the case of a Gaussian distribution (see Fig. 3.13). The ellipse can be described by the horizontal betatron function  $\tilde{\beta}_x(s)$ , the associated weighted horizontal slope

$$\tilde{\alpha}_x(s) = -\frac{1}{2} \cdot \left. \frac{d\tilde{\beta}_x(s')}{ds'} \right|_{s'=s}, \quad (3.44)$$

the horizontal gamma function

$$\tilde{\gamma}_x(s) = \frac{1 + \tilde{\alpha}_x^2(s)}{\tilde{\beta}_x(s)}, \quad (3.45)$$

and the geometric horizontal emittance  $\varepsilon_x(s)$  representing the area of the ellipse,  $A_{(x,x')}^{1\sigma}(s) = \pi\varepsilon_x(s)$  [76]. The orientation of the ellipse in the trace space is given by the correlation angle  $\tilde{\varphi}_x(s) = \arctan\left(2\tilde{\alpha}_x(s)/\left(\tilde{\gamma}_x(s) \cdot 1 \text{ m} - \tilde{\beta}_x(s)/1 \text{ m}\right)\right)/2$  [76]. The vertical terms for the  $(y, y')$ -trace space, which are  $\tilde{\beta}_y$ ,  $\tilde{\alpha}_y$ ,  $\tilde{\gamma}_y$ ,  $\varepsilon_y$ ,  $A_{(y,y')}^{1\sigma}$  and  $\tilde{\varphi}_y$ , are defined accordingly. The functions  $\tilde{\beta}$ ,  $\tilde{\alpha}$  and  $\tilde{\gamma}$  are called Twiss parameters. Both the geometric horizontal and geometric vertical emittances,  $\varepsilon_x$  and  $\varepsilon_y$ , change during acceleration or deceleration, respectively. For the purpose of comparison, the normalized horizontal emittance

$$\varepsilon_{n,x}(s) = \varepsilon_x(s)\beta_0(s)\gamma_0(s) \quad (3.46)$$

is defined, and the normalized vertical emittance  $\varepsilon_{n,y}$  accordingly. Note that the relative speed and Lorentz factor of the design particle,  $\beta_0$  and  $\gamma_0$ , appear in Eq. (3.46), not the horizontal betatron function  $\tilde{\beta}_x$  and the horizontal gamma function  $\tilde{\gamma}_x$ .

Similar to Eq. (3.22), the values of the Twiss parameters at a downstream location can be calculated by matrix multiplications [77]:

$$\begin{pmatrix} \tilde{\beta}_x(s_2) & -\tilde{\alpha}_x(s_2) \\ -\tilde{\alpha}_x(s_2) & \tilde{\gamma}_x(s_2) \end{pmatrix} = \check{R}_{xx'}(s_1 \rightarrow s_2) \cdot \begin{pmatrix} \tilde{\beta}_x(s_1) & -\tilde{\alpha}_x(s_1) \\ -\tilde{\alpha}_x(s_1) & \tilde{\gamma}_x(s_1) \end{pmatrix} \cdot \check{R}_{xx'}^T(s_1 \rightarrow s_2), \quad (3.47)$$

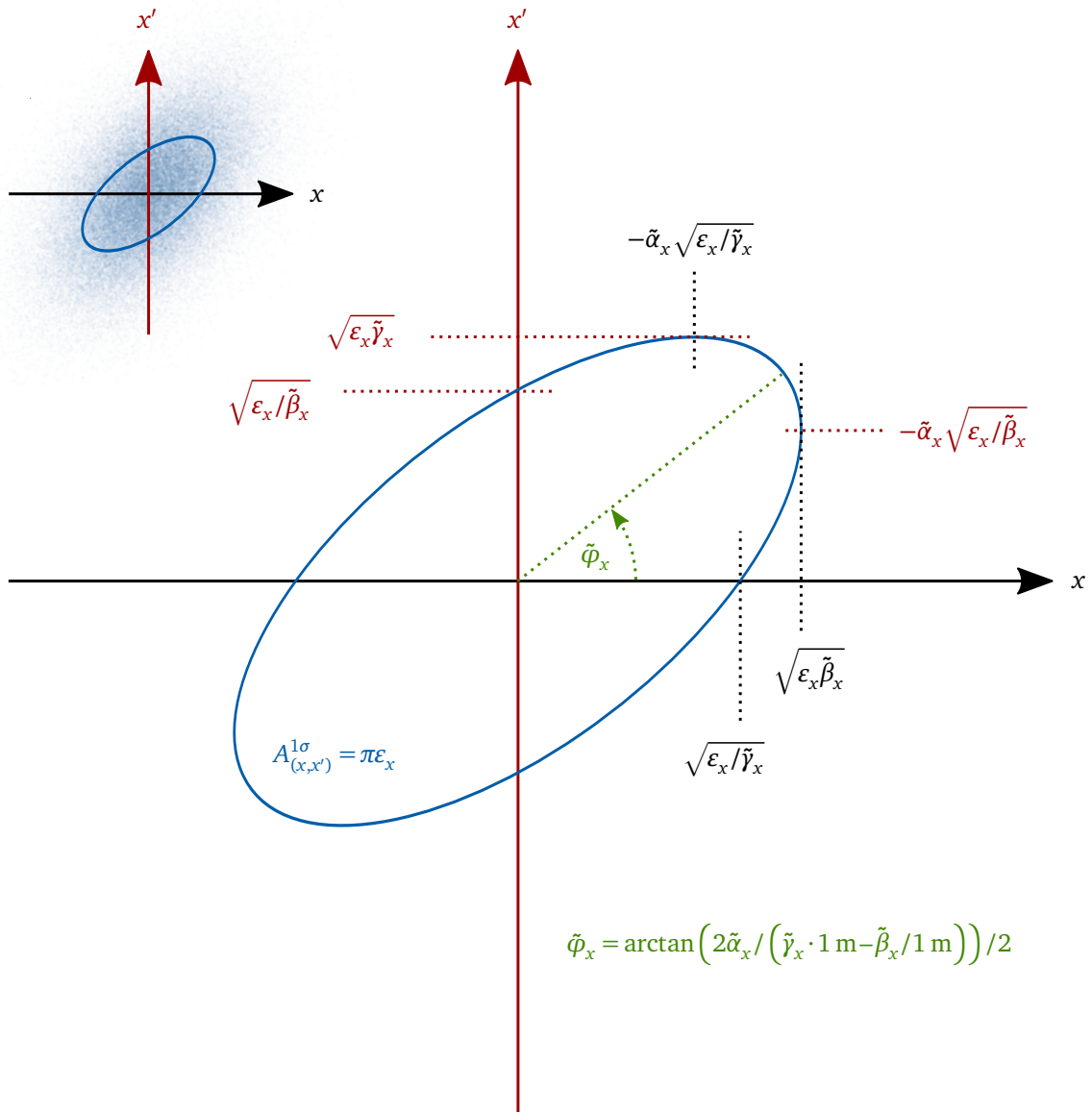


**Figure 3.13: Horizontal trace space.** (top left) Electrons of a bunch shown in the horizontal trace space  $(x, x')$  at a given location  $s$ . In this example, the horizontal position  $x$  and the horizontal slope  $x'$  of the electrons are Gaussian distributed and correlated. The  $1\sigma$ -area is enclosed by an ellipse. (center) Properties of this ellipse. The correlation angle  $\tilde{\varphi}_x$  should be interpreted with caution as it is the angle between two axes of different dimensions; the angle is geometrically correct if  $x$  is divided by meter, or if  $x'$  is multiplied by meter. Figure adapted from Ref. [76].

applies for the horizontal Twiss parameters, where

$$\check{R}_{xx'}(s_1 \rightarrow s_2) = \begin{pmatrix} R_{11,s_1 \rightarrow s_2} & R_{12,s_1 \rightarrow s_2} \\ R_{21,s_1 \rightarrow s_2} & R_{22,s_1 \rightarrow s_2} \end{pmatrix} \quad (3.48)$$

is the corresponding  $x$ - $x'$ -related submatrix of the transport matrix  $R(s_1 \rightarrow s_2)$ . Correspondingly:

$$\begin{pmatrix} \tilde{\beta}_y(s_2) & -\tilde{\alpha}_y(s_2) \\ -\tilde{\alpha}_y(s_2) & \tilde{\gamma}_y(s_2) \end{pmatrix} = \check{R}_{yy'}(s_1 \rightarrow s_2) \cdot \begin{pmatrix} \tilde{\beta}_y(s_1) & -\tilde{\alpha}_y(s_1) \\ -\tilde{\alpha}_y(s_1) & \tilde{\gamma}_y(s_1) \end{pmatrix} \cdot \check{R}_{yy'}^T(s_1 \rightarrow s_2), \quad (3.49)$$

with

$$\check{R}_{yy'}(s_1 \rightarrow s_2) = \begin{pmatrix} R_{33,s_1 \rightarrow s_2} & R_{34,s_1 \rightarrow s_2} \\ R_{43,s_1 \rightarrow s_2} & R_{44,s_1 \rightarrow s_2} \end{pmatrix}. \quad (3.50)$$

If the horizontal beam profile has a Gaussian distribution, the horizontal beam size can be described by the standard deviation  $\sigma_x$  called horizontal beam envelope, which is linked to the geometric horizontal emittance  $\varepsilon_x$ , the horizontal betatron function  $\tilde{\beta}_x$ , the first-order horizontal dispersion  $R_{16}$  and the relative momentum spread  $\sigma_\delta$ : in linear approximation,

$$\sigma_x(s) = \sqrt{\varepsilon_x(s)\tilde{\beta}_x(s) + (R_{16,0 \rightarrow s}\sigma_\delta(s))^2} \quad (3.51)$$

applies [76]. Accordingly, the standard deviation  $\sigma_y$  of the vertical beam size called vertical beam envelope can be described: in linear approximation,

$$\sigma_y(s) = \sqrt{\varepsilon_y(s)\tilde{\beta}_y(s) + (R_{36,0 \rightarrow s}\sigma_\delta(s))^2} \quad (3.52)$$

applies.

From Eqs. (3.51) and (3.52), the relative momentum spread can be determined if the corresponding dispersion value  $R_{16}$  or  $R_{36}$ , respectively, is non-zero. Here, one equation is sufficient, and since  $R_{36}$  should be zero by design in those sections of the S-DALINAC in which  $\sigma_\delta$  is to be determined in this work, while  $R_{16}$  can be tuned to suitable values at certain locations at the S-DALINAC (see chapter 5), the relative momentum spread results from rearranging Eq. (3.51):

$$\sigma_\delta(s) = \frac{\sqrt{\sigma_x^2(s) - \varepsilon_x(s)\tilde{\beta}_x(s)}}{|R_{16,0 \rightarrow s}|} \quad \text{if } R_{16,0 \rightarrow s} \neq 0. \quad (3.53)$$

Since

$$\sigma_x^2(s) \geq \varepsilon_x(s)\tilde{\beta}_x(s) \geq 0, \quad (3.54)$$



the upper-limit relative-momentum-spread  $\hat{\sigma}_\delta$  can be defined:

$$\sigma_\delta(s) = \frac{\sqrt{\sigma_x^2(s) - \varepsilon_x(s)\tilde{\beta}_x(s)}}{|R_{16,0 \rightarrow s}|} \leq \frac{\sqrt{\sigma_x^2(s)}}{|R_{16,0 \rightarrow s}|} = \frac{\sigma_x(s)}{|R_{16,0 \rightarrow s}|} =: \hat{\sigma}_\delta(s) \quad \text{if } R_{16,0 \rightarrow s} \neq 0. \quad (3.55)$$

In this way, as long as  $\sigma_x$  and  $R_{16}$  are known, the relative momentum spread  $\sigma_\delta$  can be estimated by  $\hat{\sigma}_\delta$  without knowledge of the squared intrinsic horizontal beam envelope,  $\varepsilon_x\tilde{\beta}_x$ . The estimation is more precise if  $\varepsilon_x(s_1)\tilde{\beta}_x(s_1) \ll (R_{16,0 \rightarrow s_1}\sigma_\delta(s_1))^2$  applies at the location of the measurement,  $s_1$ , and thus a large value for  $|R_{16,0 \rightarrow s_1}|$  is preferred.

To determine the relative momentum spread more precisely, the value of  $\varepsilon_x(s_1)\tilde{\beta}_x(s_1)$  has to be determined as well. This in turn requires additional diagnostics at a non-dispersive location  $s_2$ . Here, the emittance and Twiss parameters ( $\varepsilon_x(s_2), \tilde{\beta}_x(s_2), \tilde{\alpha}_x(s_2), \tilde{\gamma}_x(s_2)$ ) have to be determined (for example, via a quadrupole-magnet scan). The value  $\tilde{\beta}_x(s_1)$  can be determined from inverting Eq. (3.47) if the submatrix  $\check{R}_{xx'}(s_1 \rightarrow s_2)$  is available and if it is invertible<sup>5</sup>:

$$\begin{pmatrix} \tilde{\beta}_x(s_1) & -\tilde{\alpha}_x(s_1) \\ -\tilde{\alpha}_x(s_1) & \tilde{\gamma}_x(s_1) \end{pmatrix} = \check{R}_{xx'}^{-1}(s_1 \rightarrow s_2) \cdot \begin{pmatrix} \tilde{\beta}_x(s_2) & -\tilde{\alpha}_x(s_2) \\ -\tilde{\alpha}_x(s_2) & \tilde{\gamma}_x(s_2) \end{pmatrix} \cdot (\check{R}_{xx'}^T(s_1 \rightarrow s_2))^{-1}. \quad (3.56)$$

If  $\varepsilon_x(s_2) = \varepsilon_x(s_1)$  applies, this leads to  $\varepsilon_x(s_1)\tilde{\beta}_x(s_1)$  and thus to  $\sigma_\delta(s_1)$  via condition (3.53).

### 3.7 Influencing the Longitudinal Phase Space

In this work, it is crucial to influence the longitudinal phase space in a suitable way. An exemplary influence of the degrees of freedom  $\hat{\phi}$  and  $R_{56}$  on the longitudinal phase space is shown in Fig. 3.14. The effect of  $R_{56}$  is a shear mapping (see Eq. (3.42)). The effect of  $\hat{\phi}$  is a shear mapping in linear approximation if  $|\cos(\hat{\phi})|$  differs distinctly from one (the linear approximation is best if  $\cos(\hat{\phi}) = 0$  applies), and if the bunch is short. By a sophisticated choice of  $\hat{\phi}$  per cavity and  $R_{56}$  per arc or recirculation beamline, respectively, the longitudinal phase space can be suitably influenced (see sections 4.2.2 and 4.3.2).

For convenience, certain transformations in the phase space are called rotation (see Fig. 3.14), although the transformations are shearings (in linear approximation).

### 3.8 Instability Effects

In the previous sections of this chapter, only external influences on individual particles have been discussed. However, influences due to the particles themselves have to be taken into account as well since they can lead to instabilities. In the following, some of these effects relevant for (multi-turn) energy-recovery operation are discussed. Their influence at the S-DALINAC is numerically estimated if possible or mitigation possibilities are discussed.

<sup>5</sup>In this work, Eq. (3.56) is only to be evaluated for sections from  $s_1$  to  $s_2$  for which  $\det(\check{R}_{xx'}(s_1 \rightarrow s_2)) = 1$  applies; consequently,  $\check{R}_{xx'}(s_1 \rightarrow s_2)$  is invertible in these sections.

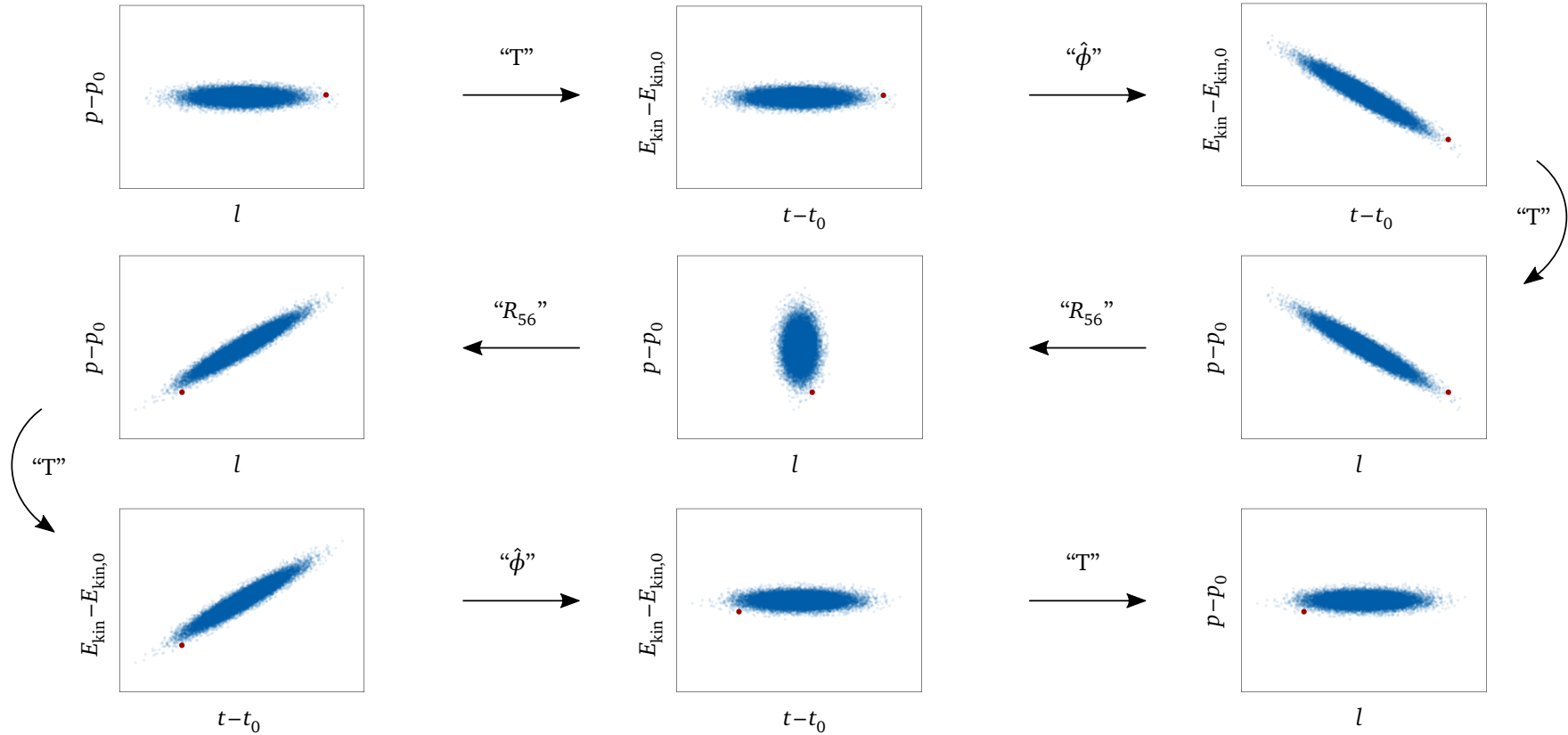


**Figure 3.14: Influence of the off-crest acceleration phase and the longitudinal dispersion on the longitudinal phase space.** The figure shows a specific case in which an initially non-correlated Gaussian distribution in the  $(l, p-p_0)$ -space is iteratively influenced by a change in kinetic energy as a function of  $\hat{\phi}$  (“ $\hat{\phi}$ ”) and by a change of the relative distance traveled as a function of  $R_{56}$  (“ $R_{56}$ ”). Since Eqs. (3.6) and (3.41) relate to different phase spaces, transformations (“T”) are necessary. In the shown case,  $\hat{\phi}$  and  $R_{56}$  are chosen so that the distribution transforms from an initial state of smallest absolute momentum spread and largest bunch length to an intermediate state of largest absolute momentum spread and smallest bunch length, and then to the final state of again smallest absolute momentum spread and largest bunch length. In this example, each “ $\hat{\phi}$ ” acts as  $\hat{\phi} \in (0^\circ, 90^\circ)$  and each “ $R_{56}$ ” acts as  $R_{56} > 0$ . A selected particle (red) initially located in the bunch’s tail [*sic*] is finally located in the bunch’s head [*sic*] (if  $l(s) > 0$  applies for an individual particle, then the individual particle has to travel on a longer orbit compared to the design particle in order to reach location  $s$ , and consequently – if the difference in speed of the very individual particle and the design particle is negligible – the very individual particle appears behind the design particle in the corresponding coordinate system in motion (see Fig. 3.11(a))). Although the transformations are shearings (in linear approximation), a transformation like from panel *top left* to panel *center*, or from panel *center* to panel *bottom right*, will be called “ $90^\circ$  rotation in phase space”, and a transformation like from panel *top left* to panel *bottom right* will be called “ $180^\circ$  rotation in phase space”.

---

### 3.8.1 Beam Breakup Due to Wakefields and Higher-Order Modes

Charged particles induce surface charges and currents in the vacuum chamber of the beamline, which thus originate fields called wakefields that act back on particles, and this can cause transverse deflections and changes of the particle's energy [71]. Depending on the severity, such impacts can lead to beam breakup (BBU). Fields originated from the particles at the head of the bunch affecting trailing particles in the same bunch are called short-range wakefields, while fields originated from a certain bunch affecting trailing bunches (and also the very same bunch during subsequent passes after a recirculation) are called long-range wakefields.

There is possible BBU due to transverse deflection in energy-recovery configurations due to resistive-wall wakefields [79]. Furthermore, the energy-spread modification caused by wakefields can become crucial in energy-recovery operation: Changes of the absolute energy spread, which are caused by wakefields, occur in each acceleration and deceleration step and thus accumulate. While in this way the resulting absolute energy spread may be relatively small after maximum acceleration, it can be relatively large after full deceleration and thus can affect the beam transport to the beam dump [80]. Due to a limited beam dump acceptance, there is a maximum acceptable total resistive-wall wakefield. Because these destructively acting wakefields increase with bunch charge but decrease with bunch length and beampipe radius, a limit for the maximum bunch charge exists depending on the bunch length and beampipe radius. This limit can be increased if the wakefield-driven energy spread is compensated [81].

However, due to the only low bunch charges available at the S-DALINAC and the existing beampipe properties at the very machine, effects due to resistive-wall wakefields are insignificant.

As mentioned, almost lossless temporary storage of the energy recovered in an ERL requires superconducting cavities with high quality factors. Due to high quality factors, excited fields are weakly attenuated and thus remain for a correspondingly long time. This also applies to long-range wakefields induced by the beam as well as by undesired modes resulting from the externally coupled fields. That is, besides the dedicated accelerating or decelerating mode ( $TM_{010}$ - $\pi$ -mode in the case of the S-DALINAC), undesired higher-order modes (HOMs) can also be excited in the cavities – depending on the cavity geometry. There are possible instabilities due to monopole HOMs [82], dipole HOMs [83] and quadrupole HOMs [84]: A monopole HOM causes energy modulations of the electrons and thus the speed and consequently the arrival time at the next cavity and/or the very same cavity after a recirculation is influenced, leading to positive feedback and further energy modulations. A dipole HOM kicks the electron beam transversely. The kicked beam then passes further cavities and/or the cavity of the original kick after a recirculation with a transverse offset and in this way excites dipole HOMs, which leads to positive feedback and further transverse kicks. A beam with a non-circular transverse profile excites quadrupole HOMs, which in turn influence the beam focus. Similarly, this can lead to positive feedback.

The HOMs become critical when their growth due to positive feedback is faster than their

---

natural decay. Growth is sped up by an increased beam current in the corresponding LINAC. Thus, if a certain threshold current is exceeded, BBU will occur. This threshold current per single beam in the main LINAC may be lower if the number of LINAC passes is increased.

Generally, BBU due to HOMs can be mitigated by (i) a smart cavity design to minimize the HOM power [85], (ii) HOM damping [86], (iii) a sophisticated bunch filling pattern [87], or (iv) suitable lattice parameters [88–90]. HOM couplers for damping cannot be used reasonably at the S-DALINAC because most of the HOMs' power is located in the middle cells of the 20-cell cavities [91]; the field at the end cells becomes weaker with an increased number of cells, and since HOM couplers are located beyond the end cells, coupling to the HOMs becomes weaker with an increased number of cells [92]. A certain bunch filling pattern can only be chosen if the frequency of the RF field inside a cavity is a higher harmonic of the bunch repetition rate, only realizable at the S-DALINAC using the photo gun, which was maintained during the experiment of this work, but not with the thermionic gun<sup>6</sup>. The lattice parameter approach was investigated at the S-DALINAC in the old machine layout (that is, with only two existing recirculation beamlines) [73] as well as in the new machine layout (that is, with three existing recirculation beamlines) [63, 90, 93]: In the old layout, BBU was observed in the two-turn conventional acceleration mode at beam currents after chopping of 5  $\mu\text{A}$  or 7.5  $\mu\text{A}$  for an injector energy of 3.5 MeV or 5.8 MeV, respectively [73]. In the case of an injector energy of 3.5 MeV, the beam current after chopping at which BBU occurred could be increased to 8.2  $\mu\text{A}$  by changing lattice parameters, which led to a coupling of the horizontal and the vertical phase space. In the new layout, BBU was neither observed in the one-turn conventional acceleration mode for an injector energy of 2.5 MeV up to the permitted maximum beam current after chopping of 20  $\mu\text{A}$  (despite an intentionally induced parallel offset of the electron beam) [63], nor observed in the three-turn conventional acceleration mode for an injector energy of about 3.4 MeV up to the maximum beam current after chopping available at that time, which was 15  $\mu\text{A}$  [90].

The goal of this work is to pass the main LINAC four times using an injector momentum of 5 MeV/c (corresponding to a kinetic energy higher than 4.5 MeV), and to achieve the highest possible permitted beam current after chopping. Although the injector energy is higher in this case compared to previous BBU studies at the S-DALINAC, the behavior is different due to the energy-recovery operation and the associated beam energies and arrival phases (apart from the fact that the lattice may differ significantly). Mitigation of HOMs requires suitable lattice and beam parameters at the locations of the cavities of the main LINAC, but setting suitable parameters in turn requires sufficient knowledge about the HOMs' voltage and polarization, which is not available for the HOMs excited at the S-DALINAC. For the two-turn energy-recovery mode at the S-DALINAC, quadrupole HOMs are potentially the

---

<sup>6</sup>Even by using the thermionic gun, the frequency of the  $\text{TM}_{010}$ - $\pi$ -mode inside a cavity can be a higher harmonic of the beam repetition rate if the beam current after chopping is less than 0.25 nA since in that case there is only one electron per several RF cycles. However, due to the already realized layout of the S-DALINAC, a certain current-dependent filling pattern results inevitably and cannot be adjusted. Furthermore, BBU due to HOMs will not occur for beam currents after chopping equal to or less than 0.25 nA.

most critical HOMs in terms of causing BBU [90]. Thus, for a general mitigation of BBU due to quadrupole HOMs, a circular transverse profile of the electron beam centered on the design orbit is desired inside the cavities. Furthermore, for a general mitigation of BBU due to dipole HOMs, small betatron functions  $\tilde{\beta}_x$  and  $\tilde{\beta}_y$  inside the cavities are desired [83].

While both a circular transverse beam profile and small betatron functions can easily be realized for the entire pass through a small LINAC without quadrupole magnets between the cavities [94], a circular transverse beam profile cannot be achieved inside the cavities of the main LINAC at the S-DALINAC; this would require equal horizontal and vertical emittances as well as – if quadrupole magnets are necessary – quadrupole-magnet triplets between cavities (due to the focusing characteristics of quadrupole magnets, see section 3.4). At the S-DALINAC, the emittance values are not equal (see section 4.2.2), and neither are quadrupole-magnet triplets available nor can the main LINAC be passed without using quadrupole magnets. The latter is due to the limited capability of the injector arc to set appropriate values for the Twiss parameters. However, small betatron functions or beam envelopes, respectively, can be achieved inside the cavities of the main LINAC (see sections 4.2.2 and 4.3.2).

### 3.8.2 Space-Charge Effects

Charged particles generate electromagnetic fields; the total field generated is the superposition of the fields from all particles in the beam. The electric component of this electromagnetic field causes a repulsive force while the magnetic component causes an attractive force [71]. To demonstrate this, a long bunch is represented by a cylinder moving at speed  $v$ : The bunch has an azimuthal symmetry with radius  $\tilde{r}$ , azimuthal angle  $\vartheta$  and charge density  $\varrho(\tilde{r})$ . Correspondingly, the radially directed electric field is [71]

$$\mathcal{E}_{\tilde{r}} = \frac{1}{\epsilon_0 \tilde{r}} \int \varrho(\tilde{r}') \tilde{r}' d\tilde{r}' \quad (3.57)$$

and the azimuthally directed magnetic field is [71]

$$B_{\vartheta} = \frac{v\mu_0}{\tilde{r}} \int \varrho(\tilde{r}') \tilde{r}' d\tilde{r}', \quad (3.58)$$

where  $\epsilon_0$  is the vacuum permittivity and  $\mu_0$  is the vacuum permeability. Thus, the radial Lorentz force is [71]

$$\begin{aligned} F_{\tilde{r}} &= q \cdot (\mathcal{E}_{\tilde{r}} - vB_{\vartheta}) = q\mathcal{E}_{\tilde{r}} \cdot \left(1 - \frac{vB_{\vartheta}}{\mathcal{E}_{\tilde{r}}}\right) = q\mathcal{E}_{\tilde{r}} \cdot (1 - v^2\mu_0\epsilon_0) \\ &= q\mathcal{E}_{\tilde{r}} \cdot \left(1 - \frac{v^2}{c^2}\right) = q\mathcal{E}_{\tilde{r}} \cdot (1 - \beta^2) = \frac{q\mathcal{E}_{\tilde{r}}}{\gamma^2}, \end{aligned} \quad (3.59)$$

where  $\mu_0\epsilon_0 = 1/c^2$ . It follows that the repulsive effects on a particle resulting from the charges of the other particles (space-charge effects) increase with bunch charge and decrease with

Lorentz factor (that is, with particle energy). The equations of motion are given by [71]

$$\frac{d^2\tilde{r}}{dt^2} = \frac{q\mathcal{E}_{\tilde{r}}}{\tilde{m}_{\text{rest}}\gamma^3} \quad \text{and} \quad \frac{d^2z}{dt^2} = \frac{q\mathcal{E}_z}{\tilde{m}_{\text{rest}}\gamma^3}. \quad (3.60)$$

Since high bunch charges are usually desired in an ERL configuration, space-charge effects can become crucial – especially in sections of low Lorentz factors. Therefore, high-bunch-charge facilities are designed in such a way that the particles of the bunch are accelerated to significantly high Lorentz factors as soon as possible after leaving the gun<sup>7</sup> in order to prevent strong emittance growth. Even downstream of the booster LINAC, space-charge effects can lead to significant emittance growth [100] and dispersion-function modifications [101] before the beam is injected into the main LINAC. Emittance degradation in the merger section can be mitigated by an appropriate merger design [102]. Depending on the bunch charge and the Lorentz factor after the first main-LINAC pass, space-charge effects in sections located further downstream have to be compensated by beam guiding elements [103].

However, due to the only low bunch charges available at the S-DALINAC, impacts due to space-charge effects in the injector section are small and can be compensated by the available beam guiding elements [104]. Impacts due to space-charge effects in the sections downstream of the injector LINAC are small as well, as demonstrated in this work (see appendix D).

### 3.8.3 Synchrotron Radiation

When a charged particle's velocity is changing, radiation is emitted [105]. Thus, the particle is losing energy during deflection, acceleration and deceleration (besides the actual intended energy withdrawal during deceleration, like for energy recovery). Those radiation losses can become especially critical for an energy-recovery operation with common recirculation transport, where certain target energies have to be reached within a certain precision: Two particles – one to be accelerated and one to be decelerated during the corresponding next main-LINAC pass – with equal energy and equal trajectory while traveling through a recirculation beamline will both lose the same amount of energy due to radiation. Without any other compensation (see below), this circumstance requires that – compared to a case with zero radiation losses – the particle to be accelerated is provided with more energy during its acceleration in the next main-LINAC pass, while less energy has to be withdrawn from the particle to be decelerated during its deceleration in the next main-LINAC pass; this is necessary to ensure that both particles reach their individual target energies after their corresponding main-LINAC passes so that they travel on the intended trajectories and thus travel adequately in the downstream located beamlines. Therefore, it is critical to

---

<sup>7</sup>Thus, the distance between the gun and the booster LINAC is as small as possible; however, depending on the gun type, some space between the gun and the booster LINAC may be required for one or more of the following devices/purposes [95–99]: a laser port, diagnostics, transverse focusing devices, and/or a buncher cavity together with a certain drift section for longitudinal compression.

know the amount of energy losses due to radiation in order to evaluate whether it has to be compensated.

If the velocity of a particle is changing due to acceleration or deceleration while moving along a straight line, the power  $P_{\parallel}$  is radiated [105]:

$$P_{\parallel} = \frac{q^2}{6\pi\epsilon_0\tilde{m}_{\text{rest}}^2c^3} \cdot \left| \frac{d\vec{p}}{dt} \right|^2 = \frac{q^2}{6\pi\epsilon_0\tilde{m}_{\text{rest}}^2c^3} \cdot \left( \frac{dE_{\text{kin}}}{ds} \right)^2. \quad (3.61)$$

The associated energy loss is

$$\Delta E_{\parallel} = \int P_{\parallel} dt. \quad (3.62)$$

Losses due to  $P_{\parallel}$  are usually negligible in a LINAC, which is evident from the ratio of  $P_{\parallel}$  and the power per particle that is provided during acceleration or saved during deceleration,  $P_{\text{acc/dec}}$ , respectively:

$$\frac{|P_{\parallel}|}{|P_{\text{acc/dec}}|} = \frac{\frac{q^2}{6\pi\epsilon_0\tilde{m}_{\text{rest}}^2c^3} \cdot \left( \frac{dE_{\text{kin}}}{ds} \right)^2}{\left| \frac{dE_{\text{kin}}}{dt} \right|} \approx \frac{\frac{q^2}{6\pi\epsilon_0\tilde{m}_{\text{rest}}^2c^3} \cdot \left( \frac{dE_{\text{kin}}}{ds} \right)^2}{\beta c \cdot \left| \frac{dE_{\text{kin}}}{ds} \right|} = \frac{q^2}{6\pi\epsilon_0\tilde{m}_{\text{rest}}^2\beta c^4} \cdot \left| \frac{dE_{\text{kin}}}{ds} \right|, \quad (3.63)$$

where the approximation applies for assuming  $\beta$  to be constant. For  $\beta \approx 1$  and a maximum value  $|dE_{\text{kin}}/ds| = 10$  MeV/m, this leads to  $P_{\parallel}/P_{\text{acc/dec}} \approx 4 \cdot 10^{-14}$  for electrons. At the S-DALINAC, the maximum value of  $|dE_{\text{kin}}/ds|$  is less than 10 MeV/m, and thus  $P_{\parallel} < 125$  eV/s  $\approx 4.3 \cdot 10^{-6}$  eV/(34 ns). Here, 34 ns is the time it takes an electron of 5 MeV/c to pass through all cavities of the main-LINAC once, including fringe-field regions. Thus, the energy loss per main-LINAC pass due to acceleration or deceleration, respectively, is less than  $4.3 \cdot 10^{-6}$  eV for an on-axis electron.

If the velocity of a particle is changing due to radial deflection, the power  $P_{\perp}$  is radiated and the associated radiation is called synchrotron radiation (SR) [105]:

$$P_{\perp} = \frac{q^2\gamma^2}{6\pi\epsilon_0\tilde{m}_{\text{rest}}^2c^3} \cdot \left( \frac{d\vec{p}}{dt} \right)^2 = \frac{q^2c\beta^4\gamma^4}{6\pi\epsilon_0\rho^2}. \quad (3.64)$$

The associated energy loss is

$$\Delta E_{\perp} = \int P_{\perp} dt = \int \frac{P_{\perp}}{\beta c} ds = \int \frac{q^2\beta^3\gamma^4}{6\pi\epsilon_0\rho^2} ds \approx \frac{q^2\beta_0^3\gamma_0^4}{6\pi\epsilon_0} \int \frac{1}{\rho^2} ds = \frac{q^2\beta_0^3\gamma_0^4}{3\epsilon_0\rho_0}, \quad (3.65)$$

where the approximation applies when (infinitesimal) changes in  $\beta$  and  $\gamma$  are not taken into account, thus constant values  $\beta_0$  and  $\gamma_0$  are present; the last equality is only valid for a total bend of  $360^\circ$  (that is, it is only valid for a recirculation where the beamline does not contain magnetic chicanes, doglegs, wigglers/undulators, etc.) and if all bending magnets have the same design and thus have the same bending radius  $\rho_0$ . Due to the dependence on the fourth power of  $\gamma$ , energy losses due to SR can become critical at high particle energies,

especially if a compact facility is desired to minimize costs, as this entails small bending radii. Hence, SR has to be taken into account in high-energy energy-recovery machines using recirculation beamlines [7, 8, 35]. There are different options to compensate for energy losses due to SR [21]. As an example for common recirculation transport: If an additional RF system that is operated at an even harmonic is installed in each recirculation beamline of superimposed beams, energy can be delivered to both beams per design energy, that is, to both the accelerated and the decelerated one, so that both beams can reach the target energy after a main LINAC pass to travel on the intended trajectories. However, using RF systems with an even harmonic to compensate for SR losses can prevent a desired linearization of the longitudinal phase space [21]. Furthermore, these additional RF systems obviously require additional externally provided RF power and thus reduce the overall energy-recovery efficiency with respect to the entire machine<sup>8</sup>. As an example for separate recirculation transport: Energy losses due to SR can already be taken into account in the design of the recirculation beamlines so that the amount of energy that the main LINAC delivers to the beam during acceleration is equal to the amount of energy that the beam delivers to the main LINAC during deceleration. However, in such a machine design, the design energy when arriving at the beam dump will differ from the design injector energy.

The section-dependent amount of energy loss due to SR at the S-DALINAC is given in Table 3.1. The amounts of the given values are less than the corresponding precision values of the beam-dynamics simulations<sup>9</sup>; furthermore, the amount of energy loss per electron per section given in Table 3.1 is in the relative order of  $10^{-12}$  to  $10^{-8}$  to the corresponding centroid energy (taking into account the conversion from momentum to energy); thus, the energy loss per electron per section due to SR is several orders of magnitude lower than the minimum value of the  $1\sigma$  energy spread (see sections 4.2.2, 4.2.5 and 4.3.2, taking into account the conversion from momentum to energy). Hence, energy losses due to SR affect the centroid energy only insignificantly.

While the reduction of the centroid energy may be negligible, the emitted synchrotron radiation may affect the bunch structure significantly: The emitted synchrotron radiation is observed as a spectrum, where the critical angular frequency  $\omega_c = 3c\gamma^3/(2\rho)$  divides the very spectrum into two sections of equal radiation power [105]. For a large number of electrons in a bunch, the low-frequency part of the spectrum is amplified with respect to the high-frequency part [106]; this is due to the length of the electron bunch that is shorter or similar to the radiation wavelength, respectively, which thus leads to coherent synchrotron radiation (CSR). Here, the total radiation intensity is proportional to the square

---

<sup>8</sup>The energy delivered by the additional RF systems is recovered in the main LINAC during deceleration, then recycled in the main LINAC for acceleration and afterward lost due to SR; the recovered energy is not transferred back to the additional RF systems.

<sup>9</sup>In the simulations for the two-turn energy-recovery mode, all sections mentioned in Table 3.1 apart from section T appear. In these simulations, the precision is 1 eV (taking into account the conversion from momentum to energy, see section 4.2.2). In the simulations for the three-turn energy-recovery mode, all sections mentioned in Table 3.1 appear. In these simulations, the precision is 630 eV (taking into account the conversion from momentum to energy, see section 4.3.2).



**Table 3.1: Calculated energy losses due to synchrotron radiation.** The table lists the energy losses per electron per section pass due to synchrotron radiation,  $\Delta E_{\perp}$ , which is dependent on the target momentum of the section,  $p_0$ .

Section	$p_0$ (MeV/c)	$\Delta E_{\perp}$ (eV)
I3	5.00	$1.0 \cdot 10^{-4}$
F	23.66	0.11
S	41.61	0.70
T	59.30	2.3
R	5.00	$4.5 \cdot 10^{-4}$

of the bunch charge. Since the bunch is traveling on a curved orbit in a dipole magnet, and since SR is emitted conically with an angle of  $2 \arctan(1/(\beta\gamma))$  [105], photons emitted from electrons in the bunch's tail can catch up with electrons in the bunch's head and interact with them. These interactions lead to a modification of the bunch's energy distribution, and since this energy modulation occurs in a dipole magnet where a non-zero transverse dispersion is present, the energy modulation affects the transverse distribution of the bunch as well [107]. Thus, CSR can have a significant impact on the bunch if large bunch charges are present [108, 109]. Mitigation possibilities are (i) an appropriate matching of the beam envelope inside an arc [110], or (ii) shielding [111]. However, since only low bunch charges are available at the S-DALINAC, CSR has only a small impact on the bunch properties (see appendix D). Consequently, matching of the beam envelopes has not to be taken into account, which in turn enables a larger set of possible working points.



---

## 4 Multi-Turn Energy-Recovery Modes at the S-DALINAC

The major goal of this work was the first realization of a multi-turn energy-recovery operation at the S-DALINAC. At the beginning of this project, the layout of this machine provided in principle a two-turn energy-recovery (2-ER) and a three-turn energy-recovery (3-ER) mode. However, some modifications of the S-DALINAC were necessary to realize a multi-turn energy-recovery operation. Due to the continuous use of the machine for experiments and the therefore only small time frame available for beamline modifications, only those modifications necessary for a 2-ER operation could be implemented in the time available for this project. Thus, the scope of this work includes the realization of the 2-ER mode and the associated machine modifications as well as simulation-based studies on the 3-ER mode.

### 4.1 Details on the Operating Principle

With the fundamentals on beam dynamics discussed in chapter 3, the operating principle of multi-turn energy-recovery concepts presented in section 1.2 can now be described in more detail. In the following, details on the operating principle are explained in general as well as in particular for the S-DALINAC. The figures in this section are tailored to the S-DALINAC (see Figs. 4.1 and 4.2) and serve as an illustration of the operating principle with more details compared to Fig. 1.1. Figures 4.1 and 4.2 highlight a case in which an off-crest phase is essential due to the machine design; different absolute changes in kinetic energy per main-LINAC pass are necessary (apart from the two consecutive passes “last acceleration” and “first deceleration”) if the S-DALINAC is operated in a mode with at least two main-LINAC passes for acceleration, which is the case in the 2-ER and the 3-ER mode (see Table 4.1).

First, the  $J/2$  consecutive accelerations are addressed: A particle passes the main LINAC for the acceleration  $a_{i+1}$  (with  $i \in \{1, \dots, J/2 - 1\}$ ) if the time  $t_{\text{rec}, a_i}$  needed for a recirculation following the acceleration  $a_i$  is an integer multiple of the oscillation period of the alternating electric fields inside the cavities plus an offset time  $t_{\text{off}, a_i}$  to take into account (i) the ratio of the design momenta of the sections, (ii) differences between electron speed and design transit-speed of the cavities (that is, phase slippage), as well as (iii) an intended phase space

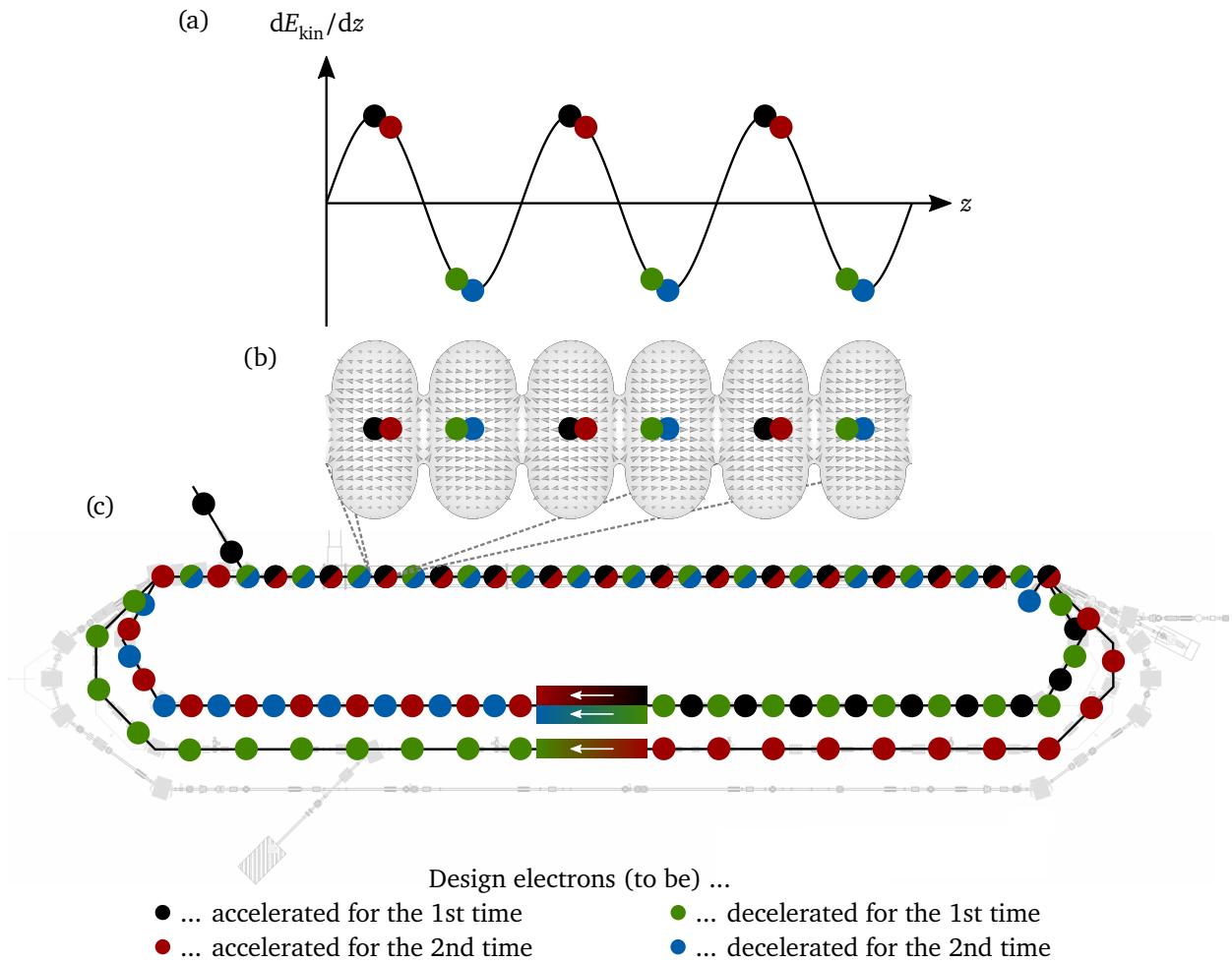


**Figure 4.1: Details on the 2-ER mode.** The figure illustrates a situation at a fixed point in time at which  $\mathcal{E}_{z,1}(z) = \hat{\mathcal{E}}_{z,1}(z)$  applies to the electric field inside the first cavity of the main LINAC (see Eq. (3.4)). Colored discs represent design electrons per bunch. (a)–(b) Electric field given in six adjacent cells of the first cavity as well as the corresponding rate of change in kinetic energy in the associated RF cycles. Since the repetition rate of subsequent generated design particles is equal to the frequency of the  $TM_{010}$ - $\pi$ -mode inside a cavity, each cavity cell and half RF cycle, respectively, is occupied by two design particles which are either accelerated or decelerated. Recovered energy from deceleration of electrons in a certain cell is recycled half an oscillation period later during acceleration of subsequent electrons in the very same cell. Since the design momenta are different for each recirculation beamline (see Table 4.1), the absolute change in kinetic energy is different from pass to pass through the main LINAC (apart from the two consecutive passes “last acceleration” and “first deceleration”) in order to enable traveling in the corresponding downstream following recirculation beamline. Thus, for some main-LINAC passes, off-crest acceleration or deceleration, respectively, is necessary in terms of an entire main-LINAC pass; however, the behavior may be different in each cavity. The illustrated locations of the electrons (especially if located at rising or falling slope) are only examples; precise positions follow from the simulation results. Speed dependent phase slippage is not taken into account in this figure. (c) Schematic representation of the locations of the design electrons on the design trajectory from the injector arc to the beam dump. Since the electrons pass certain sections several times (the main-LINAC section four times and the first recirculation beamline two times), superpositions occur in these sections. The color transition in the center of a recirculation beamline allows distinguishing the sequence of the electrons. (a)–(c) In sections of superpositions, two design electrons that have not left the gun in immediate succession are locally closest to each other. Figure created based on Ref. [45] using the S-DALINAC–adaptation based on Ref. [51].

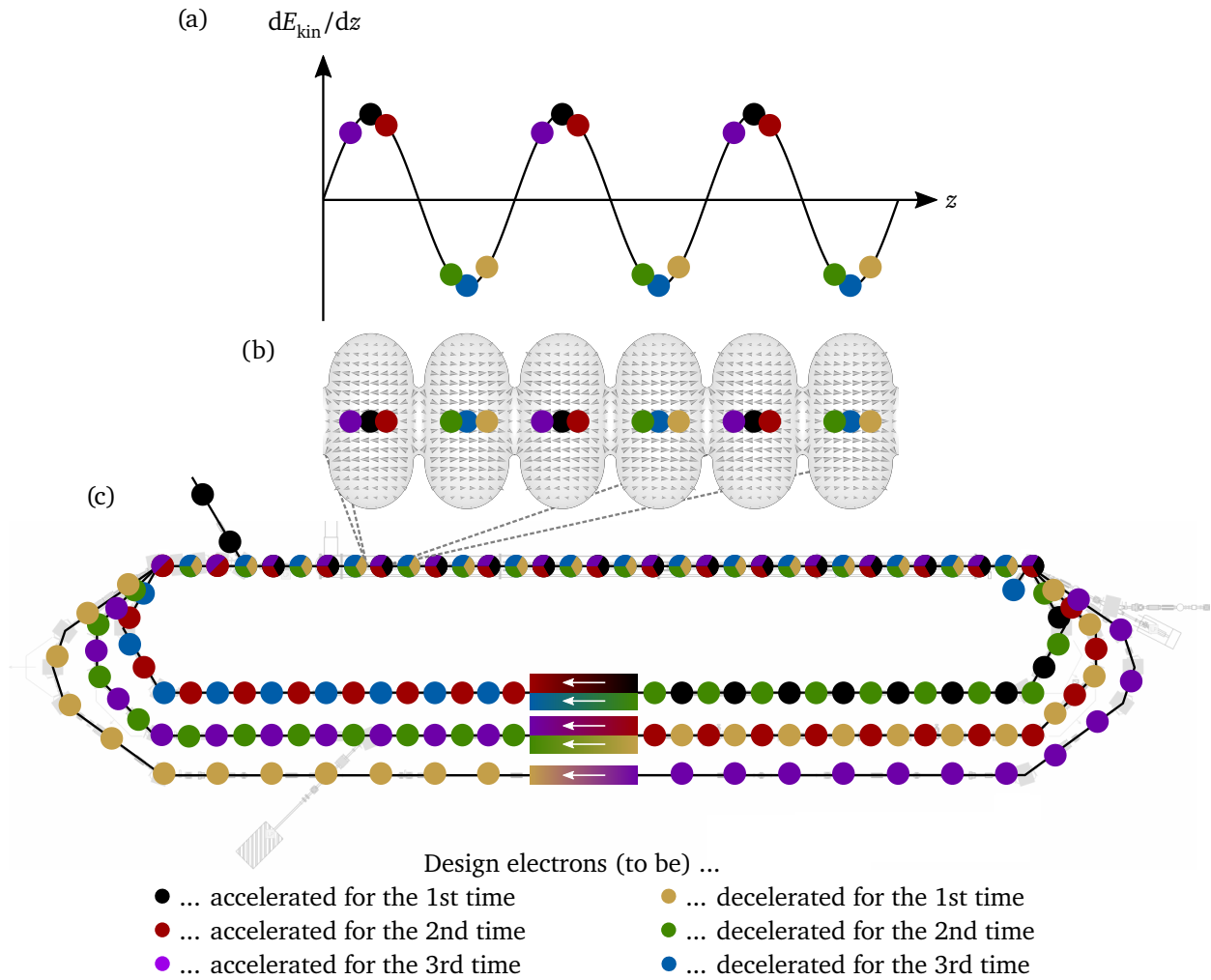


**Figure 4.2: Details on the 3-ER mode.** Similar to Fig. 4.1. Since three recirculation beamlines are present, the number of involved design momenta increases (see Table 4.1). (a)–(b) Since the repetition rate of subsequent generated design particles is equal to the frequency of the  $TM_{010}\text{-}\pi$ -mode inside a cavity, each cavity cell and half RF cycle, respectively, is occupied by three design particles which are either accelerated or decelerated. (c) Electrons are passing the main-LINAC section six times and the first and the second recirculation beamline two times. (a)–(c) Figure created based on Ref. [45] using the S-DALINAC–adaptation based on Ref. [51].

**Table 4.1: Design values per section and per main-LINAC pass.** The design momenta of the sections,  $p_0$ , are in an operation-mode-independent fixed ratio, which is defined by the layout of the S-DALINAC. Originally designed differently [45], the ratios listed here follow from a commissioning measurement. The ratios are given relative to the injector momentum  $p_{0,I3}$ . Values given for  $p_0$  are design values in this study. This results in an absolute change in the design particle’s momentum  $|\Delta p_0|$  or kinetic energy  $|\Delta E_{kin,0}|$ , respectively, referring to a single main-LINAC pass connecting the corresponding two mentioned sections.

Section	$p_0/p_{0,I3}$	$p_0$ (MeV/c)	Main-LINAC pass	$ \Delta p_0 $ (MeV/c)	$ \Delta E_{kin} $ (MeV)
I3	1.00	5.00	I3 → F	18.66	18.64
R	1.00	5.00	F → R	18.66	18.64
F	4.73	23.66	F ↔ S	17.95	17.95
S	8.32	41.61	S ↔ T	17.69	17.69
T	11.86	59.30			

manipulation:

$$t_{\text{rec},a_i} = N_{a_i} t_{\text{RF}} + t_{\text{off},a_i}, \quad N_{a_i} \in \mathbb{N}, \quad |t_{\text{off},a_i}| < \frac{t_{\text{RF}}}{4}, \quad (4.1)$$

where  $t_{\text{RF}} = 2\pi/\omega$  is the oscillation period of the  $\text{TM}_{010}$ - $\pi$ -mode of the RF fields inside the cavities. If no phase space manipulation is intended,  $t_{\text{off},a_i} = 0$  for all  $i$  applies only if the energy gain per main-LINAC pass shall be equal for all main-LINAC passes, and if the design electron shall interact with the electric field in exactly the same way during each pass, which is only possible in the ultra-relativistic limit ( $v \rightarrow c$ ). However, due to the design of the S-DALINAC, different energy gains per main-LINAC pass are necessary: The built recirculation beamlines define the design orbit. Here, a fixed design bending radius  $\rho_0$  per recirculation beamline exists at the splitter dipole magnet FOBM01. Since static magnetic fields are used to deflect the beams into the recirculation beamlines, a certain design momentum per recirculation beamline exists (see Table 4.1). Since the ratio of the design radii is fixed, the ratio of the design momenta is given. The resulting design momentum per recirculation beamline is defined by the chosen injector momentum. Due to the design of the S-DALINAC, the momentum gain per main-LINAC pass is different from pass to pass so that traveling through the corresponding recirculation beamlines is possible. Taking Eqs. (3.6) and (3.19) into account, usually the energy gain per main-LINAC pass is different from pass to pass as well. Therefore,  $t_{\text{off},a_i} \neq 0$  for all  $i$  is necessary at the S-DALINAC to provide appropriate off-crest accelerations and thus suitable energy gains.

After multiple acceleration, the first deceleration follows if a phase offset corresponding to approximately half an oscillation of the RF fields relative to the acceleration phase is ensured. An appropriate phase offset is realized if the time  $t_{\text{rec},b}$  needed for the recirculation following the last acceleration ( $a_{J/2}$ ) is an integer plus a half multiple of the oscillation period of the alternating electric fields inside the cavities plus an corresponding offset time  $t_{\text{off},b}$  to similarly take the above mentioned circumstances into account as explained for  $t_{\text{off},a_i}$ :

$$t_{\text{rec},b} = \left( N_b + \frac{1}{2} \right) t_{\text{RF}} + t_{\text{off},b}, \quad N_b \in \mathbb{N}, \quad |t_{\text{off},b}| < \frac{t_{\text{RF}}}{4}. \quad (4.2)$$

For all following decelerations, similar relations as for multiple acceleration apply, that is, a particle passes the main LINAC for the deceleration  $d_{i+1}$  if the time  $t_{\text{rec},d_i}$  needed for a recirculation following the deceleration  $d_i$  is an integer multiple of the oscillation period of the alternating electric fields inside the cavities plus an corresponding offset time  $t_{\text{off},d_i}$  to similarly take the above mentioned circumstances into account as explained for  $t_{\text{off},a_i}$ :

$$t_{\text{rec},d_i} = N_{d_i} t_{\text{RF}} + t_{\text{off},d_i}, \quad N_{d_i} \in \mathbb{N}, \quad |t_{\text{off},d_i}| < \frac{t_{\text{RF}}}{4}. \quad (4.3)$$

If  $o_{a_i} = o_{d_{J/2-i}}$  applies to the recirculation beamline  $o_{a_i}$ , which connects the acceleration  $a_i$  with the acceleration  $a_{i+1}$ , and the recirculation beamline  $o_{d_i}$ , which connects the deceleration  $d_i$  with the deceleration  $d_{i+1}$ , then there is common recirculation transport, which is the case at the S-DALINAC.

Ensuring appropriate times of flight,  $t_{\text{rec}}$ , is achievable (i) by setting a suitable amplitude and phase of the electric field per cavity to influence the energy and thus the speed of an electron when recirculating, as well as (ii) by setting the path length adjustment system and the longitudinal dispersion per recirculation beamline to influence the distance traveled when recirculating. At the S-DALINAC, the corresponding elements are the cavities A1SC01 to A1SC08, the path length adjustment systems FOPL01, SOPL01, S2PL01 and T2PL01, as well as the quadrupole magnets per arc to tune the longitudinal dispersion. More details are provided in sections 4.2.1 and 4.3.1.

## 4.2 Two-Turn Energy-Recovery Mode

In the following, the individual steps toward the realization of the 2-ER mode are discussed first. Here, the initial situation is an already tuned beam leaving the injector LINAC. The tuning until this location is essentially independent of the operation mode except for the desired centroid momentum. Afterward, measurement results of the realized operation mode are presented and the potential for energy savings is discussed. Some parts of the content presented in this section have already been published in Refs. [112–114].

### 4.2.1 Objectives and Degrees of Freedom

Due to the design of the S-DALINAC, the electron beam is guided in common recirculation transport when operating in a multi-turn energy-recovery mode. While common recirculation transport has the potential to save costs compared to separate recirculation transport, the former has fewer degrees of freedom compared to the latter in order to influence longitudinal and transverse quantities, while the number of objectives remains equal<sup>1</sup>.

#### Longitudinal Quantities

The objectives to ensure an appropriate beam transport are: (i) the electron beam has to be accelerated or decelerated, respectively, so that the centroid momentum  $\bar{p}_i$  after each of the four main-LINAC passes  $i$  ( $i \in \{1, \dots, 4\}$ ) has a certain target momentum  $p_{0,i}$ , which is necessary to ensure that the centroid beam travels on the design trajectory [22], and (ii) the longitudinal phase space has to be manipulated in a sophisticated way to achieve further goals like a small relative momentum spread  $\sigma_\delta$  or a small bunch length  $\sigma_t$  (<sup>2</sup>) at certain locations [22, 115], depending on an intended experiment. In this work, no experiment is included in the feasibility study and thus the focus is only on the relative momentum spread

<sup>1</sup>It has to be emphasized that common and separate recirculation transport can only be compared adequately if the machine layout supports both transport options, which is not the case at the S-DALINAC. Here, only common recirculation transport is available.

<sup>2</sup>In this work, the bunch length is expressed in the dimension of time.

to ensure appropriate beam transport. The target momenta  $p_{0,i}$  follow from the design values for each section (see Table 4.1) and are listed in Table B.1.

To achieve the highest overall efficiency, the electric field of each cavity has to recover exactly the amount of energy it previously supplied to the beam. This enforces a symmetric structure, which in turn further limits the number of degrees of freedom [22]. In order not to further reduce the degrees of freedom in this feasibility study, a symmetric structure is no objective in this work.

The degrees of freedom to influence the centroid momenta and the longitudinal phase space are: (i) the tuning parameters of the main LINAC, here expressed by the peak of the time-independent amplitude of the on-axis  $z$ -component of the electric field,  $\hat{\mathcal{E}}_{z,j,\text{peak}}$ , and the off-crest acceleration phase  $\hat{\phi}_j$  for each cavity  $j$  (A1SC01 to A1SC08), that is,  $j \in \{\text{A1SC01}, \dots, \text{A1SC08}\}$ , (ii) the design recirculation length  $L_m$  through the first (F) or second (S) recirculation beamline, respectively, tuned by the path length adjustment systems FOPL01, SOPL01 and S2PL01, that is,  $m \in \{\text{F}, \text{S}\}$  <sup>(3)</sup>, and (iii) the first-order longitudinal dispersion  $R_{56,n}$  acting along the injector (I) section or along a recirculation through the first (F) or second (S) recirculation beamline, respectively, tuned by the quadrupole magnets in the corresponding arc sections (I3, F0, F2, S0 and S2), that is,  $n \in \{\text{I}, \text{F}, \text{S}\}$  <sup>(4)</sup>. To be flexible for manual transverse-confinement tuning, the first-order horizontal dispersion term  $R_{16}$  and its derivative  $R_{26}$  have to be zero after each arc as well, which is realized by the very same quadrupole magnets; if the first-order vertical dispersion term  $R_{36}$  and its derivative  $R_{46}$  arise, they must be compensated accordingly. The possible ranges of the degrees of freedom are listed in Table B.1. Mentioned sections and devices are shown in Figs. 2.1 and 2.2.

## Transverse Quantities

The objective to ensure an appropriate beam transport is a transverse confinement so that  $x$  and  $y$  per electron are kept within the acceptance. More restrictive:  $|x|$  and  $|y|$  shall be small so that linear beam-dynamics apply. Furthermore, the beam should have small betatron functions or beam envelopes, respectively, at the locations of the cavities to suppress BBU (see section 3.8.1).

Degrees of freedom to influence the beam envelopes are the gradients of the quadrupole magnets located in the dispersion-free sections (I1, A1, F1 and S1).

The finding of a transverse confinement is based on other start-to-end simulations that dealt with several main-LINAC passes at the S-DALINAC and thus with superimposed beams [63, 93]. The cumulative length of those sections with superimposed beams is larger in this work compared to the corresponding ones in the works of Refs. [63, 93]; thus, mainly the number

<sup>3</sup>Note: The entire design recirculation length through a recirculation beamline is one degree of freedom, even if it is realized by two path length adjustment systems in the case of the second recirculation beamline.

<sup>4</sup>Note: In each of the sections I, F and S, there is only one overall resulting  $R_{56}$  for the corresponding section, even if several quadrupole magnets per arc and even if two arcs per recirculation beamline are involved to realize the corresponding values.



---

of algorithm steps in the corresponding simulations are increased and the solution spaces are more restricted in this work compared to those of the works of Refs. [63,93]. Because it was not dealt with common recirculation transport in the works of Refs. [63,93] (as no multi-turn energy-recovery operation modes were studied in these works), path length adjustment systems were only passed by a single beam and thus could be varied manually. For this reason, only the novel aspects, that is, finding a solution for the longitudinal objectives in common recirculation transport, are described in detail by a mathematical approach in section 4.2.2, while finding a solution for the transverse confinement is only briefly discussed.

## 4.2.2 Beam-Dynamics Simulations

Depending on the operation mode of the machine, beam-dynamics simulations can be a useful addition but may not always be necessary. However, in the case of a multi-turn energy-recovery mode in combination with common recirculation transport and a small beam acceptance, an exclusive manual beam-tuning is not possible because beam-influencing devices affect superimposed beams in a complex manner, and thus beam-dynamics simulations are necessary in order to take the coupled mode of action into account in advance.

The initial situation for the realization of the multi-turn energy-recovery mode – and thus for the beam-dynamics simulations – is a tuned electron beam leaving the injector LINAC with bunch properties resulting from a chosen centroid momentum and beam current. Consequently, the simulations described here start behind I1SC03. As mentioned, choosing a low centroid momentum for injection can increase the machine efficiency, but it leads to more pronounced phase slippage. In order to investigate the general feasibility with low injector momenta, the centroid momentum  $\bar{p} = 5 \text{ MeV}/c$  was chosen for this work. For radiation protection reasons, the initial<sup>5</sup> beam current  $I$  was approx. 1 nA during most of the beam tuning time. Since the feasible beam currents in the 2-ER mode (with regard to a BBU threshold current) are unknown, it was decided to use the beam properties of that low beam current as a basis for the beam-dynamics simulations, to tune the machine to the 2-ER mode with respect to this low beam current, and to ramp up the beam current afterward to determine the maximum beam current for which the very tuned setting remains valid. Since the thermionic gun is used in this study, the beam cannot be pulsed<sup>6</sup> and the bunch charge is in a fixed ratio to the beam current<sup>7</sup>; thus, beam tuning with a low beam current but with bunch properties such as those present when operating with a high beam current is not

---

<sup>5</sup>The initial beam current is the beam current determined at the Faraday cup IOF2, that is, after chopping the continuous beam provided by the thermionic gun to a bunched beam. As discussed below, particle losses occurred in certain sections downstream of IOF2 and the proportion of particle losses changed for different settings; for this reason, the initial beam current is used as reliable reference quantity.

<sup>6</sup>There is at least one electron per RF cycle if the beam current after chopping is greater than or equal to 0.5 nA.

<sup>7</sup>The bunch charge is in a fixed ratio to the beam current if the beam current after chopping is greater than or equal to 0.5 nA. Generally, the *average* bunch charge is in a fixed ratio to the beam current.

possible with the used gun. Hence, since the beam has to be tuned with a low beam current, the beam is inevitably tuned with corresponding low-beam-current bunch-properties.

For the beam-dynamics simulations, the corresponding beam quantities have to be known. A beam current of 1 nA can be detected with a BeO-Au screen but not with a Kapton-Al screen (see chapter 2). By using the BeO-Au screen I2T1, which is located in a dispersive section downstream of the injector LINAC, the upper-limit relative-momentum-spread  $\hat{\sigma}_\delta = (6.5 \pm 0.7) \cdot 10^{-4}$  and the upper-limit bunch-length  $\hat{\sigma}_t = (0.36 \pm 0.04)$  ps were determined. Since the measured upper-limit relative-momentum-spread during RF zero-crossing using I1SC03, which leads to the upper-limit bunch-length, was approximately equal for both slopes of the electric field, the momentum spread and the bunch length were assumed to be uncorrelated. The BeO-Au screen I2T2, which is located in a dispersion-free section downstream of the injector LINAC, was intended to be used for the determination of the transverse emittance, but it could not be used during this beamtime due to a malfunction. However, the Kapton-Al screen I2R1 is located in the same section, which thus has been used for the determination of the transverse emittance. To achieve a sufficient light yield from this screen, the initial beam current had to be increased to approx. 60 nA; since the light yield of a BeO-Au screen tends to oversaturate (see section 5.4.1), the usage of a Kapton-Al screen with a correspondingly increased beam current was a valid workaround to avoid interruption of the machine operation for maintenance work. At I2R1, conducting a quadrupole-magnet scan utilizing the quadrupole magnet I1QV01 yielded the normalized emittances  $\varepsilon_{n,x} = (0.13 \pm 0.02)$  mm mrad and  $\varepsilon_{n,y} = (0.43 \pm 0.03)$  mm mrad. Here, large uncertainties result due to the short distance between I1QV01 and the non-intended, alternative screen I2R1.

The simulations conducted to yield a working point for the S-DALINAC have been constructed iteratively: First, only longitudinal quantities (2D) have been considered. Here, a solution for only the centroid momentum was sought initially. Starting from a found solution, the optimum was sought taking the relative momentum spread into account as well. Finally, the simulations have been expanded to full 6D simulations seeking for a transverse confinement and the desired behavior of the beam envelopes inside the cavities. The individual steps of the simulations are discussed below. Details on the simulation code are provided in appendix A.

The simulations have been conducted using the particle tracking software ELEGANT [116]. Here, the implemented functions for solving optimization problems were utilized. Accordingly, the 2D optimization problem without taking the relative momentum spread into account can be formulated concisely<sup>8</sup> as follows:

$$\begin{aligned} \min \sum_{i=1}^4 f \left( \bar{p}_i \left( \hat{\mathcal{E}}_{z,A1SC01,peak}, \dots, \hat{\mathcal{E}}_{z,A1SC08,peak}, \hat{\phi}_{A1SC01}, \dots, \hat{\phi}_{A1SC08}, L_F, L_S \right), p_{0,i}, \tau_{2-ER} \right) \\ \text{subject to } \left( \hat{\mathcal{E}}_{z,A1SC01,peak}, \dots, \hat{\mathcal{E}}_{z,A1SC08,peak}, \hat{\phi}_{A1SC01}, \dots, \hat{\phi}_{A1SC08}, L_F, L_S \right) \in \mathcal{M}_2, \end{aligned} \quad (4.4)$$

<sup>8</sup>Note:  $\bar{p}_1$  does not depend on  $L_F$  and  $L_S$ , and  $\bar{p}_2$  does not depend on  $L_S$ .

where the penalty function

$$f(\bar{p}_i, p_{0,i}, \tau) := \begin{cases} 0, & |\bar{p}_i - p_{0,i}| \leq \tau \\ \left( \frac{|\bar{p}_i - p_{0,i}| - \tau}{\tau} \right)^2, & |\bar{p}_i - p_{0,i}| > \tau \end{cases} \quad (4.5)$$

provides a stop criterion. Here, the bounded set  $\mathcal{M}_2$  represents the individual technical limits within which the degrees of freedom are iterated by a simplex-based algorithm, and  $\tau_{2\text{-ER}}$  is the threshold parameter to specify the aimed precision for the centroid momenta. The chosen centroid momentum for injection (5 MeV/c) specifies the objectives mentioned in section 4.2.1 due to the fixed ratio of the momenta given in Table 4.1. Resulting numerical values for the objectives as well as limits of the available degrees of freedom are listed in Table B.1. The simulations led to an intermediate solution of the above given optimization problem, that is, a tuple of  $(\hat{\mathcal{E}}_{z,\text{A1SC01,peak}}, \dots, \hat{\mathcal{E}}_{z,\text{A1SC08,peak}}, \hat{\phi}_{\text{A1SC01}}, \dots, \hat{\phi}_{\text{A1SC08}}, L_{\text{F}}, L_{\text{S}})$ , with the behavior for  $\bar{p}$  shown in Fig. 4.3.

Fixing that found tuple, the first-order longitudinal dispersion terms  $R_{56,n}$  have been used as degrees of freedom within their technical limits (see Table B.1) to optimize the relative momentum spread. The focus was on an overall small relative momentum spread  $\sigma_\delta(s)$  to keep the beam within the acceptance, an almost symmetric behavior of  $\sigma_\delta(s)$ , and an ideally low value for  $\sigma_\delta$  at the location of a potential experiment, that is, after the last acceleration and prior to the first deceleration. There was no further restriction, like the objective to reach a minimum absolute momentum spread  $\sigma_{p-p_0}$  or a minimum bunch length  $\sigma_t$  at a certain location, since no experiment requiring one of these was involved in this feasibility study. Several tuples  $(R_{56,\text{I}}, R_{56,\text{F}}, R_{56,\text{S}})$  leading to the aimed behavior of the relative momentum spread were found<sup>9</sup>. From those found tuples, a tuple was selected that (i) consisted of  $R_{56,n}$  values that led to the most suitable behavior for the transverse confinement (since a certain  $R_{56,n}$  value inevitably requires a certain setting of the quadrupole magnets in the corresponding arc(s), which in turn influences the beam envelopes), and (ii) resulted in a suitable behavior for the bunch length  $\sigma_t(s)$ , although this was not an initial objective. The selected tuple  $(R_{56,\text{I}}, R_{56,\text{F}}, R_{56,\text{S}})$  was fixed and the tuple  $(\hat{\mathcal{E}}_{z,\text{A1SC01,peak}}, \dots, \hat{\mathcal{E}}_{z,\text{A1SC08,peak}}, \hat{\phi}_{\text{A1SC01}}, \dots, \hat{\phi}_{\text{A1SC08}}, L_{\text{F}}, L_{\text{S}})$  has again been varied starting from the previously found solution in order to again ensure centroid momenta within the precision  $\tau_{2\text{-ER}}$  – necessary, since varied  $R_{56,n}$  values slightly influence  $\bar{p}(s)$ . That led to the results for the longitudinal degrees of freedom listed in Table B.1, the behavior of the relative momentum spread and the bunch length shown in Fig. 4.3, as well as the shape of the longitudinal phase space shown in Fig. 4.4. From these figures, it can be seen that the centroid momenta are achieved as desired while the relative momentum spread has an adequate behavior along the accelerator (overall within the acceptance, almost symmetric, and small after maximum acceleration); however, the bunch performs almost a 90° rotation

<sup>9</sup>Here, several suitable tuples were found. However, if no suitable tuple would result from the simulations, solving the optimization problem (4.4) had to be repeated but for other starting conditions (since the used algorithm is deterministic).

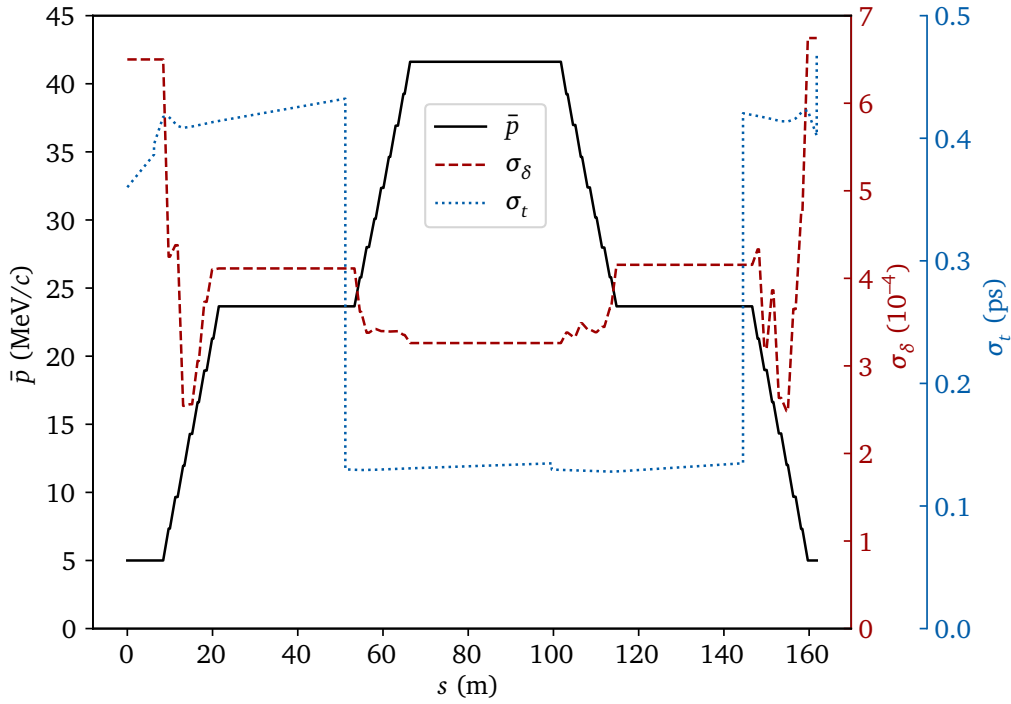


**Figure 4.3: Simulated longitudinal quantities for the 2-ER mode.** The figure shows the centroid momentum  $\bar{p}$ , the relative momentum spread  $\sigma_\delta$  and the bunch length  $\sigma_t$  as a function of the location  $s$ ; the simulation started behind the injector LINAC. The bunch length is changing due to different speeds of the electrons and due to different path lengths of the electrons caused by the longitudinal dispersion. While all these quantities are continuous functions in reality, the longitudinal dispersion is implemented here by step functions, that is, by elements of zero length at the end of the corresponding sections; this leads to jump discontinuities for  $\sigma_t$ . However, since space-charge effects and influences due to synchrotron radiation are disabled,  $\sigma_t$  is correctly evaluated in the main-LINAC section. Thus, the results for  $\bar{p}$  and  $\sigma_\delta$  are valid for the entire tracking since they are only changing inside the main LINAC. Figure first published in Ref. [114] in a modified form. Reproduced with permission from Springer Nature. All rights reserved.

in the longitudinal phase space along the travel from behind the injector LINAC to the location of maximum energy. Thus, the absolute momentum spread does not reach the minimum possible value as it is the case behind the injector LINAC – the absolute momentum spread is rather maximum. This is a consequence of the small number of possible iterative shearings in the longitudinal phase space. However, the found setting results in an almost minimum bunch length after maximum acceleration.

Based on the solution found for the longitudinal phase space, the 2D simulations were extended to 6D simulations. Here, the found longitudinal degrees of freedom have been fixed, that is, they were realized by the cavities, path length adjustment systems and

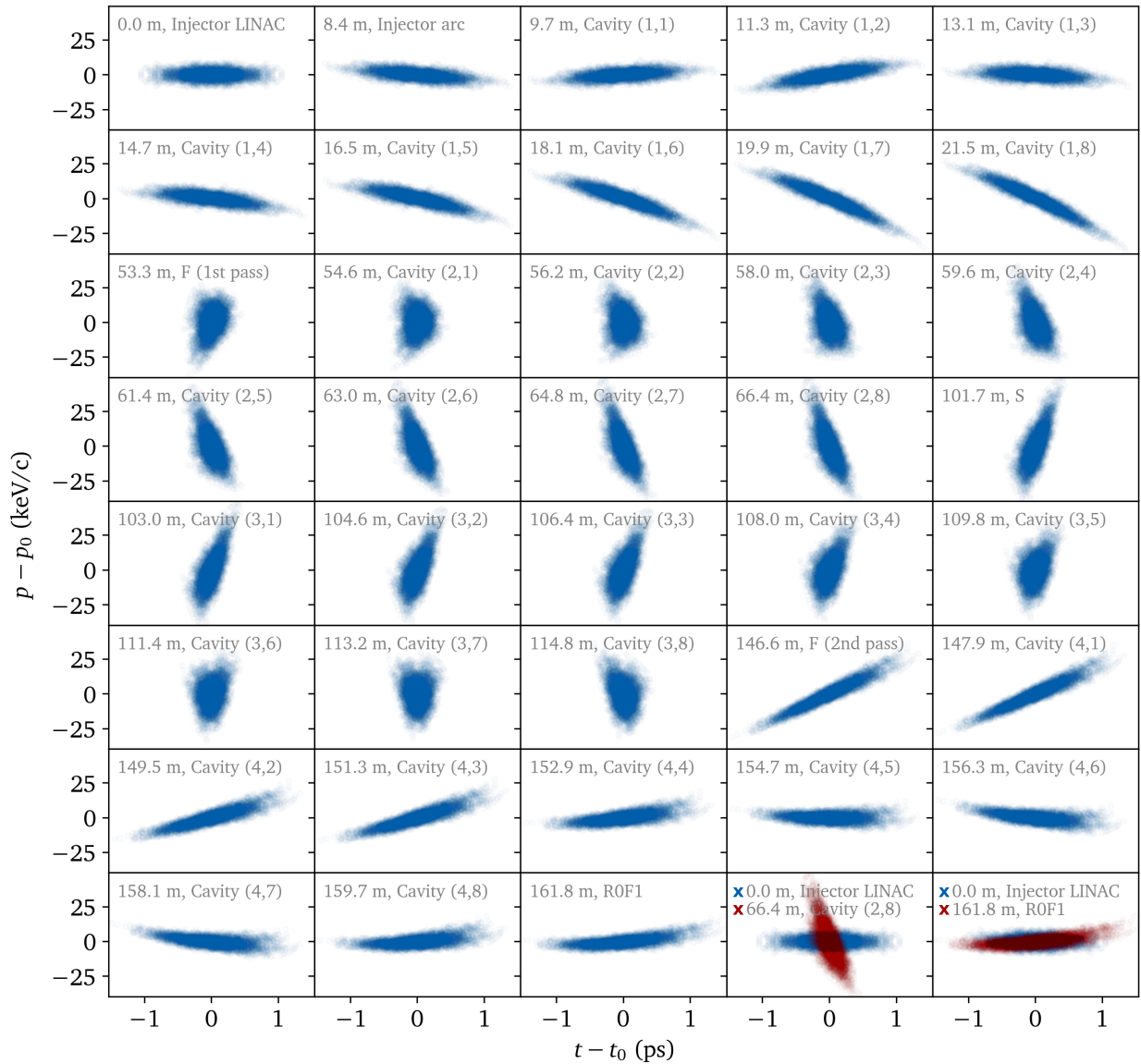


**Figure 4.4: Simulated longitudinal phase space for the 2-ER mode.** Each panel shows the phase space  $(t-t_0, p-p_0)$  present at the given location  $s$ ; the simulation started behind the injector LINAC. Additionally, a description of the last passed section leading to the shown phase space is given. Here, “Cavity  $(i,h)$ ” indicates the main-LINAC cavity with name ending “ $h$ ” (“A1SC0 $h$ ”) during main-LINAC pass  $i$ . The corresponding recirculation through the first (F) or second (S) recirculation beamline, respectively, starts and ends directly in front of the first cavity of the main LINAC. In the last two panels, phase space shapes present at selected locations are compared with each other. Figure first published in Ref. [114] in a modified form. Reproduced with permission from Springer Nature. All rights reserved.

---

quadrupole magnets in the arcs, and then the gradients<sup>10</sup> of the quadrupole magnets in the straight sections (I1, A1, F1 and S1) have been varied to ensure a transverse confinement and to mitigate BBU. For the 6D simulations, changes to the lattice were necessary (see section 4.2.3). A solution for the extended simulations is shown in Fig. 4.5. Here, the beam envelopes are small during all main-LINAC passes. However, the beam envelopes increase strongly during the final deflection ( $\alpha_0 = 125^\circ$ ,  $\rho_0 = 41$  mm) toward the beam dump R0F1. This will lead to partial particle losses in the beam-dump section; however, all particles will be decelerated as intended in the upstream located cavities and thus energy recovery takes place as intended. Since no experiment is intended in this feasibility study, a small beam spot after maximum acceleration was no objective. In the conducted simulations, impacts due to space-charge effects and synchrotron radiation were disabled since they are insignificant for a beam current of 1 nA and the present electron energies, and thus including these effects would unnecessarily have increased the simulation time significantly. Their impact in the case of higher beam currents is discussed in appendix D.

A note on the machine layout: Since its initial operation, the S-DALINAC was iteratively further developed and customized to the requirements of several operation modes, while enabling (multi-turn) energy-recovery operation has been one of the latest endeavor. The layout of the S-DALINAC has the advantage of being sufficient for many operation modes; here, in particular, the machine layout supports each arc's  $R_{56}$  to be tuned in a wide range. At the same time, it is not the optimum machine layout for a dedicated operation mode: there are limitations in realizing a setup for the transverse confinement for the multi-turn energy-recovery modes, such as non-existing symmetry of the betatron functions and partial particle losses in the beam-dump section. However, the betatron functions are almost equal for both passes through the first recirculation beamline – but different for each pass through the main-LINAC section. The S-DALINAC was not originally designed to support energy-recovery modes and thus to deal with a final momentum equal to the injector momentum. The design  $125^\circ$ -bend with  $\rho_0 = 41$  mm toward R0F1 results from the limited options to retrofit the already constructed machine with energy-recovery modes [45].

---

<sup>10</sup>For a concise notation, the term “gradient” is used here. Due to the use of ELEGANT and the associated characteristics, not the gradient but either the focusing strength or the pole tip field of a quadrupole magnet has been changed, depending on the location of the quadrupole magnet, and thus depending on the used element in ELEGANT. However, both quantities entail a change in the gradient. Details are given in appendix A.

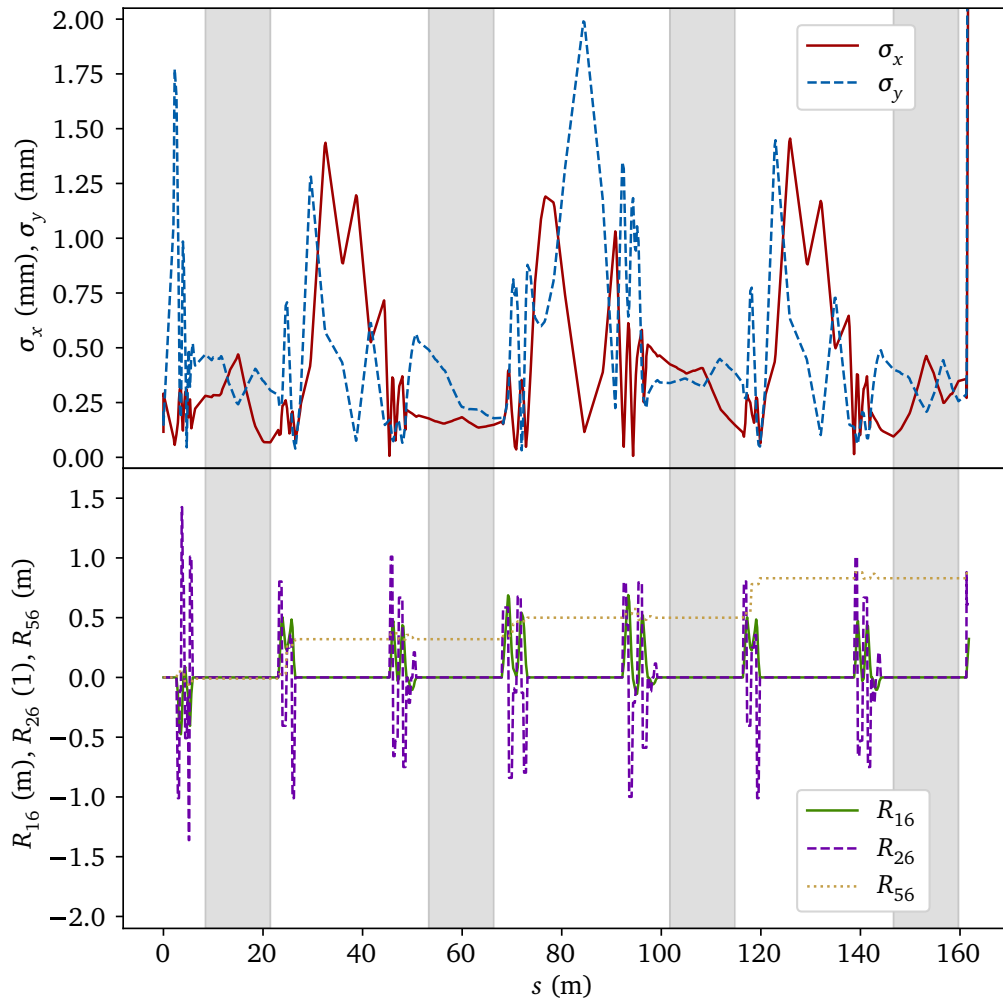


**Figure 4.5: Simulated beam envelopes and dispersion terms for the 2-ER mode.** The figure shows the beam envelopes  $\sigma_x$  and  $\sigma_y$  as well as the first-order dispersion terms  $R_{i6,0 \rightarrow s}$  as a function of the location  $s$ ; the simulation started behind the injector LINAC. Values for the beam envelopes are  $\sigma_{x,y} \leq 0.5$  mm inside the cavities (each gray zone indicates a main-LINAC pass, that is, it indicates a pass through the section that begins at the entrance of the first cavity of the main LINAC and ends at the exit of the last cavity of the main LINAC) and  $\sigma_{x,y} \leq 2.0$  mm everywhere until the last main-LINAC pass. Downstream, the beam envelopes increase strongly toward the beam dump following after a  $125^\circ$ -bend with a bending radius of 41 mm.

---

### 4.2.3 Necessary Upgrades of the S-DALINAC

For the realization of the 2-ER mode, beamline modifications were necessary: beam guiding elements had to be installed/replaced and beam diagnostics had to be implemented.

#### Beam Guiding Elements

As shown in the previous section, it is necessary to set several degrees of freedom to certain values. Prior to this work, the S-DALINAC did not provide  $R_{56,F}$  as a degree of freedom in an appropriate manner; it was not possible to set an individual value for  $R_{56,F}$  and to realize that  $R_{16}$  and  $R_{26}$  are both zero at the end of both arcs of the first recirculation beamline. This was due to only two installed quadrupole magnets per arc of that recirculation beamline. Thus, forcing  $R_{16} = R_{26} = 0$  at the end of each arc resulted in a constant value for  $R_{56,F}$ , or  $R_{16} = R_{26} = 0$  at the end of each arc had to be waived in order to set  $R_{56,F}$  to an individual value. In a previous work,  $R_{56,F}$  has been varied tolerating at least one value of  $R_{16}$  or  $R_{26}$  at the end of at least one arc of the first recirculation beamline to be non-zero [117]. However, this shall be deliberately avoided in this work because electrons pass the first recirculation beamline twice. Thus, in order to be able to realize a certain value for  $R_{56,F}$  following from the beam-dynamics simulations as well as to be flexible to alternative values,  $R_{56,F}$  had to be realized as a degree of freedom such that  $R_{16}$  and  $R_{26}$  are zero at the end of each arc of the first recirculation beamline. Based on Ref. [118], this can be sufficiently realized by replacing an installed sextupole magnet with a quadrupole magnet in each arc of the first recirculation beamline (named FOQU02 and F2QU02, see Fig. 2.2), which was realized within the scope of this work. In the long term, however, a sufficient number of sextupole magnets should be available per recirculation beamline or even per arc in order to utilize higher-order terms adequately as degrees of freedom.

Due to the common recirculation transport and the associated fact that beam guiding elements influence two superimposed beams in the first recirculation beamline, it was a challenge in the initial 6D beam-dynamics simulations to find a transverse confinement for the particles up to the last pass of the main LINAC; as a result, the number of such quadrupole magnets that do not couple the horizontal and the vertical phase space had to be increased in the straight section of the second recirculation beamline (S1), which was realized within the scope of this work (see Ref. [45] for the previous layout of S1). The solution for the 2-ER mode as shown in Fig. 4.5 (as well as the solution for the 3-ER mode as shown in Fig. 4.11) results from beam-dynamics simulations in which the additional quadrupole magnets in the arcs of the first recirculation beamline as well as the modifications of the straight section of the second recirculation beamline are implemented.

#### Beam Diagnostics

In order to be able to diagnose the second up to last beam in sections with superimposed beams, non-destructive diagnostic devices are necessary. In the main-LINAC section located



---

screens with a hole have already been successfully used in the past to ensure undisturbed passing of the first beam(s) while making one or more subsequent beams at the outer region of the very screens visible by slightly deflecting the very subsequent beam(s) [14]. For this reason, the first recirculation beamline was additionally equipped with such screens with a hole within the scope of this work.

One goal of this work is the comparison of the 2-ER mode with the corresponding conventional acceleration mode in which the main LINAC is only passed twice for an exclusive acceleration. Here, it is of interest whether the energy-recovery process influences the electromagnetic fields inside the cavities in such a way that beam properties of accelerated beams may be affected. Therefore, wire scanners (SOWS01 and S1WS01) as quasi-non-destructive diagnostic devices to investigate the beam properties in both operation modes were constructed and installed in the second recirculation beamline within the scope of this work. Further details on the wire scanners are provided in chapter 5.

Further upgrades necessary to investigate the 2-ER mode adequately have been part of other projects: Prior to the realization of the 2-ER mode, an RF power measurement system has been implemented [70], which enables comparisons of the beam loading in different operation modes. Moreover, a wire scanner (F1WS01) has been constructed and installed in the first recirculation beamline [67], which enables quasi-non-destructive beam diagnostics of superimposed beams during beam tuning for a multi-turn energy-recovery mode.

#### 4.2.4 Setting up the S-DALINAC

The electron beam was tuned from the thermionic gun to the exit of the injector LINAC according to the established procedure with the resulting beam properties mentioned in section 4.2.2. Setting up certain quantities at sections located downstream is described below. The corresponding values are given in Table B.1.

##### Transverse and Longitudinal Dispersion

Downstream of the injector LINAC, the beam has to pass several arc sections when operating in a multi-turn energy-recovery mode. For each of these arcs, the transverse and the longitudinal dispersion have to be set accurately. Due to a lack of degrees of freedom, only first-order dispersion terms are considered, that is,  $R_{16}$ ,  $R_{26}$ ,  $R_{36}$ ,  $R_{46}$  and  $R_{56}$ . Setting of these quantities is done by tuning the quadrupole magnets of an arc to suitable values following from lattice simulations using the software ELEGANT. As mentioned, besides slight vertical deflections in the gun and the chopper section, the design orbit of those sections of the S-DALINAC tuned within this work contains only deflections in the horizontal plane (with respect to a coordinate system at rest). Thus, in case  $R_{36}$  and  $R_{46}$  vanish downstream of the aperture plate of the chopper section,  $R_{36} = R_{46} = 0$  applies theoretically at each location further downstream, that is, there should be no vertical dispersion; however, due

---

to imperfections, vertical dispersion may arise at certain positions and must be corrected accordingly<sup>11</sup>.

Accurately set dispersion terms have to be verified in order to ensure a correct machine setup. Generally, observation of the transverse position as a function of the relative momentum provides information on the transverse dispersion and observation of the longitudinal position as a function of the relative momentum provides information on the longitudinal dispersion. The relative momentum can be changed intentionally for the intended observations.

At the S-DALINAC, however, positions of single electrons cannot be detected – only centroid quantities of a series of bunches can be detected: At the S-DALINAC, the centroid transverse positions  $\bar{x}$  and  $\bar{y}$  can be observed directly by using a screen monitor or a wire scanner; by measuring the magnetic field of a dipole magnet passed by the beam, the centroid relative momentum  $\bar{\delta}$  can be detected as well if the beam center is located on the design orbit, especially at the screen's or wire scanner's center, respectively. A varied  $\bar{\delta}$  is caused by changing the peak of the time-independent amplitude of the on-axis  $z$ -component of the electric field,  $\hat{\mathcal{E}}_{z,\text{peak}}$ , of a cavity located upstream. Measuring  $\bar{x}$  and  $\bar{y}$  as a function of  $\bar{\delta}$  yields the transverse dispersion. To determine the derivative of the transverse dispersion, the transverse dispersion has to be determined at two different locations  $s_1$  and  $s_2$ .

In contrast to the centroid relative momentum and the centroid transverse positions, the centroid longitudinal position cannot be observed directly at the S-DALINAC; here, a relative centroid time of flight resulting from the individual path lengths and speeds of the electrons is observable via remainder-centroid-phase measurements at cavity monitors. Measuring remainder centroid phases  $\bar{\theta}_{\text{mod}}$  or relative centroid times of flight,  $\tilde{t}$ , respectively, as a function of  $\bar{\delta}$  yields the longitudinal dispersion; details on this technique are provided in appendix E.

In this way, iterations of measuring the dispersion terms and fine-tuning of quadrupole magnets ensure the desired values. A few points regarding the dispersion measurements shall be emphasized:

As mentioned above, one challenge is the realization of a multi-turn energy-recovery mode with a low injector momentum. For low momenta, it is crucial to take into account that the electron's speed and thus arrival time changes if the momentum changes because it noticeably affects the remainder-centroid-phase measurements or time-of-flight measurements, respectively: Figure 4.6 shows simulated and measured relative centroid times of flight,  $\tilde{t}$ , in the injector arc as a function of  $\bar{\delta}$  based on  $p_0 = 5 \text{ MeV}/c$ . For the measurements,  $\bar{\delta}$  was changed by the last cavity of the injector LINAC (I1SC03) and  $\tilde{t}$  was determined from the measured  $\bar{\theta}_{\text{mod}}$  of two cavity monitors downstream of I1SC03: one upstream of the injector arc (I1HF01) and one downstream of the injector arc (A1HF01). From Fig. 4.6 it can be seen that  $\tilde{t}$  changes as a function of  $\bar{\delta}$  if there is no longitudinal dispersion; thus, changes in

---

<sup>11</sup>Due to a lack of second-order degrees of freedom, only first-order vertical dispersion can be corrected, while at the same time higher-order terms inevitably result from the very quadrupole magnet settings necessary for the first-order corrections.

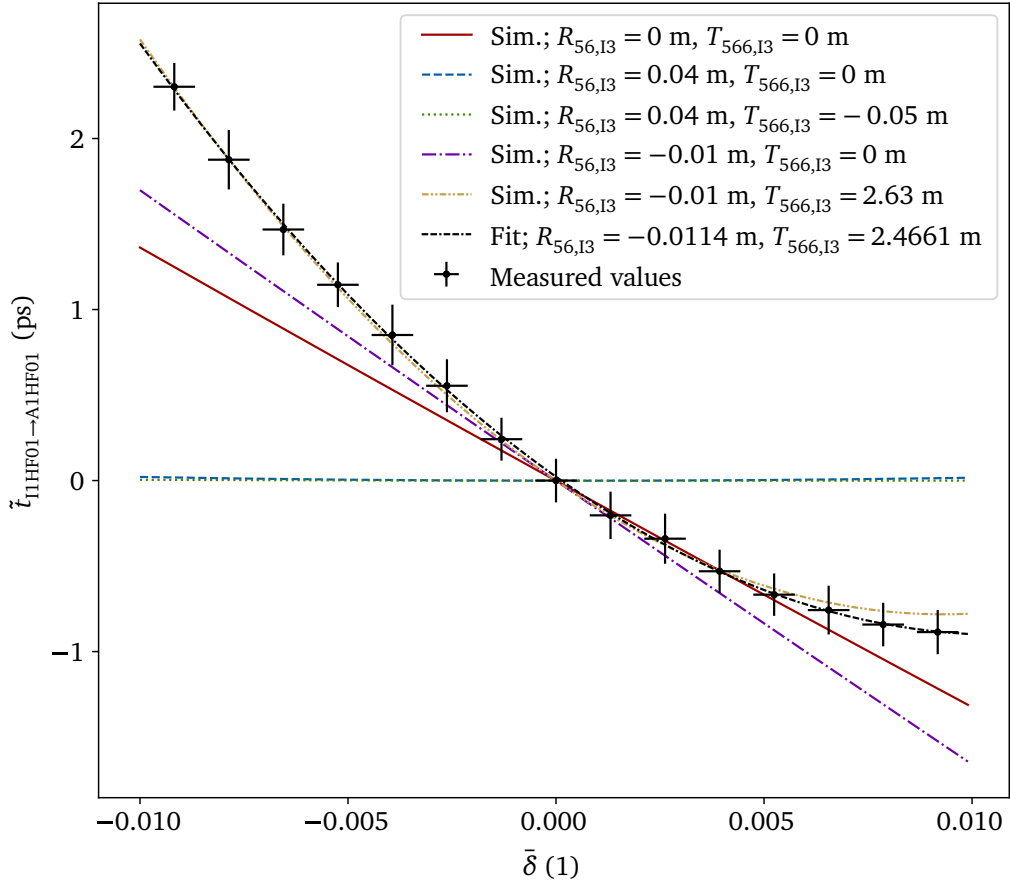


**Figure 4.6: Relative times of flight through the injector arc.** The figure shows the simulated and the based on remainder-centroid-phase measurements determined (measured) relative centroid times of flight,  $\tilde{t}_{I1HF01 \rightarrow A1HF01}$ , which is needed to cover the distance from the center of cavity monitor I1HF01 to the center of cavity monitor A1HF01 as a function of the centroid relative momentum  $\bar{\delta}$  that is based on  $p_0 = 5$  MeV/c. Shown values for  $\tilde{t}_{I1HF01 \rightarrow A1HF01}$  result from (i) simulations (Sim.) for different values of  $R_{56,13}$  and  $T_{566,13}$ , (ii) measurements, or (iii) the associated fit to the measurements. Since the electrons are not ultra-relativistic, the speed of an electron changes noticeably as a function of the relative momentum, and thus  $\tilde{t}_{I1HF01 \rightarrow A1HF01}$  is not constant in the absence of longitudinal dispersion, that is, in the case of  $R_{56,13} = T_{566,13} = 0$ . An almost constant  $\tilde{t}_{I1HF01 \rightarrow A1HF01}$  within the shown range of  $\bar{\delta}$  follows for  $R_{56,13} = 0.04$  m and  $T_{566,13} = -0.05$  m. The value  $R_{56,13} = -0.01$  m follows from the optimum of the 2D simulations, while  $T_{566,13} = 2.63$  m inevitably follows in the simulations as a result of the quadrupole magnets setting necessary to achieve  $R_{56,13} = -0.01$  m and due to a lack of degrees of freedom to adjust  $T_{566,13}$ . Within the uncertainties, the measured relative centroid time of flight matches with the one simulated for  $R_{56,13} = -0.01$  m and  $T_{566,13} = 2.63$  m. For the measured relative centroid time of flight, a fit results in  $R_{56,13} = -0.0114$  m and  $T_{566,13} = 2.4661$  m.

$\tilde{t}$  result only from changes in speed because the path length is constant in the case of zero longitudinal dispersion.

Following the injector arc tuning, the main LINAC has to be tuned accurately, which is described further below.

Downstream of the main LINAC, the recirculation beamlines are located: similar to the procedure described for the injector arc, an accurate setting of the values for  $R_{16}$ ,  $R_{26}$ ,  $R_{36}$ ,

$R_{46}$  and  $R_{56}$  has to be ensured for each arc of both the first and the second recirculation beamline. Here, however, further challenges arise: The setting of each arc of the first recirculation beamline can be verified similar to the procedure conducted for the injector arc by using (i) the last cavity of the main LINAC (A1SC08) to change the centroid momentum, and (ii) corresponding screen monitors or cavity monitors at certain locations to measure  $\bar{x}$  and  $\bar{y}$  or  $\bar{t}$ , respectively. However, the corresponding cavity monitor downstream of the second arc of each recirculation beamline is A1HF01, which is inevitably passed by the injector beam and – if applicable – each beam passed through a preceding recirculation beamline. Thus, the remainder centroid phase measured at A1HF01,  $\bar{\theta}_{\text{mod,A1HF01}}$ , utilized to evaluate a time of flight or  $R_{56}$  for a recirculation, respectively, is inevitably a superimposed signal from multiple beams. Since A1SC08, which is located downstream of the injector arc, is used to change the centroid momentum for the determination of  $R_{56}$  of a recirculation, the beam leaving the injector arc remains independent of momentum changes caused by A1SC08. Furthermore, the beam leaving the injector arc arrives first at A1HF01. Therefore, the beam leaving the injector arc was used as a reference. The arrival time of the beam leaving the first or second recirculation beamline, respectively, at A1HF01 is dependent on (i) a change in speed due to the change in the centroid relative momentum  $\bar{\delta}$  induced by tuning A1SC08, and (ii) a change in path length due to a set longitudinal dispersion in the corresponding recirculation beamline in combination with a changed  $\bar{\delta}$ . Since there was no particle loss<sup>12</sup> while measuring the dispersion terms, no dependence on current differences of the superimposed beams existed, and therefore

$$\begin{aligned} & \bar{\theta}_{\text{mod,A1HF01}}(\bar{\delta}(s), R_{56,F}) + \theta_{\text{off,A1HF01}} \\ &= \left( \frac{1}{2} \omega \cdot \left( \bar{t}_1(\bar{\delta}(s)) + \bar{t}_2(\bar{\delta}(s), R_{56,F}) \right) \right) \bmod 360^\circ \end{aligned} \quad (4.6)$$

follows for the measurement downstream of the first recirculation beamline, and

$$\begin{aligned} & \bar{\theta}_{\text{mod,A1HF01}}(\bar{\delta}(s), R_{56,F}, R_{56,S}) + \theta_{\text{off,A1HF01}} \\ &= \left( \frac{1}{3} \omega \cdot \left( \bar{t}_1(\bar{\delta}(s)) + \bar{t}_2(\bar{\delta}(s), R_{56,F}) + \bar{t}_3(\bar{\delta}(s), R_{56,F}, R_{56,S}) \right) \right) \bmod 360^\circ \end{aligned} \quad (4.7)$$

follows for the measurement downstream of the second recirculation beamline. Here,  $\bar{t}_i$  is the centroid time of flight for the electrons from the gun to the  $i$ -th pass of A1HF01, and  $\theta_{\text{off,A1HF01}}$  is a certain  $\bar{\delta}$ -independent offset phase taking into account the signal transit time of A1HF01 (see appendix E for further details). The angular frequency  $\omega$  (and consequently the oscillation period  $t_{\text{RF}} = 2\pi/\omega$ ) of the  $\text{TM}_{010}$ - $\pi$ -mode of the RF fields inside the cavity monitors is equal to the one of the superconducting cavities used for acceleration or deceleration, respectively (see section 3.3).

<sup>12</sup>Due to the length of a recirculation beamline, the momentum acceptance and thus the range of a measurement is much smaller for the section from A1SC08 to A1HF01 compared to a measurement conducted in the injector arc. Therefore, only first-order longitudinal dispersion terms were evaluated in the measurements conducted for a recirculation beamline. For this reason, only first-order terms are mentioned in Eqs. (4.6) and (4.7).

In order to verify precisely set values for the second recirculation beamline, the cavity used to change the centroid momentum is A1SC08 as well. Since the beam passes through the first recirculation beamline before entering the second recirculation beamline, the main LINAC (and thus in particular A1SC08) is passed twice. Here, the change of the momentum caused by the main LINAC is complex since an intentional change in momentum gain during the first pass of A1SC08 (intentionally changed due to the measuring method) changes the speed of the electrons and thus the arrival time at each cavity for the second pass, and thus the energy gain per cavity due to changed off-crest phases. While the change in speed is low, an additional arrival time offset and thus an additional offset to the off-crest phase occurs if  $R_{56,F}$  is non-zero (as intended in this work). In this way, the longitudinal dispersion terms can only be measured with limited precision if several recirculation beamlines and thus several main-LINAC passes are involved [63].

### Cavities of the Main LINAC

Proper operation of the main LINAC requires an accurate setting of the peak of the time-independent amplitude of the on-axis  $z$ -component of the electric field,  $\hat{\mathcal{E}}_{z,\text{peak}}$ , and the off-crest acceleration phase  $\hat{\phi}$  of each cavity. In order to ensure correct momentum changes as resulting from the beam-dynamics simulations, the cavities were set as follows: The second cavity (A1SC02) up to the last cavity (A1SC08) were switched off and detuned from the design frequency to prevent resonances with the electron beam that acts as a continuous wave with a frequency equal to the design frequency of the cavities. Following this, the first cavity (A1SC01) was set: First,  $\hat{\mathcal{E}}_{z,\text{A1SC01,peak}}$  had to be set by finding the corresponding control-system-related amplitude and phase that led to the first-pass on-crest momentum gain  $\Delta\bar{p}_{\text{on-crest,A1SC01}}$  (see Table B.1), which was sought using both a screen monitor in a dispersive section as well as the RF power measurement system. Second, the off-crest acceleration phase  $\hat{\phi}_{\text{A1SC01}}$  that led to the first-pass off-crest momentum gain  $\Delta\bar{p}_{\text{off-crest,A1SC01}}$  (see Table B.1) was set. Afterward, A1SC02 was switched on and tuned to the design frequency, before it was proceeded in the same way as for A1SC01. This procedure was repeated for each following cavity until all eight cavities of the main LINAC were set. Although the main LINAC was set up only during the first pass, the setting was valid for all four passes as follows from the beam-dynamics simulations and the verification discussed in section 4.2.5, and thus phase slippage was taken into account as intended.

### Path Length Adjustment Systems

Even if certain values for the path length adjustment systems result from the beam-dynamics simulations, these values cannot be transferred one-to-one to the machine due to the uncertainties in measuring the overall orbit lengths and thus due to the uncertainties of the overall orbit lengths used in the simulations; even small deviations in the path lengths lead to crucial offsets in the arrival times of the electrons at the cavities, and thus to inappropriate off-crest acceleration or deceleration phases, respectively. Therefore, the path length adjustment

---

systems (FOPL01, SOPL01 and S2PL01) had to be set as a function of the monitored behavior of the beam: the path length adjustment systems have been tuned appropriately if the beam has the correct momentum or energy, respectively, which was verified with screen monitors in dispersive sections and with the RF power measurement system. Furthermore, it has to be ensured that the electrons pass the RF fields with the intended slopes (rising or falling slope).

It has to be taken into account that the lengths of some drift sections change when a path length adjustment system is tuned (see Fig. 2.4), which in turn influences dispersion terms as well as Twiss parameters: if a path length adjustment system is tuned, quadrupole magnets that are located in the corresponding arc of the very path length adjustment system have to be (re)tuned to new values to ensure (again) that the first-order achromat condition is met and the desired value for the first-order longitudinal dispersion results, while quadrupole magnets located in straight sections downstream of the very path length adjustment system may need to be (re)tuned to ensure (again) a transverse confinement.

### **Quadrupole Magnets for the Transverse Confinement**

For an increasing  $s$ , simulated and observed transverse envelopes differ distinctly. Therefore, quadrupole magnets located in straight sections have been tuned (i) partly based on beam-dynamics simulations conducted with ELEGANT and (ii) partly manually. Here, it remained difficult to find an adequate solution for the transverse confinement. Thus, there was an unavoidable partial particle loss in the realized 2-ER mode. This led to limited energy-recovery efficiencies as discussed in section 4.2.5.

## **4.2.5 Verification of the Realized 2-ER Mode and Measurement Results**

By conducting the steps described in section 4.2.4, the S-DALINAC was successfully operated in the 2-ER mode, that is, the electron beam was accelerated twice in the main LINAC, followed by a double deceleration in the very same LINAC. A visual verification of this operation mode is given by the appearance of four superimposed beams on the screen located behind the main LINAC, A1H2, as shown in Fig. 4.7. This proves that the electrons must have traveled on the intended orbits, which in turn is only possible if the electrons had the correct energy, that is, if they were accelerated and decelerated suitably. Whether energy lost by the particles during deceleration was recovered and recycled will be examined below.

### **Beam Loading and Energy-Recovery Efficiency**

It remains to confirm the following: During deceleration, energy (which was previously withdrawn from the RF fields and supplied to the electrons) was withdrawn from the electrons and stored in the RF fields. After the energy was recovered in the RF fields, subsequent electrons withdrew it during acceleration, and thus the recovered energy was recycled.

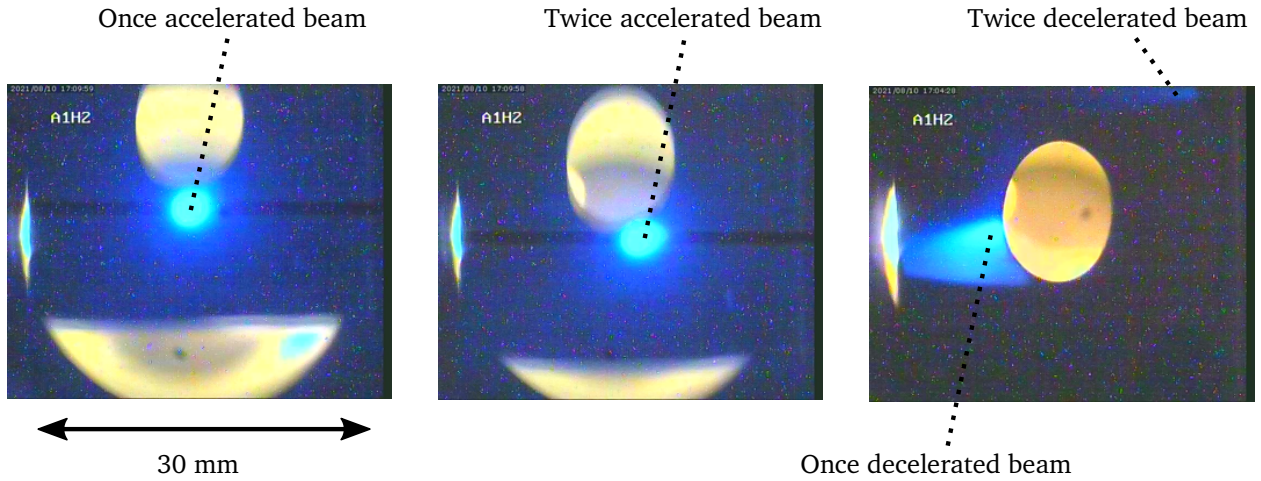


**Figure 4.7: Detection of four different beams at the location of A1H2.** The BeO-Au screen A1H2 located behind the main LINAC was used to make each of the four superimposed beams visible. While the screen was being moved, the once accelerated beam either was blocked or passed through the hole. The same applied to the twice accelerated beam at a different point in time during the monitor’s movement (as long as a part of the once accelerated beam passed through the hole – the twice accelerated beam was only visible if the once accelerated beam was not entirely blocked) since the once and the twice accelerated beam were slightly vertically displaced. When the screen was in its end position, the once and the twice accelerated beam passed through the hole entirely undisturbed, while only a small fraction of the once decelerated beam passed through the hole, and thus only a small fraction of the twice decelerated beam was faintly visible. Here, a horizontal displacement of the once decelerated beam as well as a vertical displacement of the twice decelerated beam was observed. The latter is the reason why the beam did not reach the intended dump location (R0F1) but was lost in the beampipe in the R section. The screen pictures were taken with an initial beam current of approx. 240 nA. The visible yellow shades allowing to see the hole and the movement of the screen are originated from the light of a hot-filament ionization gauge located inside the beampipe.

To prove this, energy requirements – or energy requirements per time (that is, power  $P$ ) – had to be measured. Different RF power components can be observed by using the RF power measurement system, which is hence used to evaluate the recovery process and to evaluate the efficiency of the 2-ER mode. The fraction of the externally provided RF power transferred to the beam is the beam loading [70]

$$P_b = P_f - P_r - (P_0 + P_t), \quad (4.8)$$

where  $P_f$  is the forward power,  $P_r$  is the reverse power,  $P_0$  is the dissipated power, and  $P_t$  is the transmitted power. The sum  $P_0 + P_t$  was measured by determining  $P_f$  and  $P_r$  in the absence of the beam (where  $P_b = 0$  applies by definition), which was realized by blocking the beam at the Faraday cup IOF2.

For the intended evaluations, the beam loading of the main LINAC was measured during the operation in the 2-ER mode as well as during the operation in each of the below introduced intermediate operation modes. Here, the beam loading of only the main LINAC is considered since the focus of this work is on investigating the recovery capability of that LINAC that is involved in the recovery process during the multi-turn operation; for a given beam current,

---

the beam loading of the main LINAC is the variable power component that is dependent on the operation mode, while the beam loading of the injector LINAC remains unchanged. Further power components relevant for the 2-ER mode and the potential for energy saving – one of the main purposes of energy-recovery accelerators – are discussed in section 4.2.6.

There are intermediate operation modes of the 2-ER mode that result from reducing the number of main-LINAC passes by blocking the beam or deflecting it to another orbit: The most important one of these for comparison is the two-turn conventional acceleration diagnostic (2-CA) mode (see Fig. 2.3) in which the main LINAC is passed only twice – exclusively for acceleration. That operation mode can be realized by deflecting the beam toward the high-energy beam-dump S3F1 or by blocking the beam on a Kapton-Al screen located in the second recirculation beamline (S1R1); the latter is possible if the combination of beam current and beam size does not exceed the corresponding load limit of the screen [63]. Stopping the beam on a screen is more practical since switching the dipole magnet S1BM01 on (to guide the beam to S3F1) and off (for further operation) would result in different remanence values. Measured beam-loading values for the 2-ER and the 2-CA mode provide information about how much multi-turn energy-recovery operation can outperform conventional multi-turn acceleration operation. Moreover, two further intermediate operation modes are relevant: (i) If the beam is blocked on a Kapton-Al screen located in the first recirculation beamline (F1R1), the beam is accelerated only once in the main LINAC (1-a mode). (ii) If the twice accelerated beam is slightly deflected using a dipole magnet located in the second arc of the second recirculation beamline (S2BM03), the once decelerated beam can be blocked in the first recirculation beamline on the outer region of a Kapton-Al screen with a hole (F1H2); in that case, the non-deflected once-accelerated beam also traveling through the first recirculation beamline passes the hole of that very screen undisturbed; thus, the beam is accelerated twice and decelerated once in the main LINAC (1-d mode). Those two intermediate operation modes are no design operation modes of the S-DALINAC as presented in Fig. 2.3. Measured beam-loading values of the 1-a and the 1-d mode provide information on the centroid momenta and possible beam loss.

Although the intermediate operation modes were realized chronologically prior to the 2-ER mode during beam tuning, the beam-loading values for the intermediate operation modes were only measured after the 2-ER mode was realized and the corresponding beam loading measured – the intermediate operation modes were then realized in the following order: 1-d, 2-CA, 1-a. Proceeding in this order ensures same conditions for the intermediate operation modes as for the 2-ER mode, that is, nothing was manipulated due to fine-tuning.

As mentioned, for radiation protection reasons, an initial beam current of approx. 1 nA was chosen to tune the machine to the 2-ER mode. However, such a low beam current does not enable a suitable beam-loading measurement since the absolute<sup>13</sup> values of the resulting beam-loading would be smaller than the uncertainties of the RF power measurement system. Therefore, higher beam currents are necessary to determine reliable values for the beam loading. In a first measurement, the initial beam current was increased to approx. 2.3  $\mu$ A

---

<sup>13</sup>Absolute values have to be addressed here because the beam loading can be negative as discussed below.



and the beam loading was measured in each of the above mentioned operation modes for 10 min (see Fig. 4.8(a)). Here,  $P_{b,2-CA} = (86.3 \pm 0.3)$  W and  $P_{b,2-ER} = (13.8 \pm 1.1)$  W follow, leading to an energy-recovery efficiency of the 2-ER mode,

$$\eta = \frac{P_{b,2-CA} - P_{b,2-ER}}{P_{b,2-CA}}, \quad (4.9)$$

of  $(84.0 \pm 1.2)$  % <sup>(14)</sup>;  $P_{b,2-ER} < P_{b,2-CA}$  together with the fact that subsequent electrons traveled on the intended orbits when leaving the main LINAC after an acceleration, which thus were appropriately accelerated, confirms that energy was recovered and recycled.

Following these measurements, a measurement series was conducted to investigate  $\eta$  as a function of the initial beam current: while operating in one of the above mentioned operation modes, the initial beam current was set to 0.2  $\mu$ A and ramped up to above 7  $\mu$ A; this was conducted for each of the above mentioned operation modes, thus the initial beam current has been ramped up four times in total. The results are shown in Fig. 4.8(b) and a maximum energy-recovery efficiency of approx. 87 % was determined. The shown energy-recovery efficiency was determined by calculating it via Eq. (4.9) based on the linear splines of  $P_{b,2-CA}$  and  $P_{b,2-ER}$ , and applying a Savitzky–Golay filter [119] to counteract the artificial noise.

For a given initial beam current, the measurement results presented in Fig. 4.8(b) show almost equal beam-loading values for the 1-a and the 1-d mode, that is, when operating in the 1-d mode, the energy amount required to accelerate for the second time was recovered during the first deceleration and recycled during the acceleration of subsequent electrons. The measured beam-loading values indicated that no particle losses occurred during the first deceleration or upstream, which was confirmed by using beam-loss monitors.

Ideally,  $P_{b,2-ER}$  should be zero; that is, each electron would have returned the exact amount of energy to the electric field inside the cavities of the main LINAC that was previously withdrawn from there, while the recovered energy would be recycled completely during subsequent acceleration. A non-zero  $P_{b,2-ER}$  can have different reasons: If there is no particle loss and if the recovered energy is almost completely recycled<sup>15</sup>,  $P_{b,2-ER} > 0$  implies that less energy is transferred during deceleration than during acceleration, which means that the electrons were not decelerated enough and thus the final momentum prior to beam

<sup>14</sup>The energy-recovery efficiency of an entire machine is limited to 100 %. However, because only the beam loading of the main LINAC is taken into account in the definition of  $\eta$ , the value of  $\eta$  could in principle be greater than 100 % (resulting if  $P_{b,2-ER} < 0$ ), which would be the case if the electrons would return more energy to the main LINAC during deceleration than the main LINAC delivered to the electrons previously during acceleration (over-deceleration) – like during on-crest deceleration and off-crest acceleration. This is in principle possible because the beam has already a certain kinetic energy due to the previous acceleration in the gun and the injector LINAC, and consequently the beam can be over-decelerated in the main LINAC without being stopped. However, over-deceleration is usually not desired because the RF control is limited in managing energy surpluses and the beam would leave the main LINAC in this case with a momentum not suitable to travel on the design orbit when passing the downstream located splitter dipole magnet FOBM01.

<sup>15</sup>As mentioned, finite quality factors of the cavities prevent a full recycling of the recovered energy.

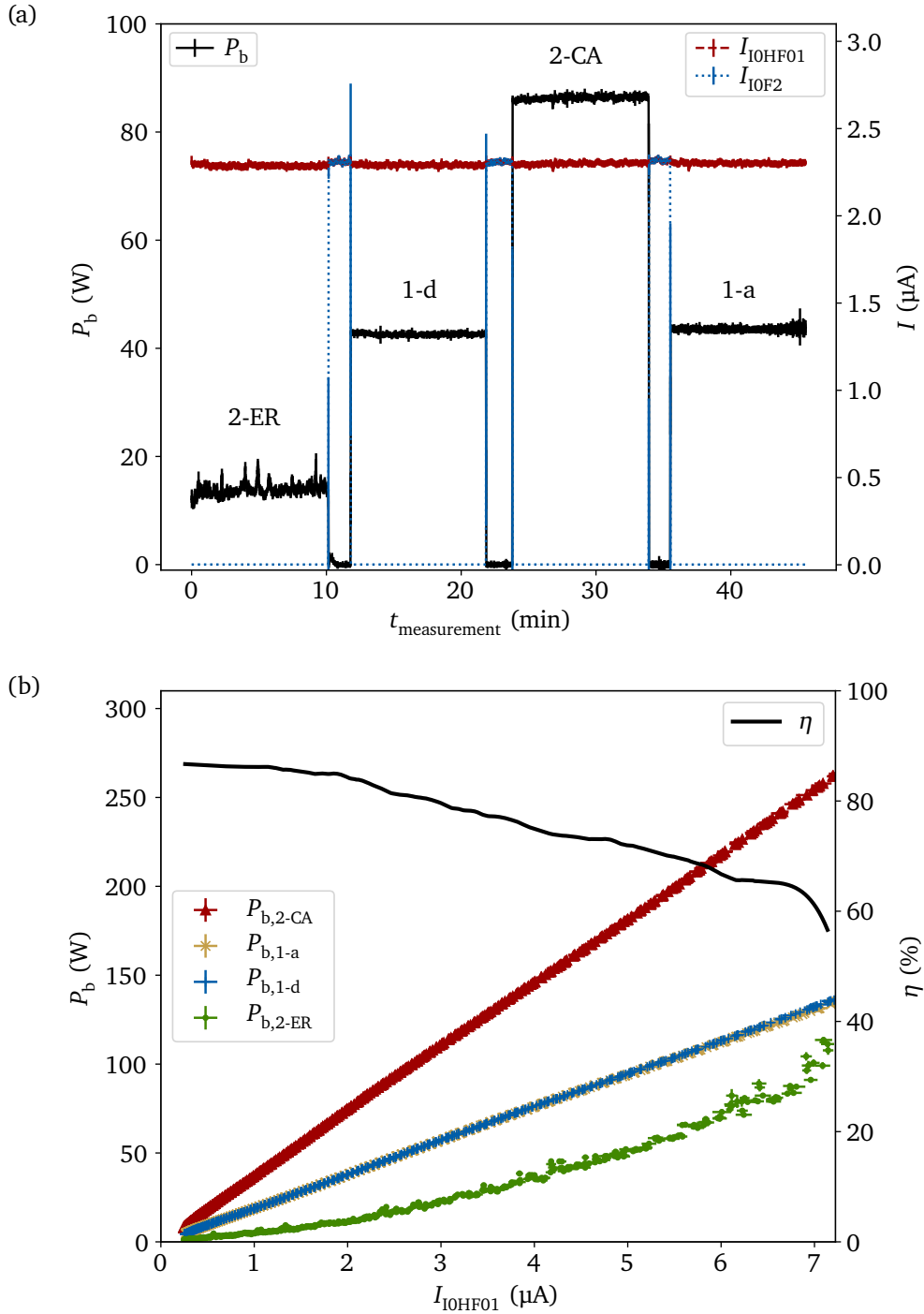


**Figure 4.8: Beam loading of the main LINAC per operation mode.** (a) For an initial beam current  $I$  of approx. 2.3  $\mu\text{A}$ , the beam loading  $P_b$  was measured for 10 min in each operation mode: the beam loading was first measured in the 2-ER mode, followed by beam-loading measurements in the intermediate operation modes set via iterative detuning. During a detuning, the beam was blocked at the Faraday cup IOF2. The value  $I$  was measured destructively using the Faraday cup IOF2 as well as non-destructively using the cavity monitor IOHF01. Values for  $I_{\text{IOF2}}$  are only valid when the beam is blocked at IOF2. (b) For a set operation mode, the initial beam current  $I$  was ramped up. Here,  $I$  was only measured using IOHF01. For a given  $I_{10HF01}$ ,  $P_{b,1-a}$  and  $P_{b,1-d}$  are almost equal. The energy-recovery efficiency  $\eta$  is decreasing as a function of  $I_{10HF01}$  as the proportion of lost electrons increased for higher initial beam currents. (a)–(b) Figure first published in Ref. [114] in a modified form. Reproduced with permission from Springer Nature. All rights reserved.

---

dumping is too high (under the condition that it is aimed for  $P_{b,2-ER} = 0$  <sup>(16)</sup>). It does not mean that the electrons are decelerated appropriately and accelerated too much, because in that case, the electrons would not arrive at the main LINAC twice for double deceleration due to the small momentum acceptance. Vice versa, in the case of  $P_{b,2-ER} < 0$ , the electrons were decelerated too much and thus the final momentum prior to beam dumping is too low (under the condition that it is aimed for  $P_{b,2-ER} = 0$ ). These relations have to be taken into account when interpreting the non-zero values for  $P_{b,2-ER}$ :

During the beam tuning with a temporarily increased initial beam current in the order of 100 nA, it was possible to make the twice decelerated beam visible on the screen ROT1 located in the dispersive section R of the low-energy beam-dump ROF1. That verified an adequate deceleration of the beam centroid. Here, the beam was strongly broadened and only a few percent of the initial beam current were detectable at ROF1. However, this setup of the machine did not enable a stable operation. For this reason, magnets had to be slightly retuned, which led to a vertically-kicked twice-decelerated beam downstream of the main LINAC in the final setting as can be seen in Fig. 4.7. Due to this kick, the beam was lost in the beampipe between A1H2 and ROT1, and consequently the beam was no longer detectable at ROT1 and ROF1, respectively. Since the beam was detected at ROT1 and ROF1, respectively, in a magnet setup only differing slightly, the main-LINAC setup can be considered as appropriate with respect to momentum gain and reduction via acceleration and deceleration. Therefore,  $P_{b,2-ER} \neq 0$  resulted due to particle losses: Electrons lost after the first deceleration consequently did not pass the main LINAC a fourth time, and thus a second deceleration in the main LINAC including corresponding energy recovery did not take place for those lost electrons. As a result, the otherwise recyclable portion of that unrecovered energy had to be provided externally in order to be able to accelerate a given amount of subsequent electrons per time.

By using beam-loss monitors, the second pass of the first recirculation beamline was identified as the origin of particle losses. The unavoidable particle losses arose because the challenge to find a transverse confinement for the superimposed beams in the first recirculation beamline remains, which in turn is due to the common recirculation transport and the associated fact that beam guiding elements influence two superimposed beams in the first recirculation beamline together with the circumstance how the quadrupole magnets for the transverse confinement were set (see section 4.2.4).

As can be seen in Fig. 4.8(b), an increased initial beam current led to a decreased energy-recovery efficiency. This was due to an increased proportion of electrons that were no longer within the acceptance, which in turn was a result of increasing transverse normalized emittances, bunch length and relative momentum spread downstream of the injector LINAC, as well as possibly more strongly excited HOMs, as a function of the initial beam current.

Apart from the particle losses, the 2-ER mode was realized successfully and it was possible

---

<sup>16</sup>There might be a case where a deceleration of the beam to a centroid particle momentum higher or lower than the one at injection is intentionally aimed for, respectively. In this study, however, the focus was on achieving a centroid particle momentum at the beam dump that is equal to the one at injection.

---

to quantify the energy-recovery efficiency. Here, the latter is primarily limited due to the particle losses; consequently, the energy-recovery efficiency can be increased if particle losses can be avoided.

## Beam Quantities

Besides the measurement of beam quantities in sections downstream of the injector LINAC as mentioned in section 4.2.2, beam quantities were measured for the tuning beam current of approx. 1 nA at the following locations: Using the last cavity of the main LINAC (A1SC08) for the RF zero-crossing method, an upper-limit bunch-length of  $\hat{\sigma}_t = (0.39 \pm 0.04)$  ps at the first pass of the second-to-last cavity of the main LINAC (A1SC07) was determined. An upper-limit relative-momentum-spread of  $\hat{\sigma}_\delta = (6 \pm 1) \cdot 10^{-4}$  and  $\hat{\sigma}_\delta = (5 \pm 1) \cdot 10^{-4}$  was determined at the corresponding first screen located in the first arc of the first and the second recirculation beamline (F0T1 and S0T1), respectively. The beam quantities have been measured after realizing the 2-ER mode but by using destructive methods, and thus not in the 2-ER mode itself but in a corresponding detuned operation mode.

To investigate whether there is a difference in beam-quantity values when operating in the 2-CA or the 2-ER mode, and thus to investigate whether there is an influence due to energy recovery, a non-destructive measurement is necessary. Within the scope of this work, wire scanners (S0WS01 and S1WS01) as quasi-non-destructive diagnostic devices were constructed and used to measure beam quantities in both the 2-CA and the 2-ER mode. Further details are given in chapter 5.

### 4.2.6 Energy Saving Aspects

There are several power components needed to operate the S-DALINAC: RF power necessary to maintain the field inside the main LINAC even during an energy-recovery operation, power required to accelerate the beam until the exit of the injector LINAC that cannot be recovered (and thus cannot be recycled) at the S-DALINAC, power needed to cool devices especially the RF structures to maintain the superconducting state, power required to operate magnets for beam guidance, and power necessary for the remaining infrastructure not mentioned. The demands on most of these power components are essentially equal for the 2-CA and the 2-ER mode if the beam properties remain unchanged; the difference in power requirements between these two operation modes is the following: On the one hand, the wall-plug power required for the RF amplifiers and the corresponding cooling is reduced when operating in the 2-ER mode compared to operating in the 2-CA mode. Furthermore, the dipole magnet S1BM01 and a downstream located quadrupole magnet (S3QU01) have not to be powered and cooled. Additionally, dumping a low-power beam at R0F1 needs less cooling of the beam dump compared to dumping a high-power beam at S3F1. All together, the required power is reduced in the order of kilowatts. On the other hand, the beam does not need to be guided back to the main LINAC after the second acceleration when operating in the 2-CA mode, that is, the second arc of the second recirculation beamline (S2) has

---

not to be powered in this operation mode. Consequently, power in the order of kilowatts for the magnets of S2 and the corresponding cooling is not necessary when operating in the 2-CA mode – in contrast to operating in the 2-ER mode. The overall power needed to operate the S-DALINAC depends primarily on the involved sections (compare Fig. 2.3) and the experiment, and is in the most cases between 0.5 MW and 1 MW. These power values have to be taken into account when addressing energy saving.

At the S-DALINAC, first beams were provided in 1987 and full operation started by the end of 1990 [19]. Although it was taken into consideration to operate the S-DALINAC in an energy-recovery mode at the time of the past FEL operation, the idea was not pursued further, partly because BBU already occurred for a beam current after chopping of some microamperes [120]. An energy-recovery operation was not possible until the retrofits in 2015/2016 (one-turn and two-turn energy-recovery mode) [121] and 2023 (three-turn energy-recovery mode) [122]. The main purpose for the retrofits was to provide the possibility to study the energy-recovery modes. Here, the recovery process in the cavities as well as beam-dynamics behavior during energy-recovery operation are of interest. Since the maximum possible (virtual) beam power at the S-DALINAC is only a small fraction of the overall power requirement for the entire machine (a high beam power is not intended here due to the specifications of the corresponding experiments), energy saving *during operation* of the very machine in an energy-recovery mode is insignificant. The potential for energy saving *during operation* becomes recognizable if the saved power due to energy recycling while operating in an energy-recovery mode predominates the other power components necessary to operate the entire facility, as discussed in section 1.4.

However, there is potential for substantial energy saving at the S-DALINAC: Even if the power requirement *during operation* cannot be reduced significantly, the energy-recovery mode can enable a reduction of the necessary *operation time* for a given experiment. Regarding a certain external RF power available for acceleration in the main LINAC, the beam current at the experiment could in principle be increased by the factor  $1/(1 - \eta)$  when operating in an energy-recovery mode compared to the maximum beam current available in the corresponding conventional acceleration mode. Thus, the necessary operation time for a given experiment can be reduced if both a higher beam current is supported by the entire machine and a higher beam current can be suitably utilized in the experiment. Here, technical limits of the S-DALINAC are (i) the maximum beam current supported by the gun, (ii) the external RF power that is available for and can be coupled into the injector LINAC, and (iii) a certain BBU threshold current. Furthermore, particle losses must be avoided and appropriate radiation protection conditions must be created so that possible higher beam currents could be permitted.

### 4.3 Three-Turn Energy-Recovery Mode

There is the potential for a 3-ER mode at the S-DALINAC due to the already existing third recirculation beamline (T section). However, before that operation mode could be realized,

further machine modifications would be necessary, which are not within the scope of this work. Here, the goal is only to examine whether such an operation mode is possible in principle and whether an upgrade could be worthwhile, which – if applicable – could form a basis for following projects.

To realize a 3-ER mode, similar steps as described in section 4.2 are necessary. It should be emphasized that in this operation mode, there are superimposed beams in the second recirculation beamline as well. Therefore, non-destructive diagnostic devices are also required in that section. Another essential machine modification is an upgrade of the path length adjustment system in the third recirculation beamline (T2PL01), which originally supported only the three-turn conventional acceleration mode; that upgrade has been conducted during a maintenance phase in 2023 [122]. Before a possible beamtime for a 3-ER mode can be considered, particle losses as mentioned above have to be avoided.

Here, the focus is on a theoretical examination of a possible realization only. Some parts of the content presented in this section have already been published in Refs. [123, 124].

### 4.3.1 Objectives and Degrees of Freedom

In the case of the 3-ER mode, there is common recirculation transport as well. Here, on the one hand, the number of objectives increases compared to the 2-ER mode: There are six instead of four main-LINAC passes, and thus the number of design momenta that have to be achieved after passing the main-LINAC increases. Transverse confinement has to be ensured for a longer beamline in which some of the focusing elements now influence an increased amount of superimposed beams: there are six instead of four superimposed beams in the main-LINAC section, and two superimposed beams instead of a single beam in the second recirculation beamline. As a further consequence of the higher number of superimposed beams in the main-LINAC section, a beam centered to the design orbit with small beam envelopes has to be reached more often to mitigate BBU. In addition, the BBU threshold current may be lower since – for a given initial beam current – the cumulative beam current in the main LINAC is 50 % higher when operating in the 3-ER mode compared to operating in the 2-ER mode. On the other hand, due to the use of the third recirculation beamline, further degrees of freedom are available, namely a path length adjustment system (T2PL01), a longitudinal dispersion ( $R_{56,T}$ ) and seven<sup>17</sup> quadrupole magnets for focusing. Therefore, the index sets are expanded as follows:  $i \in \{1, \dots, 6\}$ ,  $m \in \{F, S, T\}$ ,  $n \in \{I, F, S, T\}$ . The corresponding target momenta  $p_{0,i}$  following from the design values for each section (see Table 4.1) are listed in Table B.1.

---

<sup>17</sup>Only the quadrupole magnets located in the straight of the third recirculation beamline (T1) are additional degrees of freedom to find a transverse confinement since the quadrupole magnets in the arcs of the third recirculation beamline (T0 and T2) are used to set  $R_{16,T0} = R_{26,T0} = R_{16,T2} = R_{26,T2} = 0$  and the individual value of  $R_{56,T}$  that results from beam-dynamics simulations (see section 4.3.2).

### 4.3.2 Beam-Dynamics Simulations

For the simulations of the 3-ER mode, the same starting conditions as mentioned in section 4.2.2 were assumed. Objectives and degrees of freedom are listed in Table B.1. The corresponding 2D optimization problem without taking the relative momentum spread into account can be formulated concisely<sup>18</sup> as follows:

$$\begin{aligned} & \min \sum_{i=1}^6 f \left( \bar{p}_i \left( \hat{\mathcal{E}}_{z,A1SC01,peak}, \dots, \hat{\mathcal{E}}_{z,A1SC08,peak}, \hat{\phi}_{A1SC01}, \dots, \hat{\phi}_{A1SC08}, L_F, L_S, L_T \right), p_{0,i}, \tau_{3-ER} \right) \\ & \text{subject to } \left( \hat{\mathcal{E}}_{z,A1SC01,peak}, \dots, \hat{\mathcal{E}}_{z,A1SC08,peak}, \hat{\phi}_{A1SC01}, \dots, \hat{\phi}_{A1SC08}, L_F, L_S, L_T \right) \in \mathcal{M}_3 \end{aligned} \quad (4.10)$$

with the corresponding bounded set  $\mathcal{M}_3$  and the corresponding aimed precision  $\tau_{3-ER}$ . The simulation led to an intermediate solution of the above given optimization problem, that is, a tuple of  $(\hat{\mathcal{E}}_{z,A1SC01,peak}, \dots, \hat{\mathcal{E}}_{z,A1SC08,peak}, \hat{\phi}_{A1SC01}, \dots, \hat{\phi}_{A1SC08}, L_F, L_S, L_T)$ , with the behavior for  $\bar{p}$  shown in Fig. 4.9.

Keeping that found tuple fixed, the parameters for the first-order longitudinal dispersion have been used as degrees of freedom within their technical limits (see Table B.1) to optimize the relative momentum spread. The focus was again on an overall small relative momentum spread  $\sigma_\delta(s)$  to keep the beam within the acceptance, an almost symmetric behavior of  $\sigma_\delta(s)$ , and an ideally low value for  $\sigma_\delta$  at the location of a potential experiment, that is, after the last acceleration and prior to the first deceleration. After several tuples  $(R_{56,I}, R_{56,F}, R_{56,S}, R_{56,T})$  have been found<sup>19</sup>, the most suitable tuple was selected (according to the same criteria as described in section 4.2.2) and fixed, and the tuple  $(\hat{\mathcal{E}}_{z,A1SC01,peak}, \dots, \hat{\mathcal{E}}_{z,A1SC08,peak}, \hat{\phi}_{A1SC01}, \dots, \hat{\phi}_{A1SC08}, L_F, L_S, L_T)$  has again been varied starting from the previously found solution in order to again ensure centroid momenta within the precision  $\tau_{3-ER}$  – necessary, since varied  $R_{56,n}$  values slightly influence  $\bar{p}(s)$  as mentioned. That led to the results for the longitudinal degrees of freedom listed in Table B.1 and the behavior of the relative momentum spread and the bunch length shown in Fig. 4.9, as well as the shape of the longitudinal phase space shown in Fig. 4.10. Here, it can be seen that the centroid momenta are achieved as desired while the relative momentum spread has an adequate behavior along the accelerator (overall within the acceptance, almost symmetric, and small after maximum acceleration). Although the main focus was not on the bunch structure itself, the bunch performs an almost 180° rotation in the longitudinal phase space along the travel from behind the injector LINAC to the location of maximum energy; hence, the absolute momentum spread is minimum similar to the case behind the injector LINAC, while the bunch length is almost maximum. Furthermore, due to the small relative momentum spread after maximum acceleration,  $R_{56,T}$  has hardly any impact in this setting. A 180°

<sup>18</sup>Note:  $\bar{p}_1$  does not depend on  $L_F, L_S$  and  $L_T$ ;  $\bar{p}_2$  does not depend on  $L_S$  and  $L_T$ ; and  $\bar{p}_3$  does not depend on  $L_T$ .

<sup>19</sup>Here, several suitable tuples were found. However, if no suitable tuple would result from the simulations, solving the optimization problem (4.10) had to be repeated but for other starting conditions (since the used algorithm is deterministic).

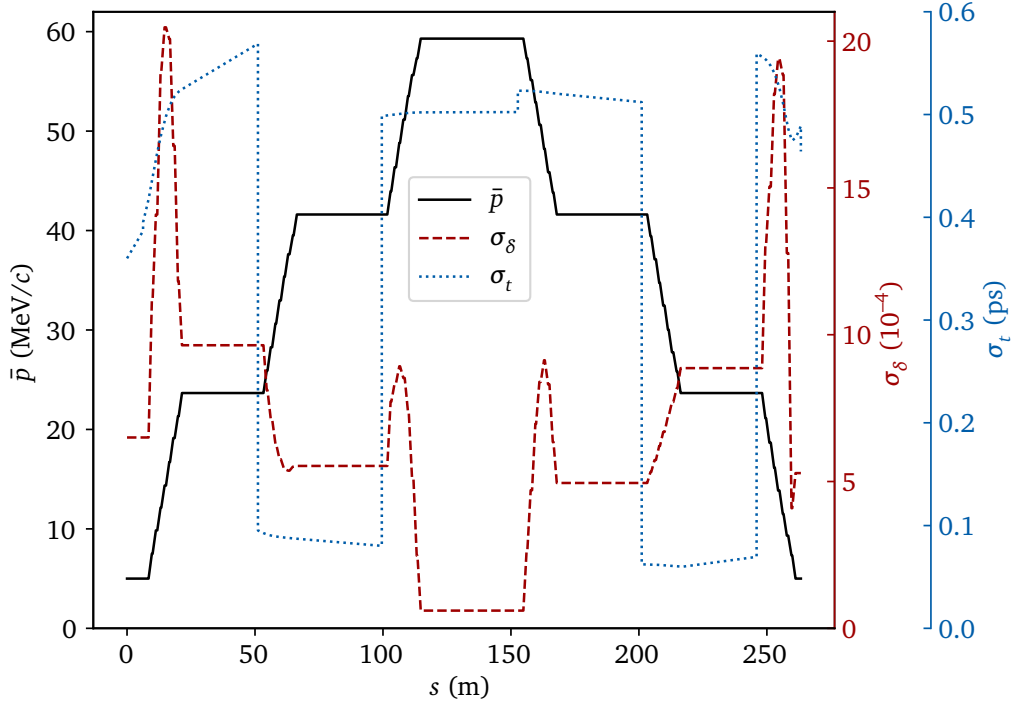


**Figure 4.9: Simulated longitudinal quantities for the 3-ER mode.** The figure shows the centroid momentum  $\bar{p}$ , the relative momentum spread  $\sigma_\delta$  and the bunch length  $\sigma_t$  as a function of the location  $s$ ; the simulation started behind the injector LINAC. The bunch length is changing due to different speeds of the electrons and due to different path lengths of the electrons caused by the longitudinal dispersion. While all these quantities are continuous functions in reality, the longitudinal dispersion is implemented here by step functions, that is, by elements of zero length at the end of the corresponding sections; this leads to jump discontinuities for  $\sigma_t$ . However, since space-charge effects and influences due to synchrotron radiation are disabled,  $\sigma_t$  is correctly evaluated in the main-LINAC section. Thus, the results for  $\bar{p}$  and  $\sigma_\delta$  are valid for the entire tracking since they are only changing inside the main LINAC. Figure first published in Refs. [123, 124] in a modified form.

rotation in the longitudinal phase space is possible due to the increased number of possible iterative shearings in this phase space compared to the case of the 2-ER mode.

The values for  $\tau_{2\text{-ER}}$  and  $\tau_{3\text{-ER}}$  should be set as small as possible to achieve high precision. In the case of the 2-ER mode,  $\tau_{2\text{-ER}} = 1$  eV/c applies, compared to  $\tau_{3\text{-ER}} = 630$  eV/c in the case of the 3-ER mode: due to the increased turn number in the latter case, the number of objectives increases by two (“reach  $p_{0,5}$  and  $p_{0,6}$ ”), while the number of degrees of freedom to achieve the objectives “reach  $p_{0,i}$ ” increases only by one<sup>20</sup> ( $L_T$ ), which is why the minimum possible value for  $\tau_{3\text{-ER}}$  is greater than the minimum possible value for  $\tau_{2\text{-ER}}$ .

Based on the presented 2D solution, 6D simulations have been conducted. The simulations led to the solution shown in Fig. 4.11. Similar to the 2-ER mode, the beam envelopes are

<sup>20</sup>The parameter  $L_T$  is the only additional degree of freedom concerning the objectives “reach  $p_{0,i}$ ”: Even if the additional parameter  $R_{56,T}$  influences the bunch length in section T and in this way the momentum (mostly the momentum spread but also slightly the centroid momentum as mentioned) in main-LINAC passes further downstream,  $R_{56,T}$  is no degree of freedom in those steps of the simulations in which it is optimized on reaching the target momenta for the bunch centroid after each main-LINAC pass.



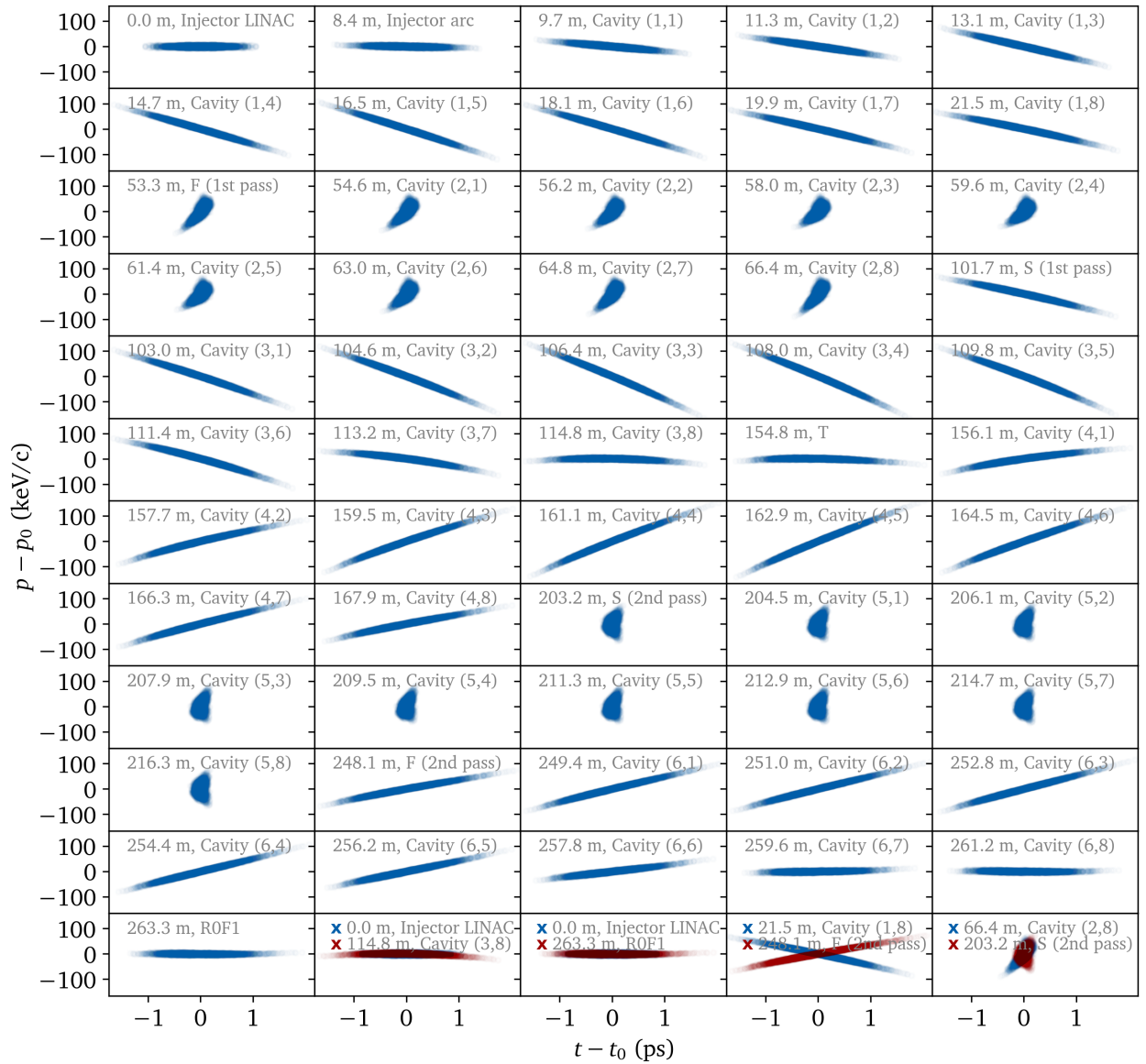


**Figure 4.10: Simulated longitudinal phase space for the 3-ER mode.** Each panel shows the phase space  $(t-t_0, p-p_0)$  present at the given location  $s$ ; the simulation started behind the injector LINAC. Additionally, a description of the last passed section leading to the shown phase space is given. Here, “Cavity ( $i,h$ )” indicates the main-LINAC cavity with name ending “ $h$ ” (“A1SC0 $h$ ”) during main-LINAC pass  $i$ . The corresponding recirculation through the first (F), second (S) or third (T) recirculation beamline, respectively, starts and ends directly in front of the first cavity of the main LINAC. In the last four panels, phase space shapes present at selected locations are compared with each other.

---

small during all main-LINAC passes while they increase strongly during the final deflection toward ROF1. No experiment was considered here, and thus a small beam spot after maximum acceleration was no objective. Similar to the simulations for the 2-ER mode, impacts due to space-charge effects and synchrotron radiation were disabled here since they are insignificant for a beam current of 1 nA and the present electron energies, and thus including these effects would unnecessarily have increased the simulation time significantly. Their impact in the case of higher beam currents is discussed in appendix D.

### 4.3.3 Conclusion

Based on the results shown, it can be concluded that the 3-ER mode is in principle possible at the S-DALINAC. However, the presented solution for this operation mode has to be improved since the largest  $|\hat{\phi}_j|$  is  $24.4^\circ$  (compared to  $13.2^\circ$  in the case of the 2-ER mode, see Table B.1), which leads to a distinct off-crest acceleration and thus to a strong transformation in the longitudinal phase space. Furthermore, largest and smallest  $\hat{\mathcal{E}}_{z,j,\text{peak}}$  differ by approx. 15 % in this operation mode (compared to approx. 2 % in the case of the 2-ER mode, see Table B.1). It is desirable to limit all  $\hat{\phi}_j$  to a certain range and to force the pairwise deviations of the  $\hat{\mathcal{E}}_{z,j,\text{peak}}$  values not to exceed a certain value, which requires a corresponding improvement of the simulations tailored to the individual specifications. Finally, the lattice has to be revised to provide a better solution for the transverse confinement.

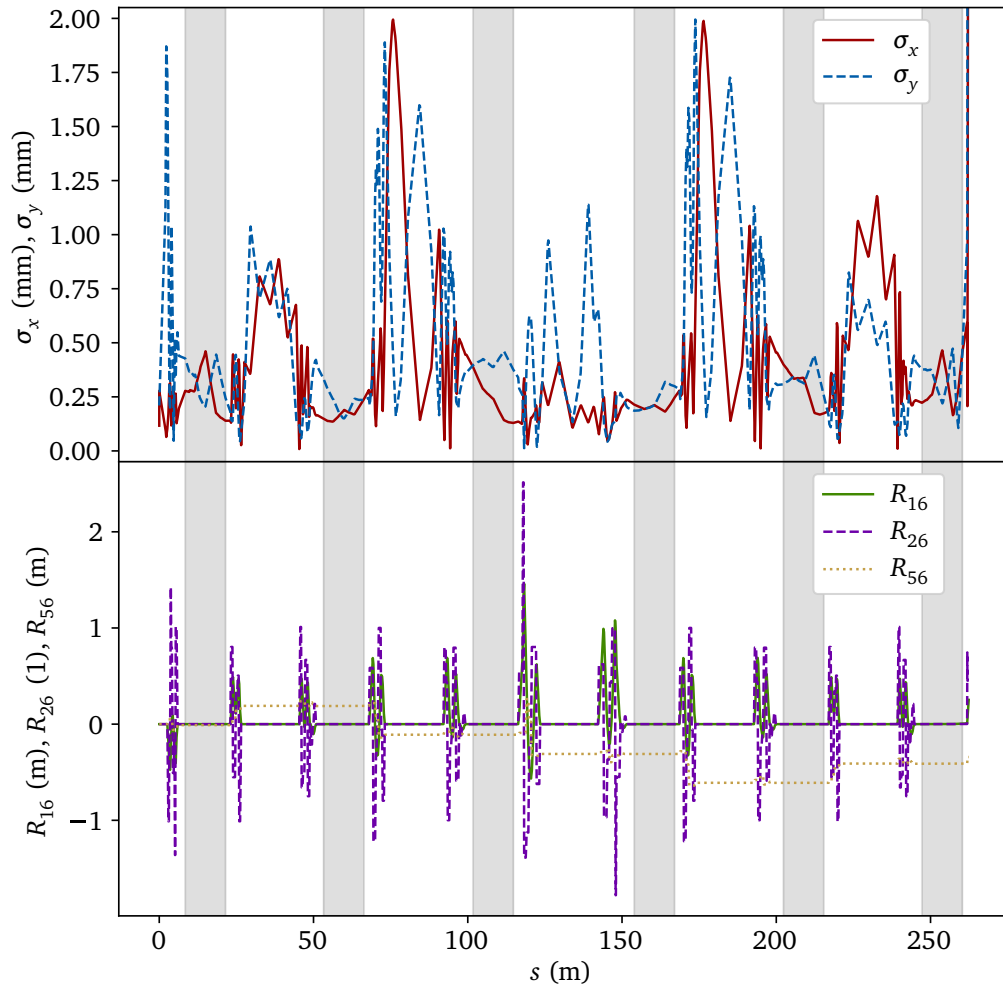


**Figure 4.11: Simulated beam envelopes and dispersion terms for the 3-ER mode.** The figure shows the beam envelopes  $\sigma_x$  and  $\sigma_y$  as well as the first-order dispersion terms  $R_{i6,0 \rightarrow s}$  as a function of the location  $s$ ; the simulation started behind the injector LINAC. Values for the beam envelopes are  $\sigma_{x,y} \leq 0.5$  mm inside the cavities (each gray zone indicates a main-LINAC pass, that is, it indicates a pass through the section that begins at the entrance of the first cavity of the main LINAC and ends at the exit of the last cavity of the main LINAC) and  $\sigma_{x,y} \leq 2.0$  mm everywhere until the last main-LINAC pass. Downstream, the beam envelopes increase strongly toward the beam dump following after a  $125^\circ$ -bend with a bending radius of 41 mm.



---

## 5 Measurement of Beam Quantities in Energy-Recovery Modes

As mentioned in sections 4.2.3 and 4.2.5, a non-destructive diagnostic device is required to determine beam properties in energy-recovery modes: if a destructive diagnostic device is used, the energy-recovery process is interrupted (apart from using it in the R section).

A goal of this work is to compare the 2-CA and the 2-ER mode: Since during an energy-recovery operation a decelerated beam influences the electromagnetic field inside a cavity and may excite or attenuate HOMs, respectively, the electromagnetic field passed by a beam to be accelerated when operating in an energy-recovery mode may differ from the electromagnetic field passed by a beam to be accelerated when operating in the corresponding conventional mode. Thus, the beam properties after maximum acceleration may differ in both operation modes. Therefore, a possible influence of the energy-recovery process on the quantities (especially on the relative momentum spread  $\sigma_\delta$ ) of the beam in the second recirculation beamline shall be investigated; the beam properties present in this beamline are of great interest since it is the beamline with the maximum electron energy in the 2-ER mode and thus the section for a potential experiment.

A first approach of the content presented in this chapter has already been partially published in Ref. [125].

### 5.1 Choice of the Diagnostic Device

Whether a method is suitable for a non-destructive measurement depends on the beam quantities and their possible values. For the determination of the momentum spread in the second recirculation beamline, (i) a synchrotron radiation monitor, (ii) a wire scanner or (iii) an LCB source can in principle be used:

- (i) If an accelerator is designed to use bending magnets in the section where beam quantities shall be measured (like in a recirculating machine), synchrotron radiation inevitably occurs during beam deflection (see section 3.8.3). The synchrotron radiation provides information on transverse and longitudinal bunch quantities [126–128], especially on the transverse beam profile. Since the synchrotron radiation occurs during deflection, it is emitted in sections of variable transverse dispersion in the corresponding deflecting plane. In this way, the detected transverse beam profile in a dispersive section provides information on the relative momentum spread (see relation (3.55)).

---

As mentioned above, synchrotron radiation inevitably occurs in a recirculating machine, and thus no further influence on the beam is necessary, that is, a completely undisturbed comparison of the 2-CA and the 2-ER mode is possible. However, utilizing the synchrotron radiation would require a suitable design of the corresponding dipole magnet and its vacuum chamber; here, an exit window would be required, which is not available in the current setup of the second recirculation beamline, and thus an expensive upgrade would be necessary (without taking into account the costs for the optical equipment needed to analyze the synchrotron radiation). Due to the low electron energy and the given bending radius of the eligible dipole magnets in the second recirculation beamline, the emitted radiation is mainly in the infrared region (critical wave length  $\lambda_c = 2\pi c/\omega_c = 2.9 \mu\text{m}$ ). Depending on (i) the camera used to detect the synchrotron radiation, and (ii) the beam current, which is rather low at the S-DALINAC, a large exposure time may be necessary.

- (ii) Using a wire scanner slightly influences the electron beam: Here, a thin wire crosses the electron beam and thus interacts with a small fraction of the beam, while the vast majority of the electrons remain undisturbed – if the area of the beam profile covered by the wire is significantly smaller than the total area of the beam profile to be measured. The collision of an electron beam with a wire moving at a constant speed produces a shower of primary scattered electrons and secondary emitted particles (photons and electrons) whose intensity is proportional to the fraction of the beam sampled by the wire [129]. A fraction of that radiation shower can be detected by a beam-loss monitor located outside of the beampipe [66, 67] such as a Cherenkov or a scintillation detector [130], and if the detected amount of radiation is synchronized to the wire position, the projection of the transverse beam profile can be determined. If the wire scanner is located in a dispersive section, the detected projected beam profile provides information on the relative momentum spread (see relation (3.55)). Thus, a measurement of only the *projected* beam profile is sufficient to determine the relative momentum spread, even if the projected beam profile contains less information than the entire beam profile.

If the vast majority of the electrons remain undisturbed when using a wire scanner in the second recirculation beamline, and thus if the vast majority of the electrons remain involved in the energy-recovery process occurring downstream, the energy-recovery process itself remains almost undisturbed. For this reason, the partly destructive wire scanner can be considered as a quasi–non-destructive diagnostic device – if the part of the area of the beam profile covered by the wire is only a small fraction of the entire area of the beam profile – and thus enables a quasi-undisturbed comparison of the 2-CA and the 2-ER mode.

- (iii) In an LCB source, a laser beam is collided (head-on) with an electron beam, leading to scattered energy-boosted photons forming a quasi-monochromatic X-ray to gamma-ray beam [122]. Due to a small cross section, only a small fraction of the electron

---

beam interacts with the laser beam, and if the energy of an incident laser photon is much lower than the rest energy of a hit electron, then the recoil on the electron is negligible. The X-ray or gamma-ray beam, respectively, provides information on the relative momentum spread of the electron beam, which can be determined from the very detected radiation spectrum [131]; thus, a determination of the momentum spread does not require the electron beam to be in a dispersive section.

If the influence on the electrons is minor, this diagnostic technique is quasi-non-destructive. Similar to a synchrotron radiation monitor, utilizing the radiation to investigate properties of the electron beam requires an almost undisturbed propagation to a detector, which is not possible in the second recirculation beamline without a cost-intensive replacement/upgrade of an existing dipole magnet and the corresponding vacuum chamber. In addition, the LCB source itself is quite expensive compared to the equipment needed for the other two measurement methods presented.

A diagnostic device to measure the beam quantities of interest for each possible beam current at the S-DALINAC is desirable, while the measurement time should ideally be short and independent of the beam current. Due to the beam properties and the existing infrastructure of the second recirculation beamline, determination of the relative momentum spread using a wire scanner is much more reasonable than using one of the other two methods presented because the focus is on short measurement times and cost efficiency; thus, a wire scanner is the favored diagnostic device to be used in this work. Investigating the electron beam using an LCB source located in the third recirculation beamline, where it is more reasonable due to the design of the installed dipole magnets and the corresponding vacuum chambers, is part of the work of Refs. [122, 132] and may thus take place during a potential 3-ER mode beamtime.

## 5.2 Locations of the Wire Scanners

Since a wire-scanner based measurement is intended, non-zero transverse dispersion is necessary to investigate the relative momentum spread of the electron beam in the second recirculation beamline. The requirement of non-zero transverse dispersion limits the number of possible locations: non-zero transverse dispersion occurs only in the arcs of the second recirculation beamline (S0 and S2) and in the magnetic chicane<sup>1</sup>. Placing the wire scanner in the magnetic chicane is not an option: apart from the facts that there is hardly any space for an installation and no possibility to influence the dispersion (whose absolute value is rather small in this section) because there is no quadrupole magnet available, there are three<sup>2</sup> beams in the magnetic chicane when operating in the 2-ER mode: the beam traveling

---

<sup>1</sup>The magnetic chicane is located downstream of each recirculation beamline and consists of four dipole magnets: the last three dipole magnets of section F3 and the last dipole magnet of section I3 (see Fig. 2.1).

<sup>2</sup>The beam traveling in the injector arc is irrelevant here since it only passes the last dipole magnet of the magnetic chicane.

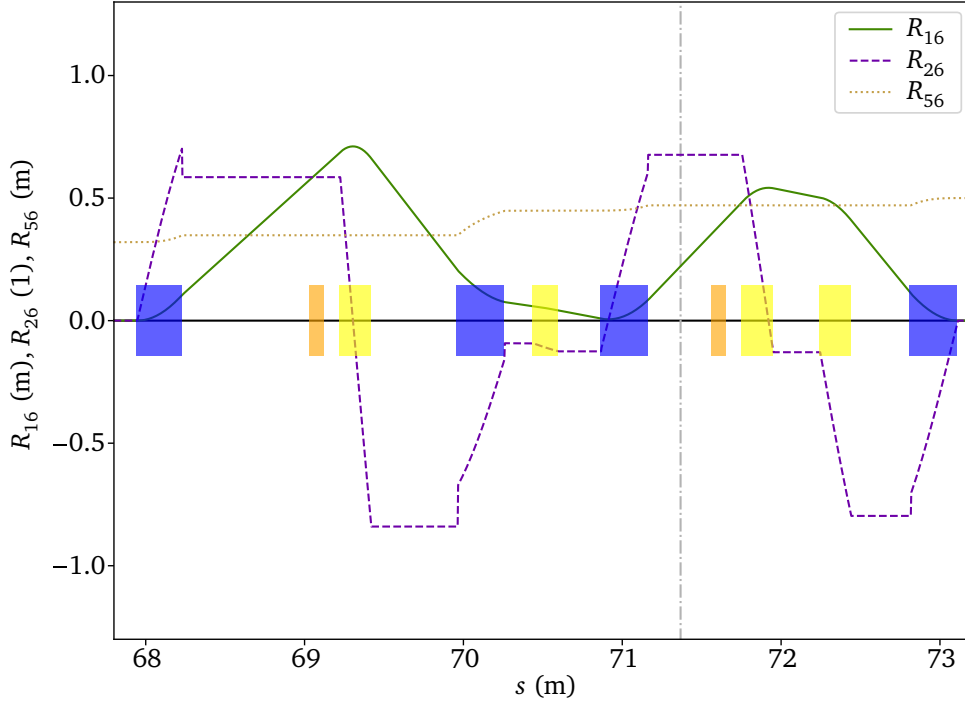


**Figure 5.1: Wire scanner SOWS01 located in a horizontal dispersive section.** Detailed view of the first-order dispersion terms  $R_{i6,0 \rightarrow s}$  from Fig. 4.5 with focus on the first arc of the second recirculation beamline, S0. The location of the center of the wire scanner SOWS01 is highlighted (grey dashdotted). While a large value for  $|R_{16}|$  is preferred at the location of SOWS01, it is limited by the target relations  $R_{16,S0} = R_{26,S0} = 0$  and  $R_{56,S0} = 0.18$  m (note:  $0.18$  m =  $0.50$  m -  $0.32$  m =  $0.50$  m -  $(-0.01$  m +  $0.33$  m) =  $0.50$  m -  $(R_{56,I} + R_{56,F})$ ). Shown beam guiding elements are dipole magnets (blue), quadrupole magnets (yellow) and sextupole magnets (orange).

in the second recirculation beamline and the two beams traveling in the first recirculation beamline; although a wire scanner could in principle be used in that case, the goal here is to investigate the beam passing the second recirculation beamline with the least possible impact on the beam. Finally, because the momentum acceptance is smaller from A1SC08 to S2 than from A1SC08 to S0 (A1SC08 is used to change the momentum to measure dispersion values), S0 is the most appropriate section for an installation of the wire scanner. Consequently, the wire scanner to be constructed is named SOWS01.

As explained in section 3.6, a large  $|R_{16}|$  is preferred at the location of SOWS01 if the squared intrinsic horizontal beam envelope,  $\epsilon_x \tilde{\beta}_x$ , cannot be determined: if  $|R_{16}|$  is large, then  $\hat{\sigma}_\delta$  is closer to  $\sigma_\delta$ . Limiting conditions for the realization of a large  $|R_{16}|$  are:  $R_{16,S0} = R_{26,S0} = 0$  has to be ensured as well as  $R_{56,S} = 0.18$  m has to be realized as determined in section 4.2.2. Because  $R_{56,S} = R_{56,S0} + R_{56,S2} + R_{56,S\text{-chicane}}$  applies,  $R_{56,S0}$  has to be realized depending on the available values for  $R_{56,S2}$ , which in turn limits available values for  $R_{16}$  at the location of the wire scanner; the value  $R_{56,S\text{-chicane}}$  originated from



passing the magnetic chicane is constant<sup>3</sup> since no quadrupole magnets are located within the magnetic chicane – thus, the value cannot be adjusted. The most suitable behavior in arc S0 results if  $R_{56,S2} + R_{56,S\text{-chicane}} = 0$  applies, which in turn results in  $R_{56,S0} = 0.18$  m. The wire scanner was installed in an already existing 6-way cross in S0 (see Fig. 2.2). As shown in Fig. 5.1,  $|R_{16}| = 0.22$  m follows at the location of the wire scanner if  $R_{16,S0} = R_{26,S0} = 0$  and  $R_{56,S0} = 0.18$  m are enforced. This value for  $|R_{16}|$  is approx. 46 % smaller than the one achieved in Ref. [125] where the limiting conditions concerning available values for  $R_{56,S0}$  and  $R_{56,S2}$  as well as  $R_{56,S} = R_{56,S0} + R_{56,S2} + R_{56,S\text{-chicane}} = 0.18$  m were not taken into account.

Due to the resulting smaller value for  $|R_{16}|$ , the squared intrinsic horizontal beam envelope shall be determined as well to provide more precise information on the relative momentum spread (see relation (3.55)). This requires another wire scanner at a dispersion-free location (see section 3.6). A possible region for the installation is the straight section of the second recirculation beamline, S1. Consequently, the second wire scanner to be constructed is named S1WS01 (see Fig. 2.2).

### 5.3 Design and Construction of the Measurement Systems

Wire scanners can in principle be designed to measure both the projected horizontal and the projected vertical beam profile by mounting two wires on a fork that is moving along an axis that is at an angle of  $45^\circ$  to both transverse planes [66,67]. In such a construction, the wire length is  $1/\cos(45^\circ) \approx 1.41$  times as long as in a construction utilizable to measure a single projected transverse beam profile only if the area to be detected shall be identical. During a measurement, the electron bombardment causes a thermal expansion of the wire. Here, a shorter wire length leads to a reduced wire deformation and thus to a reduced measurement uncertainty. Since the main application in this work is the investigation of the relative momentum spread, a measurement of only the projected horizontal beam profile (at a location with non-zero horizontal dispersion) is sufficient. Thus, wire scanners to measure only the projected horizontal beam profile are designed in order to benefit from smaller uncertainties.

Another influence on the measurement uncertainty is the wire diameter. In order to counteract the horizontal sagging of the vertically mounted wire resulting from the thermal expansion, a certain tensile force by the fork is desired. A higher tension is possible if the wire is mechanically more stable, which is the case for a thicker wire. Furthermore, the amount of secondary radiation increases if the electrons' path through the wire is longer, and thus the count rate at the beam-loss monitor increases; this supports the measurement of low beam currents. In order to keep the influence of deformation effects as low as possible, a circular profile is chosen for the wire. A suitable wire material is tungsten since (i) it has

---

<sup>3</sup>The value  $R_{56,m\text{-chicane}}$  is dependent on the associated design trajectory through the magnetic chicane, which in turn is predetermined depending on the recirculation beamline  $m$  that was passed immediately before.

a high melting point (3410 °C) necessary to withstand the electron bombardment, and (ii) the large atomic number (74) in combination with the high density (19300 kg/m<sup>3</sup>) supports a large signal-to-noise ratio at the beam-loss monitor [129]. A tungsten wire with a diameter  $\tilde{d} = (100 \pm 5) \mu\text{m}$  was used successfully at the S-DALINAC in previous measurements for electron energies of 22.5 MeV to 42.5 MeV and a beam current of approx. 100 nA [66]. In this work, the centroid kinetic energy is 41.10 MeV (centroid momentum of 41.61 MeV/c) at the locations of the wire scanners. Thus, the same wire diameter is used in this work, while the range of suitable beam currents will be determined experimentally. However, a finite wire diameter will lead to a measured profile that is broadened compared to the beam profile itself [133]: the measured profile  $\Lambda_m(x)$  is the result of the convolution of the projected beam profile  $\Lambda_b(x)$  and the wire profile

$$\Lambda_w(x) = \begin{cases} 2 \cdot \sqrt{\left(\frac{\tilde{d}}{2}\right)^2 - x^2}, & |x| \leq \frac{\tilde{d}}{2} \\ 0, & |x| > \frac{\tilde{d}}{2} \end{cases}, \quad (5.1)$$

that is,

$$\Lambda_m(x) = (\Lambda_b * \Lambda_w)(x) = \int_{-\infty}^{\infty} \Lambda_b(x') \Lambda_w(x - x') dx', \quad (5.2)$$

where Eq. (5.1) is given for a wire centered at  $x = 0$ . Consequently, a deconvolution is necessary to obtain  $\Lambda_b$  from  $\Lambda_m$ .

Additionally, two types of destructive screens are installed at the locations of the wire scanners, which enables the measurement of the horizontal and the vertical beam profile: A BeO-Au screen suitable for low beam currents and a Kapton-Al screen suitable for high beam currents (see section 2.2). The combination of a wire scanner and two screens is below addressed as a measurement system. The light emitted by a screen during electron bombardment is detected with a CCD camera. In a measurement system, however, only the wire scanner or a screen monitor can be used at a time.

The movement of each screen is pneumatically controlled and the movement of each wire is controlled by a corresponding linear actuator. The design of the measurement systems is based on designs from Refs. [63, 67, 134, 135].

As one measurement system is located in S0 and one measurement system is located in S1, the corresponding names are S0T2/S0R1/S0WS01 and S1T3/S1R1/S1WS01 to address the BeO-Au screen/Kapton-Al screen/wire scanner. A picture of the mounted measurement system S0T2/S0R1/S0WS01 and a sectional view of the corresponding computer-aided design (CAD), which was created using the CAD software NX [136], are shown in Fig. 5.2.

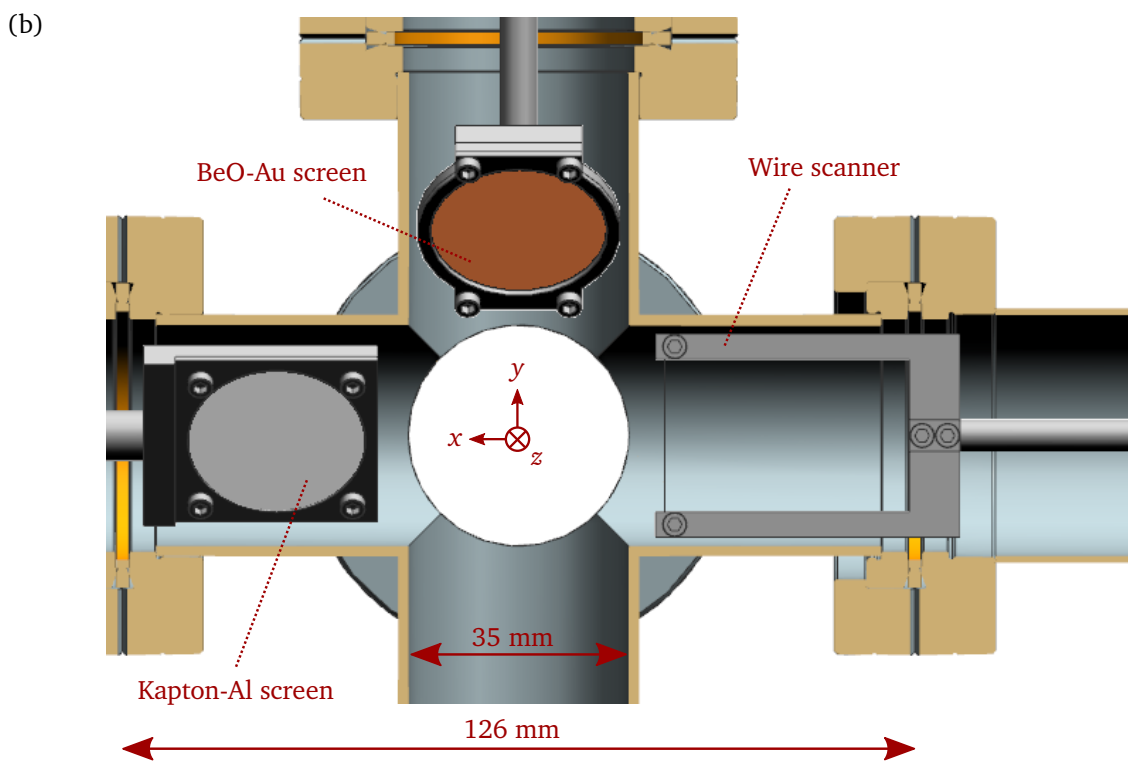
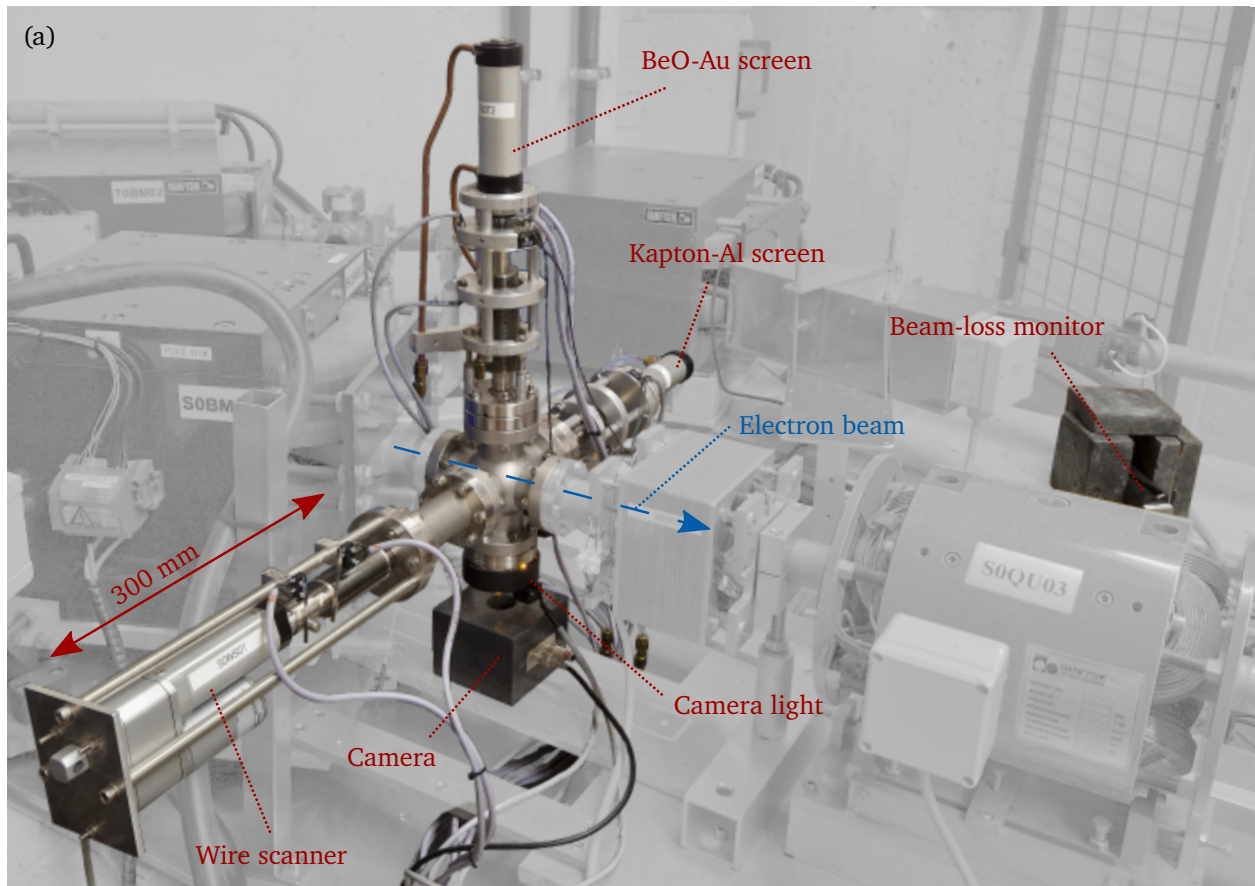


**Figure 5.2: Details on the measurement systems.** (a) Picture of the mounted measurement system S0T2/S0R1/S0WS01 in the S0 arc. (b) CAD view of the interior of the 6-way cross.

---

## 5.4 Measurement Results

In the following, results from the commissioning measurements as well as from the measurement during the beamtime of the 2-ER operation are presented.

### 5.4.1 Commissioning Measurements

During the commissioning of SOT2/SOR1/SOWS01 prior to the 2-ER mode beamtime, the beam was guided directly into the second recirculation beamline after a single main-LINAC pass with a centroid kinetic energy of 21.8 MeV. In order to compare all three diagnostic devices of the measurement system and in this way to calibrate the wire scanner, the initial beam current was set to approx. 30 nA in the first measurement, since this current value allows the detection of the beam on both screens in a sufficient way and thus to determine the transverse beam profile with both screens. Figure 5.3 shows the results of a single measurement, that is, a single picture taken per screen and a single wire-beam crossing. That figure shows the non-deconvolved projected transverse profile measured with the wire scanner. The screen pictures clearly show a difference in intensity based on the underlying physical effect (scintillation or optical transition radiation). The measurements were repeated several times for statistical reasons.

The data measured with the wire scanner show a periodic behavior in the count rate of the beam-loss monitor. Since the wire speed is known, the frequency of this periodic behavior was determinable by a Fourier transform and is approx. 50 Hz. The periodic behavior does not allow for deconvoluting the measured profile  $\Lambda_m$  itself reasonably; instead, a Gaussian distribution is fitted to the measured profile  $\Lambda_m$  and the very fitted distribution is deconvolved to obtain the projected beam profile  $\Lambda_p$ . However, due to the beam size present during the commissioning measurements and the relatively small wire diameter, the measured profile is only insignificantly broadened. Determined beam envelopes are listed in Table 5.1.

Finally, the initial beam current was increased to approx. 6.5  $\mu$ A, which was the maximum permitted initial beam current during the time of the commissioning measurements. For this beam current, the wire scanner was used without damaging the wire.

**Table 5.1: Beam envelopes during the commissioning measurements.** Determined horizontal beam envelopes  $\sigma_x$  at SOT2/SOR1/SOWS01 for a centroid kinetic energy of 21.8 MeV and an initial beam current of approx. 30 nA.

Device	$\sigma_x$ (mm)
BeO-Au screen (measured)	$1.70 \pm 0.04$
Kapton-Al screen (measured)	$1.30 \pm 0.03$
Wire scanner (measured)	$1.20 \pm 0.09$
Wire scanner (deconvolved)	$1.20 \pm 0.09$

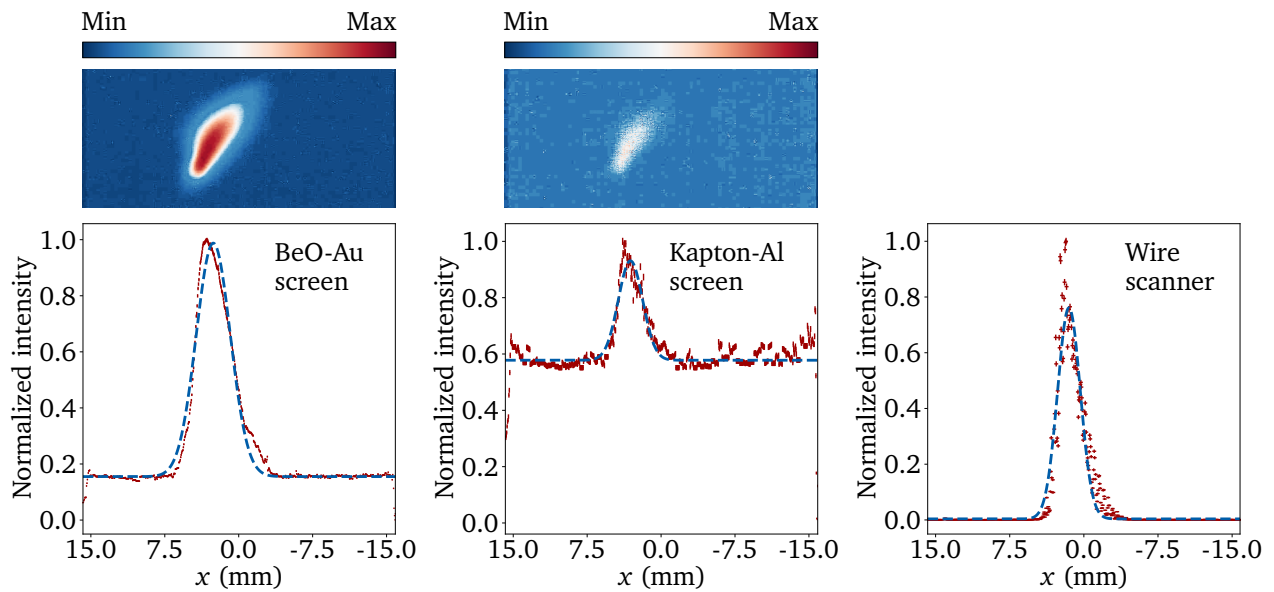


**Figure 5.3: Commissioning measurement for S0T2/S0R1/S0WS01.** The visualized data are obtained from a corresponding single measurement. (left) BeO-Au screen. (center) Kapton-Al screen. (right) Wire scanner. (top) Determined  $x$ - $y$ -profiles. (bottom) Determined projected horizontal profiles. A Gaussian distribution (blue dashed) is fitted to the intensities resulting from the measurements (red). The centroid kinetic energy was 21.8 MeV and the initial beam current was approx. 30 nA.

### 5.4.2 Comparison of Operating Voltages of the Linear Actuator

The detected periodic behavior in the wire scanner data could be the result of wire vibrations during the movement of the fork, which in turn could potentially be reduced by a speed reduction of the linear actuator [137]. To investigate this, the used linear actuator designed for 24 V operation was operated with various operating voltages in a later beamtime following the commissioning measurements. Here, the initial beam current was approx. 150 nA and the centroid kinetic energy was the target value of the 2-ER mode, that is, 41.10 MeV (momentum of 41.61 MeV/c).

The minimum operating voltage that supports a smooth movement of the linear actuator is 8 V. By operating with 8 V instead of 24 V, the speed is reduced to about a third and thus the number of data points per driving distance is increased by a factor of about three. When operating at 24 V, the driving speed is approx. 24 mm/s. Figure 5.4 shows measured projected beam profiles of single wire-beam crossings for three different operating voltages. The desired smoothing effect by a speed reduction as observed in Ref. [137] could not be achieved here. However, to benefit from an increased amount of data, both wire scanners were operated with 8 V in all below presented measurements.

In a further study, pictures of the Kapton-Al screen have been taken with a CCD camera with 200 frames per second. In this way, it was possible to determine an intensity oscillation as well as a position oscillation of the electron beam; both had a frequency of approx. 50 Hz. Finding and eliminating the sources of these oscillations or developing mitigations for these oscillations is the subject of ongoing work. However, it follows that the periodic behavior in

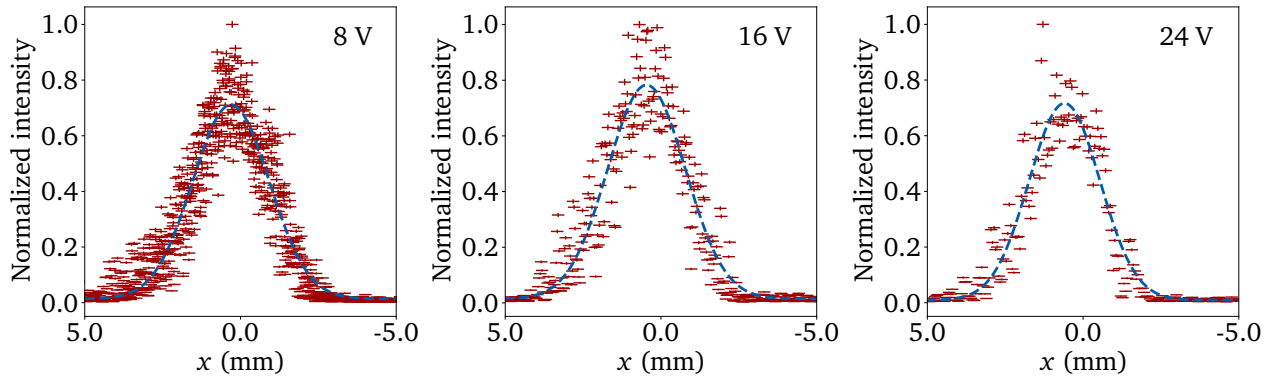


**Figure 5.4: Comparison of operating voltages of the linear actuator of S0WS01.** The visualized projected beam profiles are obtained from a corresponding single wire–beam crossing. The driving speed of the wire is almost proportional to the operating voltage of the linear actuator, while the number of data points per driving distance is almost inversely proportional to the operating voltage of the linear actuator. A Gaussian distribution (blue dashed) is fitted to the intensities resulting from the measurements (red). The centroid kinetic energy was 41.10 MeV and the initial beam current was approx. 150 nA.

the count rate of the beam-loss monitor is rather caused from the beam itself than from a vibrating wire scanner.

### 5.4.3 Comparison of Beam Properties in the 2-CA and the 2-ER Mode

During the 2-ER beamtime, the (projected) beam profile was investigated in the 2-CA and the 2-ER mode at the location of S0T2/S0R1/S0WS01 as well as at the location of S1T3/S1R1/S1WS01 in order to obtain information on the beam profile itself, the relative momentum spread and the transverse emittance.

#### Measurement at S0T2/S0R1/S0WS01

For different electron beam currents, first the 2-ER mode was realized followed by a measurement of the projected beam profile using the wire scanner, and afterward the 2-CA mode was realized by blocking the beam prior to entering the main LINAC for the first deceleration followed by a measurement of the (projected) profile using the wire scanner and both screens. While operating in one of these operation modes, several camera pictures were taken and the wire crossed the electron beam several times for statistical reasons.

Figure 5.5 shows the measured (projected) profile of a single measurement in the 2-CA mode (since the screens are destructive, they cannot be used in the 2-ER mode). The strongly focused transverse beam profile at the location of S0T2/S0R1/S0WS01 is the result of the fine-tuning of the quadrupole magnets necessary to ensure a stable operation in the 2-ER mode. Due to the focused beam and thus the high intensity in the center of the beam, an initial beam current of approx. 15 nA was chosen for this measurement to prevent an overly saturated camera picture of the BeO-Au screen. Beam envelopes resulting from these measurements are listed in Table 5.2. Here, the beam envelope determined with the wire

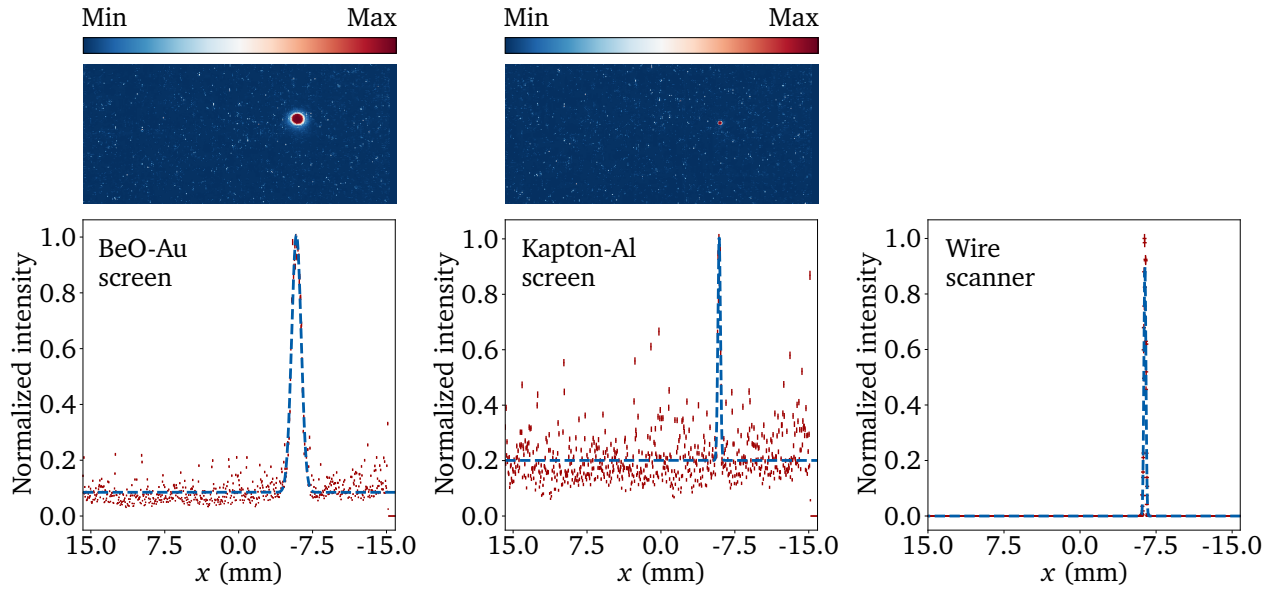


**Figure 5.5: Beam size in the 2-CA mode using SOT2/SOR1/SOWS01.** The visualized data are obtained from a corresponding single measurement. (left) BeO-Au screen. (center) Kapton-Al screen. (right) Wire scanner. (top) Determined  $x$ - $y$ -profiles. (bottom) Determined projected horizontal profiles. A Gaussian distribution (blue dashed) is fitted to the intensities resulting from the measurements (red). The centroid kinetic energy was 41.10 MeV and the initial beam current was approx. 15 nA.

**Table 5.2: Beam envelopes during the 2-ER beamtime.** Determined horizontal beam envelopes  $\sigma_x$  at SOT2/SOR1/SOWS01 for a centroid kinetic energy of 41.10 MeV and an initial beam current of approx. 15 nA. While operating in the 2-ER mode, no data can be obtained via the BeO-Au screen or the Kapton-Al screen due to their destructive characteristics.

Operation Mode	Device	$\sigma_x$ ( $\mu\text{m}$ )
2-CA	BeO-Au screen (measured)	$447 \pm 4$
2-CA	Kapton-Al screen (measured)	$148 \pm 3$
2-CA	Wire scanner (measured)	$113 \pm 11$
2-CA	Wire scanner (deconvolved)	$110 \pm 11$
2-ER	Wire scanner (measured)	$112 \pm 11$
2-ER	Wire scanner (deconvolved)	$109 \pm 11$

scanner is in the order of the wire diameter, thus the profile broadening is significant. Within the uncertainties, the beam envelope does not change in the 2-ER mode compared to the beam envelope in the 2-CA mode. Thus – as long as the conducted beam envelope measurement can be considered as a quasi–non-destructive measurement and the energy-recovery process is not interrupted – at least for a small initial beam current of approx. 15 nA, the energy-recovery process does not or only insignificantly change the horizontal beam envelope (and thus the relative momentum spread) in the second recirculation beamline.

However, it has to be evaluated whether the conducted measurement can be classified as a quasi–non-destructive measurement: Since  $\sigma_x$  is  $(109 \pm 11)$   $\mu\text{m}$  in the 2-ER mode (see Table 5.2), a fraction of  $(\tilde{d}/2)/\sigma_x = (45.9 \pm 5.2)$  % of the standard deviation of a Gaussian distributed horizontal beam size is covered by the wire when the wire center is located in the center of the beam. That is, a fraction of

$$\int_{-\infty}^{\infty} \int_{-\tilde{d}/2}^{+\tilde{d}/2} \frac{1}{2\pi\sigma_x\sigma_y} e^{-\frac{x^2}{2\sigma_x^2} - \frac{y^2}{2\sigma_y^2}} dx dy \approx 35.4 \% \quad (5.3)$$

of the area of an uncorrelated Gaussian distributed beam<sup>4</sup> is covered by the vertically mounted wire when the wire center is located in the center of the beam. Consequently, even in the worst case, that is, for the infinitesimal duration in which the wire center is located in the center of the beam, approx. 64.6 % of the electrons can participate undisturbed in the downstream occurring energy-recovery process (without taking into account any electron losses downstream of the wire scanner location that are not caused by the wire–beam crossing). Since at any other time significantly more electrons participate undisturbed in the downstream occurring energy-recovery process, the measurement can be classified as a quasi–non-destructive measurement.

The wire scanner was utilized to measure the beam envelopes in the 2-CA and the 2-ER mode for further initial beam currents between 200 nA and 800 nA. However, the corresponding measured projected beam profiles cannot be reliably evaluated due to the periodic behavior occurring during the measurements. Thus, for higher beam currents, the measured projected beam profiles did not allow for a reasonable comparison of beam properties present in the 2-CA mode with those present in the 2-ER mode.

### Measurement at S1T3/S1R1/S1WS01

The transverse emittance and the horizontal betatron function were to be determined at the location of S1T3/S1R1/S1WS01. For this determination, a quadrupole-magnet scan using the upstream located quadrupole magnet S1QU05 was intended.

In the setting ensuring a stable operation in the 2-ER mode, a defocused beam was present at the location of S1T3/S1R1/S1WS01. In order to be able to determine the horizontal emittance with sufficient precision, the horizontal focus must be achieved during

---

<sup>4</sup>The integral limits in y direction are finite in reality but would still exceed the extent of the beam since the latter is truncated in reality.



---

the quadrupole-magnet scan. Unfortunately, there was hardly any leeway to perform a quadrupole-magnet scan while operating in the 2-ER mode: the resulting modified beam led to an increased particle loss downstream and thus the 2-ER mode was disabled. Even counteracting with downstream located quadrupole magnets did not enable a sufficient quadrupole-magnet scan.

While operating in the 2-CA mode, beam losses downstream of the location of the quadrupole-magnet scan do not affect the operation mode. Thus, the quadrupole-magnet scan could be conducted. However, the detected projected beam profiles again could not be reliably evaluated due to the periodic behavior of the beam.

## 5.5 Conclusion

The functionality of the constructed wire scanners was demonstrated, while the oscillations of the electron beam's intensity and position present during the time of the wire scanner measurements prevent a reliable evaluation of several measured projected beam profiles. Regardless of the elimination of the sources of these oscillations or striven mitigations for these oscillations, the wire scanners should be upgraded in the future to provide an increased resolution. A possible variation is a smaller wire diameter. Revising and/or exchanging the linear actuator has the potential to reduce vibrations. In addition, the number of data points per driving distance should be increased for the 24 V operation mode.

Furthermore, the measurements highlight the limits of an inflexible 2-ER mode setting, which prevents a proper quadrupole-magnet scan. Therefore, a more flexible energy-recovery mode setting is required. Here, a higher number of quadrupole magnets following the one used for the quadrupole-magnet scan could potentially provide a more sophisticated way to counteract beam detuning resulting from the quadrupole-magnet scan; hence, a higher number of quadrupole magnets following the one used for the quadrupole-magnet scan could increase the possible range for the very quadrupole-magnet scan without particle losses downstream. Alternatively, no quadrupole-magnet scan has to be conducted and thus no quadrupole magnet has to be detuned at all, but in that case at least three locally separated profile measurements (that is, three wire scanners) are necessary to determine the emittance and the Twiss parameters [68], while statistically reliable results would require a corresponding higher number of locally separated profile measurements.



---

## 6 Conclusion and Outlook

The major goal of this work was the first realization of a multi-turn energy-recovery mode at the S-DALINAC.

A challenge of such an operation mode is the common recirculation transport in which beam guiding elements and path length adjustments influence superimposed beams in the recirculation beamlines. As a consequence, a beam cannot be tuned entirely manually as it is possible in the one-turn energy-recovery mode or any multi-turn conventional acceleration mode at the S-DALINAC. Instead, beam-dynamics simulations are necessary to find a working point prior to beam tuning. Since a small injector momentum has been used in this study in order to investigate its feasibility (which is relevant for the design of new ERL concepts since it enables an increased machine efficiency), the change in kinetic energy during a cavity pass has been significantly influenced by phase slippage; consequently, the main-LINAC passes had to be simulated by field-map tracking in order to ensure a sufficient precision.

The working point resulting from the simulations for a two-turn energy-recovery mode could not be set in the initial machine layout; for that reason, the beamline was modified within the scope of this work. Here, quadrupole magnets were installed in order to provide further degrees of freedom for the longitudinal dispersion and the transverse confinement. Furthermore, the beamline was equipped with additional, specific diagnostic devices required to investigate beam properties (i) of superimposed beams and/or (ii) without an interruption of an energy-recovery process.

In this way, a two-turn energy-recovery mode with an injector momentum of 5 MeV/c, a maximum momentum of 41.61 MeV/c and a maximum initial beam current of approx. 7  $\mu\text{A}$  has been realized. Depending on the beam current, a maximum energy-recovery efficiency of approx. 87 % was achieved. Limited energy-recovery efficiencies resulted primarily due to particle losses, which in turn occurred due to the challenge of finding a transverse confinement for the beam in common recirculation transport. If particle losses can be avoided in future multi-turn energy-recovery operation, increased energy-recovery efficiencies can be achieved.

Thus, it can be concluded that the combination of energy recovery and multiple acceleration can lead to an overall increased machine efficiency. Therefore, to further increase the machine efficiency, a potential three-turn energy-recovery mode was additionally studied in this work. In that operation mode, the number of objectives as well as the number of degrees of freedom increases compared to the two-turn energy-recovery mode. First simulation results indicate that this operation mode is feasible in principle – but with less precision

---

compared to the two-turn energy-recovery mode. In the future, the simulations need to be improved, especially with regard to more suitable values for the parameters of the RF fields inside the cavities. A further goal could be a symmetric setup in which, however, the number of degrees of freedom is reduced.

Within the scope of this work, wire scanners have been constructed, installed and utilized to determine projected horizontal beam profiles for different electron energies and different beam currents. Since the measuring method is quasi-non-destructive, it enables an investigation of beam properties while operating in an energy-recovery mode; thus, it enables a comparison of beam properties present in an energy-recovery mode with those present in the corresponding conventional acceleration mode.

During the conducted measurements, the electron beam's intensity and position oscillated significantly, which in turn resulted in correspondingly large uncertainties for the measured quantities. Within the uncertainties, no influence on the horizontal beam envelope (and thus on the relative momentum spread) due to the energy-recovery process was determinable for a low initial beam current of approx. 15 nA, while no comparison was possible for higher beam currents. However, since a greater impact is to be expected for a higher beam current (see BBU discussion below), a comparison at high beam currents is essential. To enable this, a stable electron beam without intensity and position oscillations has to be provided in future beamtimes. In addition, the resolution of the wire scanners should be increased.

Because the BBU threshold current was initially unknown, the electron beam was simulated and tuned for a low initial beam current of approx. 1 nA and afterward increased to the maximum possible beam current. In this way, a two-turn energy-recovery operation was possible with an initial beam current of approx. 7  $\mu$ A while there were significant particle losses downstream of the third main-LINAC pass. On the one hand, the particle losses occurred already for the low beam current present during beam tuning. Thus, the particle losses are primarily the result of the quadrupole setting for the transverse confinement rather than exceeding a certain BBU threshold current. On the other hand, the proportion of lost particles increased as a function of the initial beam current; besides increasing transverse normalized emittances, bunch length and relative momentum spread downstream of the injector LINAC, this could be a result of an increased impairment of the beam quality caused by the interactions of the electrons with possibly more strongly excited HOMs – possibly more strongly excited as a result of a higher beam current in the cavities. Thus, no BBU-threshold-current value can be specified here, but two-turn energy-recovery operation without particle losses is expected to be feasible for beam currents in the order of microamperes – as long as a sufficient transverse confinement can be realized, which has to be ensured in future beamtimes.

Consequently, if multi-turn energy-recovery operation with high beam currents is aimed for in the future, the corresponding bunch properties of high beam currents have to be taken into account in the simulations. Here, it may be necessary that the second-order longitudinal

---

dispersion is additionally available as degree of freedom. Providing this during beam tuning in turn requires several sextupole magnets to be installed at the S-DALINAC.

Moreover, the focus of this work was on the first realization of a multi-turn energy-recovery mode at the S-DALINAC and the study of the operation mode itself, but without utilizing this operation mode for an experiment. The latter is the goal for a future realization of a multi-turn energy-recovery mode at the S-DALINAC. For such a realization, the requirements on the properties of the electron beam at the interaction point as well as the influence on the electron beam due to the interaction have to be taken into account in the simulations.



---

# A Details on the Beam-Dynamics Simulations

Parts of the simulation code created within the scope of this work have been stored in a public repository [112]. The published code is provided with extensive details on the individual simulation steps (in the Manual.pdf file and in the comments in the corresponding files). The functionalities of the used tools (the software ELEGANT, the Self Describing Data Sets (SDDS) file protocol and the programming language Python) follow from the corresponding manuals [138–140]. In this appendix, only some characteristics of the code will be described in more detail based on excerpts of the code used for the simulations for the two-turn energy-recovery mode:

As mentioned in section 4.2.2, the software ELEGANT provides implemented functions for solving optimization problems. Here, a simplex-based algorithm was used to minimize the corresponding problem:

```
&optimization_setup
  mode="minimize",
  method="simplex",
  ...
&end
```

The corresponding optimization problem is the sum of terms in which penalty functions are used. In this way, only one objective function results and consequently a Pareto optimization problem is avoided. The markers M18 to M48 indicate the main-LINAC exit after the corresponding pass. The penalty function is given by the soft-edge not-equal function `sene` using the reverse Polish notation. For the unit of a parameter see the manual [138]; for example, the momentum values are given in the unit  $\tilde{m}_{\text{rest},e} c$ , where  $\tilde{m}_{\text{rest},e}$  is the rest mass of an electron:

```
&optimization_term
  term="M18#1.pCentral 46.3005041399792 1.95695118355918e-6 sene"
&end
&optimization_term
  term="M28#1.pCentral 81.4368366118952 1.95695118355918e-6 sene"
&end
&optimization_term
  term="M38#1.pCentral 46.3005041399792 1.95695118355918e-6 sene"
```

```

&end
&optimization_term
  term="M48#1.pCentral 9.78475591779592 1.95695118355918e-6 sene"
&end

```

In this work, the degrees of freedom are  $\hat{\mathcal{E}}_{z,j,\text{peak}}$ ,  $\hat{\phi}_j$ ,  $L_m$  and  $R_{56,n}$  (see section 4.2.1). However, since ELEGANT is used for the simulations, the degrees of freedom available in the software are used, which are  $\hat{\mathcal{E}}_{z,j,\text{peak}}$ ,  $\psi_j - \psi_{\text{off},j}$ ,  $\Delta L_m$  and  $R_{56,n}$ , that is, the parameters `EZ_PEAK`, `PHASE`, `L` and `R56`, respectively; while  $\hat{\phi}_j$  is in principle available in ELEGANT, it cannot be used for the optimization algorithm due to a known software bug. The meaning of  $\psi_{\text{off},j}$  is discussed below. Contrary to what is explained in Ref. [112], the default values for `lower_limit`, `upper_limit` and `differential_limits` can be kept; taking into account modulo operation and except for insignificant decimal places, this leads to the same result as presented in Ref. [112]. The used notations `FPLAS` and `SPLAS` indicate the path length adjustments of the first and the second recirculation beamline relative to the corresponding minimum possible recirculation-beamline length, respectively. Furthermore, `R56` is not used as an `item` of an `optimization_variable` when working with the simplex-based algorithm; instead, `R56` is varied in a brute-force method:

```

&optimization_variable
  name=A1SC01,
  item=EZ_PEAK,
  lower_limit=0,
  upper_limit=5e6,
  step_size =1e3
&end
...
&optimization_variable
  name=A1SC08,
  item=EZ_PEAK,
  lower_limit=0,
  upper_limit=5e6,
  step_size =1e3
&end
&optimization_variable
  name=A1SC01,
  item=PHASE,
  step_size =0.0001
&end
...
&optimization_variable
  name=A1SC08,
  item=PHASE,
  step_size =0.0001

```



```

&end
&optimization_variable
  name=FPLAS,
  item=L,
  lower_limit=0,
  upper_limit=0.074,
  step_size =0.0001
&end
&optimization_variable
  name=SPLAS,
  item=L,
  lower_limit=0,
  upper_limit=0.1012,
  step_size =0.0001
&end

```

The change in the electron's kinetic energy while passing a cavity (see Eq. (3.6)) is computed by field-map tracking using a non-adaptive Runge-Kutta method. Here, the field in the fringe-field region is considered as well, leading to a field map covering a range of 1.282 m compared to the geometric length of a 20-cell cavity of 1 m (see Fig. 3.4). Due to a known software bug in ELEGANT, setting `FIDUCIAL="t,light"` per cavity is necessary to utilize the optimization algorithm available in ELEGANT adequately. In this way, a cavity begins to oscillate with the set phase when a particle traveling constantly at speed of light arrives at the very cavity for the first time (contrary to what is explained in Ref. [112]), which allows the corresponding phase to be independent of an arrival event of an electron with a certain variable speed (for a certain section, the speed of an electron may change from simulation iteration to simulation iteration as a result of variations of `EZ_PEAK`, `PHASE` and `L`). Since the time of flight needed by a particle, which starts at the origin and travels constantly at speed of light to arrive at a cavity, is constant, this time of flight contributes to  $\psi_j$  only in the form of a constant offset phase  $\psi_{\text{off},j}$ . However, since the off-crest acceleration phase

$$\begin{aligned}
\hat{\phi}_j &= ((\psi_j - \psi_{\text{off},j}) - (\hat{\psi}_j - \psi_{\text{off},j}) + 180^\circ) \bmod 360^\circ - 180^\circ \\
&= (\psi_j - \hat{\psi}_j + 180^\circ) \bmod 360^\circ - 180^\circ
\end{aligned} \tag{A.1}$$

(compare the definitions (3.10) and (3.14)) is required to set up the main LINAC (see section 4.2.4), where any offset phase  $\psi_{\text{off},j}$  vanishes, the value of  $\psi_{\text{off},j}$  is irrelevant. Conversion from `PHASE` to  $\hat{\phi}_j$  using ELEGANT is described in Ref. [112] (where (i)  $\psi_{\text{off},j}$  is constant zero, which, however, is irrelevant for  $\hat{\phi}_j$  as shown in Eq. (A.1), and (ii) a modulo operation is not necessary due to the absence of the restriction that  $\hat{\psi}_j$  has to be in  $[0^\circ, 360^\circ)$  as well as due to the different setting of `lower_limit`, `upper_limit` and `differential_limits`):

```
A1SC01: RFTMEZ0,L=1.282,&
```

---

```
INPUTFILE="fieldmap.sdds",METHOD="non-adaptive runge-kutta",&
FIDUCIAL="t,light",PHASE_REFERENCE=1, ...
```

```
...
```

```
A1SC08: RFTMEZ0,L=1.282,&
```

```
INPUTFILE="fieldmap.sdds",METHOD="non-adaptive runge-kutta",&
FIDUCIAL="t,light",PHASE_REFERENCE=8, ...
```

In the 2D simulations, the effect of the first-order longitudinal dispersion  $R_{56,n}$  is realized by elements of zero length located at the end of the corresponding section  $n$ . The corresponding values change in the iterations of the simulation if they are degrees of freedom; the longitudinal dispersion acting along the path from the exit of the fourth main-LINAC pass to the low-energy dump (R section) is not variable but given as a fixed value:

```
IMATRIX: EMATRIX, R11=1, R22=1, R33=1, R44=1, R55=1, R66=1, R56=...
```

```
FMATRIX: EMATRIX, R11=1, R22=1, R33=1, R44=1, R55=1, R66=1, R56=...
```

```
SMATRIX: EMATRIX, R11=1, R22=1, R33=1, R44=1, R55=1, R66=1, R56=...
```

```
RMATRIX: EMATRIX, R11=1, R22=1, R33=1, R44=1, R55=1, R66=1, R56=0.05858...
```

To find a solution for the transverse confinement, quadrupole magnets were implemented mostly as a matrix to speed up the simulations. Since the corresponding element `QUAD` does not provide an absolute field parameter but only the focusing strength, which is a relative field parameter, this element can only be used if the design momentum does not vary at the location of a quadrupole magnet (in the case that no momentum conversions are made), that is, it can only be used in the I1 section and the straight sections of the recirculation beamlines. Varied design momenta are only present in the four quadrupole magnets located in the main-LINAC section. Here, the symplectic tracking element `KQUAD` was used where the pole tip field as absolute field parameter is provided:

```
&optimization_variable
```

```
name=I1QH01,
```

```
item=K1,
```

```
lower_limit=-78,
```

```
upper_limit=78,
```

```
step_size = 0.001
```

```
&end
```

```
...
```

```
&optimization_variable
```

```
name=A1QU01,
```

```
item=B,
```

```
lower_limit=-0.018,
```

```
upper_limit=0.018,
```

```
step_size = 0.000001
```

```
&end
```

```
...
```

## B Parameters of the Simulations

**Table B.1: Simulation related values.** For the 2D optimization problem of the 2-ER and the 3-ER mode, respectively, the table lists the corresponding values and range (if applicable) of the parameters that are (i) fixed in, (ii) degrees of freedom of, or (iii) resulting from the beam-dynamics simulations. The upper limit for  $\tau$  was set to 1000 to ensure a certain reasonable precision; the other limits follow from the technical limits.

Parameter	Value (2-ER)	Value (3-ER)	Range
$p_{0,1}$ (MeV/c)	23.66	23.66	fixed
$p_{0,2}$ (MeV/c)	41.61	41.61	fixed
$p_{0,3}$ (MeV/c)	23.66	59.30	fixed
$p_{0,4}$ (MeV/c)	5.00	41.61	fixed
$p_{0,5}$ (MeV/c)	—	23.66	fixed
$p_{0,6}$ (MeV/c)	—	5.00	fixed
$\tau_{2\text{-ER}}$ (eV/c)	1	—	[0,1000]
$\tau_{3\text{-ER}}$ (eV/c)	—	630	[0,1000]
$\hat{\mathcal{E}}_{z,\text{A1SC01,peak}}$ (MV/m)	4.540	4.997	[0,5]
$\hat{\mathcal{E}}_{z,\text{A1SC02,peak}}$ (MV/m)	4.457	4.676	[0,5]
$\hat{\mathcal{E}}_{z,\text{A1SC03,peak}}$ (MV/m)	4.487	4.794	[0,5]
$\hat{\mathcal{E}}_{z,\text{A1SC04,peak}}$ (MV/m)	4.478	4.433	[0,5]
$\hat{\mathcal{E}}_{z,\text{A1SC05,peak}}$ (MV/m)	4.467	4.595	[0,5]
$\hat{\mathcal{E}}_{z,\text{A1SC06,peak}}$ (MV/m)	4.472	4.623	[0,5]
$\hat{\mathcal{E}}_{z,\text{A1SC07,peak}}$ (MV/m)	4.506	4.357	[0,5]
$\hat{\mathcal{E}}_{z,\text{A1SC08,peak}}$ (MV/m)	4.517	4.479	[0,5]
$\hat{\phi}_{\text{A1SC01}}$ (°)	-9.7	17.2	[-180,180]
$\hat{\phi}_{\text{A1SC02}}$ (°)	-5.7	15.9	[-180,180]
$\hat{\phi}_{\text{A1SC03}}$ (°)	13.2	24.4	[-180,180]
$\hat{\phi}_{\text{A1SC04}}$ (°)	4.0	17.4	[-180,180]
$\hat{\phi}_{\text{A1SC05}}$ (°)	6.1	10.6	[-180,180]
$\hat{\phi}_{\text{A1SC06}}$ (°)	7.2	-5.2	[-180,180]
$\hat{\phi}_{\text{A1SC07}}$ (°)	5.6	-16.2	[-180,180]
$\hat{\phi}_{\text{A1SC08}}$ (°)	3.2	-6.0	[-180,180]
$L_F$ (m)	44.8913	44.8853	[44.8780,44.9520]
$L_S$ (m)	48.4371	48.3946	[48.3860,48.4872]
$L_T$ (m)	—	53.1519	[53.1390,53.2374]
$R_{56,I}$ (m)	-0.01	-0.01	[-0.7,0.4]
$R_{56,F}$ (m)	0.33	0.20	[-0.1,0.8]
$R_{56,S}$ (m)	0.18	-0.30	[-0.7,0.7]
$R_{56,T}$ (m)	—	-0.20	[-2.0,1.9]

**Table B.1: Simulation related values.** (continued)

Parameter	Value (2-ER)	Value (3-ER)	Range
$\Delta\bar{p}_{\text{on-crest,A1SC01}}$ (MeV/c)	2.37	2.61	—
$\Delta\bar{p}_{\text{on-crest,A1SC02}}$ (MeV/c)	2.33	2.45	—
$\Delta\bar{p}_{\text{on-crest,A1SC03}}$ (MeV/c)	2.35	2.51	—
$\Delta\bar{p}_{\text{on-crest,A1SC04}}$ (MeV/c)	2.35	2.32	—
$\Delta\bar{p}_{\text{on-crest,A1SC05}}$ (MeV/c)	2.34	2.41	—
$\Delta\bar{p}_{\text{on-crest,A1SC06}}$ (MeV/c)	2.34	2.42	—
$\Delta\bar{p}_{\text{on-crest,A1SC07}}$ (MeV/c)	2.36	2.28	—
$\Delta\bar{p}_{\text{on-crest,A1SC08}}$ (MeV/c)	2.37	2.35	—
$\Delta\bar{p}_{\text{off-crest,A1SC01}}$ (MeV/c)	2.34	2.49	—
$\Delta\bar{p}_{\text{off-crest,A1SC02}}$ (MeV/c)	2.32	2.35	—
$\Delta\bar{p}_{\text{off-crest,A1SC03}}$ (MeV/c)	2.29	2.29	—
$\Delta\bar{p}_{\text{off-crest,A1SC04}}$ (MeV/c)	2.34	2.22	—
$\Delta\bar{p}_{\text{off-crest,A1SC05}}$ (MeV/c)	2.33	2.37	—
$\Delta\bar{p}_{\text{off-crest,A1SC06}}$ (MeV/c)	2.33	2.41	—
$\Delta\bar{p}_{\text{off-crest,A1SC07}}$ (MeV/c)	2.35	2.19	—
$\Delta\bar{p}_{\text{off-crest,A1SC08}}$ (MeV/c)	2.36	2.33	—

# C Relations Between Matrix Elements

Here, details are given for the relations mentioned in section 3.5.

## C.1 Causing and Influencing Dispersion

Since each transport matrix  $R$  given in section 3.4 has the form

$$R = \begin{pmatrix} R_{11} & R_{12} & R_{13} & R_{14} & 0 & R_{16} \\ R_{21} & R_{22} & R_{23} & R_{24} & 0 & R_{26} \\ R_{31} & R_{32} & R_{33} & R_{34} & 0 & 0 \\ R_{41} & R_{42} & R_{43} & R_{44} & 0 & 0 \\ R_{51} & R_{52} & 0 & 0 & 1 & R_{56} \\ 0 & 0 & 0 & 0 & 0 & 1 \end{pmatrix}, \quad (\text{C.1})$$

an arbitrary multiplication of a matrix of the same form,  $\tilde{R}$ , and  $R$  leads to the following dispersion terms (second index equal to six):

$$\begin{aligned} (\tilde{R} \cdot R)_{16} &= \tilde{R}_{11} \cdot R_{16} + \tilde{R}_{12} \cdot R_{26} + \tilde{R}_{13} \cdot R_{36} + \tilde{R}_{14} \cdot R_{46} + \tilde{R}_{15} \cdot R_{56} + \tilde{R}_{16} \cdot R_{66} \\ &= \tilde{R}_{11} \cdot R_{16} + \tilde{R}_{12} \cdot R_{26} + \tilde{R}_{13} \cdot 0 + \tilde{R}_{14} \cdot 0 + 0 \cdot R_{56} + \tilde{R}_{16} \cdot 1 \\ &= \tilde{R}_{11} \cdot R_{16} + \tilde{R}_{12} \cdot R_{26} + \tilde{R}_{16}, \end{aligned} \quad (\text{C.2})$$

$$\begin{aligned} (\tilde{R} \cdot R)_{26} &= \tilde{R}_{21} \cdot R_{16} + \tilde{R}_{22} \cdot R_{26} + \tilde{R}_{23} \cdot R_{36} + \tilde{R}_{24} \cdot R_{46} + \tilde{R}_{25} \cdot R_{56} + \tilde{R}_{26} \cdot R_{66} \\ &= \tilde{R}_{21} \cdot R_{16} + \tilde{R}_{22} \cdot R_{26} + \tilde{R}_{23} \cdot 0 + \tilde{R}_{24} \cdot 0 + 0 \cdot R_{56} + \tilde{R}_{26} \cdot 1 \\ &= \tilde{R}_{21} \cdot R_{16} + \tilde{R}_{22} \cdot R_{26} + \tilde{R}_{26}, \end{aligned} \quad (\text{C.3})$$

$$\begin{aligned} (\tilde{R} \cdot R)_{36} &= \tilde{R}_{31} \cdot R_{16} + \tilde{R}_{32} \cdot R_{26} + \tilde{R}_{33} \cdot R_{36} + \tilde{R}_{34} \cdot R_{46} + \tilde{R}_{35} \cdot R_{56} + \tilde{R}_{36} \cdot R_{66} \\ &= \tilde{R}_{31} \cdot R_{16} + \tilde{R}_{32} \cdot R_{26} + \tilde{R}_{33} \cdot 0 + \tilde{R}_{34} \cdot 0 + 0 \cdot R_{56} + 0 \cdot 1 \\ &= \tilde{R}_{31} \cdot R_{16} + \tilde{R}_{32} \cdot R_{26}, \end{aligned} \quad (\text{C.4})$$

$$\begin{aligned} (\tilde{R} \cdot R)_{46} &= \tilde{R}_{41} \cdot R_{16} + \tilde{R}_{42} \cdot R_{26} + \tilde{R}_{43} \cdot R_{36} + \tilde{R}_{44} \cdot R_{46} + \tilde{R}_{45} \cdot R_{56} + \tilde{R}_{46} \cdot R_{66} \\ &= \tilde{R}_{41} \cdot R_{16} + \tilde{R}_{42} \cdot R_{26} + \tilde{R}_{43} \cdot 0 + \tilde{R}_{44} \cdot 0 + 0 \cdot R_{56} + 0 \cdot 1 \\ &= \tilde{R}_{41} \cdot R_{16} + \tilde{R}_{42} \cdot R_{26}, \end{aligned} \quad (\text{C.5})$$

$$\begin{aligned}
(\tilde{R} \cdot R)_{56} &= \tilde{R}_{51} \cdot R_{16} + \tilde{R}_{52} \cdot R_{26} + \tilde{R}_{53} \cdot R_{36} + \tilde{R}_{54} \cdot R_{46} + \tilde{R}_{55} \cdot R_{56} + \tilde{R}_{56} \cdot R_{66} \\
&= \tilde{R}_{51} \cdot R_{16} + \tilde{R}_{52} \cdot R_{26} + 0 \cdot 0 + 0 \cdot 0 + 1 \cdot R_{56} + \tilde{R}_{56} \cdot 1 \\
&= \tilde{R}_{51} \cdot R_{16} + \tilde{R}_{52} \cdot R_{26} + R_{56} + \tilde{R}_{56},
\end{aligned} \tag{C.6}$$

$$\begin{aligned}
(\tilde{R} \cdot R)_{66} &= \tilde{R}_{61} \cdot R_{16} + \tilde{R}_{62} \cdot R_{26} + \tilde{R}_{63} \cdot R_{36} + \tilde{R}_{64} \cdot R_{46} + \tilde{R}_{65} \cdot R_{56} + \tilde{R}_{66} \cdot R_{66} \\
&= 0 \cdot R_{16} + 0 \cdot R_{26} + 0 \cdot 0 + 0 \cdot 0 + 0 \cdot R_{56} + 1 \cdot 1 \\
&= 1.
\end{aligned} \tag{C.7}$$

Thus, besides the identity  $(\tilde{R} \cdot R)_{66}$ , non-zero values for the terms  $(\tilde{R} \cdot R)_{i6}$  can only result from a matrix multiplication if at least one non-zero dispersion term  $R_{i6}$  or  $\tilde{R}_{i6}$ ,  $i \in \{1, \dots, 5\}$ , exists. For those matrices mentioned in section 3.4, this is only the case for the matrix specified in Eq. (3.28). Therefore, a horizontal deflecting dipole magnet (or a rotated one resulting from  $R_{SD}$  and  $R_{tot}$ ) is required in a section to provide non-zero dispersion values in the very section. After dispersion has arisen due to a dipole magnet, an influence of the dispersion function may be possible by downstream located quadrupole magnets (as long as not all transverse dispersion terms did vanish after another dipole magnet that is located upstream to these quadrupole magnets).

## C.2 Matrix Component Relating to the Relative Distance Traveled

Since each transport matrix  $R$  given in section 3.4 has the form given in Eq. (C.1), an arbitrary multiplication of a matrix of the same form,  $\tilde{R}$ , and  $R$  leads to:

$$\begin{aligned}
(\tilde{R} \cdot R)_{55} &= \tilde{R}_{51} \cdot R_{15} + \tilde{R}_{52} \cdot R_{25} + \tilde{R}_{53} \cdot R_{35} + \tilde{R}_{54} \cdot R_{45} + \tilde{R}_{55} \cdot R_{55} + \tilde{R}_{56} \cdot R_{65} \\
&= \tilde{R}_{51} \cdot 0 + \tilde{R}_{52} \cdot 0 + 0 \cdot 0 + 0 \cdot 0 + 1 \cdot 1 + \tilde{R}_{56} \cdot 0 \\
&= 1.
\end{aligned} \tag{C.8}$$

## C.3 Properties of an Achromat

The proof below is based on Refs. [77, 141]:

In the following, only these sections from  $s_1$  to  $s_2$  are dealt with in which no  $R_{tot}(\Phi)$  is used. Consequently, each transport matrix  $R$  given in section 3.4 excluding  $R_{tot}(\Phi)$  has the

form

$$R = \begin{pmatrix} R_{11} & R_{12} & 0 & 0 & 0 & R_{16} \\ R_{21} & R_{22} & 0 & 0 & 0 & R_{26} \\ 0 & 0 & R_{33} & R_{34} & 0 & 0 \\ 0 & 0 & R_{43} & R_{44} & 0 & 0 \\ R_{51} & R_{52} & 0 & 0 & 1 & R_{56} \\ 0 & 0 & 0 & 0 & 0 & 1 \end{pmatrix}, \quad (\text{C.9})$$

and an arbitrary multiplication of a matrix of the same form,  $\tilde{R}$ , and  $R$  results in

$$\tilde{R} \cdot R = \begin{pmatrix} \tilde{R}_{11}R_{11} + \tilde{R}_{12}R_{21} & \tilde{R}_{11}R_{12} + \tilde{R}_{12}R_{22} & 0 & 0 & 0 & \tilde{R}_{11}R_{16} + \tilde{R}_{12}R_{26} + \tilde{R}_{16} \\ \tilde{R}_{21}R_{11} + \tilde{R}_{22}R_{21} & \tilde{R}_{21}R_{12} + \tilde{R}_{22}R_{22} & 0 & 0 & 0 & \tilde{R}_{21}R_{16} + \tilde{R}_{22}R_{26} + \tilde{R}_{26} \\ 0 & 0 & \tilde{R}_{33}R_{33} + \tilde{R}_{34}R_{43} & \tilde{R}_{33}R_{34} + \tilde{R}_{34}R_{44} & 0 & 0 \\ 0 & 0 & \tilde{R}_{43}R_{33} + \tilde{R}_{44}R_{43} & \tilde{R}_{43}R_{34} + \tilde{R}_{44}R_{44} & 0 & 0 \\ \tilde{R}_{51}R_{11} + \tilde{R}_{52}R_{21} + R_{51} & \tilde{R}_{51}R_{12} + \tilde{R}_{52}R_{22} + R_{52} & 0 & 0 & 1 & \tilde{R}_{51}R_{16} + \tilde{R}_{52}R_{26} + R_{56} + \tilde{R}_{56} \\ 0 & 0 & 0 & 0 & 0 & 1 \end{pmatrix}, \quad (\text{C.10})$$

which is again a transport matrix of the same form. Hence, it is sufficient to deal with  $R$  only as a representative for an entire section from  $s_1$  to  $s_2$ . For  $R$ , the determinant can be calculated and is

$$(R_{11}R_{22} - R_{12}R_{21}) \cdot (R_{33}R_{44} - R_{34}R_{43}). \quad (\text{C.11})$$

Due to the given form of  $R$ , the horizontal components are decoupled from the vertical ones. Consequently, the submatrices  $\check{R}_{xx'}$  and  $\check{R}_{yy'}$  can be considered independently. Here,

$$\det(\check{R}_{xx'}) = R_{11}R_{22} - R_{12}R_{21} = 1 \quad (\text{C.12})$$

and

$$\det(\check{R}_{yy'}) = R_{33}R_{44} - R_{34}R_{43} = 1 \quad (\text{C.13})$$

apply [141].

For convenience but without loss of generality,  $s_1 = 0$ ,  $s_2 = s$  and  $R_{s_1 \rightarrow s_2} = R_{0 \rightarrow s} = R(s)$  apply until the end of this section, and accordingly for the corresponding matrix elements.

The following relations apply [77]:

$$R_{16}(s) = R_{12}(s) \int_0^s \frac{R_{11}(s')}{\rho_0(s')} ds' - R_{11}(s) \int_0^s \frac{R_{12}(s')}{\rho_0(s')} ds', \quad (\text{C.14})$$

$$R_{21}(s) = \left. \frac{\partial R_{11}(s')}{\partial s'} \right|_{s'=s}, \quad (\text{C.15})$$

$$R_{22}(s) = \left. \frac{\partial R_{12}(s')}{\partial s'} \right|_{s'=s}, \quad (\text{C.16})$$

$$R_{26}(s) = \left. \frac{\partial R_{16}(s')}{\partial s'} \right|_{s'=s}, \quad (\text{C.17})$$

$$R_{51}(s) = \int_0^s \frac{R_{11}(s')}{\rho_0(s')} ds', \quad (\text{C.18})$$

$$R_{52}(s) = \int_0^s \frac{R_{12}(s')}{\rho_0(s')} ds'. \quad (\text{C.19})$$

Thus, it follows:

$$\begin{aligned}
R_{26}(s) &= \left. \frac{\partial R_{16}(s')}{\partial s'} \right|_{s'=s} \\
&= \left. \frac{\partial}{\partial s'} \left( R_{12}(s') \int_0^{s'} \frac{R_{11}(s'')}{\rho_0(s'')} ds'' - R_{11}(s') \int_0^{s'} \frac{R_{12}(s'')}{\rho_0(s'')} ds'' \right) \right|_{s'=s} \\
&= \left. \frac{\partial}{\partial s'} \left( R_{12}(s') \int_0^{s'} \frac{R_{11}(s'')}{\rho_0(s'')} ds'' \right) \right|_{s'=s} - \left. \frac{\partial}{\partial s'} \left( R_{11}(s') \int_0^{s'} \frac{R_{12}(s'')}{\rho_0(s'')} ds'' \right) \right|_{s'=s} \\
&= \left. \frac{\partial R_{12}(s')}{\partial s'} \right|_{s'=s} \int_0^s \frac{R_{11}(s'')}{\rho_0(s'')} ds'' + R_{12}(s) \left. \frac{\partial}{\partial s'} \left( \int_0^{s'} \frac{R_{11}(s'')}{\rho_0(s'')} ds'' \right) \right|_{s'=s} \\
&\quad - \left[ \left. \frac{\partial R_{11}(s')}{\partial s'} \right|_{s'=s} \int_0^s \frac{R_{12}(s'')}{\rho_0(s'')} ds'' + R_{11}(s) \left. \frac{\partial}{\partial s'} \left( \int_0^{s'} \frac{R_{12}(s'')}{\rho_0(s'')} ds'' \right) \right|_{s'=s} \right] \\
&= R_{22}(s) \int_0^s \frac{R_{11}(s'')}{\rho_0(s'')} ds'' + R_{12}(s) \frac{R_{11}(s)}{\rho_0(s)} \\
&\quad - \left[ R_{21}(s) \int_0^s \frac{R_{12}(s'')}{\rho_0(s'')} ds'' + R_{11}(s) \frac{R_{12}(s)}{\rho_0(s)} \right] \\
&= R_{22}(s) \int_0^s \frac{R_{11}(s'')}{\rho_0(s'')} ds'' - R_{21}(s) \int_0^s \frac{R_{12}(s'')}{\rho_0(s'')} ds''. \tag{C.20}
\end{aligned}$$

By using Eqs. (C.18) and (C.19), Eqs. (C.14) and (C.20) simplify to

$$R_{16}(s) = R_{12}(s)R_{51}(s) - R_{11}(s)R_{52}(s), \tag{C.21}$$

$$R_{26}(s) = R_{22}(s)R_{51}(s) - R_{21}(s)R_{52}(s). \tag{C.22}$$

For sections where  $R_{16}(s) = R_{26}(s) = 0$  applies, it follows:

$$0 = R_{16}(s) = R_{12}(s)R_{51}(s) - R_{11}(s)R_{52}(s) \tag{C.23}$$

$$\Leftrightarrow R_{12}(s)R_{51}(s) = R_{11}(s)R_{52}(s) \tag{C.24}$$

$$\Leftrightarrow R_{22}(s)R_{12}(s)R_{51}(s) = R_{22}(s)R_{11}(s)R_{52}(s) \tag{C.25}$$

if and only if  $R_{22}(s) \neq 0$ , and

$$0 = R_{26}(s) = R_{22}(s)R_{51}(s) - R_{21}(s)R_{52}(s) \tag{C.26}$$

$$\Leftrightarrow R_{22}(s)R_{51}(s) = R_{21}(s)R_{52}(s) \tag{C.27}$$

$$\Leftrightarrow R_{11}(s)R_{22}(s)R_{51}(s) = R_{11}(s)R_{21}(s)R_{52}(s) \tag{C.28}$$



if and only if  $R_{11}(s) \neq 0$ .

Combining the equations of the relations (C.24) and (C.28) leads to:

$$R_{11}(s)R_{22}(s)R_{51}(s) = R_{21}(s)R_{12}(s)R_{51}(s) \quad (\text{C.29})$$

$$\Leftrightarrow R_{11}(s)R_{22}(s)R_{51}(s) - R_{12}(s)R_{21}(s)R_{51}(s) = 0 \quad (\text{C.30})$$

$$\Leftrightarrow (R_{11}(s)R_{22}(s) - R_{12}(s)R_{21}(s))R_{51}(s) = 0. \quad (\text{C.31})$$

Combining the equations of the relations (C.25) and (C.27) leads to:

$$R_{12}(s)R_{21}(s)R_{52}(s) = R_{11}(s)R_{22}(s)R_{52}(s) \quad (\text{C.32})$$

$$\Leftrightarrow R_{11}(s)R_{22}(s)R_{52}(s) - R_{12}(s)R_{21}(s)R_{52}(s) = 0 \quad (\text{C.33})$$

$$\Leftrightarrow (R_{11}(s)R_{22}(s) - R_{12}(s)R_{21}(s))R_{52}(s) = 0. \quad (\text{C.34})$$

Since  $R_{11}(s)R_{22}(s) - R_{12}(s)R_{21}(s) = 1 \neq 0$  (see Eq. (C.12)),

$$R_{51}(s) = 0 \quad \text{and} \quad R_{52}(s) = 0 \quad (\text{C.35})$$

follow from the equations of the relations (C.31) and (C.34).

If  $R_{11}(s) = 0$  and/or  $R_{22}(s) = 0$  apply, the equivalences in the relations (C.25) and/or (C.28) may not be assumed as valid in general, respectively. However, if  $R_{11}(s) = 0$  and/or  $R_{22}(s) = 0$  apply, then  $R_{12}(s)R_{21}(s) = -1 \neq 0$  follows from Eq. (C.12), and thus  $R_{12}(s) \neq 0$  and  $R_{21}(s) \neq 0$  apply in these cases. Hence, if  $R_{11}(s) = 0$  applies, then  $R_{51}(s) = 0$  follows from Eq. (C.23) and in this way  $R_{52}(s) = 0$  follows from Eq. (C.26), and if  $R_{22}(s) = 0$  applies, then  $R_{52}(s) = 0$  follows from Eq. (C.26) and in this way  $R_{51}(s) = 0$  follows from Eq. (C.23).

In summary, if  $R_{16}(s) = R_{26}(s) = 0$  applies, then  $R_{51}(s) = R_{52}(s) = 0$  follows.



---

## D Impacts Due to Space-Charge Effects and Synchrotron Radiation

Space-charge effects and synchrotron radiation influences were not taken into account in the previously described simulations conducted to find results for a beam current of 1 nA, since their impact is negligible for such a low beam current and the present electron energies, and thus including these effects would unnecessarily increase the simulation time significantly. Below, it is shown that these effects are small for higher beam currents downstream of the injector LINAC by comparing (i) tracking with disabled space-charge effects and disabled synchrotron radiation with (ii) tracking with enabled space-charge effects and/or enabled synchrotron radiation.

For this purpose, the final lattice setting of the 6D results of the 2-ER and the 3-ER mode (see sections 4.2.2 and 4.3.2) have been fixed and space-charge effects and/or synchrotron radiation have been enabled. Those effects have been realized using the options available in the particle tracking software ELEGANT: longitudinal space-charge effects have been simulated based on the longitudinal space-charge impedance per unit length [142], and coherent synchrotron radiation has been simulated based on the energy change of a line charge distribution as a function of the location within the bunch and in a dipole magnet [107]. While both methods have their limitations (the latter especially for low electron energies [143]), they were sufficient in this work to indicate the order of magnitude of the influences.

Figures D.1 to D.4 show the relative behaviors of beam quantities along the accelerator as a function of the beam current after chopping; the shown behaviors are relative to the case with disabled space-charge effects and disabled synchrotron radiation, which is referred to as “0  $\mu\text{A}$ ”. The relative behaviors are shown for the maximum beam current after chopping achieved in the 2-ER mode (7  $\mu\text{A}$ ), the maximum permitted beam current after chopping when operating in a multi-turn energy-recovery mode due to radiation protection reasons (20  $\mu\text{A}$ ), and the technical maximum beam current after chopping limited due to the specifications of the injector LINAC (60  $\mu\text{A}$ ). For a beam current after chopping of 7  $\mu\text{A}$ /20  $\mu\text{A}$ /60  $\mu\text{A}$ , the maximum absolute change of a relative behavior shown in Figs. D.1 to D.2 (2-ER mode) is less than 2%/3%/9%, and the maximum absolute change of a relative behavior shown in Figs. D.3 to D.4 (3-ER mode) is less than 3%/7%/17%, respectively. Note that only the charge of the macro particles was changed in these simulations; all other properties of the initial bunch (including the number of macro particles) remained unchanged.

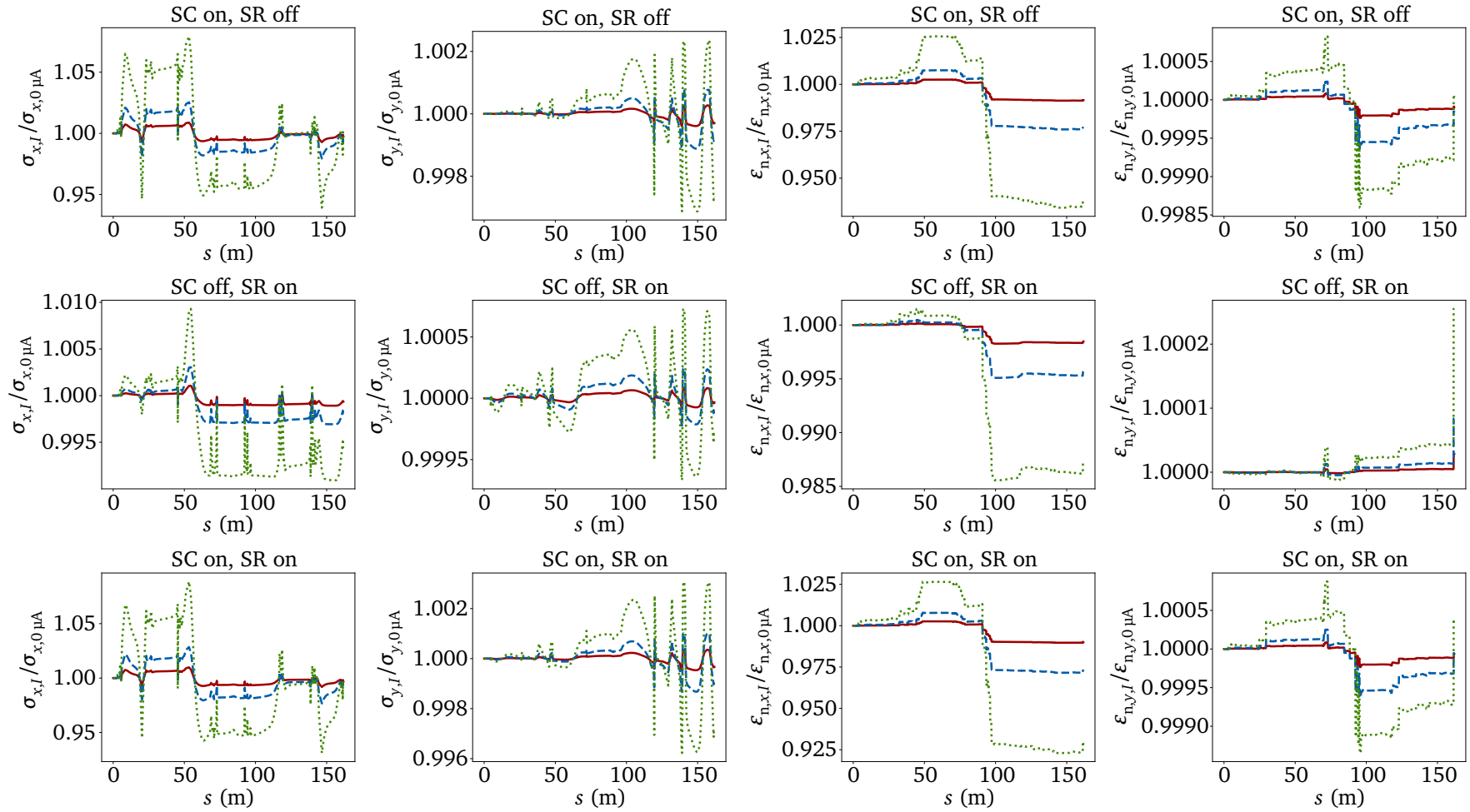


**Figure D.1: Influence on the 2-ER mode due to space-charge effects and synchrotron radiation (1/2).** For enabled space-charge effects (SC) and/or enabled synchrotron radiation (SR), relative behaviors of beam quantities along the accelerator as a function of the location  $s$  are shown for different beam currents after chopping,  $I$ . The simulations started behind the injector LINAC. Legend: 7  $\mu\text{A}$  (—), 20  $\mu\text{A}$  (- - -), 60  $\mu\text{A}$  (· · ·).

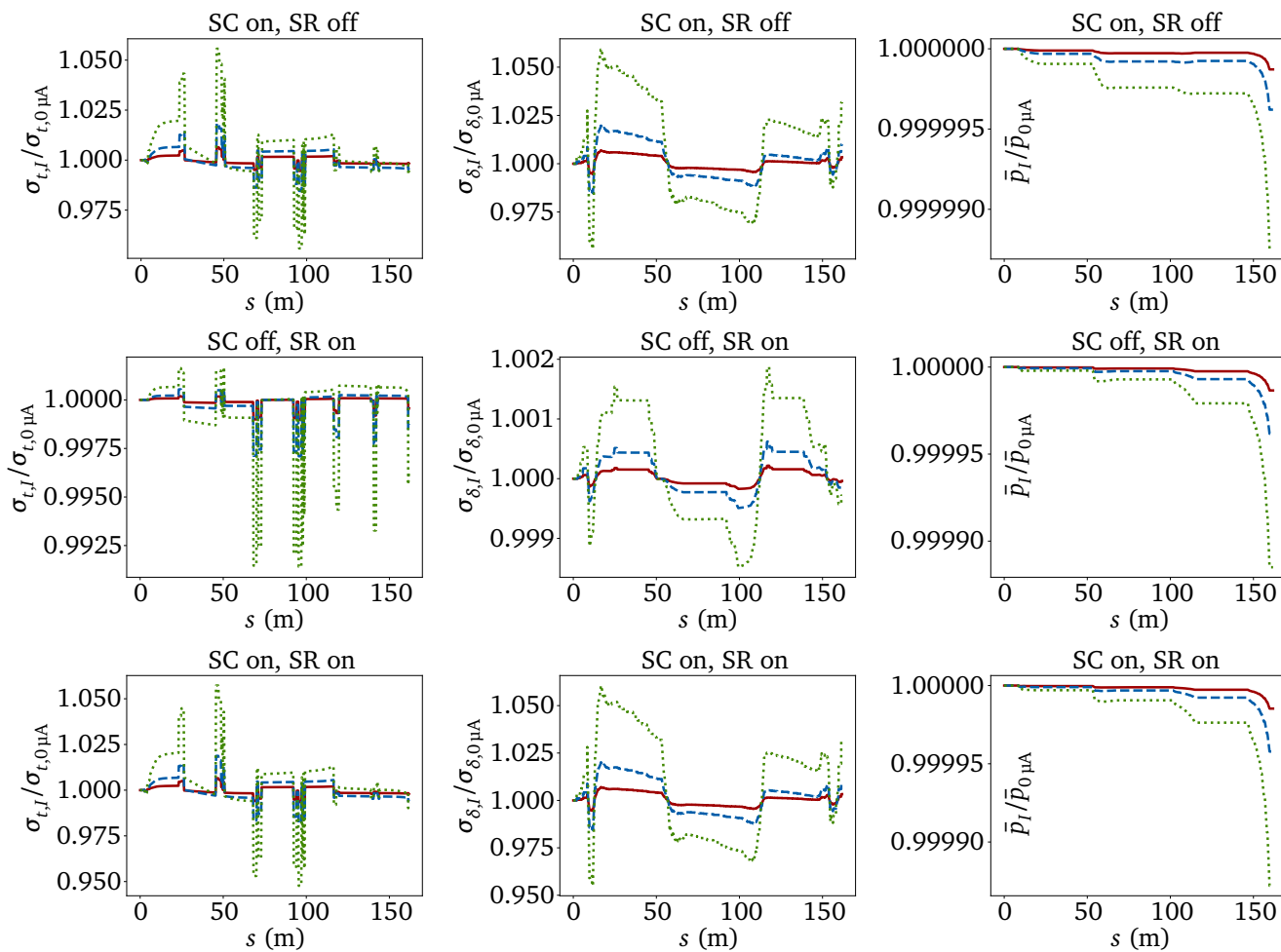


**Figure D.2: Influence on the 2-ER mode due to space-charge effects and synchrotron radiation (2/2).** For enabled space-charge effects (SC) and/or enabled synchrotron radiation (SR), relative behaviors of beam quantities along the accelerator as a function of the location  $s$  are shown for different beam currents after chopping,  $I$ . The simulations started behind the injector LINAC. Legend: 7  $\mu A$  (—), 20  $\mu A$  (---), 60  $\mu A$  (····).

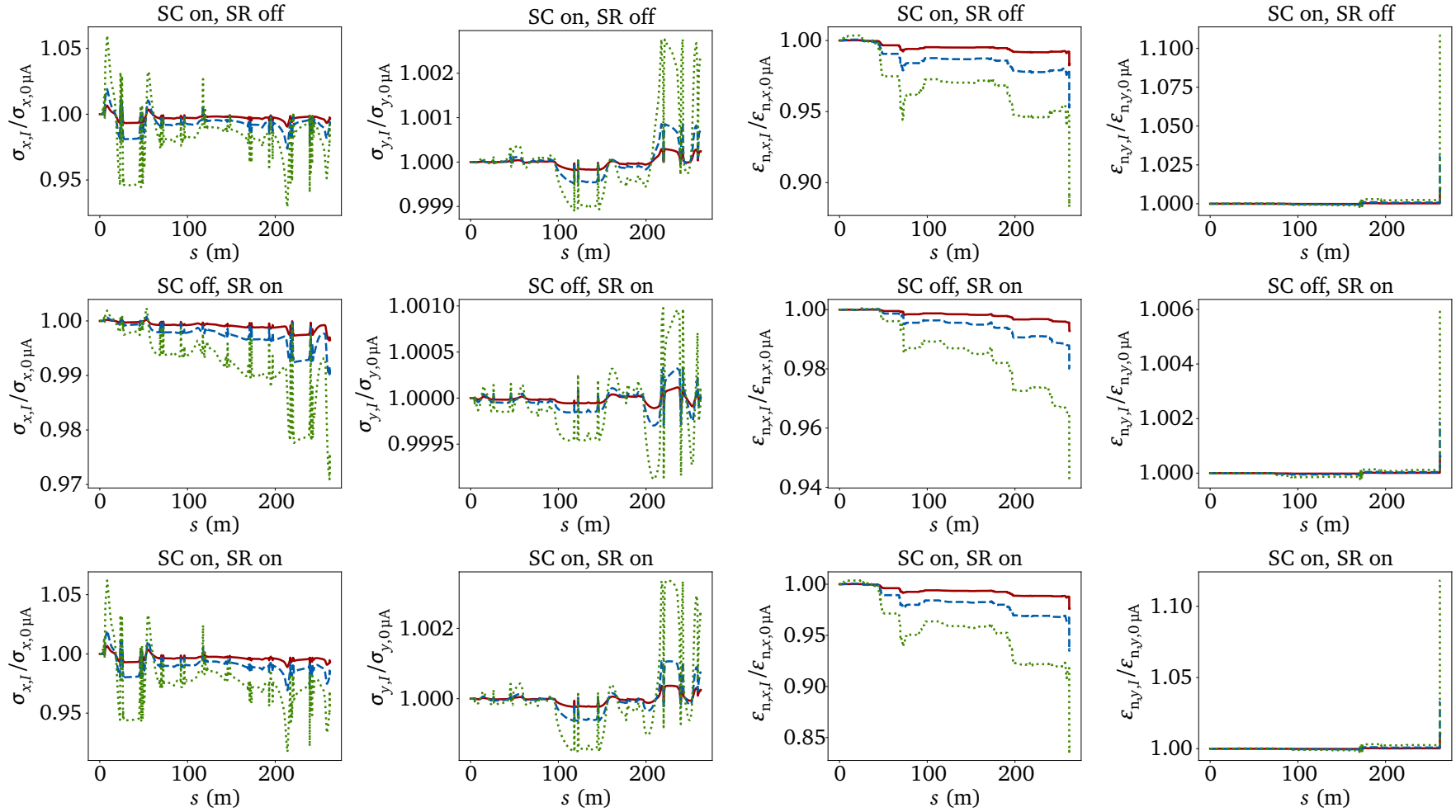


**Figure D.3: Influence on the 3-ER mode due to space-charge effects and synchrotron radiation (1/2).** For enabled space-charge effects (SC) and/or enabled synchrotron radiation (SR), relative behaviors of beam quantities along the accelerator as a function of the location  $s$  are shown for different beam currents after chopping,  $I$ . The simulations started behind the injector LINAC. Legend: 7  $\mu\text{A}$  (—), 20  $\mu\text{A}$  (- - -), 60  $\mu\text{A}$  (· · ·).

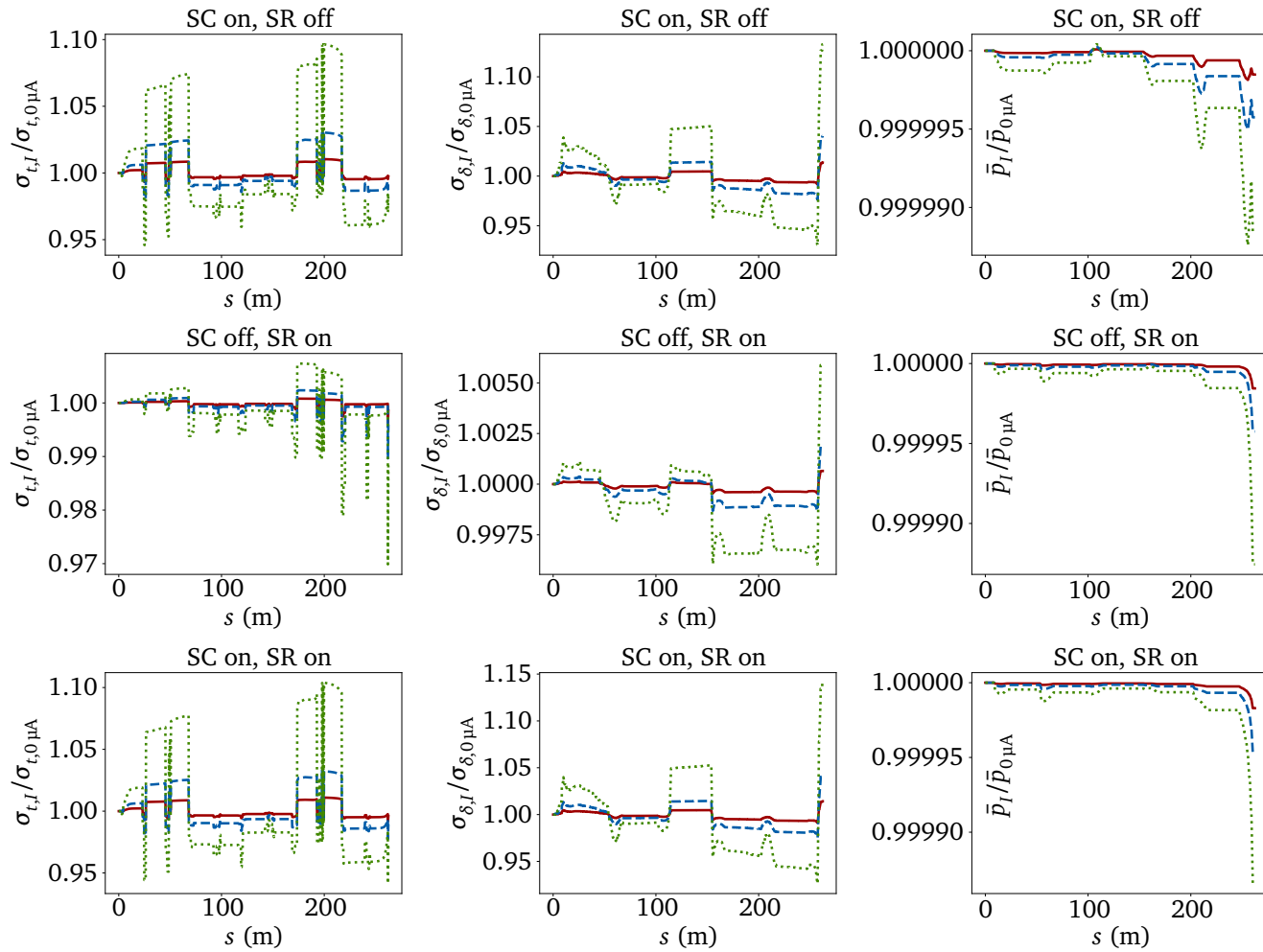


**Figure D.4: Influence on the 3-ER mode due to space-charge effects and synchrotron radiation (2/2).** For enabled space-charge effects (SC) and/or enabled synchrotron radiation (SR), relative behaviors of beam quantities along the accelerator as a function of the location  $s$  are shown for different beam currents after chopping,  $I$ . The simulations started behind the injector LINAC. Legend: 7  $\mu\text{A}$  (—), 20  $\mu\text{A}$  (- - -), 60  $\mu\text{A}$  (· · ·).





---

## E Determination of the Longitudinal Dispersion

As mentioned in section 4.2.4, the centroid longitudinal position cannot be observed directly at the S-DALINAC, but a centroid relative time of flight resulting from the individual path lengths and speeds of the electrons is determinable via remainder-centroid-phase measurements. Determining remainder centroid phases  $\bar{\theta}_{\text{mod}}$  as a function of the centroid relative momentum  $\bar{\delta}$  yields the longitudinal dispersion. This technique is explained here. First, the relation between the longitudinal dispersion and arrival times will be discussed, before the relation between arrival times and remainder centroid phases will be addressed. Linking both relations enables fitting the longitudinal dispersion to a remainder-centroid-phases measurement as a function of the centroid relative momentum.

In the following, a section from  $s_1$  to  $s_2$  is dealt with for which a certain design momentum  $p_0$  is defined. The individual momentum  $p$  and thus the relative momentum  $\delta$  can have an arbitrary<sup>1</sup> value but has to be constant along the path from  $s_1$  to  $s_2$ . Consequently, the speed  $v(\delta)$  of an individual electron is constant along the path from  $s_1$  to  $s_2$ . If  $t_s$  is the arrival time at the longitudinal position related to  $s$ , then the difference  $t_{s_2} - t_{s_1}$  is the time needed to cover the total distance from  $s_1$  to  $s_2$ ,  $\hat{l}(s_2) - \hat{l}(s_1)$ . Since the speed is constant for a given electron traveling from  $s_1$  to  $s_2$ ,  $t_{s_2} - t_{s_1}$  and  $\hat{l}(s_2) - \hat{l}(s_1)$  are related by:

$$t_{s_2} - t_{s_1} = \frac{\hat{l}(s_2) - \hat{l}(s_1)}{v(\delta)}. \quad (\text{E.1})$$

Using Eq. (3.21),  $\hat{l}(s_2) - \hat{l}(s_1)$  can be expressed in terms of the longitudinal dispersion acting from  $s_1$  to  $s_2$  as follows:

$$\begin{aligned} & \hat{l}(s_2) - \hat{l}(s_1) \\ &= (s_2 + l(s_2)) - (s_1 + l(s_1)) \\ &= s_2 - s_1 - l(s_1) + l(s_2) \end{aligned}$$

---

<sup>1</sup>Here, only beam dynamics up to the second order are addressed; this is only valid if the deviations from the corresponding design values have an appropriate size.

$$\begin{aligned}
&= s_2 - s_1 - l(s_1) \\
&\quad + \sum_{j=1}^6 R_{5j, s_1 \rightarrow s_2} X_j(s_1) \\
&\qquad\qquad\qquad + \sum_{j=1}^6 \sum_{k=j}^6 T_{5jk, s_1 \rightarrow s_2} X_j(s_1) X_k(s_1)
\end{aligned}$$

$$\begin{aligned}
&= s_2 - s_1 - l(s_1) \\
&\quad + \sum_{j=1}^4 R_{5j, s_1 \rightarrow s_2} X_j(s_1) \\
&\quad + \sum_{j=5}^5 R_{5j, s_1 \rightarrow s_2} X_j(s_1) \\
&\quad + \sum_{j=6}^6 R_{5j, s_1 \rightarrow s_2} X_j(s_1) \\
&\qquad\qquad\qquad + \sum_{j=1}^5 \sum_{k=j}^6 T_{5jk, s_1 \rightarrow s_2} X_j(s_1) X_k(s_1) \\
&\qquad\qquad\qquad + \sum_{j=6}^6 \sum_{k=j}^6 T_{5jk, s_1 \rightarrow s_2} X_j(s_1) X_k(s_1)
\end{aligned}$$

$$\begin{aligned}
&= s_2 - s_1 - l(s_1) \\
&\quad + \sum_{j=1}^4 R_{5j, s_1 \rightarrow s_2} X_j(s_1) \\
&\quad + 1 \cdot l(s_1) \\
&\quad + R_{56, s_1 \rightarrow s_2} \delta \\
&\qquad\qquad\qquad + \sum_{j=1}^5 \sum_{k=j}^6 T_{5jk, s_1 \rightarrow s_2} X_j(s_1) X_k(s_1) \\
&\qquad\qquad\qquad + \sum_{k=6}^6 T_{56k, s_1 \rightarrow s_2} \delta X_k(s_1)
\end{aligned}$$

$$\begin{aligned}
&= s_2 - s_1 \\
&\quad + \sum_{j=1}^4 R_{5j, s_1 \rightarrow s_2} X_j(s_1) \\
&\quad + R_{56, s_1 \rightarrow s_2} \delta \\
&\qquad\qquad\qquad + \sum_{j=1}^5 \sum_{k=j}^6 T_{5jk, s_1 \rightarrow s_2} X_j(s_1) X_k(s_1) \\
&\qquad\qquad\qquad + T_{566, s_1 \rightarrow s_2} \delta^2
\end{aligned}$$

$$\begin{aligned}
&=s_2 - s_1 \\
&\quad + \sum_{j=1}^4 R_{5j,s_1 \rightarrow s_2} X_j(s_1) \\
&\quad + R_{56,s_1 \rightarrow s_2} \delta \\
&\quad + \sum_{j=1}^5 \sum_{k=j}^5 T_{5jk,s_1 \rightarrow s_2} X_j(s_1) X_k(s_1) \\
&\quad + \sum_{j=1}^5 \sum_{k=6}^6 T_{5jk,s_1 \rightarrow s_2} X_j(s_1) X_k(s_1) \\
&\quad + T_{566,s_1 \rightarrow s_2} \delta^2 \\
&=s_2 - s_1 \\
&\quad + \sum_{j=1}^4 R_{5j,s_1 \rightarrow s_2} X_j(s_1) \\
&\quad + R_{56,s_1 \rightarrow s_2} \delta \\
&\quad + \sum_{j=1}^5 \sum_{k=j}^5 T_{5jk,s_1 \rightarrow s_2} X_j(s_1) X_k(s_1) \\
&\quad + \sum_{j=1}^5 T_{5j6,s_1 \rightarrow s_2} X_j(s_1) \delta \\
&\quad + T_{566,s_1 \rightarrow s_2} \delta^2. \tag{E.2}
\end{aligned}$$

By combining Eqs. (E.1) and (E.2), the longitudinal dispersion terms  $R_{56}$  and  $T_{566}$  are related to the difference of arrival times. As will be discussed later, the arrival time of a single electron at location  $s$ ,  $t_s$ , cannot be measured. Also the exact value of the centroid arrival time of a series of electrons arriving at  $s$ ,  $\bar{t}_s$ , cannot be measured, but a related remainder can be measured; however, the interest is only in a difference of centroid arrival times,  $\bar{t}_{s_2} - \bar{t}_{s_1}$ , which can be determined sufficiently from the remainder measurements (what will be discussed below). Hence,  $\bar{t}_{s_2} - \bar{t}_{s_1}$  can be assumed to be available. Since the relation

$$\bar{t}_{s_2} - \bar{t}_{s_1} = \frac{1}{N} \sum_{m=1}^N t_{s_2,m} - \frac{1}{N} \sum_{m=1}^N t_{s_1,m} = \frac{1}{N} \sum_{m=1}^N (t_{s_2,m} - t_{s_1,m}) = \langle t_{s_2} - t_{s_1} \rangle \tag{E.3}$$

applies, where the sums are evaluated over all  $N$  electrons (indicated by the index  $m$ ), which contribute to the centroid of a quantity, and where  $\langle \cdot \rangle$  denotes the centroid of the term between the angle brackets, the following applies:

$$\begin{aligned}
\bar{t}_{s_2} - \bar{t}_{s_1} &= \langle t_{s_2} - t_{s_1} \rangle = \left\langle \frac{\hat{l}(s_2) - \hat{l}(s_1)}{v} \right\rangle = \left\langle \frac{1}{v} \left( s_2 - s_1 + R_{56,s_1 \rightarrow s_2} \delta + T_{566,s_1 \rightarrow s_2} \delta^2 \right. \right. \\
&\quad \left. \left. + \sum_{j=1}^4 R_{5j,s_1 \rightarrow s_2} X_j(s_1) \right. \right. \\
&\quad \left. \left. + \sum_{j=1}^5 \sum_{k=j}^5 T_{5jk,s_1 \rightarrow s_2} X_j(s_1) X_k(s_1) \right. \right. \\
&\quad \left. \left. + \sum_{j=1}^5 T_{5j6,s_1 \rightarrow s_2} X_j(s_1) \delta \right) \right\rangle \\
&\approx \frac{1}{v(\bar{\delta})} \left( s_2 - s_1 + R_{56,s_1 \rightarrow s_2} \bar{\delta} + T_{566,s_1 \rightarrow s_2} \bar{\delta}^2 \right. \\
&\quad \left. + \sum_{j=1}^4 R_{5j,s_1 \rightarrow s_2} \langle X_j(s_1) \rangle \right. \\
&\quad \left. + \sum_{j=1}^5 \sum_{k=j}^5 T_{5jk,s_1 \rightarrow s_2} \langle X_j(s_1) X_k(s_1) \rangle \right. \\
&\quad \left. + \sum_{j=1}^5 T_{5j6,s_1 \rightarrow s_2} \langle X_j(s_1) \delta \rangle \right) \\
&\approx \frac{s_2 - s_1 + R_{56,s_1 \rightarrow s_2} \bar{\delta} + T_{566,s_1 \rightarrow s_2} \bar{\delta}^2 + C}{v(\bar{\delta})}, \quad (\text{E.4})
\end{aligned}$$

where  $\bar{\delta}$  is the centroid relative momentum intentionally changed during the measurement and

$$C = \sum_{j=1}^4 R_{5j,s_1 \rightarrow s_2} \langle X_j(s_1) \rangle + \sum_{j=1}^5 \sum_{k=j}^5 T_{5jk,s_1 \rightarrow s_2} \langle X_j(s_1) X_k(s_1) \rangle \quad (\text{E.5})$$

is a momentum independent term (as long as each component of  $\vec{X}(s_1)$  besides  $\delta(s_1)$  is independent of momentum changes upstream of  $s_1$  caused during the measurement, which is assumed here) and thus constant during the measurement. The centroid relative momentum  $\bar{\delta}$  is changed using a cavity located upstream of  $s_1$ ; this ensures a constant  $\delta$  per electron along the path from  $s_1$  to  $s_2$  as required. The first approximation in relation (E.4) is valid if  $\sigma_\delta$  is small. Note: even if large values for  $|\bar{\delta}|$  are intentionally caused during the measurement,  $\sigma_\delta$  remains small for all set  $\bar{\delta}$  if it was already small for  $\bar{\delta} = 0$  since it is the standard deviation with respect to the *corresponding*  $\bar{\delta}$  and not with respect to the *design*  $\bar{\delta}$  (which is zero). The second approximation in relation (E.4) is valid if the contribution of

$$\sum_{j=1}^5 T_{5j6,s_1 \rightarrow s_2} \langle X_j(s_1) \delta \rangle \quad (\text{E.6})$$

is insignificant, which is at least true in the first sections of the accelerator.

To analyze the moment of arrival at location  $s_1$  and  $s_2$ , respectively, a cavity monitor is used per position ( $s_1$  and  $s_2$  indicate the centers of the cavity monitors). However, centroid arrival times  $\bar{t}_s(\bar{\delta})$  <sup>(2)</sup> cannot be measured directly but only the remainder (with respect to a modulo operation) of the centroid phase of a cavity monitor: If a cavity monitor with suitable design angular frequency  $\omega$  (and consequently suitable oscillation period  $t_{\text{RF}} = 2\pi/\omega$ ) matched to  $2\pi$  times the bunch repetition rate is available at location  $s$ , each arriving electron will contribute to an appropriate electromagnetic field arising inside the cavity monitor. The electromagnetic field has a certain centroid phase  $\bar{\theta}_s(\bar{\delta})$  relative to a master oscillator. Here, only the remainder of  $\bar{\theta}_s(\bar{\delta})$ ,

$$\bar{\theta}_{\text{mod},s}(\bar{\delta}) := \bar{\theta}_s(\bar{\delta}) \bmod 360^\circ, \quad (\text{E.7})$$

is measurable. This measurable remainder centroid phase is related to a certain remainder time  $\bar{t}_{\text{mod},s}(\bar{\delta})$  by

$$\bar{\theta}_{\text{mod},s}(\bar{\delta}) + \theta_{\text{off},s} = \omega \bar{t}_{\text{mod},s}(\bar{\delta}), \quad (\text{E.8})$$

where  $\theta_{\text{off},s}$  is a certain  $\bar{\delta}$ -independent offset phase. There exists a value for  $\theta_{\text{off},s}$  so that  $\bar{t}_{\text{mod},s}(\bar{\delta})$  is the remainder of the centroid arrival time:

$$\bar{t}_{\text{mod},s}(\bar{\delta}) = \bar{t}_s(\bar{\delta}) \bmod t_{\text{RF}}. \quad (\text{E.9})$$

If Eq. (E.9) applies,  $\bar{t}_{\text{mod},s}(\bar{\delta})$  is called remainder centroid arrival time. By considering the difference of  $\bar{t}_{s_2}(\bar{\delta}_2) - \bar{t}_{s_1}(\bar{\delta}_2)$  and  $\bar{t}_{s_2}(\bar{\delta}_1) - \bar{t}_{s_1}(\bar{\delta}_1)$  for two different centroid relative momenta  $\bar{\delta}_1$  and  $\bar{\delta}_2$ , any  $\theta_{\text{off},s}$  vanishes (that is, determining the value for  $\theta_{\text{off},s}$  so that Eq. (E.9) applies is not necessary): Since

$$\begin{aligned} \bar{t}_{\text{mod},s_2}(\bar{\delta}) - \bar{t}_{\text{mod},s_1}(\bar{\delta}) &= \frac{\bar{\theta}_{\text{mod},s_2}(\bar{\delta}) + \theta_{\text{off},s_2}}{\omega} - \frac{\bar{\theta}_{\text{mod},s_1}(\bar{\delta}) + \theta_{\text{off},s_1}}{\omega} \\ &= \frac{\bar{\theta}_{\text{mod},s_2}(\bar{\delta}) - \bar{\theta}_{\text{mod},s_1}(\bar{\delta})}{\omega} + \frac{\theta_{\text{off},s_2} - \theta_{\text{off},s_1}}{\omega} \end{aligned} \quad (\text{E.10})$$

---

<sup>2</sup>Note: “ $\bar{t}_s(\bar{\delta})$ ” must be understood as the centroid value  $\bar{t}_s$  resulting from several electrons, which independently thereof have a certain centroid property ( $\bar{\delta}$ ); it must not be confused with “ $t_s(\delta)$ ” or “ $t_s(\bar{\delta})$ ”, which are the arrival times of a single electron having the mentioned individual relative momentum spread, which in the latter case is equal to the centroid relative momentum spread.

applies,

$$\begin{aligned}
& \left( \bar{t}_{\text{mod},s_2}(\bar{\delta}) - \bar{t}_{\text{mod},s_1}(\bar{\delta}) \right) - \left( \bar{t}_{\text{mod},s_2}(\bar{\delta}=0) - \bar{t}_{\text{mod},s_1}(\bar{\delta}=0) \right) \\
&= \left( \frac{\bar{\theta}_{\text{mod},s_2}(\bar{\delta}) - \bar{\theta}_{\text{mod},s_1}(\bar{\delta})}{\omega} + \frac{\theta_{\text{off},s_2} - \theta_{\text{off},s_1}}{\omega} \right) \\
&\quad - \left( \frac{\bar{\theta}_{\text{mod},s_2}(\bar{\delta}=0) - \bar{\theta}_{\text{mod},s_1}(\bar{\delta}=0)}{\omega} + \frac{\theta_{\text{off},s_2} - \theta_{\text{off},s_1}}{\omega} \right) \\
&= \left( \frac{\bar{\theta}_{\text{mod},s_2}(\bar{\delta}) - \bar{\theta}_{\text{mod},s_1}(\bar{\delta})}{\omega} \right) - \left( \frac{\bar{\theta}_{\text{mod},s_2}(\bar{\delta}=0) - \bar{\theta}_{\text{mod},s_1}(\bar{\delta}=0)}{\omega} \right) \tag{E.11}
\end{aligned}$$

follows, that is, the offset phases  $\theta_{\text{off},s_1}$  and  $\theta_{\text{off},s_2}$  are irrelevant if differences of differences of [sic] remainder centroid arrival times are to be evaluated. Utilizing that

$$\begin{aligned}
(\bar{t}_{s_2} - \bar{t}_{s_1}) \bmod t_{\text{RF}} &= (\bar{t}_{s_2} \bmod t_{\text{RF}} - \bar{t}_{s_1} \bmod t_{\text{RF}}) \bmod t_{\text{RF}} \\
&= (\bar{t}_{\text{mod},s_2} - \bar{t}_{\text{mod},s_1}) \bmod t_{\text{RF}} \tag{E.12}
\end{aligned}$$

applies for each two centroid arrival times  $\bar{t}_{s_1}$  and  $\bar{t}_{s_2}$  allows linking  $\bar{\theta}_{\text{mod},s}$  measurements to the longitudinal dispersion terms  $R_{56,s_1 \rightarrow s_2}$  and  $T_{566,s_1 \rightarrow s_2}$ :

$$\begin{aligned}
& \left( \left( \frac{\bar{\theta}_{\text{mod},s_2}(\bar{\delta}) - \bar{\theta}_{\text{mod},s_1}(\bar{\delta})}{\omega} \right) - \left( \frac{\bar{\theta}_{\text{mod},s_2}(\bar{\delta}=0) - \bar{\theta}_{\text{mod},s_1}(\bar{\delta}=0)}{\omega} \right) \right) \bmod t_{\text{RF}} + \Pi(\bar{\delta}) \\
&= \left( \left( \bar{t}_{\text{mod},s_2}(\bar{\delta}) - \bar{t}_{\text{mod},s_1}(\bar{\delta}) \right) - \left( \bar{t}_{\text{mod},s_2}(\bar{\delta}=0) - \bar{t}_{\text{mod},s_1}(\bar{\delta}=0) \right) \right) \bmod t_{\text{RF}} + \Pi(\bar{\delta}) \\
&= \left( \left( \bar{t}_{\text{mod},s_2}(\bar{\delta}) - \bar{t}_{\text{mod},s_1}(\bar{\delta}) \right) \bmod t_{\text{RF}} - \left( \bar{t}_{\text{mod},s_2}(\bar{\delta}=0) - \bar{t}_{\text{mod},s_1}(\bar{\delta}=0) \right) \bmod t_{\text{RF}} \right) \bmod t_{\text{RF}} \\
&\quad + \Pi(\bar{\delta}) \\
&= \left( (\bar{t}_{s_2}(\bar{\delta}) - \bar{t}_{s_1}(\bar{\delta})) \bmod t_{\text{RF}} - (\bar{t}_{s_2}(\bar{\delta}=0) - \bar{t}_{s_1}(\bar{\delta}=0)) \bmod t_{\text{RF}} \right) \bmod t_{\text{RF}} + \Pi(\bar{\delta}) \\
&= \left( (\bar{t}_{s_2}(\bar{\delta}) - \bar{t}_{s_1}(\bar{\delta})) - (\bar{t}_{s_2}(\bar{\delta}=0) - \bar{t}_{s_1}(\bar{\delta}=0)) \right) \bmod t_{\text{RF}} + \Pi(\bar{\delta}) \\
&\approx \left( \frac{s_2 - s_1 + R_{56,s_1 \rightarrow s_2} \bar{\delta} + T_{566,s_1 \rightarrow s_2} \bar{\delta}^2 + C}{v(\bar{\delta})} - \frac{s_2 - s_1 + C}{v(\bar{\delta}=0)} \right) \bmod t_{\text{RF}} + \Pi(\bar{\delta}) \\
&= \left( \frac{R_{56,s_1 \rightarrow s_2} \bar{\delta} + T_{566,s_1 \rightarrow s_2} \bar{\delta}^2}{v(\bar{\delta})} + (s_2 - s_1 + C) \cdot \left( \frac{1}{v(\bar{\delta})} - \frac{1}{v(\bar{\delta}=0)} \right) \right) \bmod t_{\text{RF}} + \Pi(\bar{\delta}) \\
&\approx \left( \frac{R_{56,s_1 \rightarrow s_2} \bar{\delta} + T_{566,s_1 \rightarrow s_2} \bar{\delta}^2}{v(\bar{\delta})} + (s_2 - s_1) \cdot \left( \frac{1}{v(\bar{\delta})} - \frac{1}{v(\bar{\delta}=0)} \right) \right) \bmod t_{\text{RF}} + \Pi(\bar{\delta}), \tag{E.13}
\end{aligned}$$

where  $\Pi$  is an appropriate step function defined so that jump discontinuities potentially caused by the modulo operations are avoided. The last approximation in relation (E.13) is valid if  $s_2 - s_1 \gg |C|$ , which is at least true for the case in which  $s_1$  and  $s_2$  are the centers of

the cavity monitors of the injector arc, I1HF01 and A1HF01, respectively. Here,  $s_2 - s_1$  is in the order of meters while  $|C|$  is in the order of millimeters or smaller; additionally,  $|C|$  is smaller than the measurement uncertainty of  $s_2 - s_1$ .

Finally, the parameters  $R_{56, s_1 \rightarrow s_2}$  and  $T_{566, s_1 \rightarrow s_2}$  are fit to the measured  $\bar{\theta}_{\text{mod}, s}(\bar{\delta})$  based on relation (E.13).

For convenience, the definition of the relative centroid time of flight from  $s_1$  to  $s_2$ ,

$$\begin{aligned} \tilde{t}_{s_1 \rightarrow s_2}(\bar{\delta}) &:= (\bar{t}_{s_2}(\bar{\delta}) - \bar{t}_{s_1}(\bar{\delta})) - (\bar{t}_{s_2}(\bar{\delta} = 0) - \bar{t}_{s_1}(\bar{\delta} = 0)) \\ &= \left( (\bar{t}_{s_2}(\bar{\delta}) - \bar{t}_{s_1}(\bar{\delta})) - (\bar{t}_{s_2}(\bar{\delta} = 0) - \bar{t}_{s_1}(\bar{\delta} = 0)) \right) \bmod t_{\text{RF}} + \Pi(\bar{\delta}), \end{aligned} \quad (\text{E.14})$$

is used in section 4.2.4 (in particular in Fig. 4.6).





---

# Bibliography

- [1] R. Abela *et al.*, “XFEL: The European X-Ray Free-Electron Laser – Technical Design Report”, DESY (2006).
- [2] A. V. Mishin, “Advances in X-band and S-band linear accelerators for security, NDT, and other applications”, In Proc. PAC 2005, 240–244 (2005).
- [3] Y. S. Lee *et al.*, “Development of side-coupled X-band medical linear accelerator for radiotherapy”, In Proc. LINAC 2018, 139–141 (2019).
- [4] M. Tigner, “A possible apparatus for electron clashing-beam experiments”, *Nuovo Cim.* **37**, 1228–1231 (1965).
- [5] P. Williams, “A route to greener Big Science”, *Nat. Phys.* **19**, 479–480 (2023).
- [6] L. Merminga *et al.*, “High-Current Energy-Recovering Electron Linacs”, *Annu. Rev. Nucl. Part. Sci.* **53**, 387–429 (2003).
- [7] V. N. Litvinenko, T. Roser, M. Chamizo-Llatas, “High-energy high-luminosity  $e^+e^-$  collider using energy-recovery linacs”, *Phys. Lett. B* **804**, 135394 (2020).
- [8] P. Agostini *et al.*, “The Large Hadron-Electron Collider at the HL-LHC”, *J. Phys. G* **48**, 110501 (2021).
- [9] B. S. Schlimme *et al.*, “Operation and characterization of a windowless gas jet target in high-intensity electron beams”, *Nucl. Instrum. Methods Phys. Res. A* **1013**, 165668 (2021).
- [10] Y. Derbenev, Y. Zhang, “Electron Cooling for Electron-Ion Collider at JLAB”, In Proc. COOL 2009, 181–184 (2010).
- [11] G. R. Neil *et al.*, “The JLab high power ERL light source”, *Nucl. Instrum. Methods Phys. Res. A* **557**, 9–15 (2006).
- [12] T. Akagi *et al.*, “Narrow-band photon beam via laser Compton scattering in an energy recovery linac”, *Phys. Rev. Accel. Beams* **19**, 114701 (2016).
- [13] L. R. Elias, J. Hu, G. Ramian, “The UCSB electrostatic accelerator free electron laser: First operation”, *Nucl. Instrum. Methods Phys. Res. A* **237**, 203–206 (1985).

- 
- [14] M. Arnold *et al.*, “First operation of the superconducting Darmstadt linear electron accelerator as an energy recovery linac”, *Phys. Rev. Accel. Beams* **23**, 020101 (2020).
- [15] S. O. Schriber, E. A. Heighway, “Double pass linear accelerator – reflexotron”, *IEEE Trans. Nucl. Sci.* **22**, 1060–1064 (1975).
- [16] D. W. Feldman *et al.*, “The Los Alamos Free-Electron Laser Energy-Recovery Experiment”, In *Proc. PAC 1987*, 221–223 (1987).
- [17] G. Spalek *et al.*, “The Free Electron Laser Variable Bridge Coupler”, *IEEE Trans. Nucl. Sci.* **32**, 2860–2862 (1985).
- [18] C. A. Brau *et al.*, “High efficiency free-electron laser systems”, In *Proc. Lasers 1979*, 26–32 (1980).
- [19] A. Richter, “Operational Experience at the S-DALINAC”, In *Proc. EPAC 1996*, 110–114 (1996).
- [20] N. Pietralla, “The institute of nuclear physics at the TU Darmstadt”, *Nucl. Phys. News* **28**, 4–11 (2018).
- [21] G. Pérez Segurana, I. R. Bailey, P. H. Williams, “Construction of self-consistent longitudinal matches in multipass energy recovery linacs”, *Phys. Rev. Accel. Beams* **25**, 021003 (2022).
- [22] R. Koscica *et al.*, “Energy and rf cavity phase symmetry enforcement in multiturn energy recovery linac models”, *Phys. Rev. Accel. Beams* **22**, 091602 (2019).
- [23] C. Adolphsen *et al.*, “The Development of Energy-Recovery Linacs”, arXiv:2207.02095 [physics.acc-ph] (2022).
- [24] C. Wang, J. Noonan, J. Lewellen, “Dual-Axis Energy Recovery Linac”, In *Proc. ERL 2007*, 122–125 (2007).
- [25] F. Marhauser *et al.*, “Method for energy recovery of spent ERL beams”, United States Patent, Patent Number 9,872,375 B2 (2018).
- [26] T. I. Smith *et al.*, “Development of the SCA/FEL for use in biomedical and materials science experiments”, *Nucl. Instrum. Methods Phys. Res. A* **259**, 1–7 (1987).
- [27] J. B. Flanz, C. P. Sargent, “Tests with an isochronous recirculation system”, *IEEE Trans. Nucl. Sci.* **32**, 3213–3215 (1985).
- [28] R. Hajima *et al.*, “First demonstration of energy-recovery operation in the JAERI superconducting linac for a high-power free-electron laser”, *Nucl. Instrum. Methods Phys. Res. A* **507**, 115–119 (2003).

- 
- [29] J. Alexander *et al.*, “Progress on the commissioning of ALICE, the energy recovery linac-based light source at Daresbury Laboratory”, In Proc. PAC 2009, 1281–1283 (2009).
- [30] M. Akemoto *et al.*, “Construction and commissioning of the compact energy-recovery linac at KEK”, Nucl. Instrum. Methods Phys. Res. A **877**, 197–219 (2018).
- [31] N. A. Vinokurov *et al.*, “Novosibirsk free electron laser: operation and second stage commissioning”, In Proc. RuPAC 2008, 181–184 (2008).
- [32] O. A. Shevchenko *et al.*, “Commissioning status and further development of the Novosibirsk Multiturn ERL”, In Proc. ERL 2013, 6–10 (2013).
- [33] A. Bartnik *et al.*, “CBETA: first multipass superconducting linear accelerator with energy recovery”, Phys. Rev. Lett. **125**, 044803 (2020).
- [34] A. Bogacz *et al.*, “CEBAF energy recovery experiment”, In Proc. PAC 2003, 195–197 (2003).
- [35] S. A. Bogacz *et al.*, “ER@CEBAF: a test of 5-pass energy recovery at CEBAF”, BNL (2016).
- [36] A. Neumann *et al.*, “bERLinPro Becomes SEALab: Status and Perspective of the Energy Recovery Linac at HZB”, In Proc. IPAC 2022, 1110–1113 (2022).
- [37] D. Angal-Kalinin *et al.*, “PERLE. Powerful energy recovery linac for experiments. Conceptual design report”, J. Phys. G: Nucl. Part. Phys. **45**, 065003 (2018).
- [38] C. Curatolo, L. Serafini, “Electrons and X-rays to Muon Pairs (EXMP)”, Appl. Sci. **12**, 3149 (2022).
- [39] A. Abada *et al.*, “FCC Physics Opportunities”, Eur. Phys. J. C **79**, 474 (2019).
- [40] V. I. Telnov, “A high-luminosity superconducting twin  $e^+e^-$  linear collider with energy recovery”, JINST **16**, P12025 (2021).
- [41] “Strive towards sustainability”, Nat. Phys. **19**, 761 (2023).
- [42] A. Hutton, “Energy-recovery linacs for energy-efficient particle acceleration”, Nat. Rev. Phys. **5**, 708–716 (2023).
- [43] M. Klein *et al.*, Ch. 6 “Energy-recovery linacs” in “European Strategy for Particle Physics – Accelerator R&D Roadmap”, CERN Yellow Rep. Monogr. 1, 187–229 (2022).
- [44] F. Gudden *et al.*, “Eine Anordnung für Experimente zur Elektronenstreuung unterhalb 60 MeV”, Z. Phys. **181**, 453–478 (1964).

- 
- [45] M. Arnold, “Auslegung, Planung und Aufbau einer dritten Rezirkulation mit ERL-Modus für den S-DALINAC”, Dissertation, TU Darmstadt (2017).
- [46] Y. Fritzsche, “Aufbau und Inbetriebnahme einer Quelle polarisierter Elektronen am supraleitenden Darmstädter Elektronenlinearbeschleuniger S-DALINAC”, Dissertation, TU Darmstadt (2011).
- [47] M. Wagner, “Erzeugung und Untersuchung gepulster polarisierter Elektronenstrahlen am S-DALINAC”, Dissertation, TU Darmstadt (2013).
- [48] M. Gros, “Optimierung der thermionischen Elektronenquelle des S-DALINAC und Konzeptionierung einer Strahlstrommessung”, Master thesis, TU Darmstadt (2016, unpublished).
- [49] N. Somjit *et al.*, “Numerical Simulation and Optimization of a 3-GHz Chopper/Pre-buncher System for the S-DALINAC”, In Proc. EPAC 2006, 2185–2187 (2006).
- [50] T. Bahlo, “Konfiguration und Test eines Hochfrequenz-Chopper- und Bunchersystems für den S-DALINAC”, Bachelor thesis, TU Darmstadt (2010, unpublished).
- [51] L. Jürgensen *et al.*, “A High-Energy-Scrapersystem for the S-DALINAC Extraction – Design and Installation”, In Proc. IPAC 2016, 101–104 (2016).
- [52] D. Bazyl, “Development of an SRF Reduced-beta Cavity for the Injector of the S-DALINAC”, Dissertation, TU Darmstadt (2019).
- [53] S. M. Weih, “Injector Optimization at the Superconducting Darmstadt Linear Electron Accelerator S-DALINAC”, Dissertation, TU Darmstadt (2022).
- [54] K. Sonnabend *et al.*, “The Darmstadt High-Intensity Photon Setup (DHIPS) at the S-DALINAC”, Nucl. Instrum. Methods Phys. Res. A **640**, 6–12 (2011).
- [55] D. Savran *et al.*, “The low-energy photon tagger NEPTUN”, Nucl. Instrum. Methods Phys. Res. A **613**, 232–239 (2010).
- [56] C. Lüttge *et al.*, “Large aperture system for high-resolution 180° electron scattering”, Nucl. Instrum. Methods Phys. Res. A **366**, 325–331 (1995).
- [57] D. Schüll *et al.*, “High Resolution Electron Scattering Facility at the Darmstadt Linear Accelerator (DALINAC)”, Nucl. Instrum. Methods **153**, 29–41 (1978).
- [58] M. Arnold *et al.*, “First ERL operation of S-DALINAC and commissioning of a path length adjustment system”, In Proc. IPAC 2018, 4859–4862 (2018).
- [59] M. Reichenbach, “Bau und Erprobung von Strom- und Positionsmonitoren zur Strahlüberwachung am S-DALINAC sowie Rechnungen zur Strahlführung des FEL”, Diploma thesis, TU Darmstadt (1996, unpublished).

- 
- [60] S. Döbert, “Nichtlineare Zeitreihenanalyse der Feldamplitude der supraleitenden Beschleunigungsstrukturen und Aufbau eines HF-Monitorsystems zur zerstörungsfreien Strahldiagnose am S-DALINAC”, Dissertation, TU Darmstadt (1999).
- [61] M. Herbert, “Aufbau und Test eines Phasenmonitors für die Strahlstabilisierung am Injektor des S-DALINAC”, Bachelor thesis, TU Darmstadt (2013, unpublished).
- [62] L. Jürgensen, “Aufbau eines Strahlverlustmesssystems für den S-DALINAC”, Bachelor thesis, TU Darmstadt (2011, unpublished).
- [63] J. Pforr, “Strahldynamik und -diagnose am Energie-rückgewinnenden S-DALINAC”, Dissertation, TU Darmstadt (2020).
- [64] P. Lecoq *et al.*, “Inorganic Scintillators for Detector Systems – Physical Principles and Crystal Engineering”, 2nd edition, Springer (2006).
- [65] V. L. Ginzburg, I. M. Frank, “Radiation of a uniformly moving electron due to its transition from one medium into another”, *J. Phys. (USSR)* **9**, 353–362 (1945).
- [66] M. Dutine, “Entwicklung und Test einer Messung der Strahlqualität am S-DALINAC”, Master thesis, TU Darmstadt (2018, unpublished).
- [67] M. Dutine *et al.*, “Concept of a Beam Diagnostics System for the Multi-Turn ERL Operation at the S-DALINAC”, In Proc. IPAC 2022, 254–256 (2022).
- [68] M. G. Minty, F. Zimmermann, “Measurement and Control of Charged Particle Beams”, 1st edition, Springer (2003).
- [69] L. Rivkin *et al.*, “Bunch Lengthening in the SLC Damping Ring”, In Proc. EPAC 1988, 634–637 (1988).
- [70] M. Steinhorst *et al.*, “RF average power measurement system at the S-DALINAC”, *Nucl. Instrum. Methods Phys. Res. A* **1010**, 165567 (2021).
- [71] T. P. Wangler, “RF Linear Accelerators”, 2nd edition, WILEY-VCH (2008).
- [72] Dassault Systèmes, CST Studio Suite 2024.
- [73] T. Kürzeder *et al.*, “Beam Break-up Measurements at the Recirculating Electron Accelerator S-DALINAC”, In Proc. IPAC 2016, 1714–1716 (2016).
- [74] K. Floettmann, “ASTRA – A Space Charge Tracking Algorithm”, V 4.0, DESY (2022).
- [75] K. L. Brown, “A First- and Second-Order Matrix Theory for the Design of Beam Transport Systems and Charged Particle Spectrometers”, SLAC Report 75, Revision 2 (1971).
- [76] H. Wiedemann, “Particle Accelerator Physics”, 4th edition, Springer (2019).

- 
- [77] K. L. Brown *et al.*, “TRANSPORT: a computer program for designing charged-particle beam-transport systems”, CERN Report 80-04 (1980).
- [78] P. H. Williams *et al.*, “Arclike variable bunch compressors”, *Phys. Rev. Accel. Beams* **23**, 100701 (2020).
- [79] N. Nakamura, “Effects of Longitudinal and Transverse Resistive-Wall Wakefields on ERLs”, In Proc. ERL 2009, 85–89 (2009).
- [80] M. Billing, H. Williams, “Effect of Wake Fields in an Energy Recovery Linac”, In Proc. PAC 2009, 4625–4627 (2009).
- [81] G. H. Hoffstaetter, Y. H. Lau, “Compensation of wakefield-driven energy spread in energy recovery linacs”, *Phys. Rev. ST Accel. Beams* **11**, 070701 (2008).
- [82] J. J. Bisognano, M. L. Fripp, “Requirements for longitudinal HOM damping in superconducting”, In Proc. LINAC 1988, 388–390 (1988).
- [83] G. H. Hoffstaetter, I. V. Bazarov, “Beam-breakup instability theory for energy recovery linacs”, *Phys. Rev. ST Accel. Beams* **7**, 054401 (2004).
- [84] B. C. Yunn, “A Beam Breakup Instability in a Recirculating Linac Caused by a Quadrupole Mode”, In Proc. PAC 2003, 3246–3248 (2003).
- [85] C. Xu, I. Ben-Zvi, “HOM frequency control of SRF cavity in high current ERLs”, *Nucl. Instrum. Methods Phys. Res. A* **883**, 136–142 (2018).
- [86] F. Marhauser, “Next generation HOM-damping”, *Supercond. Sci. Technol.* **30**, 063002 (2017).
- [87] S. Setiniyaz, R. Apsimon, P. H. Williams, “Filling pattern dependence of regenerative beam breakup instability in energy recovery linacs”, *Phys. Rev. Accel. Beams* **24**, 061003 (2021).
- [88] R. E. Rand, T. I. Smith, “Beam Optical Control of Beam Breakup In a Recirculating Electron Accelerator”, *Part. Accel.* **11**, 1–13 (1980).
- [89] V. N. Litvinenko, “Chromaticity of the lattice and beam stability in energy recovery linacs”, *Phys. Rev. ST Accel. Beams* **15**, 074401 (2012). ; V. N. Litvinenko, “Erratum: Chromaticity of the lattice and beam stability in energy recovery linacs [Phys. Rev. ST Accel. Beams **15**, 074401 (2012)]”, *Phys. Rev. ST Accel. Beams* **18**, 039901 (2015).
- [90] S. Glukhov, “Multipass beam breakup instability countermeasures in energy recovery linacs”, Dissertation, TU Darmstadt (2022).
- [91] T. Kürzeder *et al.*, “Investigations on Transverse Beam Break Up Using a Recirculated Electron Beam”, In Proc. ERL 2015, 30–33 (2015).

- 
- [92] M. Liepe, J. Knobloch, “Superconducting RF for energy-recovery linacs”, Nucl. Instrum. Methods Phys. Res. A **557**, 354–369 (2006).
- [93] J. Pforr, “Erste Start-to-End Strahldynamiksimulation des S-DALINAC mit *elegant* und Einstellungen für Experimente zu transversalem Beam Breakup”, Master thesis, TU Darmstadt (2016, unpublished).
- [94] D. Simon *et al.*, “Lattice and Beam Dynamics of the Energy Recovery Mode of the Mainz Energy-recovering Superconducting Accelerator MESA”, In Proc. IPAC 2015, 220–222 (2015).
- [95] C. Gerth, F. E. Hannon, “Injector Design for the 4GLS Energy Recovery Linac Prototype”, In Proc. EPAC 2004, 437–439 (2004).
- [96] B. Kuske *et al.*, “The Injector Layout of BERLinPro”, In Proc. IPAC 2013, 288–290 (2013).
- [97] S. Sakanaka *et al.*, “Construction and Commissioning of Compact-ERL Injector at KEK”, In Proc. ERL 2013, 16–21 (2013).
- [98] C. Gulliford *et al.*, “Demonstration of low emittance in the Cornell energy recovery linac injector prototype”, Phys. Rev. ST Accel. Beams **16**, 073401 (2013).
- [99] B. Hounsell *et al.*, “Conceptual Design of the PERLE Injector”, In Proc. LINAC 2022, 743–746 (2022).
- [100] B. Muratori, C. Gerth, N. Vinokurov, “Space Charge Effects for the ERL Prototype Injector Line at Daresbury Laboratory”, In Proc. EPAC 2004, 446–448 (2004).
- [101] A. Khan *et al.*, “Beam matching with space charge in energy recovery linacs”, Nucl. Instrum. Methods Phys. Res. A **948**, 162822 (2019).
- [102] V. N. Litvinenko *et al.*, “Merger designs for ERLs”, Nucl. Instrum. Methods Phys. Res. A **557**, 165–175 (2006).
- [103] J.-G. Hwang *et al.*, “Effects of space charge in a compact superconducting energy recovery linac with a low energy”, Nucl. Instrum. Methods Phys. Res. A **684**, 18–26 (2012).
- [104] M. Michael, “Simulationsbasierte Analyse der Strahldynamik im Injektor des S-DALINAC”, Master thesis, TU Darmstadt (2018, unpublished).
- [105] K. Wille, “Physik der Teilchenbeschleuniger und Synchrotronstrahlungsquellen”, 2nd edition, Teubner (1996).
- [106] S. Di Mitri, “Coherent Synchrotron Radiation and Microbunching Instability”, In Proc. CAS 2016, CERN Yellow Reports: School Proceedings, CERN-2018-001-SP (2018).

- 
- [107] M. Borland, “Simple method for particle tracking with coherent synchrotron radiation”, *Phys. Rev. ST Accel. Beams* **4**, 070701 (2001).
- [108] W. Lou, G. H. Hoffstaetter, “Coherent synchrotron radiation wake expressions with two bending magnets and simulation results for a multiturn energy-recovery linac”, *Phys. Rev. Accel. Beams* **23**, 054404 (2020).
- [109] K. D. J. André, B. J. Holzer, S. A. Bogacz, “Studies of the Energy Recovery Performance of the PERLE Project”, In *Proc. IPAC 2021*, 2744–2747 (2021).
- [110] R. Hajima, “Emittance compensation in a return arc of an energy-recovery linac”, *Nucl. Instrum. Methods Phys. Res. A* **528**, 335–339 (2004).
- [111] V. Yakimenko *et al.*, “Experimental Observation of Suppression of Coherent-Synchrotron-Radiation-Induced Beam-Energy Spread with Shielding Plates”, *Phys. Rev. Lett.* **109**, 164802 (2012).
- [112] F. Schliessmann *et al.*, “2D beam-dynamics simulations code for the twofold energy-recovery mode at S-DALINAC”, TUdataLib 963 (2022).
- [113] F. Schliessmann *et al.*, “Data set for the twofold energy-recovery mode at S-DALINAC”, TUdataLib 964 (2022).
- [114] F. Schliessmann *et al.*, “Realization of a multi-turn energy recovery accelerator”, *Nat. Phys.* **19**, 597–602 (2023).
- [115] P. Piot, D. R. Douglas, G. A. Krafft, “Longitudinal phase space manipulation in energy recovering linac-driven free-electron lasers”, *Phys. Rev. ST Accel. Beams* **6**, 030702 (2003).
- [116] M. Borland, “elegant: a Flexible SDDS-Compliant Code for Accelerator Simulation”, *Advanced Photon Source LS-287* (2000).
- [117] F. R. J. Hug, “Erhöhung der Energieschärfe des Elektronenstrahls am S-DALINAC durch nicht-isochrones Rezirkulieren”, *Dissertation*, TU Darmstadt (2013).
- [118] F. Schließmann, “Untersuchungen zur nichtlinearen Strahldynamik und Optionen für Strahlführungsmodifikationen am S-DALINAC”, *Master thesis*, TU Darmstadt (2017, unpublished).
- [119] A. Savitzky, M. J. E. Golay, “Smoothing and differentiation of data by simplified least squares procedures”, *Anal. Chem.* **36**, 1627–1639 (1964).
- [120] F. Hug *et al.*, “Beam Dynamics Calculations and Magnet Design for Future Measurements of Transverse Beam Break-Up at the S-DALINAC”, In *Proc. LINAC 2014*, 729–732 (2014).



- 
- [121] M. Arnold *et al.*, “Construction and Status of the Thrice Recirculating S-DALINAC”, In Proc. IPAC 2017, 1384–1387 (2017).
- [122] M. Meier *et al.*, “Development of a setup for laser-Compton backscattering at the S-DALINAC”, In Proc. IPAC 2023, 2139–2142 (2023).
- [123] F. Schliessmann *et al.*, “Studies on a triple-turn energy-recovery mode at the S-DALINAC”, Preprint in Proc. IPAC 2023, 2143–2146 (2023).
- [124] F. Schliessmann *et al.*, “Studies on a Triple-Turn Energy-Recovery Mode at the S-DALINAC”, J. Phys.: Conf. Ser. **2687**, 032023 (2024).
- [125] F. Schließmann *et al.*, “Determination of the Momentum Spread While Running in the ERL Mode at the S-DALINAC”, In Proc. IBIC 2019, 300–303 (2019).
- [126] A. Hofmann, “The Physics of Synchrotron Radiation”, 1st edition, Cambridge University Press (2004).
- [127] P. Chevtsov *et al.*, “Non-invasive energy spread monitoring for the JLAB experimental program via synchrotron light interferometers”, Nucl. Instrum. Methods Phys. Res. A **557**, 324–332 (2006).
- [128] D. X. Wang *et al.*, “A fast coherent synchrotron radiation monitor for the bunch length of the short CEBAF bunches”, AIP Conference Proceedings **367**, 502–511 (1996).
- [129] J. Wan *et al.*, “Simulation of wire scanner for high repetition free electron laser facilities”, Nucl. Instrum. Methods Phys. Res. A **1026**, 166200 (2022).
- [130] H. Kolanoski, N. Wermes, “Teilchendetektoren, Grundlagen und Anwendungen”, 1st edition, Springer (2016).
- [131] C. Sun *et al.*, “Energy and energy spread measurements of an electron beam by Compton scattering method”, Phys. Rev. ST Accel. Beams **12**, 062801 (2009).
- [132] M. G. Meier, “Entwicklung und Aufbau der Laser-getriebenen Compton-Rückstreuquelle COBRA für Strahldiagnose am S-DALINAC”, Dissertation, TU Darmstadt (2024).
- [133] Q. King, “Analysis of the Influence of Fibre Diameter on Wirescanner Beam Profile Measurements”, CERN-SPS-ABM-Note-88-02 (1988).
- [134] A. Krugmann, “Entwicklung einer lokalen Target-Steuerung am S-DALINAC”, Bachelor thesis, TU Darmstadt (2006, unpublished).
- [135] L. E. Jürgensen, “Entwicklung und Aufbau eines Hochenergie-Elektronen-Scrapersystems für den S-DALINAC”, Dissertation, TU Darmstadt (2018).
- [136] Siemens Digital Industries Software, NX 12.0.

- 
- [137] J. Frisch *et al.*, “Beam Measurements at LCLS”, In Proc. BIW 2008, 17–26 (2008).
- [138] M. Borland, “User’s Manual for elegant. Program Version 2023.4”, Advanced Photon Source (2023).
- [139] M. Borland *et al.*, “User’s Guide for SDDS Toolkit Version 5.0”, Advanced Photon Source (2020).
- [140] G. van Rossum, F. L. Drake, “Python 3 Reference Manual”, CreateSpace (2009).
- [141] K. G. Steffen, “High Energy Beam Optics”, 1st edition, Interscience Publishers (1965).
- [142] Z. Huang *et al.*, “Suppression of microbunching instability in the linac coherent light source”, Phys. Rev. ST Accel. Beams **7**, 074401 (2004).
- [143] I. V. Bazarov, T. Miyajima, “Calculation of coherent synchrotron radiation in general particle tracer”, In Proc. EPAC 2008, 118–120 (2008).

---

# Danksagung

Abschließend möchte ich die Gelegenheit nutzen, um mich bei allen zu bedanken, die zum Gelingen dieser Arbeit beigetragen haben:

An erster Stelle möchte ich mich bei Norbert Pietralla zusätzlich zur fachlichen Betreuung auch für das in mich gesetzte Vertrauen, die stetige Förderung sowie die gewährten Freiheiten bei der Gestaltung und Umsetzung dieses Projektes bedanken. Durch die Aufnahme als Doktorand in seine Arbeitsgruppe hatte ich das große Privileg an einem spannenden und innovativen Thema arbeiten zu dürfen. Joachim Enders danke ich für viele konstruktive Hinweise zu Themen der Beschleunigerphysik. Michaela Arnold möchte ich für viele fachliche Ratschläge und zielführende Denkanstöße sowie das in mich gesetzte Vertrauen, mich eigenverantwortlich als Operateur am S-DALINAC arbeiten zu lassen, danken. Lars Jürgensen gilt ein besonderer Dank für die tatkräftige Unterstützung während des Strahlfädelns. Für die Hilfe bei auftretenden Fragen zur Hochfrequenztechnik möchte ich mich bei Ruben Grewe bedanken. Jonas Pforr und Simon Weih bin ich für zahlreiche Tipps zu den genutzten Strahldynamiksimulationsprogrammen dankbar. Manuel Dutine, Roger Flath und Felix Heyer danke ich für jegliche Hilfe bei der Konstruktion der Drahtscanner. Uwe Bonnes, Jan Hanten und Manuel Steinhorst gilt ein großer Dank für die hard- und softwareseitige Einbindung der Drahtscanner in das Kontrollsystem. Für die Hilfe bei kleineren und vielfältigen Aufgaben im Rahmen dieser Arbeit danke ich Adrian Brauch, Marco Fischer, Kurt Haßler, Maximilian Herbert, Manfred Hess, Maximilian Meier, Jürgen Müller, Dominic Schneider und Lennart Stobbe. Auch möchte ich mich bei Sergei Glukhov, Katharina Ide und Sonja Storck-Dutine für konstruktive Kommentare zur Dissertation bedanken. Der größte Dank gilt zweifelsfrei meinen Eltern für ihren stetigen Rückhalt während der Promotion und ihre bedingungslose Unterstützung während des gesamten Studiums.

Ich bedanke mich für die finanzielle Förderung durch die Deutsche Forschungsgemeinschaft im Rahmen des Graduiertenkollegs GRK 2128 AccelencE (Projektkennung 264883531), das Bundesministerium für Bildung und Forschung (Förderkennzeichen 05H21RDRB1) sowie das Land Hessen im Rahmen der Förderung Nukleare Photonik innerhalb des LOEWE-Programms und im Rahmen des Forschungscluster-Projekts ELEMENTS (Projektkennung 500/10.006), ohne welche diese Arbeit nicht möglich gewesen wäre.